Seismic Control of Rocking Structures Using Inerters

Rodrigo Thiers Moggia

Department of Civil and Environmental Engineering

Imperial College London

A thesis submitted for the degree of

Doctor of Philosophy

October 2020

Statement of Originality

I confirm that this submission is my own work. In it, I give references and citations whenever I refer to, describe or quote from the published, or unpublished, work of others.

Rodrigo Thiers Moggia

Copyright Declaration

The copyright of this thesis rests with the author. Unless otherwise indicated, its contents are licensed under a Creative Commons Attribution-Non Commercial 4.0 International Licence (CC BY-NC).

Under this licence, you may copy and redistribute the material in any medium or format. You may also create and distribute modified versions of the work. This is on the condition that: you credit the author and do not use it, or any derivative works, for a commercial purpose.

When reusing or sharing this work, ensure you make the licence terms clear to others by naming the licence and linking to the licence text. Where a work has been adapted, you should indicate that the work has been changed and describe those changes.

Please seek permission from the copyright holder for uses of this work that are not included in this licence or permitted under UK Copyright Law.

Acknowledgements

The work presented in this thesis was funded by ANID (Agencia Nacional de Investigación y Desarrollo, Chile), through grant no. 72170284. Their generous financial support is gratefully acknowledged.

I would like to thank Dr. Christian Málaga-Chuquitaype for his support and guidance during the different stages of this study. Without his acceptance and encouragement, this research would not have been possible.

Finally, I would like to express my deepest gratitude to my family in Chile, Totti, my family in the UK, and the friends I made along the way. Thanks for all your support and for making these last four years an unforgettable experience.

Abstract

When subjected to lateral excitations, a variety of structures, such as museum artefacts, historical buildings, bridge piers and post-tensioned walled buildings, might uplift and set into rocking motion. Although this mechanism can efficiently limit the internal forces at their base, the possibility of overturning or experiencing increased lateral deformations and accelerations may severely affect the functionality of rocking structures. Nevertheless, suitable seismic control strategies are presently limited and consist mostly in preventing rocking motion altogether, which may induce undesirable stress concentrations and lead to impractical interventions. This thesis examines the alternative of using supplemental rotational inertia devices to control the seismic response of rocking structures. The newly proposed strategy employs inerters, which are mechanical devices that develop resisting forces proportional to the relative acceleration between their terminals and can be combined with a clutch to ensure they act only in opposition to the motion. The fundamental dynamic behaviour of the system is firstly examined considering a free-standing rigid block model. By deriving the corresponding equations of motion, it is demonstrated that the inclusion of the inerter effectively reduces the frequency parameter of the block, resulting in lower seismic demands and enhanced stability due to the well-known size effects of the rocking behaviour. In subsequent chapters, this simplified single-degree-of-freedom model is gradually extended in order to incorporate the effects of post-tensioned tendons, structural flexibility and higher modes on the response. Overall, the analyses conducted under coherent pulses and real ground motion records show that inerter-equipped structures experience reduced seismic demands and lower probabilities of exceeding limit states usually associated with structural and non-structural damage.

The fundamental knowledge acquired in the first part of this thesis is finally applied to control the seismic response of rocking timber buildings. To this end, a set of three post-tensioned rocking walled buildings, comprising 3, 6 and 9 storeys, is designed following direct-displacement-based design guidelines. Additionally, a set of clutched and non-clutched ball-screw and gear inerters is designed using a newly proposed pre-dimensioning procedure. The performance of bare and protected structures with different levels of apparent mass ratios is then compared in terms of peak inter-storey drifts and floor accelerations. Special attention is paid to the resisting forces developed in the inerters and the mechanism to transfer them to the structural diaphragm. Likewise, the ability of the inerters to control higher-mode effects is

closely examined. Finally, a performance-based assessment with particular emphasis on non-structural and contents damage is conducted considering a database of 202 pulse-like ground motion records. Overall, the results of this assessments confirm the trends observed in the analytical examinations of the earlier chapters.

Contents

List of Figures

List of Tables

Notation

a_g	=	pulse acceleration amplitude
A_{pt}	=	area of the post-tensioned tendons
A_s	=	area of the external dissipaters
B	=	half-length of the rocking structure base
c	=	neutral axis depth
c_c	=	timber compression centroid
C_t	=	compressive force in the timber
DCR_{LS}	=	demand to capacity ratio for a given limit state LS
e_f	=	thickness of the flywheel
E_{fc}	=	energy of the fictitious full-contact phase
E_{par}	=	parallel-to-grain stiffness of the CLT panel
E_{pt}	=	modulus of elasticity of the post-tensioning tendons
E_r	=	energy of the fictitious rocking phase
E_{rs}	=	stiffness of the rocking surface
E_s	=	modulus of elasticity of the external dissipaters
$f_{y,pt}$	=	yielding stress of the post-tensioned tendons
$f_{y,s}$	=	yielding stress of the external dissipaters
F_r	=	resisting force in the inerter
F_{pt}	=	post-tensioning force
g	=	acceleration of gravity equal to $9.81[m/s^2]$
G	=	shear modulus of the CLT panel
H	=	height of a rocking structure
H_e	=	effective height of the substitute structure
I_0	=	moment of inertia of a rocking structure about its pivot points
I_{wi}	=	moment of inertia of the $i-th$ flywheel

J	=	linear momentum of a mass
J_p	=	rotational inertia of a multi-mass rocking structure
K_e	=	effective stiffness of the substitute structure
k_{el}	=	elastic deformation contribution factor
l_{ub}	=	unbonded length of the post-tensioning tendons
l'_{ub}	=	unbonded length of the external dissipaters
l_w	=	length of the base of a rocking wall
L_e	=	effective length of an equivalent Winkler spring
L_s	=	ball-screw lead
m	=	mass of the structure
m_e	=	effective mass of the substitute structure
m_r	=	inertance or apparent mass of the inerter
m_{sis}	=	seismic mass of the rocking structure
m_{ratio}	=	ratio between the seismic mass and the gravitational mass exerting the restoring moment
M_d	=	design moment
M_{pt}	=	moment provided by the post-tensioned tendons
M_s	=	moment provided by the external dissipaers
M_w	=	moment exerted by the gravity loads
p	=	frequency parameter of a rigid block
p_n	=	frequency parameter of a multi-mass rocking structure
p_σ	=	frequency parameter of an inerter-equipped rigid block
p_w	=	frequency parameter of a rocking wall
$p_{w,\sigma}$	=	frequency parameter of an inerter-equipped rocking wall
P_0	=	initial post-tensioning force
PGA	=	peak ground velocity
PGV	=	peak ground acceleration
r	=	coefficient of restitution of a rigid block
r_σ	=	coefficient of restitution of an inerter-equipped rocking structure
R_ξ	=	Design spectrum damping reduction factor
$S_a(T_1)$	=	5% damped spectral acceleration at the first fixed-base structural period
t_{uni}	=	uniform time duration
T_e	=	effective period of the substitute structure

T_g = period of the acceleration pulse

$T_{pt,i}$ = post-tensioning force in each tendon

u = elastic deformation in the rocking structure

u_{cr} = critical uplift displacement

$\ddot{u}_g$ = ground acceleration

V_b = base shear

W = weight of the rocking structure

α = rigid block slenderness

α_{cg} = slenderness of the centre of gravity of a multi-mass rocking structure

α_g = gear amplification ratio

δ_i = displacement profile for the DDBD procedure

Δ = inter-storey drift

$\Delta_{y,e}$ = yield displacement

Δ_d = displacement design for the DDBD procedure

ϵ_c = compression strain at the extreme fibre

$\epsilon_{t,y}$ = timber compression yielding stress

λ = re-centring ratio

Λ = moment of momentum of a mass

θ = rigid body rotation

θ_0 = initial base rotation

θ_f = rotational angle of the flywheel

θ_{imp} = imposed base rotation

θ_s = rotational angle of the screw

ϕ = inerter rotation reduction factor

ϕ_{el} = inerter displacement reduction factor

σ = apparent mass ratio = m_r/m

ω_g = circular frequency of the acceleration pulse

ω_n = fundamental frequency of a fixed-base structure

ξ = damping ratio

ξ_{fc} = damping ratio of the full-contact phase

ξ_{hyst} = hysteretic damping

ξ_{up} = damping ratio of the uplifted phase

Chapter 1

Preamble

1.1 Background

Traditional seismic design methodologies aim to prevent structural collapse by ensuring a minimum level of strength and deformation capacity in the lateral-load-resisting system of a building. Initially developed in the 50's and 60's [1], these strength and ductility considerations remain today as the basis for current seismic design provisions. Although, in general, this philosophy has succeeded in preventing structural collapse and protecting lives, recent earthquakes have revealed that in many cases the extent of damage can make repairs infeasible, highlighting the mismatch between social expectations and the actual seismic performance of civil structures. Over the last decades, the alternative approach of allowing structures to uplift and rock has been gaining popularity as a strategy to control structural damage during earthquakes. Although the survival of ancient Greek temples has been attributed to this unintended response mechanism [2], it was not until 1963 that George Housner elucidated a size-frequency scale effect that explained the counter-intuitive seismic stability of tall, slender rocking structures [3]. Since then, his simplified analytical model has been used to analyse the seismic response of a wide range of non-structural components, and has served as the basis for the development of low-damage post-tensioned rocking buildings [4]. While experimental studies have demonstrated that these systems can efficiently control structural damage, modern performance-based methodologies have also highlighted the importance of assessing non-structural and contents damage, which can significantly affect the total losses and downtime costs after a seismic event.

Most seismic control strategies for rocking structures have been proposed in the context of enhancing the stability of non-structural equipment and museum artefacts, adapting measures previously developed for fixed-base structures. Thus, several researchers have examined the potential advantages of using anchorages, base isolation and viscous dampers, among others, for the seismic protection of free-standing bodies. An alternative strategy that has received

increasing attention during the last decade is the use of supplemental rotational inertia. Based on this concept, a device capable of generating a resisting force proportional to the relative acceleration between its terminals was developed in the late 90s [5]. Under the name inerter, this device was re-discovered in the west [6] and has subsequently been applied to the seismic protection of fixed-base civil structures [7, 8], where the seismic-induced displacements are governed primarily by the structural stiffness, damping, and strength [9]. In the case of rocking structures, the dominant motion is rotational and the seismic stability originates mainly from the difficulty of mobilizing their rotational inertia. In this context, the use of inerters appears as an attractive alternative to improve the seismic performance of rocking structures.

1.2 Motivation and objectives

The previous section has highlighted the potential advantages of employing inerters to control the seismic response of rocking structures. A comprehensive evaluation of this strategy requires, in the first place, the development of analytical models that can capture the fundamental dynamic behaviour of the system. Similarly, reliable numerical tools are needed to assess its implementation in more complex structural configurations such as post-tensioned rocking buildings. Importantly, the efficiency of the proposed strategy ought to be evaluated within a performance-based framework, including limit states associated with both structural and non-structural damage.

Motivated by the above-mentioned factors, this thesis aims to: *provide a comprehensive examination of the dynamic response of rocking structures equipped with supplemental rotational inertia devices, and explore the alternative of using inerters to improve the seismic performance of post-tensioned timber buildings.*

In light of the above, a number of issues related to the seismic behaviour of rocking structures and post-tensioned timber systems are examined in this thesis. To this end, analytical and numerical methods are formulated and applied as outlined in the following section.

1.3 Outline of the thesis

As stated above, this thesis aims to provide a comprehensive examination of the seismic performance of inerter-equipped rocking structures. To this end, a simplified analytical model of the system is presented in Chapter 3 and gradually extended throughout the thesis in order to represent increasingly complex dynamic phenomena. Firstly, a revision of previous work on the subject is presented in Chapter 2. The aim of this literature review is to identify existing research gaps and to set the context for the contributions made in subsequent chapters.

Chapter 3 examines the fundamental dynamic behaviour of rocking structures equipped with inerters using a rigid block approximation. By deriving the equations of motion of the system, it is demonstrated that the inclusion of the inerter effectively reduces the frequency parameter of the block. Importantly, this reduction generally results in lower rotation seismic demands and enhanced stability due to the well-known size effects of the rocking behaviour. Additionally, the alternative of incorporating a clutch to ensure that the inerter only resists the motion of the structure is also evaluated. The proposed model is then used to study the effect of the inerter device on self-similarity, rocking demands and the overturning response of free-standing blocks under a wide range of trigonometric pulse excitations and real pulse-like ground motions.

In Chapter 4, the previously described model is adapted in order to analyse the response of systems representative of rocking walled buildings. To this end, post-tensioned tendons and a seismic mass independent from the weight exerting the restoring moment are introduced. The effects of these features on the rocking response of the structure are assessed in terms of maximum rotations and peak angular accelerations for a wide range of pulse excitations. Subsequently, the inerter device is introduced and original equations that describe the rocking motion of the post-tensioned wall-inerter system are derived. In addition to the reductions in rotation and acceleration demands, the effects of the inerter on the base shear are also evaluated.

Chapter 5 evaluates the effect of structural flexibility on the efficiency of the proposed seismic control strategy. To this end, the analytical model used in previous chapters is modified to allow elastic deformations in the oscillator, while two different impact formulations are implemented and compared. The results of analyses under coherent pulses demonstrate that, although the inerter does not significantly reduce the elastic deformations in the structure, it does control its base rotation response, resulting in considerably lower overall drift demands. The response of flexible rocking structures under high frequency excitations is also considered, while the possibility of using inerters to control the elastic deformation at uplifted resonance is examined. The conclusions obtained under these coherent cycloidal pulses are then extended to real ground motions by evaluating the response of rocking structures to a set of recorded ground motions.

While Chapters 3 to 5 examine the rocking response of simplified rigid blocks and single-mass oscillators, Chapter 6 considers multi-mass rocking structures connected to inerters at the first-mass level. To this end, a previously proposed finite element model is implemented in OpenSees [10] and extended to incorporate the effects of grounded supplemental rotational inertia devices. The full structural model is subsequently validated against previous experimental and analytical results, and used to examine the effect of the inerter on the rotation and

elastic deformation demands of a set of 3, 6 and 9-storey structures. Additionally, the interaction between impact forces and higher vibration modes is examined, while the effectiveness of the inerter for controlling the associated acceleration demands and increased bending moments is also evaluated. Like in previous chapters, the conclusions obtained for analytical pulses are later extended to real earthquakes by evaluating the response of the structural systems to a set of pulse-like ground motion records.

In Chapter 7, the fundamental knowledge acquired in previous chapters is applied to the control of the seismic response of post-tensioned timber wall structural systems. Accordingly, a representative set of three post-tensioned rocking walled buildings, comprising 3, 6 and 9 storeys, is designed following direct-displacement based design guidelines. Based on conclusions drawn from the analytical models presented in Chapters 3 to 6, a simplified procedure to pre-dimension the inerter device is proposed and used to design a set of ball-screw and gear inerters, with and without clutches. In a first stage, the performance of bare and protected structures with different levels of apparent mass ratios is assessed and compared considering a set of 7 records consistent with the displacement design spectrum. Special attention is paid to the resisting force developed in the inerter and the mechanism to transfer it to the structural diaphragm. Likewise, the ability of the inerters to control higher-mode effects is closely examined. Finally, a performance-based assessment with particular emphasis on non-structural and contents damage is conducted considering a database of 202 real pulse-like ground motion records. Overall, the results of this assessment are in line with conclusions obtained in previous analyses, thus confirming the response improvements predicted by the simplified models developed in the earlier chapters.

In the final chapter, a summary of the main conclusions is drawn alongside recommendations for future research on the topics addressed in this thesis.

1.4 Dissemination

The research work presented in this thesis has contributed to the following publications:

Peer-reviewed journals

- Thiers-Moggia R, Malaga Chuquitaype C, 2020, Seismic control of flexible rocking structures using inerters, *Earthquake Engineering and Structural Dynamics*, ISSN: 0098-8847

- Thiers-Moggia R, Málaga-Chuquitaype C, 2020, Dynamic response of post-tensioned rocking structures with inerters, *International Journal of Mechanical Sciences*, Vol: 187, Pages: 1-15, ISSN: 0020-7403
- Thiers-Moggia R, Malaga Chuquitaype C, 2019, Seismic protection of rocking structures with inerters, *Earthquake Engineering and Structural Dynamics*, Vol: 48, Pages: 528-547, ISSN: 0098-8847
- Malaga Chuquitaype C, Menendez-Vicente C, Thiers-Moggia R, 2019, Experimental and numerical assessment of the seismic response of steel structures with clutched inerters, *Soil Dynamics and Earthquake Engineering*, Vol: 121, Pages: 200-211, ISSN: 0267-7261
- Thiers-Moggia R, Malaga Chuquitaype C, 2020, Effect of base-level inerters on higher mode response of uplifting structures (under review)
- Thiers-Moggia R, Malaga Chuquitaype C, 2020, Seismic control of rocking Cross-Laminated Timber buildings using inerters (under preparation)

Conference papers

- Thiers-Moggia R, Málaga-Chuquitaype C, 2020, Performance-based seismic assessment of rocking Cross-Laminated Timber buildings protected with inerters, World Conference on Timber Engineering (submitted)
- Thiers-Moggia R, Málaga-Chuquitaype C, 2020, Seismic protection of multi-storey rocking structures with inerters, XI International Conference on Structural Dynamics (EuroDyn2020)
- Thiers-Moggia R, Malaga Chuquitaype C, 2019, Seismic control of post-tensioned rocking walls with inerters, SECED 2019, Earthquake Risk and Engineering Towards a Resilient World
- Thiers Moggia R, Malaga Chuquitaype C, 2018, Seismic protection of cross-laminated timber buildings with supplemental inertia devices, 16th European Conference on Earthquake Engineering (16ECEE)

Chapter 2

Literature Review

2.1 Introduction

This chapter presents a brief summary of the most relevant studies that precede the work described in this thesis. The main aim of this review is to set up the context for the contributions made in subsequent chapters. Considering the scope of the research topic, it is natural to organize the literature review in two main categories: (i) rocking structures, and (ii) supplemental rotational inertia devices. This approach intends to facilitate the recognition of research needs in the field of uplifting structures and the potential advantages of employing inerter devices to improve their dynamic response. In the following section, previous research on rocking structures is reviewed and divided into three main sections: fundamental dynamics, seismic control strategies, and applications to building structures. Subsequently, preceding studies regarding supplemental rotational inertia devices are presented with particular emphasis on inerter realizations and their application to vibration control in civil structures. The chapter concludes with a summary of research needs.

2.2 Rocking structures

2.2.1 Fundamentals of rocking dynamics

The dynamic behaviour of a wide range of structural systems, including historical buildings [11, 12], post-tensioned structures [13, 14], bridges [15], walled structures [16], and unanchored equipment [17,18] can be characterized by the rocking response of a rigid block. After noting the survival of several tall slender structures following severe ground shaking, Housner [3] examined the dynamic behaviour of rigid bodies and developed equations to describe their rocking motion based on an elegant use of angular momentum conservation through impact. Using this simplified analytical model, Housner demonstrated that the oscillation period of a rocking structure depends on the amplitude of the base rotation. His study also unveiled

an unexpected scale effect which makes the larger of two geometrically similar blocks more stable than the smaller one. Moreover, Housner demonstrated that a free-standing block subjected to earthquake motion is more stable than it would be inferred from constant lateral force analyses. Several researchers have built on Housner's classical model, extending the analysis to rocking frames [19, 20] and 3-dimensional rocking structures [21, 22].

Housner's analytical model assumes that the rocking base is perfectly rigid and that friction at the contact surface is enough to prevent sliding. The implications of these assumptions on the stability of rocking bodies has been studied in a series of subsequent papers. Ishiyima [23] and Shenton and Jones [24] investigated the interaction between sliding and uplifting, while the deformability of the ground was considered in Psycharis and Jennings [25], Koh et al. [26], and Palmeri and Makris [27]. The results of these studies demonstrated the relevance of such considerations, highlighting that they should not be omitted unless they can be minimized by mechanical means.

Aside from the equations of motion, a complete description of the dynamic response of a rocking structure entails an appropriate description of energy dissipation during impact. Most of the studies concerning rigid blocks have considered a classical impact framework, where impact forces are assumed to be instantaneous and concentrated at the pivot corners. Under these assumptions, conservation of angular momentum about the post-impact pivot point results in a coefficient of restitution that depends only on the geometrical characteristics of the structure [3]. Although this approach rightly identifies the slenderness of the block as the main parameter affecting impact, several experimental studies have demonstrated the inaccuracy of these assumptions [28, 29]. An alternative impact model was proposed by Chopra and Yim [30] in which the kinetic energy associated with the vertical component of the mass velocity is completely dissipated during impact. This approach has later been shown to adequately predict the response of single-mass rocking oscillators [31, 32]. Recognizing that immediate rocking is only one of the possible post-impact states of a rocking structure, Giouvanidis and Dimitrakopoulos [33] proposed a nonsmooth dynamic approach and studied the conditions under which full contact, bouncing and flying phases can occur. Acikgoz and DeJong [34], on the other hand, simulated the impact behaviour of flexible rocking structures exhibiting large rocking angles with impulsive Dirac-delta forces, generalizing the approach originally introduced for slender rigid rocking blocks by Prieto et al. [35].

Although a precise prediction of the full response history of a rocking oscillator under a given ground motion may be impractical [32] due to the strong non-linearities involved (e.g. negative stiffness [36]) and the uncertainties associated with modelling impact phenomena [33, 37], Housner's model has been shown capable of predicting the main statistics of the seismic response of rocking structures [38]. In this regard, early studies recognized

that rocking motion is highly sensitive to the velocity and acceleration characteristics of the ground motion [23]. Dimitrakopoulos and DeJong [39] studied the deterministic response of rocking structures to simplified pulse-type excitations and proposed a group of dimensionless-orientationless parameters that define a unique response for slender blocks and a practically self-similar response for nonslender structures. Several other researchers have proposed the use of intensity measures based on the peak ground velocity (PGV) and peak ground acceleration (PGA) [40], [41] while Giouvanidis and Dimitrakopoulos [42] found that an intensity measure that efficiently correlates with the rocking demand is not necessarily efficient for predicting overturning. More specifically, they showed that rocking amplification is sensitive to the duration of the ground motion exceeding the uplifting threshold, whereas the overturning response depends strongly on the velocity and acceleration features of the ground excitation.

While some structural systems may be reasonably modelled as rigid bodies (i.e. Greek temples, stocky electrical equipment), other practical applications (like buildings, wind turbine support towers, etc.) will exhibit appreciable degrees of flexibility. Moreover, some of the underlying assumptions of the analytical models used to study rigid bodies imply that the structures are slender, and therefore more likely to deform during the rocking motion. This problem was first studied by Chopra and Yim [30] who considered a flexible single-degree of freedom system attached to a rigid base allowed to uplift. Assuming that the structural dimensions and excitation are such that the resulting rotation and deformation responses are small, they derived the equations that govern the motion of the system and demonstrated that foundation-uplift can reduce the associated base shear and moment demands. Oliveto et al. [43] extended Chopra and Yim's model to large deformations, while Acikgoz and DeJong [44] further developed Housner's impact formulation and used it to examine the interaction between rocking and elasticity. Their analyses showed that, in general, flexible structures are more stable than their rigid counterparts, but also highlighted the possibility of significant deformations being generated in the oscillator due to uplifted resonance under high-frequency ground motions. Accordingly, they concluded that stiffer configurations are more likely to fail due to overturning, while more flexible structures are susceptible to suffer excessive deformations. Further analytical and experimental studies reached similar conclusions [31, 32].

Psycharis [45] and Yim and Chopra [46] first addressed the problem of multi-storey rocking structures considering a shear frame supported by a viscoelastic two-spring foundation. Assuming the presence of classical orthogonal vibration modes and small rotations during the rocking motion, their studies concluded that a reasonable approximation of the maximum response of multi-storey structures could be obtained by considering that rocking only influences the response contribution of the first mode of vibration. Accordingly, higher vibration modes were considered to be uncoupled from the rocking action. Acikgoz and DeJong [34] later extended this formulation to large rotations and introduced a Dirac-delta impact model able to

describe the interaction of impact forces with structural vibrations. Their study also proposed a modal decomposition method, demonstrating that the vibration characteristics of several vibration modes are affected by the rocking action, and that these modes can be excited at impact. Importantly, their experimental results [47] identified high acceleration spikes during impact which have the potential of causing significant non-structural and contents damage.

2.2.2 Seismic protection of rocking structures

In comparison with studies concerning the estimation of rocking response, investigations on control strategies suitable to rocking bodies have been more limited and have mainly concentrated on the protection of museum artefacts and nonstructural equipment [48, 49]. Early strategies were based on simple measures, such as lowering the centre of mass or anchoring the object to a fixed support [50, 51]. While the former approach is not very practical, the latter prevents the rigid-body rocking motion and may therefore induce undesirable deformations that can damage the object. Makris and Zhang [50] first analysed the stability of rigid blocks tied down with brittle and ductile restrainers, concluding that anchorages can have an adverse effect on the stability of the structure. Aiming to address this issue, Ceravolo et al. [49, 52] proposed the use of semi-active anchorages with variable stiffness and compared different strategies for their implementation. Their analyses showed that feedback control strategies based on the block's angular position and velocity significantly improved its dynamic response and stability. Importantly, the controlled cases were generally more stable than both the free-standing blocks and structures anchored with passive restraint systems such as elastic-brittle plates and viscous dampers.

Although the previous proposals can reduce the overturning vulnerability of free-standing bodies, they are generally not suitable for rocking building structures. Recognizing the advantages associated with the reduction of shear and moment demands in rocking structures, more recent studies have focused on controlling the rotation response instead of completely hampering it. Vassiliou and Makris [53] built on Housner's basic model and studied the dynamic response of a vertically restrained solitary rocking column, concluding that post-tensioned tendons can reduce rotation demands in smaller columns subjected to long-period excitations but have little effect on taller structures. Dimitrakopoulos and DeJong [39] studied the response of rigid blocks connected to linear viscous dampers and showed that supplemental damping can efficiently improve the seismic stability of rocking structures. A similar approach was recently applied by Makris and Aghagholizadeh [54] to the protection of free-standing bridge piers. Alternative passive approaches have also been proposed by a number of researchers. De Leo et al. [55] studied the use of a pendulum mass damper hinged at the top of a rigid block, showing that the system is effective for a limited range of frequencies. Vassiliou and Makris [56], on the other hand, examined the rocking response and stability of rigid bodies standing free on

three different types of isolated bases concluding that seismic isolation is only beneficial for small structures. More recently, Pan and Málaga-Chuquitaype [57] explored the alternative of using external resonators as a means to control the peak seismic rotational demands of rocking monumental structures. Their study highlighted the need to provide innovative nonintrusive solutions to attenuate the rocking response of historical buildings and monuments.

2.2.3 Application of rocking to building structures

During the last decades, the advantages of rocking have been applied to the development of a family of self-centring systems that can sustain large lateral deformations with no significant damage. By allowing structural connections to open and rock, rotation demands can be concentrated in these pre-defined sections while the rest of the structural elements remain largely elastic. Based on this concept, several low damage frame [4, 58] and shear wall systems [59, 60] have been proposed and experimentally assessed. In such configurations, post-tensioned tendons are usually incorporated in order to increase the lateral strength and re-centring capabilities of the system. Likewise, additional energy dissipation can be provided through unbonded mild steel reinforcement [61] or external devices such as buckling-restrained bars [62] or U-shaped flexural plates (UFPs) [63, 64]. The combination of the self-centring effect provided by the vertical loads (self-weight and post-tensioned tendons) and the energy dissipated by the external devices results in the typical flag-shape hysteretic behaviour of rocking structural systems.

The structural performance of post-tensioned rocking systems was systematically evaluated in the PREcast Structural Seismic Systems (PRESSS) program [4, 64]. This study extensively assessed the response of post-tensioned concrete beam-to-column and wall-base rocking connections, developing comprehensive design procedures [65] and showing, through a series of experiments, that the proposed hybrid system had a stable cyclic response, good ductility and minimal damage at large drifts [64, 66]. Later studies have also applied the advantages of post-tensioned systems to the design of self-centring bridge piers [14, 67, 68]. As the concept of hybrid rocking connections is not significantly affected by the mechanical properties of the structural members, the system has later been extended to other construction materials. Steel beam-to-column post-tensioned connections were developed by Garlock et al. [69] and Christopoulos et al. [58], while Eatherton et al. [70] conducted experiments on braced frames allowed to rock about their base. Similarly, Sause et al. [71] conducted a series of large scale experimental studies on post-tensioned base rocking concentrically braced frames and Pollino and Bruneau [72] developed a controlled base rocking pier for steel truss bridges.

Recognizing the ductility limitations of traditional timber connectors [73, 74], Palermo et al. [75, 76] proposed the implementation of post-tensioned rocking connections as a solution for

multi-storey timber buildings in earthquake-prone regions. In this case, solid timber elements were connected with unbonded post-tensioned tendons, while additional energy dissipation was provided through internal epoxied rods or externally mounted replaceable devices. To reduce the probability of timber crushing at the contact zone, Laminated Veneer Lumber (LVL) elements were used for the structural members. Iqbal et al. [77] extended the hybrid system proposed by Palermo et al. to double-wall sub-assemblies, and conducted several cyclic quasi-static and pseudo-dynamic tests. The modified system consisted of two post-tensioned LVL panels coupled with U-shaped Flexural Plates (UFPs). As with reinforced concrete, the proposed timber rocking systems exhibited good energy dissipation and re-centring capabilities with minimal damage at large deformations. Importantly, the concept of post-tensioned timber is not restricted to LVL, and has also been applied to Glulam [78] and Cross-Laminated Timber (CLT) structures [79].

While the experimental studies mentioned above have provided useful information regarding the behaviour of post-tensioned rocking connections, simplified analytical procedures are required to estimate the response of the system for design purposes. Since Bernoulli's hypothesis of strain compatibility is no longer valid after decompression, an alternative approach is needed for the analysis of rocking sections. The monolithic beam analogy, developed by Pampanin et al. [80], provides a member compatibility condition that allows to relate the imposed rotation with the strain profile in the connected members. This methodology, originally developed for concrete structures, has later been adapted and used in cross-sectional analysis procedures for post-tensioned timber sections [61, 81].

Performance-based design guidelines for post-tensioned rocking systems were first introduced during the PRESSS program. Based on experimental observations, Kurama et al. [59,65] identified a series of limit states for post-tensioned concrete walls and proposed a seismic design approach based on pre-defined performance objectives. More recently, several seismic design methodologies for post-tensioned rocking structures [82–84] have been proposed based on the Direct-Displacement-Based Design (DDBD) procedure developed by Priestley et al. [85]. Within this framework, structures are designed to achieve, rather than to be bounded by, a specific limit state under a given level of seismic intensity. Special considerations related to the displacement profile, yield displacement and equivalent viscous damping in rocking timber structures have been extensively discussed in [61, 81, 84, 86].

Simplified finite element models for post-tensioned rocking systems have been developed and validated against experimental results. Building on Priestley's early model [64], Spieth et al. [87] developed a multi-spring contact element capable of accurately capturing the global behaviour of rocking frames, including local effects such as neutral axis shift and tendon elongation. In this formulation, the overall stiffness of the contact surface is weighted

and distributed using a Lobatto Integration scheme. Although alternative integration methods can also be used, the adopted scheme has the natural advantage of placing springs on the boundaries of the integration interval, thus providing contact points at the edges of the rocking section. The study also investigated the influence of the number of integration points, concluding that at least eight springs are required in order to adequately predict the response of a rocking section. Aiming to incorporate energy dissipation during impact, Vassiliou et al. [88] extended the multi-spring formulation including a dissipative model of the ground under the base rocking surface. Multi-spring elements have subsequently been adapted for the analysis of post-tensioned concrete and timber cantilever walls [61, 81, 83].

In terms of design approaches for rocking structures, capacity design is a seismic design philosophy that aims to ensure a structure undergoes controlled ductile behaviour during an earthquake. The methodology requires the assumption of a collapse mechanism where selected non-linear zones are designed to withstand large ductility demands while the rest of the structure remains elastic. Considering the idealized case of non-positive post-uplift stiffness, no further forces that increase the moment at the base of a cantilever wall can be applied after the opening of the rocking section. The contribution of the first mode is therefore limited by the formation of the mechanism. Nevertheless, higher modes can still be excited, increasing the bending moments and shear forces throughout the structure [89]. Moreover, previous research has suggested that rocking structures can be more susceptible to higher-mode effects than an equivalent fixed-base structure [90]. Wiebe et al. examined the alternative of using multiple rocking sections over the height of a base-rocking system in order to control the higher-mode response [89]. Results of an experimental program [91, 92] showed that the proposed strategy significantly reduced peak storey shears, floor accelerations, and bending moments for ground motions that had big amplitudes or considerable high-frequency content, although an average increase of 18% was observed in the peak roof displacements.

Modern design frameworks generally quantify seismic risk in terms of overall performance, looking at both the structural and non-structural components of a building [93]. Although post-tensioned rocking systems have proven to be highly effective in controlling structural damage, very limited attention has been dedicated to the associated floor acceleration demands. A preliminary assessment conducted by Newcombe [81] revealed that significant inter-storey drifts and floor accelerations can develop in post-tensioned timber buildings for the design earthquake intensity. Similarly, Aragaw and Calvi [94] examined the non-linear response of a set of base-rocking wall buildings and proposed two simplified methodologies to estimate floor acceleration spectra in this type of structures. Their study highlighted the importance of an adequate consideration of seismic accelerations in the design of non-structural elements and pointed out the need for control strategies to limit these demands.

2.3 Supplemental rotational inertia devices

2.3.1 The inerter

An efficient seismic control strategy that has been gaining popularity over the last years involves the use of supplemental rotational inertia. Based on this concept, Arakaki et al. [5] developed a damper formed of a cylindrical mass rotating inside a chamber filled with a viscous fluid. This mechanical arrangement, known as inerter, develops a resisting force that is proportional to the relative acceleration between its terminals. Accordingly, in a force-current/velocity-voltage analogy, the inerter is the mechanical analogue of the capacitor and its constant of proportionality is called inertance (with units of mass) [6].Typical inerter realizations employ rack-and-pynion [6,95] or ball-screw mechanisms [7,96] to transform the relative displacement between the terminals into a rotation in a flywheel. Papageorgiou et al. [97, 98] tested both of these configurations, showing that rotation-amplification mechanisms can significantly increase the inertance of the device while keeping the associated gravitational mass minimum. Upon its conceptual development and experimental validation, the inerter has been used to improve the dynamic performance of vehicle suspension systems under the name of J-damper [99, 100].

Alternative inerter implementations have also been proposed by a number of researchers. Exploiting the inertial effect of a fluid flowing in a helical channel, Swift et al. [101] developed a hydraulic inerter capable of reducing the ratcheting, backlash and friction phenomena that can significantly affect the performance of mechanical devices [102]. The proposed hydraulic inerter also benefited from the inherent damping associated with the fluid's viscosity and density. Gonzalez-Buelga et al. [103], on the other hand, proposed an alternative inerter realization using a linear motor whose mechanical rotation was transformed into a voltage difference across the transducer coil. Their study highlighted the potential of electromagnetic devices for the development of real time tunable vibration absorbers and energy harvesting.

2.3.2 Vibration control of civil structures using inerters

Recent studies have highlighted the potential advantages of employing inerters to control the seismic response of civil structures. Hwang et al. [104] investigated the vibration control effect of a rotational inertia damper combined with a toggle bracing on a fixed-base single degree-of-freedom structure. A similar evaluation was conducted by Ikago et al. [7], who included a flywheel to increase the inertial effects of the device. Makris and Kampas [95] studied the case of an elastic frame connected to rack-pinion-flywheel system and demonstrated that inerters are particularly effective in reducing peak displacements for long-period structures. Importantly, they noted that this happens at the expense of transferring considerable forces to the support of the flywheels. Their study also explored the use of a clutch to ensure the inerter

only resists the structural motion without inducing additional deformations, a strategy that was further investigated experimentally and numerically by Málaga-Chuquitaype et al. [105]. The proposed arrangement was able to further reduce the structural displacements, whereas mixed results were obtained for the transferred forces. Chen et al. [106], on the other hand, studied the influence of supplemental rotational inertia on the natural frequencies of multi-degree-of-freedom systems.

Several applications of the inerter have been proposed within the context of enhancing the performance of tuned mass dampers. Ikago et al. [7, 107] proposed a Tuned Viscous Mass Damper (TVMD) consisting of a viscous inerter connected in series to a linear spring and used it to control the response of a simplified 10-storey structure. In this case, the TVMDs were equally distributed along the height of the building, following the recommendations given by Takewaki et al. [108]. Similarly, Lazar et al. [8] developed a Tuned Inerter Damper (TID) and presented expressions to obtain the optimal parameters of the device based on H_∞ optimization criteria [109,110]. Their study also investigated the influence of the vertical distribution of dampers, concluding that the optimal configuration for TIDs corresponds to a single grounded device connected at the first level. A similar proposal was made by Giaralis and Taflanidis [111], who examined the performance of Tuned Mass Damper-Inerter systems (TMDI) under stochastic excitations and proposed an optimum design framework for their implementation. The main advantages of these configurations included an improved reduction of peak deformations and a wider suppression band. The mass-amplification effect of the inerter has also been harnessed to improve the performance of vibration barriers [57, 112] and to reduce the displacement demands of base isolation systems [113, 114]. In a later study, Makris [115] examined the basic frequency-response functions of simple inertoelastic and inertoviscous elements, consisting of a combination of inerters, springs and dashpots. Importantly, all these previous studies have focused on the seismic control of fixed-based structures and the potential advantages of using inerters to control the seismic response of rocking structures are still unexplored.

2.4 Summary

This chapter has presented a brief summary of previous work with the aim of identifying research needs in the fields of rocking structures and supplemental rotational inertia devices. The conclusions drawn from this review, which in turn have motivated the contributions presented in subsequent chapters, are described below.

- Applications of the inerter to seismic control strategies have exclusively focused on the protection of fixed-based systems, where the lateral deformations are controlled primarily via stiffness, damping and strength. In the case of rocking structures, the dominant

motion is rotational and the seismic stability originates mainly from the difficulty of mobilizing their rotational inertia. In this context, the use of supplemental rotational inertia devices appears as an attractive alternative to improve the seismic performance of rocking structures. This is the main concept advanced in this thesis. The fundamental dynamic behaviour of rocking blocks equipped with inerters is thoroughly studied in Chapter 3, while Chapters 4 and 5 assess the effects of post-tensioning and compliance on the efficiency of the proposed strategy.

- While extensive research has been conducted on the fundamental dynamics of the rocking motion, investigations on control strategies suitable to rocking structures have been more limited and have mainly concentrated on the protection of museum artefacts and non-structural equipment. Some of these strategies have attempted to prevent the rocking motion altogether, potentially inducing deformations that can damage the objects. On the other hand, alternatives that aim to control the rotation response without hampering it are usually only effective for a limited range of frequencies or structural dimensions. These observations highlight the need for more robust non-intrusive solutions suitable for uplifting bodies such as museum artefacts and monuments. Chapters 3 and 5 address this issue offering a comprehensive assessment of the seismic demands and overturning response of bare and inerter-equipped rigid and flexible rocking oscillators. Likewise, strategies suitable for larger-scale structures, such as historical buildings and post-tensioned systems, are also needed. In this regard, Chapters 4 and 6 examine the efficiency of the proposed seismic control strategy for SDOF and MDOF rocking systems representative of building structures.

- Despite the relevance of peak accelerations in performance-based assessments, the seismic response of rocking structures has been examined mainly in terms of rotation demands and overturning stability. Moreover, the effect of previously proposed seismic control strategies on the acceleration response of rocking bodies has been mostly ignored. These issues are addressed in Chapters 3 to 5, where an in-depth examination of the acceleration demands of bare and inerter-equipped rocking structures is presented.

- The lack of numerical models for the inerter in finite element software has prevented the evaluation of more complex structural systems. This issue is addressed in Chapter 6, where a numerical strategy to represent the inerter in finite element frameworks is presented and implemented in OpenSees.

- Although strategies involving multiple rocking sections have been shown to effectively control higher-mode effects in MDOF systems, numerical and experimental studies suggest that they can also increase the associated roof displacements. In this context, Chapters 6 and 7 explore the alternative of using inerters to control the higher-mode

response of base-rocking MDOF systems, while also reducing the total lateral deformations.

- Post-tensioned rocking systems have proven to be highly effective in controlling structural damage in building applications. Nevertheless, the associated drift and floor acceleration demands, which can cause significant non-structural and contents damage, have been mostly overlooked. Moreover, suitable strategies to control these seismic demands have not been proposed. Chapter 7 addresses these issues presenting a comprehensive performance-based assessment of post-tensioned timber buildings considering limit states related to non-structural and contents damage. Additionally, the inerter-based strategy studied in the previous chapters is applied to the protection of three case-study structures in Chapter 7.

Chapter 3

Rocking response of rigid blocks equipped with inerters

3.1 Introduction

The literature review presented in the previous chapter has highlighted the potential advantages of employing inerters for the seismic control of rocking structures. The main concept behind this strategy entails increasing the rotational inertia of the free-standing body, thus enhancing its dynamic and seismic stability. In this chapter, a comprehensive examination of the rocking response of rigid blocks equipped with supplemental rotational inertia devices is presented. Besides comparing the response of rocking oscillators equipped with an inerter that can oppose and drive the motion against the response of uncontrolled rocking blocks, the chapter also considers a pair of clutched inerters designed to only resist the motion of the structure. The following section presents original equations that govern the motion of the inerter-rocking system derived by considering a simple discontinuous acceleration-based function for the clutch. The proposed analytical model is subsequently used to assess the effects of the inerter on the self-similar scaling of the response, as well as on associated rocking demands and overturning potential of the blocks under a wide range of trigonometric pulse excitations. Special attention is also dedicated to the effect of the inerter on the impact phenomenon. Finally, a probabilistic assessment of the seismic performance of rocking blocks is conducted using a set of 202 pulse-like ground motions obtained from the Pacific Earthquake Engineering Research Center (PEER) database. The results of the assessment demonstrate that rocking structures equipped with a single inerter experience smaller rotation and acceleration demands than unprotected ones and that the incorporation of the clutch further reduces their rotation demands as well as their probability of overturning.

3.2 Rocking structures and the concept of supplemental rotational inertia

3.2.1 Seismic response of rigid rocking blocks

When subjected to a horizontal ground excitation, $\ddot{u}_g$, the rigid block shown in Figure 3.1 uplifts and starts rocking if the overturning moment exceeds the restoring moment due to its self-weight; this condition can be expressed as follows:

$$|\ddot{u}_g| \geq g \, \tan\alpha \tag{3.1}$$

where g is the acceleration of gravity and α is the slenderness of the block. Assuming that no sliding or bouncing occurs during impact, the planar rocking motion of the structure can be described by means of Housner's model [3] as follows:

$$\ddot{\theta} = -p^2 \left(\sin(\alpha \, sgn(\theta) - \theta) + \frac{\ddot{u}_g}{g} \cos(\alpha \, sgn(\theta) - \theta) \right) \tag{3.2}$$

Although the free vibration frequency of a rocking block is not constant, its dynamic properties can be characterized by the frequency parameter p, which represents the in-plane pendulum frequency of the same block dangling from its pivot point [116]. For a rectangular block $p = \sqrt{3g/4R}$.

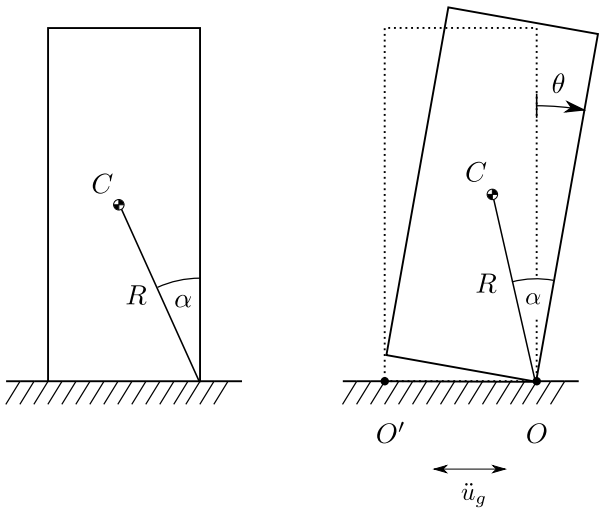

Figure 3.1: Rigid block under a horizontal ground excitation.

When the angle of rotation θ reverses, the block impacts on the base and loses some of its kinetic energy. Assuming that there is no bouncing, the block then continues rotating smoothly about point O'. Energy losses due to impact are usually considered through a coefficient of restitution that relates the pre-impact angular velocity, $\dot{\theta}_1$, to the post-impact angular velocity,

$\dot{\theta}_2$.

$$r = \left(\frac{\dot{\theta}_2}{\dot{\theta}_1} \right)^2 \tag{3.3}$$

By equating the moment of momentum before and after impact, Housner derived an expression for the coefficient of restitution that depends only on the geometry of the rectangular block.

$$r = \left(1 - \frac{3}{2} \sin^2 \alpha \right)^2 \tag{3.4}$$

3.2.2 Supplemental rotational inertia: the inerter

As previously mentioned, the inerter is a linear mechanical device that develops a resisting force proportional to the relative acceleration between its terminals [6]. Although several types of inerters have been proposed and patented, the general properties of the system can be studied by considering the particular case of a rack-pinion-flywheel device, like the one shown in Figure 3.2a. The system consists of two flywheels of radius R_i and mass m_{wi}, free to rotate about axis O_i and connected to a linear rack through a pinion-gear mechanism. Figure 3.2b shows the free-body diagram of the rotating flywheels.

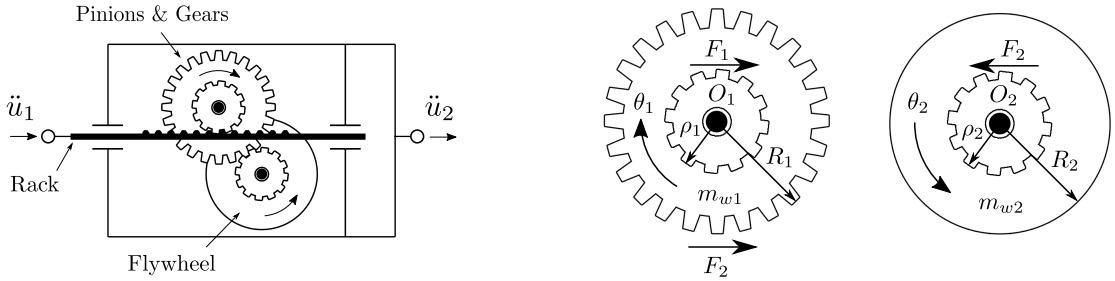

(a) Two-flywheel configuration.

(b) Free-body diagram of the flywheels.

Figure 3.2: Rack-pynion-flywheel supplemental rotational inertia system.

When a positive relative displacement is imposed ($u_2 > u_1$), the first flywheel is subjected to a clockwise rotation θ_1, while the second flywheel rotates θ_2 anticlockwise. If there is no slippage between the rack, pinions, and gears, the rotations and relative displacement are related through:

$$\theta_1 = \frac{u_2 - u_1}{\rho_1} \quad ; \quad \theta_2 = \frac{(u_2 - u_1)\, R_1}{\rho_1\, \rho_2} \tag{3.5}$$

Evaluating the rotational equilibrium of the flywheels around pivot points O_1 and O_2 yields:

$$F_1\, \rho_1 = I_{w1}\, \ddot{\theta}_1 + F_2\, R_1 \tag{3.6}$$

$$F_2\,\rho_2 = I_{w2}\,\ddot{\theta}_2 \tag{3.7}$$

where $I_{wi} = \frac{1}{2}\,m_{wi}\,R_i^2$ is the moment of inertia of the flywheel around point O_i. Replacing Equation 3.5 into Equation 3.6 and combining it with 3.7 leads to:

$$F_1 = m_r\,(\ddot{u}_2 - \ddot{u}_1) \tag{3.8}$$

with

$$m_r = \frac{1}{2}\,\frac{m_{w1}\,R_1^2}{\rho_1^2} + \frac{1}{2}\,\frac{m_{w2}\,R_1^2\,R_2^2}{\rho_1^2\,\rho_2^2} \tag{3.9}$$

where m_r is the inertance or apparent mass of the inerter. The inertance of the system can be significantly amplified by installing multiple flywheels in series connected through a gearing system. The previous derivation can be extended to a system with n rotating flywheels where the apparent mass of the system is given by [6]:

$$m_r = \frac{1}{2}\,\frac{m_{w1}\,R_1^2}{\rho_1^2} + \frac{1}{2}\,\frac{m_{w2}\,R_1^2\,R_2^2}{\rho_1^2\,\rho_2^2} + ... + \frac{1}{2}\,\frac{m_{wn}\,R_1^2\,R_2^2\,...\,R_n^2}{\rho_1^2\,\rho_2^2\,...\,\rho_n^2} \tag{3.10}$$

Accordingly, regardless of how small the total mass of the inerter is, any value of inertance can be obtained with the sufficient number and size of flywheels [95]. For instance, for a two-flywheel system of radius ratio $R_i/\rho_i = 10$, only one ten thousandth of the structure's mass, m, would be required to obtain a mass ratio, m_r/m, of 0.5.

Makris and Kampas [95] recognized that the rotating flywheels store energy that is then transferred back to the primary structure. To overcome this issue, they proposed the use of rotational inertia systems equipped with clutches to ensure that the inerters act only in opposition to the motion without inducing additional deformations. Since one-way clutches can only oppose one direction of motion, a pair of parallel inerters is required in this configuration. While there are several types of one-way clutches available, the most commonly used fall within one of three categories: i) ratchet and pawl, ii) roller and spring, and iii) sprag. Figure 3.3 presents a schematic comparison of their envelope sizes according to [117].

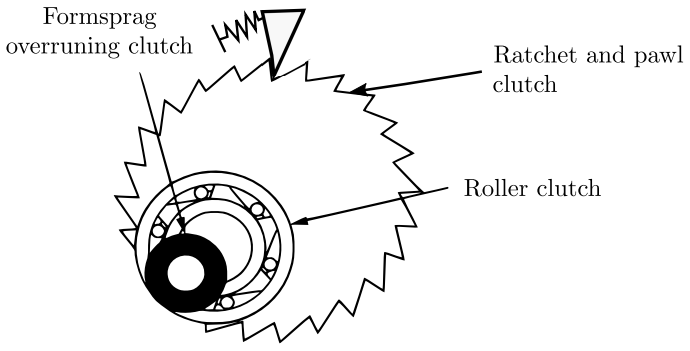

Figure 3.3: Schematic comparison of different clutch types. Adapted from [117].

The ratchet type is obviously the most limited in capacity, and usually requires large dimensions in order to comply with maximum stresses on the ratchet and the tooth. Moreover, ratchet-pawl clutches are also associated with non-negligible levels of rotation before engagement. In contrast, sprag clutches offer a good load carrying capacity and are not significantly affected by friction [118]. However, the complexity of their fabrication and assembly contribute to higher costs of manufacture and maintenance. The roller clutch, on the other hand, needs smaller envelopes than the ratchet-pawl type to transfer the same amount of torque, is reliable and relatively inexpensive.

Considering that a one-way clutch like the ones described above is incorporated into the system, the sequential engagement and disengagement of the two parallel inerters can be expressed mathematically as [95]:

$$F_1(t) = \begin{cases} m_r\ \ddot{u}, & \left[\frac{\ddot{u}}{\dot{u}}\right] > 0 \\ \\ 0, & \left[\frac{\ddot{u}}{\dot{u}}\right] < 0 \end{cases} \tag{3.11}$$

This formulation assumes that friction within the inerter is enough to decelerate the flywheel once it disengages [105]. Alternatively, viscous fluids can be added to ensure sufficient energy dissipation [5, 7, 95]. On the other hand, the influence of the clutch stiffness, gears play, viscous damping and dry friction, on the non-linear dynamics of the system has been comprehensively assessed in [105].

3.3 Rocking Block - Inerter systems

The overall rational behind the proposed strategy is that the vibration-absorbing capabilities of supplemental rotational inertia devices can be applied to the seismic protection of rocking structures. To this end, Figure 3.4 shows some possible configurations of the proposed block-inerter system. In the case of single rocking structures (such as storage tanks and post-tensioned columns and walls) a pair of vertical inerters can be attached near their base and connected to a rigid foundation (Figure 3.4a). In this way, the inerters are sequentially activated by the vertical acceleration at the connected nodes following rocking motion. This configuration will be more effective for stocky blocks, since the vertical acceleration in slender structures will be small. In the case of slender blocks, a horizontal inerter can be used as presented in Figure 3.4b. In this arrangement, a horizontal support will be required to attach the inerter to the structure. This can be useful when protecting electrical equipment or non-structural elements that can be tied to a stiff wall or support. Alternatively, a variety of pulley systems can be used to transfer and amplify the acceleration from any tying point within the rocking structure while carrying the forces to a more practical inerter location (as in Figure 3.4c). This is particularly attractive for the protection of rocking bodies as it opens

the possibility of non-locally modifying the dynamic response of rocking structures without altering their geometry.

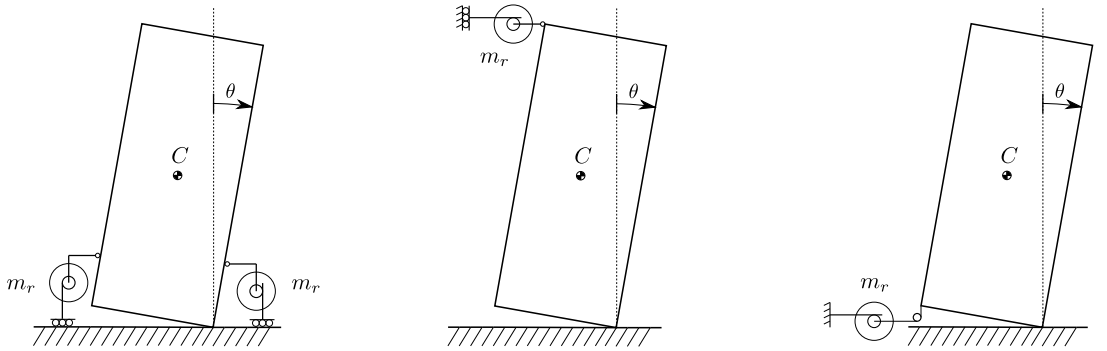

(a) Vertical pair of inerters. (b) Horizontal inerter. (c) Pulley-inerter system.

Figure 3.4: Examples of rigid block-inerter configurations.

3.3.1 Equations of motion

The general dynamic characteristics of the systems depicted in Figure 3.4 can be studied with reference to the rocking block shown in Figure 3.5, where a horizontal inerter of apparent mass, m_r, connected to the centre of mass is considered for clarity. The rigid block is characterized by its mass, m, and the location of the centre of mass, C, defined by the slenderness α and the size parameter R. The block is free to rotate about points O and O', and it is assumed that the coefficient of friction is large enough to prevent sliding between the block and the base. The rotation of the block is measured by the angle θ.

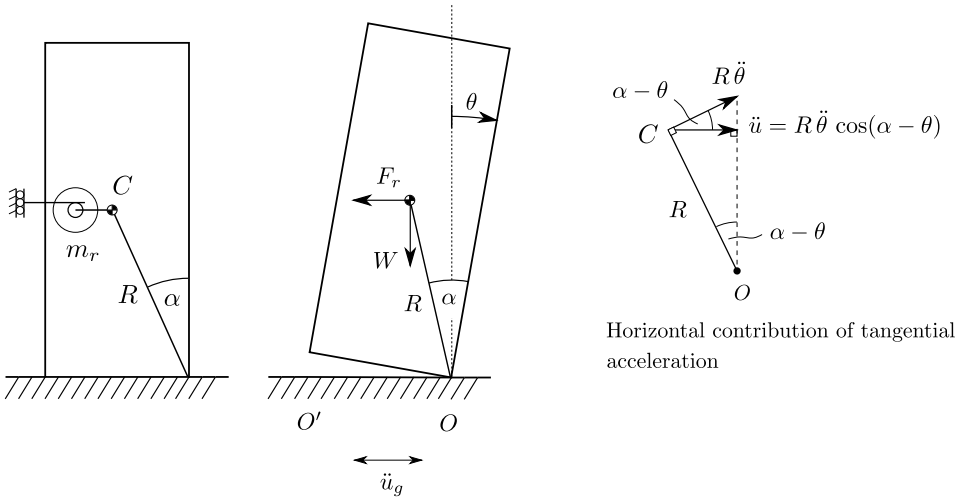

Figure 3.5: Block-inerter system under a horizontal ground excitation.

Rocking motion initiates when the overturning moment due to the ground excitation exceeds the restoring moment exerted by the self-weight (Equation 3.1). Until this instant, the resisting force in the inerter is zero, since there is no relative acceleration between its termin-

als. Once the block uplifts, the tangential relative acceleration at point C is $R\ddot{\theta}$. In slender blocks, the centripetal acceleration is practically vertical and its horizontal component can be neglected. Thus, the horizontal linear acceleration at the point of connection of the inerter can be expressed as follows (Figure 3.5):

$$\ddot{u} = R\,\ddot{\theta}\cos(\alpha\, sgn(\theta) - \theta) \tag{3.12}$$

Therefore, the resisting force in the inerter is:

$$F_r = m_r\, R\,\ddot{\theta}\, cos(\alpha\, sgn(\theta) - \theta) \tag{3.13}$$

Evaluating the rotational equilibrium about the rocking pivot point gives:

$$\left(I_0 + m_r R^2 \cos^2(\alpha\, sgn(\theta) - \theta)\right)\ddot{\theta} + mgR\,\sin((\alpha\, sgn(\theta) - \theta)) = -m\ddot{u}_g R\,\cos(\alpha\, sgn(\theta) - \theta) \tag{3.14}$$

where I_0 is the moment of inertia about the centres of rotation O and O'. For rectangular blocks $I_0 = (4/3)mR^2$ and

$$\left(\frac{4R}{3} + \sigma R\cos^2(\alpha sgn(\theta) - \theta)\right)\ddot{\theta} = -g\,\sin((\alpha sgn(\theta) - \theta)) - \ddot{u}_g\cos(\alpha sgn(\theta) - \theta) \tag{3.15}$$

where $\sigma = m_r/m$ is the apparent mass ratio. Equation 3.15 can be rearranged to obtain an expression similar to Equation 3.2:

$$\ddot{\theta} = -p_\sigma^2\left(\sin((\alpha sgn(\theta) - \theta)) + \frac{\ddot{u}_g}{g}\cos(\alpha sgn(\theta) - \theta)\right) \tag{3.16}$$

with

$$p_\sigma = \sqrt{\frac{3\,g}{R\big(4 + 3\,\sigma\cos^2(\alpha sgn(\theta) - \theta)\big)}} \tag{3.17}$$

Equation 3.17 shows that the inclusion of the inerter has an effect equivalent to reducing the frequency parameter, p, of the block. This effect depends on the magnitude of the rotation θ, reaching a maximum when $\theta = \alpha$ and becoming less significant for higher rotations. In general, the reduction of the frequency parameter should result in lower seismic demands due to the size effect of rocking behaviour [3]. This principle dictates that among two blocks of the same slenderness α, the one with the lower frequency parameter, p (larger in size), is more stable and therefore has lower levels of structural demands. It is important to note that for a given rectangular block, the frequency parameter, p, depends only on the size, R, and therefore cannot be modified without altering its geometry. Consequently, the use of supplemental rotational inertia devices configures a practical alternative to modify the dynamic response and reduce seismic demands in rocking structures.

Equation 3.16 can be linearized if slender blocks are considered (small $\alpha - \theta$), such that:

$$\ddot{\theta} = -p_\sigma^2 \left(\alpha sgn(\theta) - \theta + \frac{\ddot{u}_g}{g}\right) \tag{3.18}$$

with

$$p_\sigma = \sqrt{\frac{3\,g}{R(4+3\,\sigma)}} \tag{3.19}$$

Importantly, the clutched pair of inerters proposed by Makris and Kampas [95] can be easily incorporated into the above mathematical formulation. To this end, in order to represent an arrangement that can only resist the rocking motion, the effects of the apparent mass of the inerter are reevaluated after each integration step according to Equation 3.11.

3.3.2 Transition upon impact

Housner's restitution coefficient needs to be modified in order to account for the effect of the inerter during impact. Figure 3.6 shows the rigid rocking block studied in the previous section at the instant of impact.

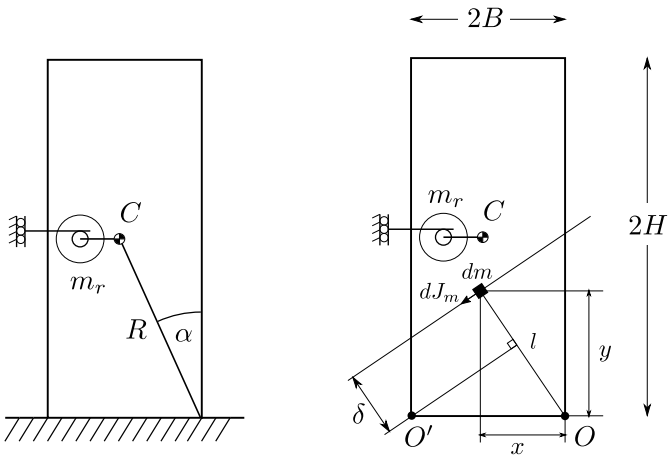

Figure 3.6: Rigid rocking block connected to an inerter at the instant of impact.

Just before impact, the momentum of a mass element dm located at a distance $l = \sqrt{x^2 + y^2}$ from the pivot point O is:

$$dJ_m = l\,\dot{\theta}_1 dm \tag{3.20}$$

and the momentum of the inerter's apparent mass:

$$J_{m_r} = m_r\,\dot{\theta}_1 R\cos\alpha \tag{3.21}$$

where $\dot{\theta}_1$ is the angular velocity before impact. The corresponding moment of momentum about the opposite corner, O', can be obtained as:

$$d\Lambda_m = dJ\delta = \rho\, l\, \dot{\theta}_1 \delta\, dxdy \tag{3.22}$$

and

$$\Lambda_{m_r} = J_{m_r} R\cos\alpha = m_r R^2\, \dot{\theta}_1 \cos^2\alpha \tag{3.23}$$

where ρ is the constant density of the block, and $\delta = l - 2Bx/l$ is the lever arm of the element momentum vector dJ about point O'. The total moment of momentum of the rocking structure about point O' is then given by:

$$\Lambda_1 = \rho\,\dot{\theta}_1 \left(\int_A (x^2 + y^2) dxdy - 2B \int_A x dxdy \right) + m_r\, \dot{\theta}_1 R^2 \cos^2\alpha \tag{3.24}$$

where A is the total area of the block. Integration yields:

$$\Lambda_1 = I_0\dot{\theta}_1 - 2m\dot{\theta}_1 R^2 \sin^2\alpha + m_r\, \dot{\theta}_1 R^2 \cos^2\alpha \tag{3.25}$$

On the other hand, the moment of momentum about point O' after impact is:

$$\Lambda_2 = I_0\dot{\theta}_2 + m_r R^2\, \dot{\theta}_2 \cos^2\alpha \tag{3.26}$$

Then, conservation of moment of momentum before and after impact gives:

$$I_0\dot{\theta}_1 - 2M\dot{\theta}_1 R^2 \sin^2\alpha + m_r R^2\, \dot{\theta}_1 \cos^2\alpha = I_0\dot{\theta}_2 + m_r R^2\, \dot{\theta}_2 \cos^2\alpha \tag{3.27}$$

On the other hand, the ratio of kinetic energy before and after impact is:

$$r_\sigma = \frac{\dot{\theta}_2^2}{\dot{\theta}_1^2} < 1 \tag{3.28}$$

Combination of Equations 3.27 and 3.28 yields:

$$r_\sigma = \left(\frac{1 - \frac{3}{2}\sin^2\alpha + \frac{3}{4}\sigma\cos^2\alpha}{1 + \frac{3}{4}\sigma\cos^2\alpha} \right)^2 \tag{3.29}$$

Equation 3.29 defines the coefficient of restitution of a rigid rocking block connected to an inerter of apparent mass ratio σ. When $\sigma = 0$ (no inerter case), this expression becomes identical to the one obtained by Housner (Equation 3.4). Figure 3.7 shows the effect of increasing levels of inertance on the coefficient of restitution of blocks of different slenderness. The plot shows that as the apparent mass of the inerter increases, the coefficient r_σ becomes larger, indicating a lower amount of energy dissipation during impact. Importantly, this effect is much more significant for stocky structures.

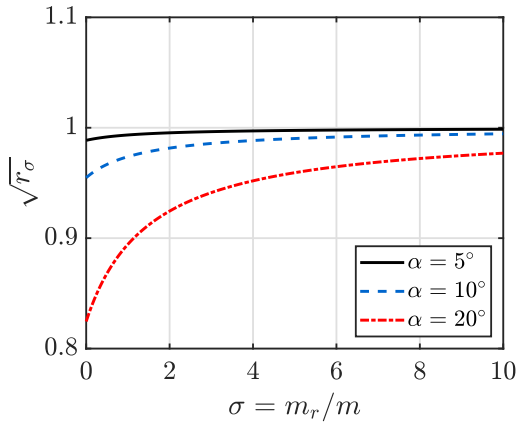

Figure 3.7: Effect of the inerter on the restitution coefficient.

The equations of motion presented in the previous section are solved using Matlab's standard solver for ordinary differential equations *ode45*. This function implements a Runge-Kutta method with a variable time step for efficient computation [119]. An event function is also defined in order to stop the integration at the instant of impact ($\theta \to 0$). The angular velocities are then redefined using the coefficient of restitution given in Equation 3.29, and the integration is resumed using these new values as initial conditions.

Figure 3.8 compares the response of a rigid block of slenderness $\alpha = 10°$ equipped with a single inerter (left) and a pair of clutched-inerters (right) of apparent mass ratio $\sigma = 0.5$, subjected to a sine pulse ground acceleration of $a_g/g\alpha = 1.5$ and $\omega_g/p = 4$. Accordingly the coefficients of restitution of the bare and inerter-equipped blocks are $r = 0.955$ and $r_\sigma = 0.967$, respectively. The sequential engagement and disengagement of the clutched-inerters during the rocking motion can be clearly appreciated in the transferred force response.

The results plotted in Figure 3.8a show that the inclusion of the inerter significantly improves the stability of the block, while at the same time it reduces the amount of energy dissipated during each impact. This results in lower peak rotations, with similar amplitudes in the later cycles of the rocking response. Figure 3.8b, on the other hand, shows a significant increase in the energy dissipated by the clutched-inerter configuration, which is reflected in a fastest decrease of the rocking amplitude. This observation may be explained by the assumption underlying Equation 3.11 by which the energy stored in the idle rotating flywheel is completely dissipated before it re-engages. A more detailed analysis of the rocking demands for a wider range of pulse excitations is conducted in the following sections.

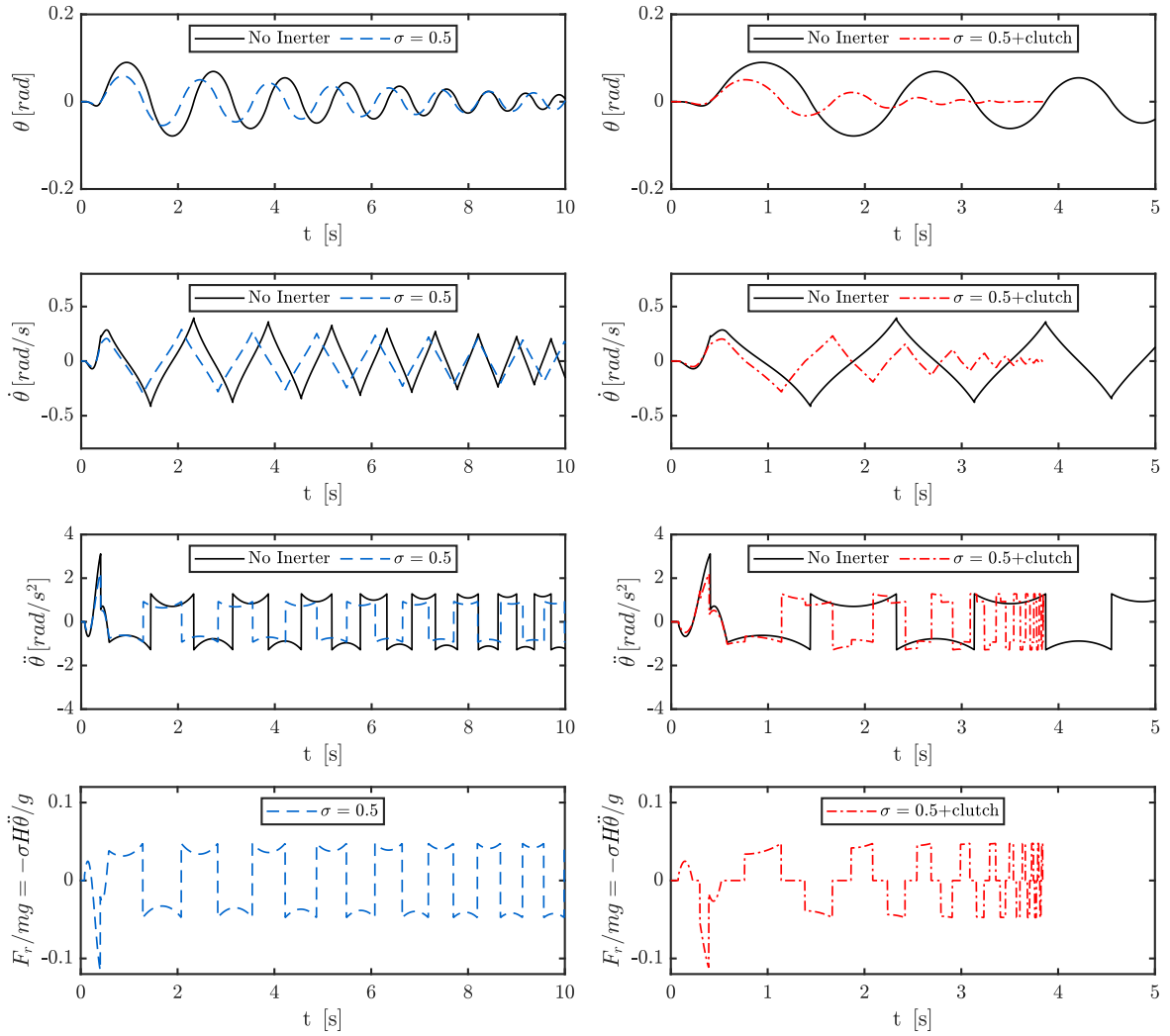

(a) Single Inerter

(b) Clutched pair of inerters

Figure 3.8: Response of a rigid block of $\alpha = 10°$, with and without inerters, to a sine pulse ground acceleration of $a_g/g\alpha = 1.5$ and $\omega_g/p = 4$.

3.3.3 Impact and the acceleration response

The formulation presented in the previous section considered a classical impact framework, where vertical forces are assumed to be instantaneous and concentrated at the pivot corners. Although this model provides a good estimation of the amount of energy dissipated during impact [38], Equation 3.28 predicts an instantaneous change of velocity and, therefore, an unrealistic infinite acceleration at the transition instant. A more detailed assessment of the acceleration response can be performed if Dirac-Delta functions are considered in order to distribute the impact forces over time, as suggested by Prieto et al. [35] and Acikgoz and DeJong [34]. In this formulation, a vertical force is considered to act on the impending pivot point as the structure approaches $\theta = 0$, applying a moment that counteracts the rocking motion and decelerates the rotating structure. After the phase transition at $\theta = 0$, the force is

terminated as any forcing from the pivot point will no longer influence the moment equilibrium. This process is schematically illustrated in Figure 3.9a.

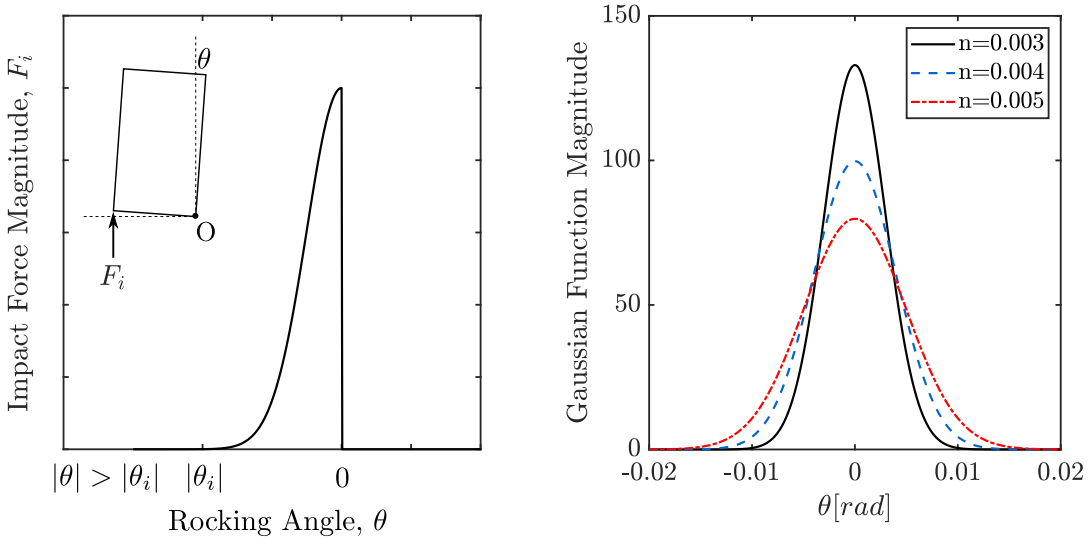

(a) Varitation of impact force with θ.

(b) Effect of n on the shape of the impact force.

Figure 3.9: Impact forces in the Dirac-Delta model.

The impact force, F_i, is approximated by a Gaussian function of the rocking angle, defined by a zero mean and a standard deviation of $n/\sqrt{2}$, where n represents a width parameter that influences the sharpness of the impact force. The effect of changing the value of n on the form of the function is illustrated in Figure 3.9b. Regardless of the value of n, the energy dissipated during a single impact cycle is given by:

$$E_{loss} = 2B \int_{-\infty}^{0} \frac{1}{n\sqrt{\pi}} e^{-\theta^2/n^2} d\theta = B \tag{3.30}$$

Using this property, the Gaussian function can then be scaled to obtain any desired energy loss, $E_{ini}(1-r)$:

$$F_i = \frac{E_{ini}(1-r)}{B\, n\, \sqrt{\pi}} e^{-\theta^2/n^2} \tag{3.31}$$

In order to ensure that the specified amount of energy is dissipated during impact, the force-activation rotation is defined as $\theta_i = 2.576(n/\sqrt{2})$, corresponding to the 99.5% confidence interval of the Gaussian function [34]. On the other hand, n is assumed to be an independent parameter of the system.

Figure 3.10 compares the response of the same rigid block analysed in the previous section, considering a classical impact framework (Housner) and the Dirac-Delta model for different values of n. The magnitude of the impact forces is defined based on Housner's coefficient of restitution, r, according to Equation 3.31. Accordingly, the three models compared in Figure 3.10 have equivalent energy dissipation ratios during impact.

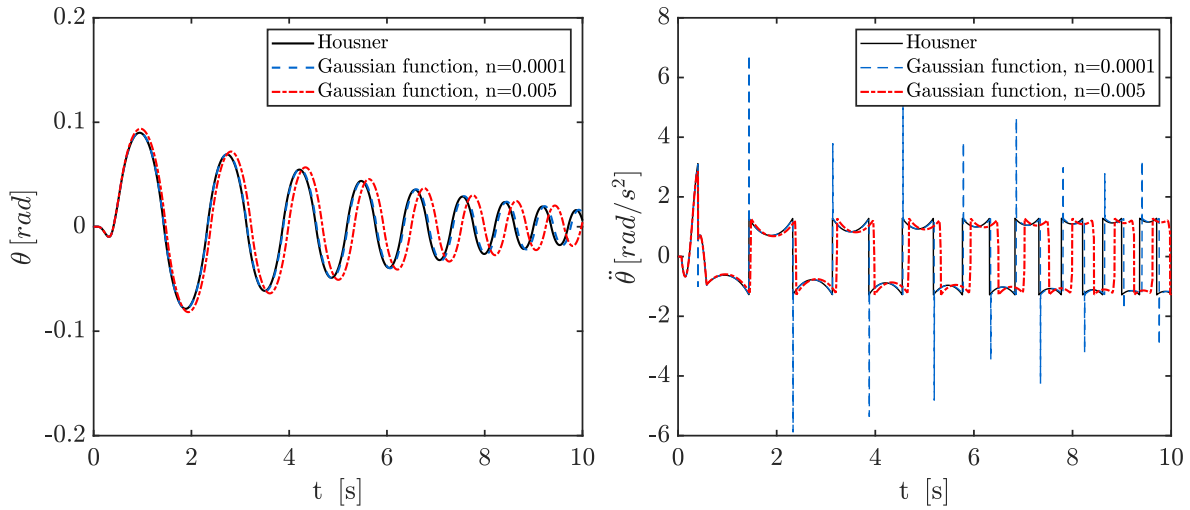

(a) Base rotation.

(b) Angular acceleration.

Figure 3.10: Response of a rigid block of $\alpha = 10°$ and $\sigma = 0$, to a sine pulse ground acceleration of $a_g/g\alpha = 1.5$ and $\omega_g/p = 4$ for different impact models.

Figure 3.9b showed that impact forces become sharper as n decreases, tending to instantaneous impact as n approaches zero. This is evident in Figure 3.10a, where the rotation responses obtained with Housner's formulation and the Dirac-Delta model converge when $n = 0.0001$. Moreover, the acceleration spikes predicted by the classical formulation are clearly observed in Figure 3.10b. As the impact forces become more distributed over time ($n = 0.005$), these spikes disappear and the acceleration history approaches the in-between-impacts response obtained with Housner's model. Likewise, very similar rotation amplitudes are obtained with the three models under consideration, even though changes in the duration of impact cause shifts in the phase of the response.

The results presented in Figure 3.10 demonstrate that Housner's model can be used to assess the acceleration response of rocking blocks under the assumption that impact forces are sufficiently distributed over time as to cause continuous velocity transitions, but sharp enough not to appreciably affect the rotation response. Accordingly, the analyses presented in the following sections consider the classical impact framework developed in Section 3.3.2, ignoring the velocity discontinuity (i.e. infinite acceleration) when assessing peak acceleration demands.

3.4 Self-Similar response of rocking block-inerter systems

The response of a rigid block to an analytical pulse ground motion of acceleration amplitude a_g and dominant frequency ω_g is a function of four variables:

$$\theta_{max} = f\left(\alpha\,,\, p\,,\, \frac{a_g}{g}\,,\, \omega_g\right) \tag{3.32}$$

Applying Vaschy-Buckingham's Π-theorem [120, 121] the number of independent parameters required to define a unique response can be reduced to three:

$$\theta_{max} = f\left(\frac{\omega_g}{p}\,,\,\frac{a_g}{g}\,,\,\alpha\right) \tag{3.33}$$

Considering the coefficient of restitution, r, as an independent parameter, Dimitrakopoulos and DeJong [122] used a dimensionless and orientationless analysis to show that the response of slender blocks can be described by three dimensionless and orientationless terms:

$$\frac{\theta_{max}\, g}{a_g} = \phi\left(\frac{\omega_g}{p}\,,\,\frac{g\,\tan\alpha}{a_g}\,,\,r\right) \tag{3.34}$$

When stocky blocks are considered, α cannot be incorporated entirely into the other parameters and appears as an isolated argument, $\cos(\alpha)$. However, for small rotation angles, the influence of α is relatively small, and it is convenient to eliminate $\cos(\alpha)$ as an independent group [122] such that:

$$\frac{\theta_{max}\, g}{a_g\,\cos\alpha} \simeq \phi\left(\frac{\omega_g}{p}\,,\,\frac{g\,\tan\alpha}{a_g}\,,\,r\right) \tag{3.35}$$

It can be appreciated from Equation 3.17 that the inclusion of the inerter only modifies the frequency parameter, p, and as such it should not affect the validity of Equations 3.34 and 3.35. However, in the case of clutched systems, the inclusion of the inerter-clutch device adds an additional source of non-linearity to the equation of motion, and therefore, its self-similar response must be verified. To this end, Figure 3.11 compares the response of two blocks of dimensionless-orientationless parameters $g\alpha/a_g = 0.57$ and $r = 0.85$, connected to a single inerter and to a pair of clutched inerters, when subjected to a single sine pulse of frequency $w_g/p = 4$. The inerter device is described in terms of the mass ratio $\sigma = m_r/m$, which is a dimensionless-orientationless quantity and can be treated as an independent parameter such that:

$$\frac{\theta_{max}\, g}{a_g} = \phi\left(\frac{\omega_g}{p}\,,\,\frac{g\,\tan\alpha}{a_g}\,,\,r\,,\,\sigma\right) \tag{3.36}$$

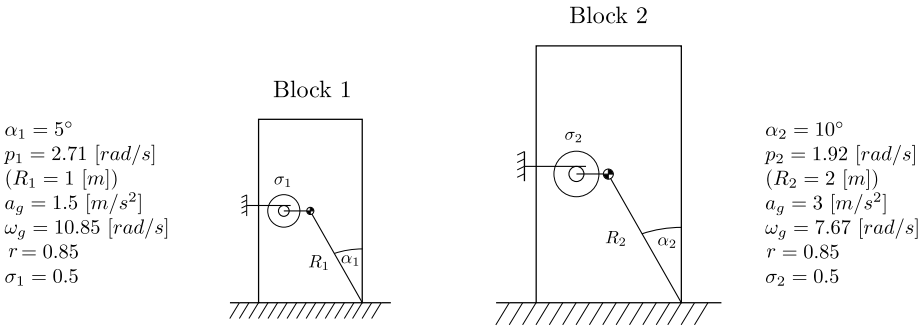

(a) Slender block-inerter systems.

$$\frac{\omega_g}{p} = 4; \quad \frac{g\alpha}{a_g} = 0.57; \quad r = 0.85; \quad \sigma = 0.5;$$

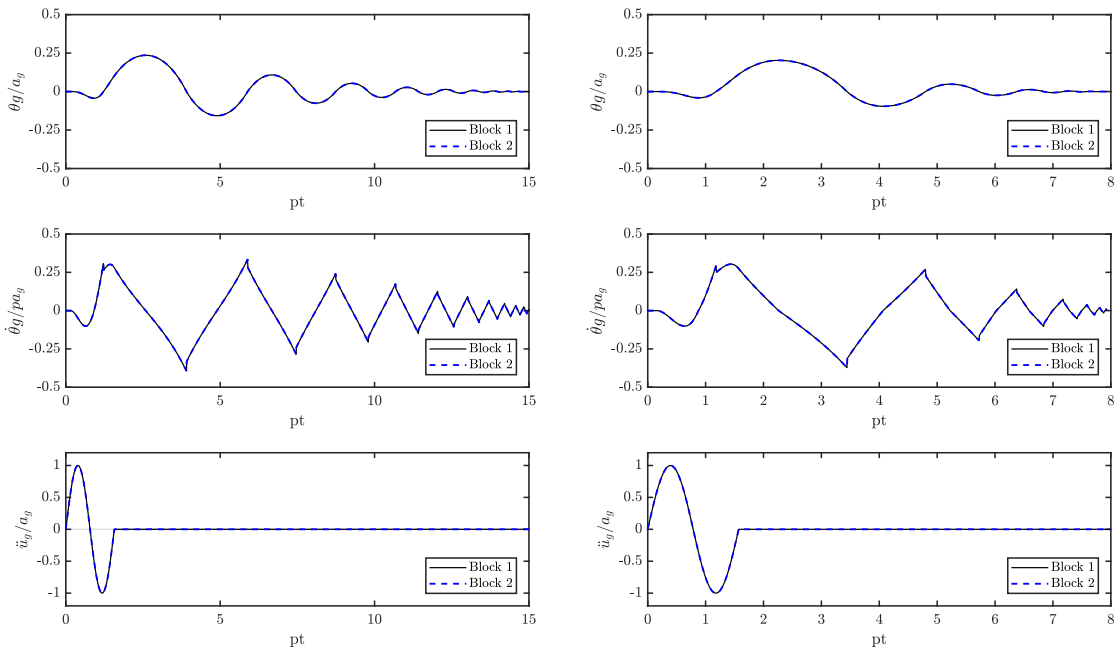

Single Inerter Pair of Clutched Inerters

(b) Response of blocks 1 and 2 presented in terms of dimensionless-orientionless parameters [122].

Figure 3.11: Self-similar response of slender block-inerter systems.

It is evident from Figure 3.11b that, when presented in terms of the proposed parameters, the responses collapse into a single master curve, showing that the inclusion of inerters or clutched inerters preserves the self-similarity in the response of slender blocks. In the case of non-slender blocks, the effects of the inerter depend on the magnitude of the rotation θ (Equation 3.17). Therefore, it is expected that the practically self-similar formulation developed by Dimitrakopoulos and DeJong (Equation 3.35) will not be directly applicable to stocky rocking block-inerter systems. In order to examine this, Figure 3.12 compares the response of two rocking blocks of equivalent dimensionless-orientationless parameters connected to (a) a single inerter and (b) a pair of clutched inerters. The rocking response of these blocks is calculated by solving the full nonlinear equation of motion (Equation 3.16).

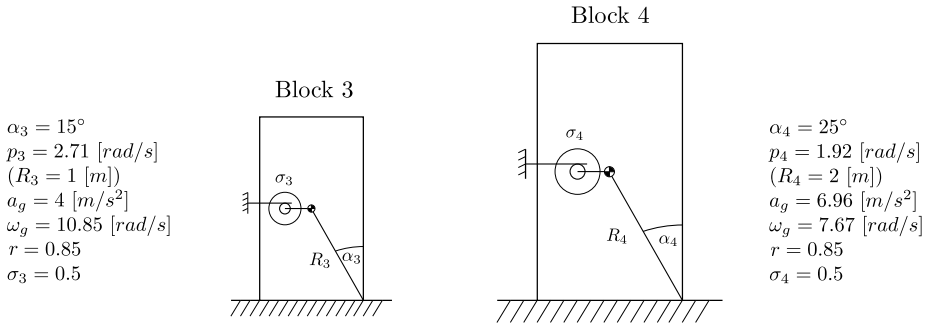

(a) Non-slender block-inerter systems.

$\frac{\omega_g}{p} = 4; \quad \frac{g \tan\alpha}{a_g} = 0.66; \quad r = 0.85; \quad \sigma = 0.5;$

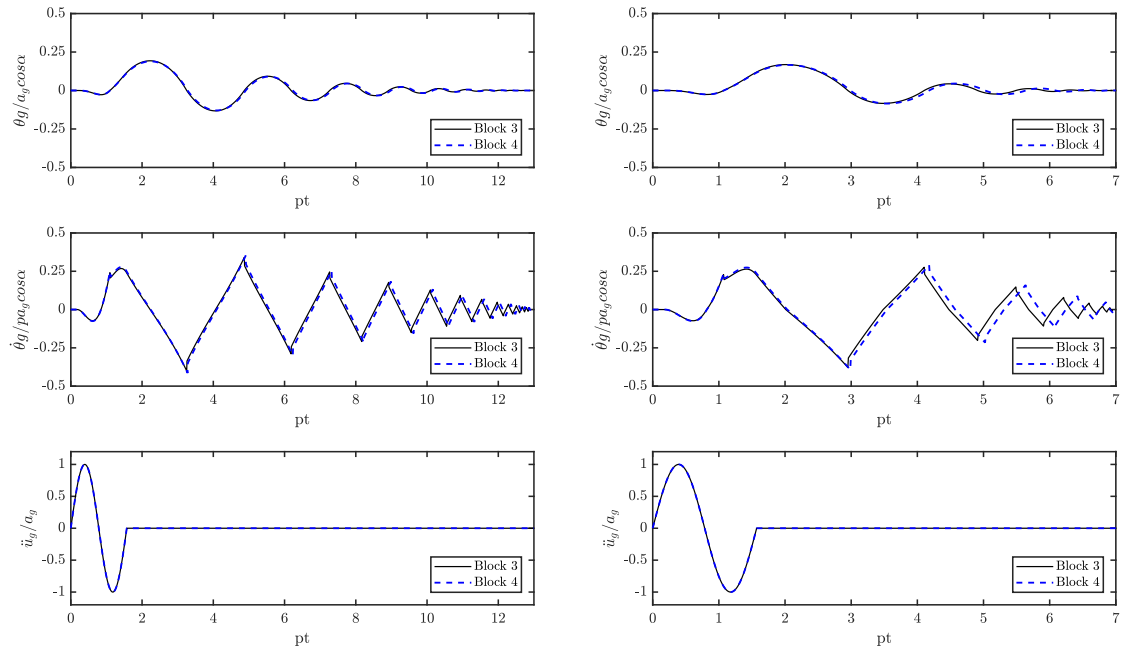

(b) Response of blocks 3 and 4 presented in terms of dimensionless-orientionless parameters [122].

Figure 3.12: Self-similar response of non-slender block-inerter systems.

The left side of Figure 3.12b shows that the response of the single inerter case remains practically self-similar, as the plots virtually collapse to a single curve. However, the incorporation of the clutch modifies this behaviour and the response becomes non or less self-similar (Figure 3.12b, right). This is an important finding that affects more the later stage of the response, as can be observed from Figure 3.12.

3.5 Overturning under single pulse excitations

The rocking response of a rigid block can result in one of two outcomes: (a) safe rocking, where the block survives the ground motion and the energy is dissipated through successive impacts at the base until the motion stops; and (b) overturning, where the equation of motion (Equation 3.16) leads to an arbitrarily large rotation value ($|\theta_{max}|/\alpha \rightarrow \infty$) and the block topples. Overturning is usually studied by means of overturning plots like the ones presented in Figure 3.13. These plots show the regions in the frequency-amplitude acceleration space that result in safe rocking or overturning of the block. The area above the upper curves in the graphs of Figure 3.13a represent overturning without impact (Region 1), whereas the areas enclosed by the lower curves correspond to overturning taking place after impact at the base [123] (Region 2). The remaining regions of the plot are associated with safe rocking (Region 3).

In this section, the effects of incorporating inerters on the overturning behaviour of rocking blocks is examined by considering sinusoidal and cosinusoidal acceleration pulses. Figure 3.13 shows the overturning plots obtained for slender ($\alpha = 10°$) and non-slender blocks ($\alpha = 20°$) equipped with a single inerter and a pair of clutched inerters. It can be appreciated that, in general, the inclusion of the inerter reduces the areas of overturning (Regions 1 and 2) and translates them to the lower frequency region. This frequency shift, which is otherwise beneficial, is particularly relevant for the case of overturning after impact (Region 2), as certain blocks that would rock safely without the inerter, may overturn when the protective device is incorporated. Similar trends are observed for the non-slender block (Figure 3.13b). The effect of the inerter system on the overturning response is considerably less significant for smaller objects ($\omega_g/p < 2$). Therefore, the use of a higher mass ratio, σ, will be necessary to further improve the stability of such blocks under single pulse excitations.

It is worth noting that overturning without impact can involve motion reversals, especially when clutched inerters are employed, leading to the difference in Region 1 of the overturning plots observed in Figure 3.13. This can be further examined with reference to Figure 3.14a, where the response of a slender block with no, single, and a pair of clutched inerters is depicted. It can be seen from this figure that the response of the blocks equipped with a single inerter and a pair of clutched inerters are identical until the condition for disengagement is attained (Equation 3.11), leading to the avoidance of overturning by the twin clutched inerter configuration.

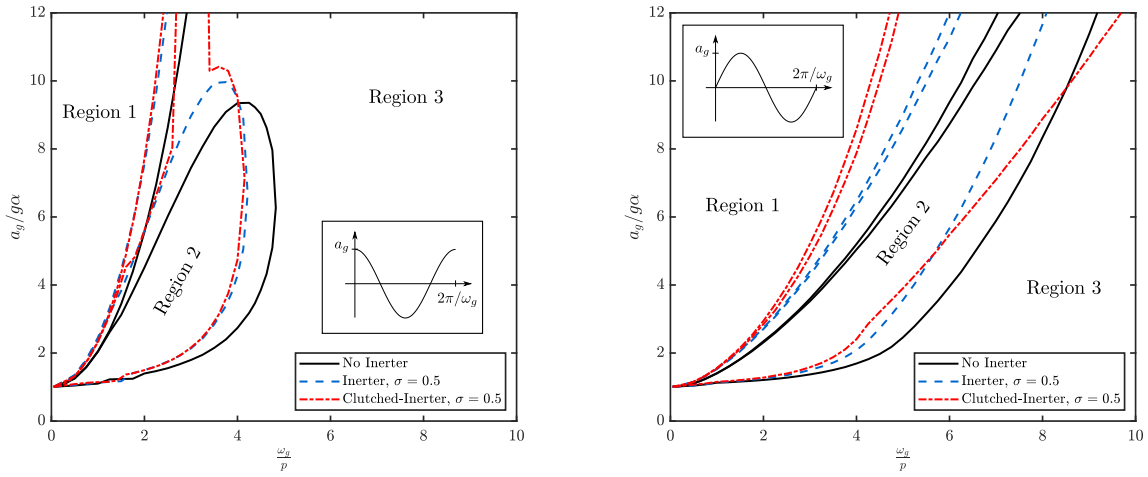

(a) Slender-block-inerter system ($\alpha = 10°$).

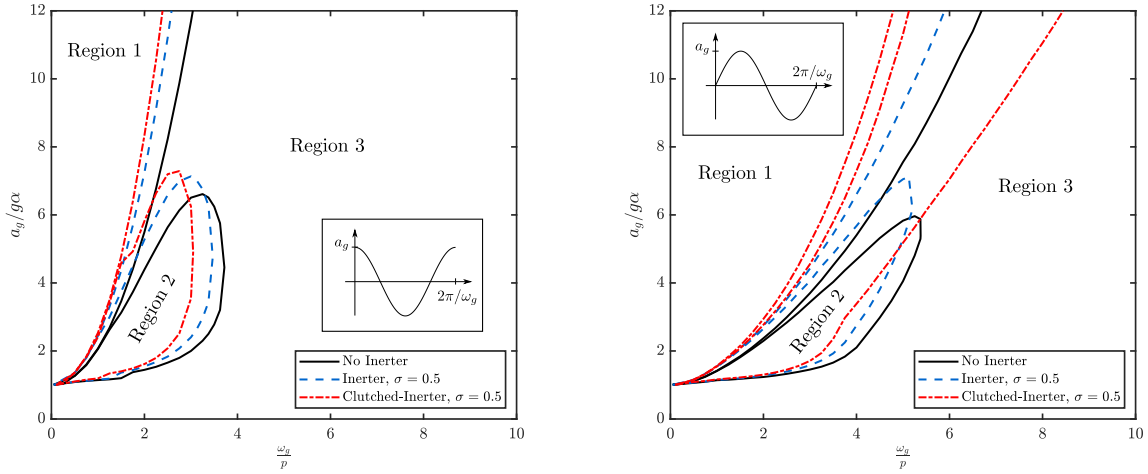

(b) Non-slender-block-inerter system ($\alpha = 20°$).

Figure 3.13: Overturning plots of rocking-block-inerter systems subjected to trigonometric pulses.

The incorporation of the clutch shows different results for cosine and sine acceleration pulses. In the first case, a slight reduction in the areas of overturning is observed, with a small further shift to the region of lower frequencies in comparison with the single inerter configuration. This translation is also observed for the sinusoidal pulses. However, in the case of sinusoidal pulses, the area of overturning after impact (Region 2) is significantly extended for both slender and stocky blocks. This is an important finding and suggests that although the inerter improves the general overturning resistance of the block, the incorporation of a clutch may have a detrimental effect on the rocking response in some cases, especially in relation to overturning after impact. To further examine these effects, Figure 3.14b compares the rotations of slender blocks with no, single, and a pair of clutched inerters under a sine pulse of $\omega_g/p = 8$ and $a_g/g\alpha = 10$. It can be appreciated from this figure that a shift in the impact time is induced by the change in the frequency parameter brought about by the

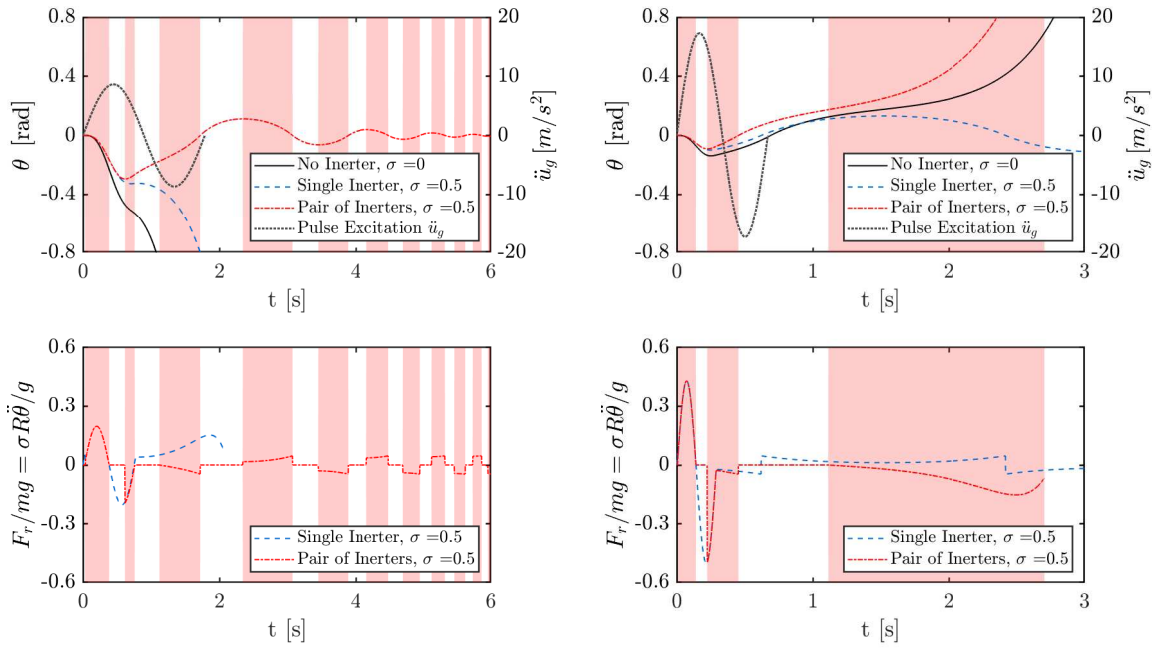

(a) $\omega_g/p = 3$, $a_g/g\alpha = 5$.

(b) $\omega_g/p = 8$, $a_g/g\alpha = 10$.

Figure 3.14: Response history of slender blocks to sine pulses of different amplitude and frequency. The shaded areas show clutch engagement.

inerter. In the case of the unprotected and single inerter structures, impact takes place close to the end of the sinusoidal excitation meaning that the second half of the pulse, after reversal of acceleration, can effectively help to restrain the motion of these blocks. The introduction of the clutch, however, leads to impact occurring closer to the instant of acceleration reversal, causing most of the second half of the ground motion to exacerbate the rotation after impact.

3.6 Rocking demands under single pulse excitations

Even if the block survives the ground motion (no overturning), high rotations and angular accelerations associated with the rocking motion can cause significant damage to the structure and its contents. The results of analyses under single pulse excitations (Figure 3.8) suggest that the use of supplemental rotational inertia can help to reduce seismic demands and improve the dynamic response of rocking structures. In this section, a more complete analysis considering a wider range of trigonometric pulse excitations is offered. The response parameters are presented in terms of rocking spectra, which consist of contour plots of the normalized response variable in the frequency ratio (ω_g/p) and acceleration amplitude ($a_g/g\tan\alpha$) plane, for a block of a given slenderness α. Accordingly, Figures 3.15 and 3.16 compare the rotation and acceleration demands for a rigid block of slenderness $\alpha = 20°$ subjected to cosinusoidal and sinusoidal pulses, respectively, of dominant frequency ω_g and acceleration amplitude a_g.

Results are offered for three different configurations: (a) no inerter, (b) single inerter ($\sigma = 0.5$), and (c) pair of clutched inerters ($\sigma = 0.5$).

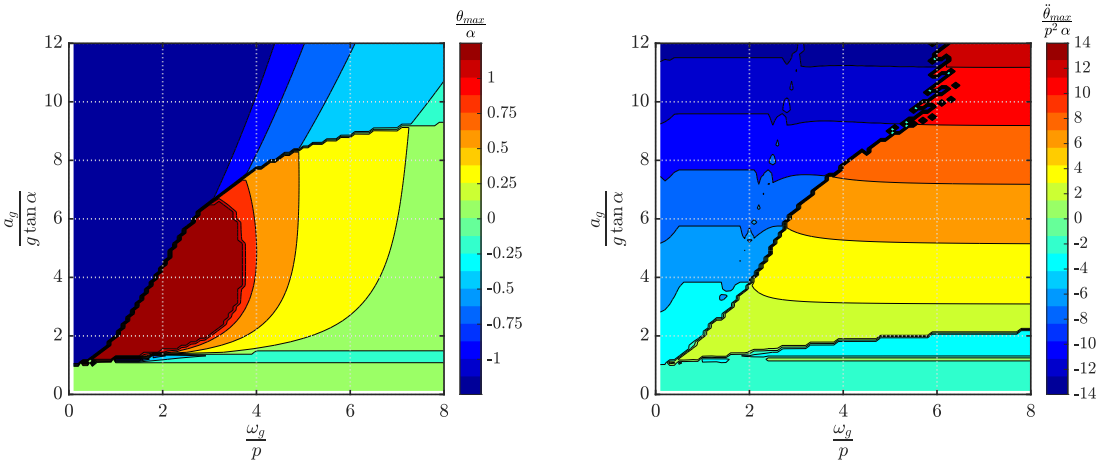

(a) Single rigid block (no inerter).

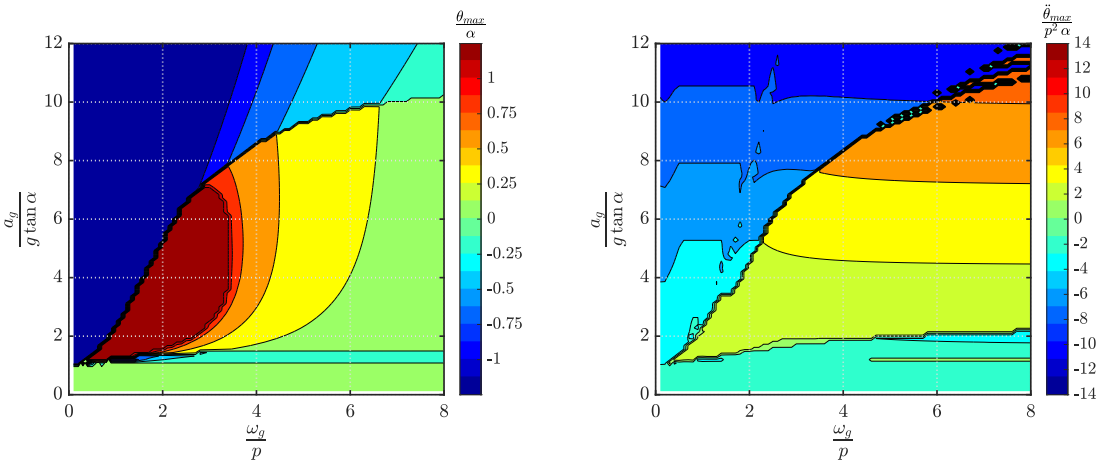

(b) Rigid block connected to a single inerter ($\sigma = 0.5$).

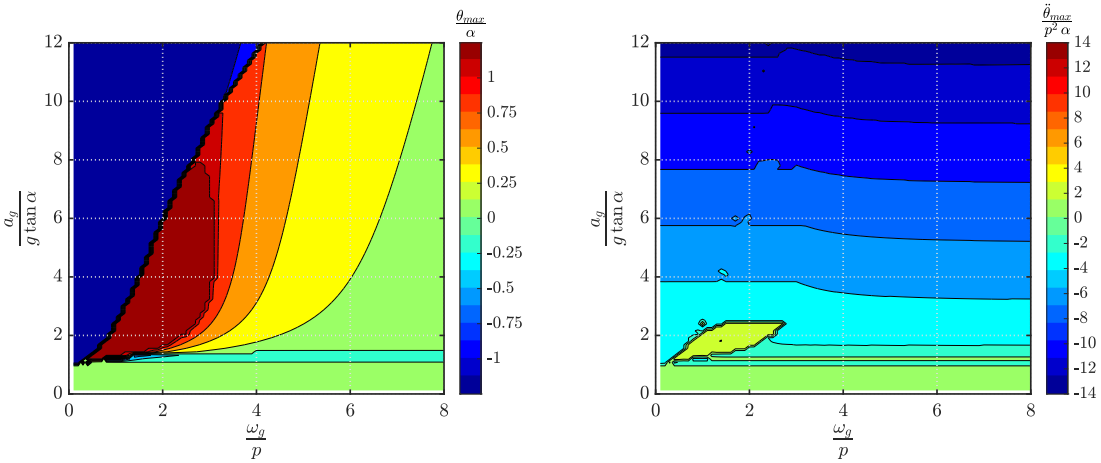

(c) Rigid block connected to a pair of clutched inerters ($\sigma = 0.5$).

Figure 3.15: Rocking spectra for a non-slender block ($\alpha = 20°$) subjected to cosine pulse excitations.

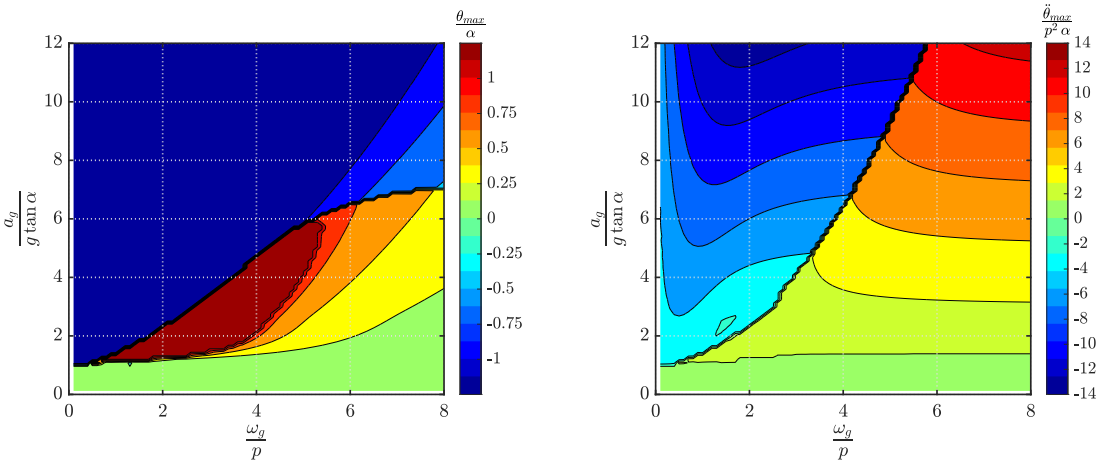

(a) Single rigid block (no inerter).

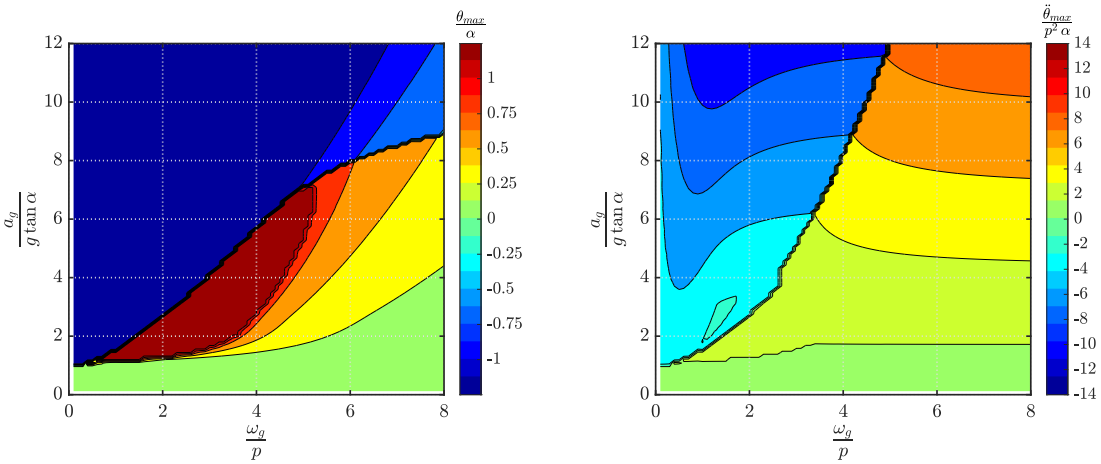

(b) Rigid block connected to a single inerter ($\sigma = 0.5$).

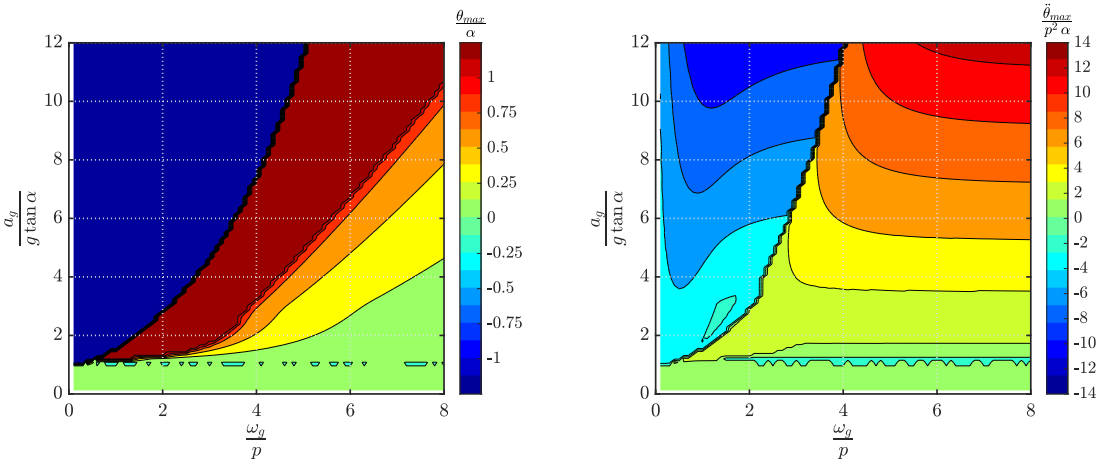

(c) Rigid block connected to a pair of clutched inerters ($\sigma = 0.5$).

Figure 3.16: Rocking spectra for a non-slender block ($\alpha = 20°$) subjected to sine pulse excitations.

The rocking spectra presented in Figures 3.15 and 3.16 reveal a considerable reduction in the rotation and acceleration demands for the single inerter case (Figures 3.15b and 3.16b). Moreover, the reduction in angular accelerations is more significant for larger pulse acceleration amplitudes. On the other hand, blocks connected to a pair of clutched inerters (Figures 3.15c and 3.16c) exhibit a different behaviour depending on the type of excitation and the magnitude of acceleration amplitude, a_g.

The trends identified above can be better appreciated if a single acceleration amplitude is considered, and the response variables are presented only in terms of the frequency ratio ω_g/p. To this end, Figure 3.17 compares the response of the same block ($\alpha = 20°$) subjected to cosine and sine pulses of dominant frequency ω_g and acceleration amplitudes $a_g/g\tan\alpha = 2$ and $a_g/g\tan\alpha = 8$ for the three configurations under study.

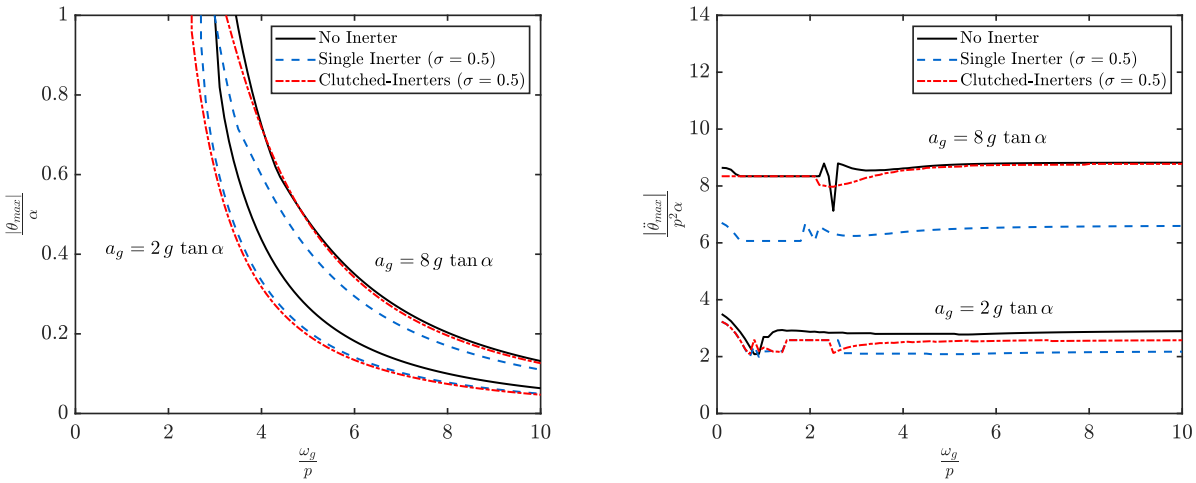

(a) Cosine pulse excitations.

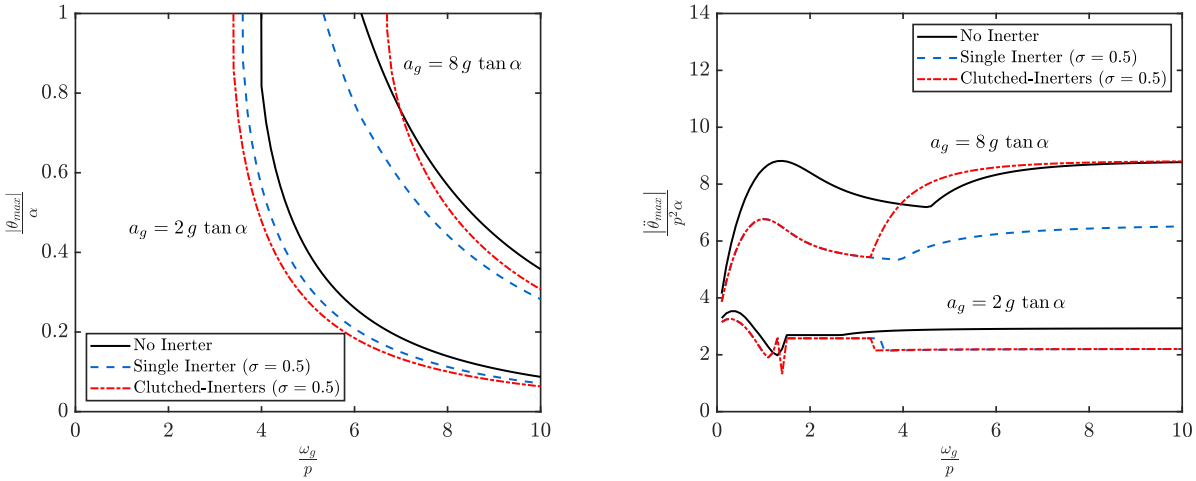

(b) Sine pulse excitations.

Figure 3.17: Rotation and angular acceleration spectra for a non-slender block ($\alpha = 20°$) subjected to trigonometric pulse excitations of $a_g/g\tan\alpha = 2$ and $a_g/g\tan\alpha = 8$.

It can be seen from Figure 3.17 that under cosine pulse ground motions of small accel-

eration amplitudes ($a_g/g \tan\alpha \leqslant 2$), the incorporation of the clutch brings minor additional benefits over rotation demands in comparison with the single inerter case. Instead, it increases accelerations for frequency ratios higher than 2 (Figure 3.17a). For larger accelerations ($a_g/g \tan\alpha \geqslant 8$), the clutch is clearly detrimental, offsetting the reduction brought about by the inerter on the rotations and practically cancelling it on angular accelerations. A similar behaviour is observed in the rotation demands for the blocks subjected to sinusoidal pulse excitations. A minor additional reduction can be observed for small amplitude pulses, whereas higher rotation demands are obtained for larger acceleration excitations. The detrimental effects of the clutch on the overturning response are also evident in this region, as the proportion of blocks (frequency ratios) that survive the ground motion is smaller than for the no inerter case. In terms of angular accelerations, the blocks equipped with the pair of clutched inerters show practically the same maximum response than the blocks connected to a single inerter for small acceleration amplitudes ($a_g/g \tan\alpha \leqslant 2$). Moreover, when higher ground motion accelerations are considered ($a_g/g \tan\alpha \geqslant 8$), the addition of the clutch considerably increases acceleration demands, even surpassing the no inerter case. The region where both cases (single inerter and clutched inerters) overlap corresponds to the area of overturning without impact. In these cases, there is no inversion of the direction of motion, and therefore, the clutch has no effect on the response. Equivalent analyses were conducted for slender rocking blocks and similar results were obtained (see Appendix A).

3.7 Pulse-like Ground Motion Analyses

Previous sections have examined the fundamental dynamic behaviour of rocking blocks equipped with inerter devices subjecting them to single trigonometric pulse excitations. However, recorded near-field ground motions contain, besides coherent long-period pulses, some high-frequency spikes and fluctuations that can increase the seismic demands on rocking structures. In this section, the effectiveness of the inerter for the protection of rocking structures is assessed employing a set of 202 real pulse-like ground motion records obtained from the Pacific Earthquake Engineering Research Center (PEER) database. Records from 21 earthquakes with magnitudes M_w ranging from 5.4 to 7.9 are considered. Table 3.1 summarizes the catalogue of earthquakes used in the analyses.

3.7.1 Dimentionless intensity measures

A critical task for the probabilistic assessment of rocking structures under real seismic ground motions is the selection of adequate intensity measures (IMs) that correlate strongly with the structural demands. Previous studies have shown that rocking response is particularly sensitive to the velocity and acceleration characteristics of the ground motion and have proposed IMs built upon the peak ground velocity PGV (e.g. pPGV/gtanα) and the peak ground accelera-

Earthquake event	Year	Magnitude M_w	Mechanism	N° of Records
San Fernando	1971	6.61	Reverse	1
Tabas Iran	1978	7.35	Reverse	1
Coyote Lake	1979	5.74	Strike Slip	4
Imperial Valley-06	1979	6.53	Strike Slip	12
Irpinia Italy-01	1980	6.9	Normal	2
Westmorland	1981	5.9	Strike Slip	1
Morgan Hill	1984	6.19	Strike Slip	2
Kalamata Greece-02	1986	5.4	Normal	1
San Salvador	1986	5.8	Strike Slip	2
Superstition Hills-02	1987	6.54	Strike Slip	2
Loma Prieta	1989	6.93	Reverse Oblique	6
Cape Mendocino	1992	7.01	Reverse	1
Landers	1992	7.28	Strike Slip	3
Northridge-01	1994	6.69	Reverse	14
Kobe	1995	6.9	Strike Slip	4
Kocaeli	1999	7.51	Strike Slip	4
Chi-Chi Taiwan	1999	7.62	Reverse Oblique	36
Chi-Chi Taiwan-04	1999	6.2	Strike Slip	1
Chi-Chi Taiwan-06	1999	6.3	Reverse	2
Duzce Turkey	1999	7.14	Strike Slip	1
Denali Alaska	2002	7.9	Strike Slip	1
			Total	**202**

Table 3.1: Ground motion database used in the analyses

tion PGA (e.g. PGA/gtanα) [23, 40]. Petrone et al. [124] showed that velocity-based IMs are more effective for large rocking structures ($R > 2[m]$), whereas acceleration-based IMs show a better correlation with smaller structures ($R < 1[m]$). Likewise, several researchers [3, 42, 125] have stressed the importance of the duration and temporal signature of the ground motion on rocking demands. For these reasons, in what follows, the dimensionless-orientationless IM, $p\,t_{uni}$ (Figure 3.18), is employed when assessing rocking demands (maximum rotation and angular acceleration of the safe rocking cases), whereas $pPGV/g\tan\alpha$ is used when evaluating overturning fragilities.

3.7.2 Seismic demand analysis

A cloud analysis considering the earthquakes database described in Table 3.1 was conducted in order to assess the seismic demands of inerter-protected rocking structures. A stable slender

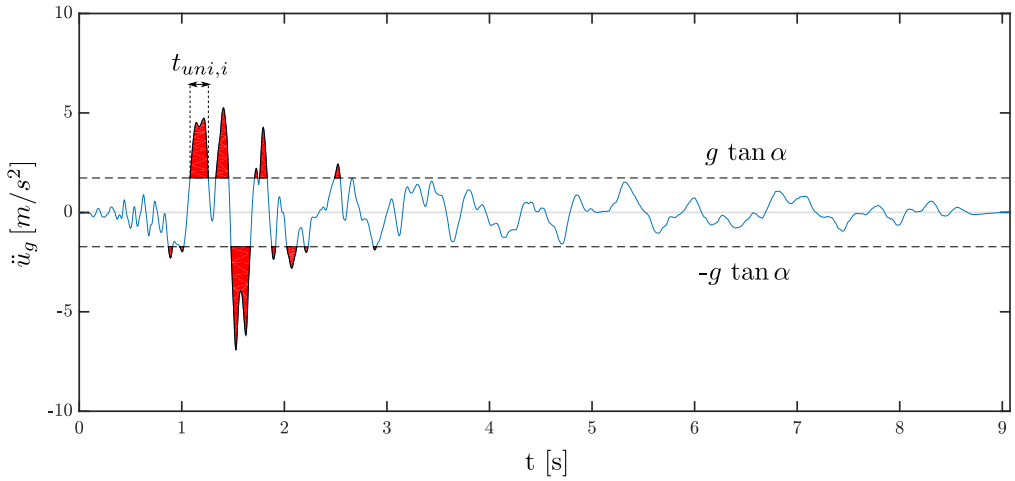

Figure 3.18: Dimentionless-orientationless IM for the rocking demands assessment: Uniform duration $p\,t_{uni}$.

block ($\alpha = 10°$ and $R = 3[m]$) representative of a bridge pier or rocking column was selected as a case of study in order to minimize the number of overturning events. Similarly to Section 3.6, the structural demands are described in terms of the dimensionless peak rotation, θ_{max}/α, and the dimensionless peak angular acceleration, $\ddot{\theta}_{max}/p^2\,\alpha$.

A common assumption in seismic demand models is to consider that the median estimated demand, $\overline{D}_m$, follows a power law IM distribution:

$$\overline{D}_m = a\,IM^b \tag{3.37}$$

When plotted on a $ln(\overline{D}_m) - ln(IM)$ plane, Equation 3.37 becomes a straight line:

$$\ln(\overline{D}_m) = \ln a + b\,\ln(IM) \tag{3.38}$$

where a and b are the linear regression coefficients. Figure 3.19 shows the results of the cloud analysis and the corresponding fitted seismic demand models for three cases: (a) no inerter, (b) single inerter ($\sigma = 1$), and (c) pair of clutched inerters ($\sigma = 1$).

The results of the regression analyses of Figure 3.19 show a good correlation between the selected intensity measure, $p\,t_{uni}$, and the seismic demands, validating the estimation model proposed in Equation 3.37. Importantly, 3.19a shows that the effect of the inerter on the rotation demands is only beneficial for mid to high seismic intensities. This behaviour is further examined in Figure 3.20, where the response of blocks subjected to ground motions with large and small values of $p\,t_{uni}$ is compared. Figure 3.20a shows that the peak rotation of the unprotected structure is governed by the main acceleration pulse highlighted at the beginning of the record. Since the inclusion of the inerter increases the rotational inertia of the block, the amplitude of this rocking oscillation is significantly reduced. The subsequent high frequency spikes, however, cause further rocking cycles which are strongly influenced by the amount of

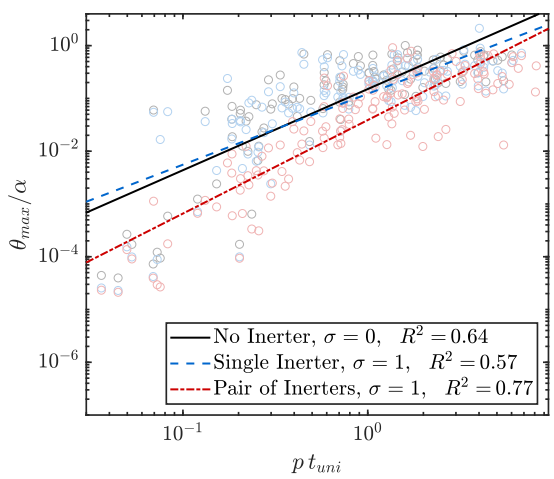

(a) Linear regression for the dimensionless peak rotation.

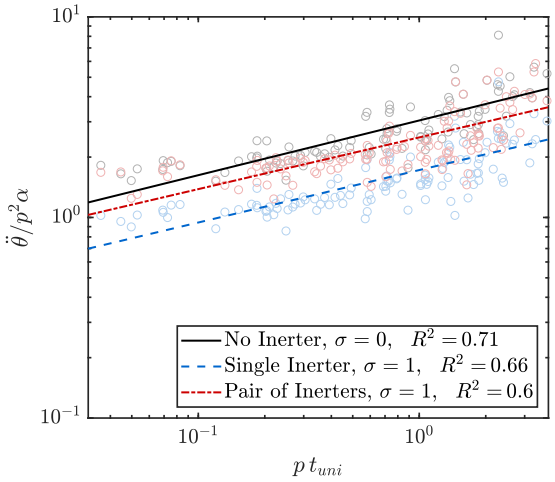

(b) Linear regression for the dimensionless peak angular acc.

Figure 3.19: Seismic demand analysis of a slender rigid block ($\alpha = 10°$ and $R = 3[m]$) subjected to the suite of records described in Table 3.1.

energy dissipated during impact. As the incorporation of the inerter increases the coefficient of restitution of the block (see Figure 3.7), these oscillations grow to exceed the amplitude of the initial rocking cycle, although they remain smaller than the maximum rotation of the unprotected structure. Nevertheless, when lower seismic intensities are considered, the relative importance of the main acceleration pulse diminishes, and the increasing oscillations associated with larger coefficients of restitution can cause the inerter-equipped structure to experience larger rotation demands than the unprotected block (Figure 3.20b). The introduction of the clutch, on the other hand, significantly improves the performance of the blocks equipped with inerters, causing important reductions in the rotation demands across the whole range on intensities under consideration. Whereas peak rotations of up to 35% lower are observed in the structures equipped with single inerters, reductions of around 65% are obtained when the clutch is added. Moreover, the faster attenuation of the rocking response brought about by the clutch (see Figure 3.8), also enhances the response of the system under lower seismic intensities.

Important reductions are also observed in the maximum angular accelerations across the whole range of intensities under consideration (Figure 3.19a). Nevertheless, a reversed trend can be identified when the clutch is incorporated; 40% lower demands are observed for the single inerter configuration; however, these values rise again when the clutch is introduced. This behaviour is consistent with the results obtained from the single pulse analyses presented in Section 3.6.

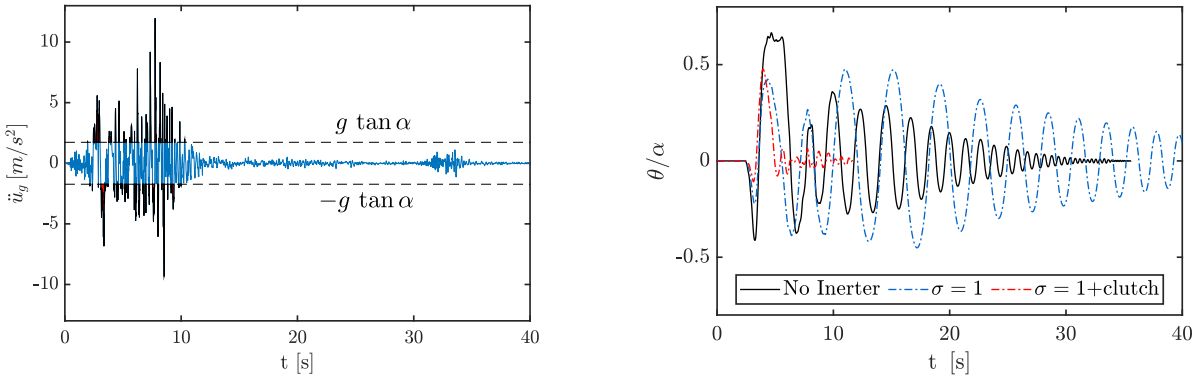

(a) Response to the 1971 San Fernando - Pacoima Dam (upper left abut) record ($p\,t_{uni} = 6.01$).

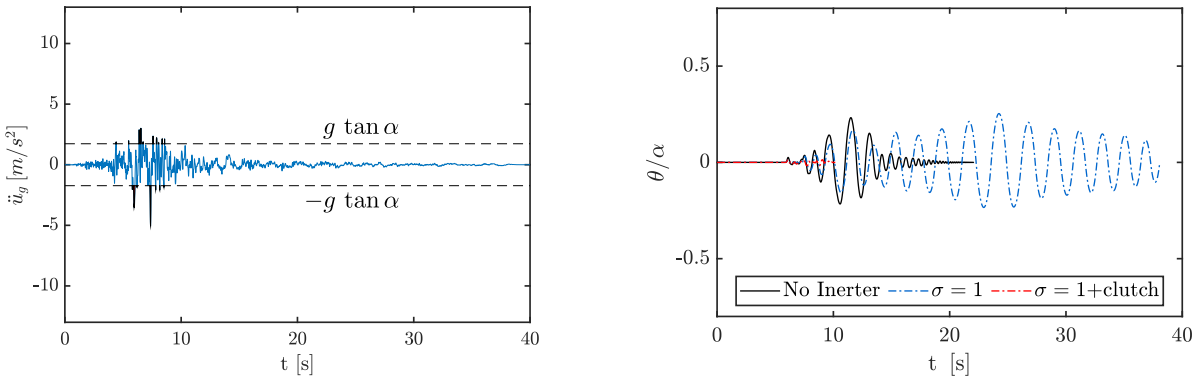

(b) Response to the 1989 Loma Prieta - Saratoga - Aloha Ave record ($p\,t_{uni} = 1.11$).

Figure 3.20: Rotation response of a rigid block of $\alpha = 10°$ and $R = 3[m]$ to ground motions of low and high $p\,t_{uni}$.

3.7.3 Probability of overturning

The probability of rocking overturning can be expressed as a categorical variable z_j, where $z = 1$ represents overturning, and $z = 0$ safe or no rocking motion. Although the categorical nature of the response prevents the calculation of the statistical moments (mean μ and standard deviation β) [126], the overturning probability can be estimated following the maximum likelihood estimation (MLE) [127] approach assuming a log-normal distribution [40]. The MLE calculates the fragility function parameters, $\hat{\mu}$ and $\hat{\beta}$, that maximize the likelihood of reproducing the observed data, such that:

$$\{\hat{\mu}, \hat{\beta}\} = \max_{\mu,\beta} \prod_{j=1}^{n} \Phi\left(\frac{\ln x_j - \mu}{\beta}\right)^{z_j} \left(1 - \Phi\left(\frac{\ln x_j - \mu}{\beta}\right)\right)^{1-z_j} \tag{3.39}$$

where Φ is the normal cumulative distribution function and x_j the intensity measure values. A small slender rigid block ($\alpha = 10°$ and $R = 1[m]$), which is comparatively more unstable than the one considered above for assessing the seismic demands, was selected as a case study. Cloud analyses were then performed by considering the same suite of pulse-like ground motion records described in Table 3.1. Figure 3.21 plots the probability of overturning (P_{ro}) functions

obtained for the three block configurations under study (no inerter, single inerter, and pair of clutched inerters) for apparent mass ratios of $\sigma = 0.5$ and 1.0. The graph also summarizes the data obtained from the numerical analyses. The y-coordinate of each circle represents the percentage of overturning observed for the corresponding IM strip, while the size scale of the circle indicates the number of observations.

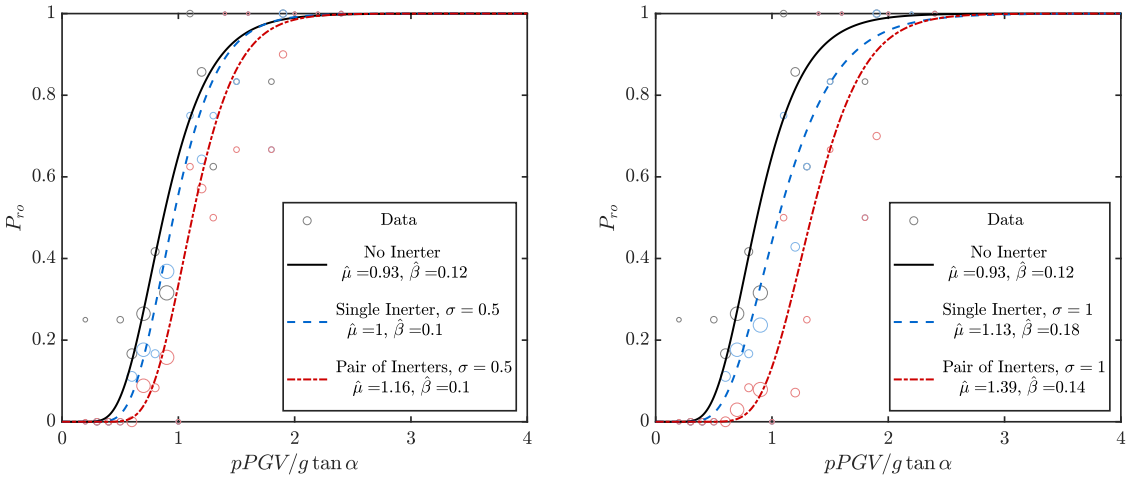

(a) $\sigma = 0.5$. (b) $\sigma = 1$.

Figure 3.21: Comparison of overturning probabilities for a slender rigid block of $\alpha = 10°$ and $R = 1[m]$ and different values of apparent mass ratio.

The fragility functions depicted in Figure 3.21 show a significant improvement in the overturning performance of the block equipped with inerters. The estimated mean IM for the unprotected block is $\hat{\mu} = 0.93$, whereas this parameter increases to $\hat{\mu} = 1$ and $\hat{\mu} = 1.16$ when a single inerter and a pair of clutched inerters with $\sigma = 0.5$ are employed. The overturning probabilities are further reduced if higher inertances are employed (i.e. $\sigma = 1$ in Figure 3.21b) where reductions in mean probabilities of toppling of around 50% are experienced for the clutched inerters configuration. These reduction levels are maintained for probabilities of exceedance of 10% as appreciated from Figure 3.21. These results are in line with the demand reductions observed in the previous section and allow to conclude that the use inerters is an efficient mechanism to reduce maximum rotations and improve the overturning response of rocking blocks under pulse-like ground motions.

3.8 Concluding remarks

This chapter has explored the potential advantages of using supplemental rotational inertia to control the seismic response of rocking structures. The newly proposed system employs inerters, a mechanical device that develops a resisting force proportional to the relative acceleration between its terminals. These devices can be combined with a clutch to ensure they only oppose, and not lead, the rocking motion. The results presented here showed that the

inclusion of the inerter reduces the frequency parameter of the block resulting in lower seismic demands due to the well-known size effect of rocking behaviour. This finding is particularly interesting as it opens the possibility of modifying the dynamic characteristics of a rigid rocking block without altering its geometry.

The effect of the inerter on the rotation transition was evaluated using an extension of Housner's impact formulation. This analysis showed that, in general, the inclusion of the inerter results in higher coefficients of restitution, indicating lower energy dissipation during impact. Importantly, this effect was found not to be significant in slender blocks, although it can affect the efficiency of the proposed strategy when high apparent mass ratios or non-slender structures are considered.

Formal dimensional-orientational assessments of rocking block-inerter systems under single pulse excitations demonstrated that the rocking response of slender blocks with inerters remains perfectly self-similar if the apparent mass ratio, σ, is incorporated as an additional dimensionless-orientationless parameter. On the other hand, the practical self-similarity in the response of non-slender blocks connected to a single inerter is preserved if the block slenderness, α, is eliminated as in independent group but this formulation becomes less accurate if a clutch is introduced, especially at later stages of the rocking response.

Examination of the overturning response of rocking structures under single pulse excitations showed that the inclusion of the inerter reduces the overturning areas in the frequency-amplitude acceleration space and shifts them towards lower frequency regions. This frequency shift is particularly relevant for the cases of overturning after impact, as certain unprotected blocks that would survive the ground motion may overturn when an inerter is attached. Besides, the added non-linearities brought about by the clutch result in inconsistent trends in the rocking response to sinusoidal pulses. Rocking demands were also studied in terms of maximum rotations and peak angular accelerations. Overall, blocks equipped with a single inerter showed smaller rotations and accelerations than unprotected ones. The incorporation of the clutch further reduced the rotation demands but at the expense of diminishing the acceleration reduction effects.

Finally, a probabilistic assessment of the seismic performance of protected and unprotected blocks was conducted using a set of 202 real pulse-like acceleration records. The results of this assessment confirmed the behavioural trends observed under single pulse excitations. Firstly, blocks connected to a single inerter presented lower maximum rotations and accelerations, while blocks with a pair of clutched inerters experienced some detrimental effects on their acceleration demands. A comparison of the overturning fragility curves revealed that the inerter reduces the probability of overturning of the block, while the addition of the clutch further

improves its resistance to overturning.

The analyses presented above considered a rigid block model which reasonably represents the rocking response of free-standing bodies, such as non-structural equipment, museum artefacts or rigid monumental structures. In the next chapter, a modified model is introduced in order to incorporate features commonly observed in rocking building structures, namely post-tensioned tendons and independent levels of seismic mass and weight.

Chapter 4

Fundamental dynamics of post-tensioned rocking structures

4.1 Introduction

In the previous chapter, the response of rocking structures equipped with supplemental rotational inertia devices was examined using a simplified rigid-block formulation. While this model reasonably captures the behaviour of free-standing bodies, such as non-structural equipment and museum artefacts, it does not generally represent the response of rocking building structures. In particular, rocking walled systems usually mobilize a seismic mass that is higher than the gravitational mass exerting the restoring moment. Moreover, post-tensioned tendons are commonly incorporated in order to increase the lateral strength and improve the re-centring capabilities of the system. In this chapter, these particular characteristics of rocking building structures are incorporated into the model and subsequently used to analyse the response of post-tensioned rigid walled systems. Firstly, the effect of the vertical tendons on the rocking response of the structure is assessed in terms of maximum rotations and peak angular accelerations for a wide range of pulse excitations. Subsequently, the inerter device is introduced and original equations that describe the rocking motion of the post-tensioned wall-inerter system are derived. In addition to the reductions in rotation and acceleration demands, the effects of the inerter on the base shear are also evaluated. Finally, a probabilistic assessment of the seismic performance of a typical building structure is conducted using the set of 202 pulse-like ground motions introduced in the previous chapter. The results of the analyses demonstrate that post-tensioned rocking structures equipped with inerters experience smaller rotation and acceleration demands than unprotected ones and have lower probabilities of exceeding limit states associated with non-structural damage.

4.2 Fundamental dynamics of a free-standing rocking wall

The free-standing rigid block considered in Housner's [3] early study corresponds to a particular case in which the only mass mobilized by the horizontal and gravity accelerations is the mass of the body itself. This assumption is reasonable for many rocking objects, such as museum artefacts and non structural equipment, but is not usually valid for rocking building structures. In these cases, additional masses attached to the structural elements change the inertial forces and the use of gravity resistance systems (e.g. gravity frames) or in-plane lateral resistance elements (e.g rectangular walls) can modify the ratio between the tributary seismic mass, m_{sis}, and the gravity load, W, exerting the restoring moment (Figure 4.1).

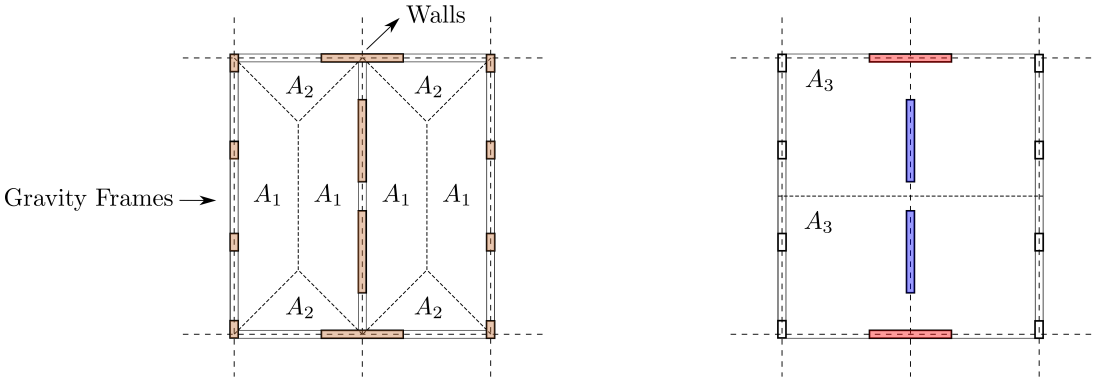

(a) Vertical gravity elements (indicated in brown) and their corresponding tributary areas.

(b) Seismic mass taken by each lateral resistant element (red: X direction, blue: Y direction).

Figure 4.1: Gravity load and seismic mass in building structures.

The dynamic response of such structures can be better represented by the model depicted in Figure 4.2, where the rigid free-standing wall is free to rotate about points O and O', and appropriate arrangements to prevent slipping (such as shear keys) have been considered. If a diaphragm connection with rotational decoupling is assumed (e.g. large diameter pin [128]), the seismic mass and gravity loads can be concentrated and considered to act at point C. The geometry of the wall is characterized by the slenderness α and the size parameter R, while its rotation is measured by the angle θ. In this formulation impact is treated following Housner's approach [3], considering the coefficient of restitution as an independent parameter and equal to $r = 0.85$.

In most practical building applications the rotational inertia and weight of the rocking wall are significantly smaller than the corresponding translational seismic mass, m_{sis}, and tributary gravity load, W, and can be neglected. Then, under a horizontal ground excitation, $\ddot{u}_g$, the rigid wall uplifts and starts rocking if:

$$\ddot{u}_g \geq \frac{g}{m_{ratio}} \tan \alpha \tag{4.1}$$

where $m_{ratio} = m_{sis}/m_g$ is the ratio between the seismic mass and the gravitational mass

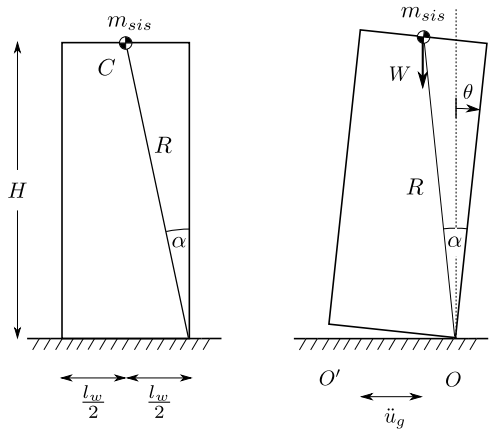

Figure 4.2: Single-degree-of-freedom system representing a rocking wall.

associated to the gravity load transferred to the wall (i.e. $m_g = W/g$). Evaluating the rotational equilibrium around the rocking pivot point gives (Figure 4.2):

$$\ddot{\theta}\cancelto{0}{I_0} + m_{sis}\,R^2\,\ddot{\theta} + WR\,\sin(\alpha\,sgn(\theta) - \theta) = -m_{sis}\,\ddot{u}_g\,R\,\cos(\alpha\,sgn(\theta) - \theta) \tag{4.2}$$

The equation above can be rearranged and presented in a compact form:

$$\ddot{\theta} = -p_w^2\big(\sin(\alpha\,sgn(\theta) - \theta) + m_{ratio}\,\frac{\ddot{u}_g}{g}\cos(\alpha\,sgn(\theta) - \theta)\big) \tag{4.3}$$

where p_w is the frequency parameter of the rigid rocking wall defined as

$$p_w = \sqrt{\frac{g}{R\,m_{ratio}}} \tag{4.4}$$

4.2.1 Response scaling and similarity

The dynamic response of the classic rocking block studied by Housner [3] is governed by four independent dimensionless parameters [122].

$$\theta_{max} = f\left(\frac{\omega_g}{p}\,,\,\frac{a_g}{g}\,,\,\alpha\,,\,r\right) \tag{4.5}$$

Equations 4.3 and 4.4 show that the ratio between the seismic and gravitational masses in a rocking building divide the gravity acceleration, g. Therefore, the response of a rocking building wall is governed by:

$$\theta_{max} = f\left(\frac{\omega_g}{p_w}\,,\,\frac{a_g\,m_{ratio}}{g}\,,\,\alpha\,,\,r\right) \tag{4.6}$$

For most practical applications the wall slenderness, α, will be smaller than 20° (e.g. $l_w = 3[m]$ and $H = 9[m] \rightarrow \alpha = 9.5°$), and the dimension-orientationless properties developed by

Dimitrakopoulos and DeJong [122] for slender blocks can be applied:

$$\frac{\theta_{max}\, g}{a_g\, m_{ratio}} = \phi\left(\frac{\omega_g}{p_w}\,,\, \frac{a_g\, m_{ratio}}{g\, \tan\alpha}\,,\, r\right) \tag{4.7}$$

Figure 4.3 compares the response of two different slender blocks of equivalent dimension-orientationless parameters ($a_g\, m_{ratio}/g \tan\alpha = 23.3$ and $\eta = 0.85$), subjected to a pulse excitation of frequency ratio $\omega_g/p_w = 8$. It is evident from Figure 4.3 that, when presented in terms of the proposed parameters, the responses collapse into a single master curve.

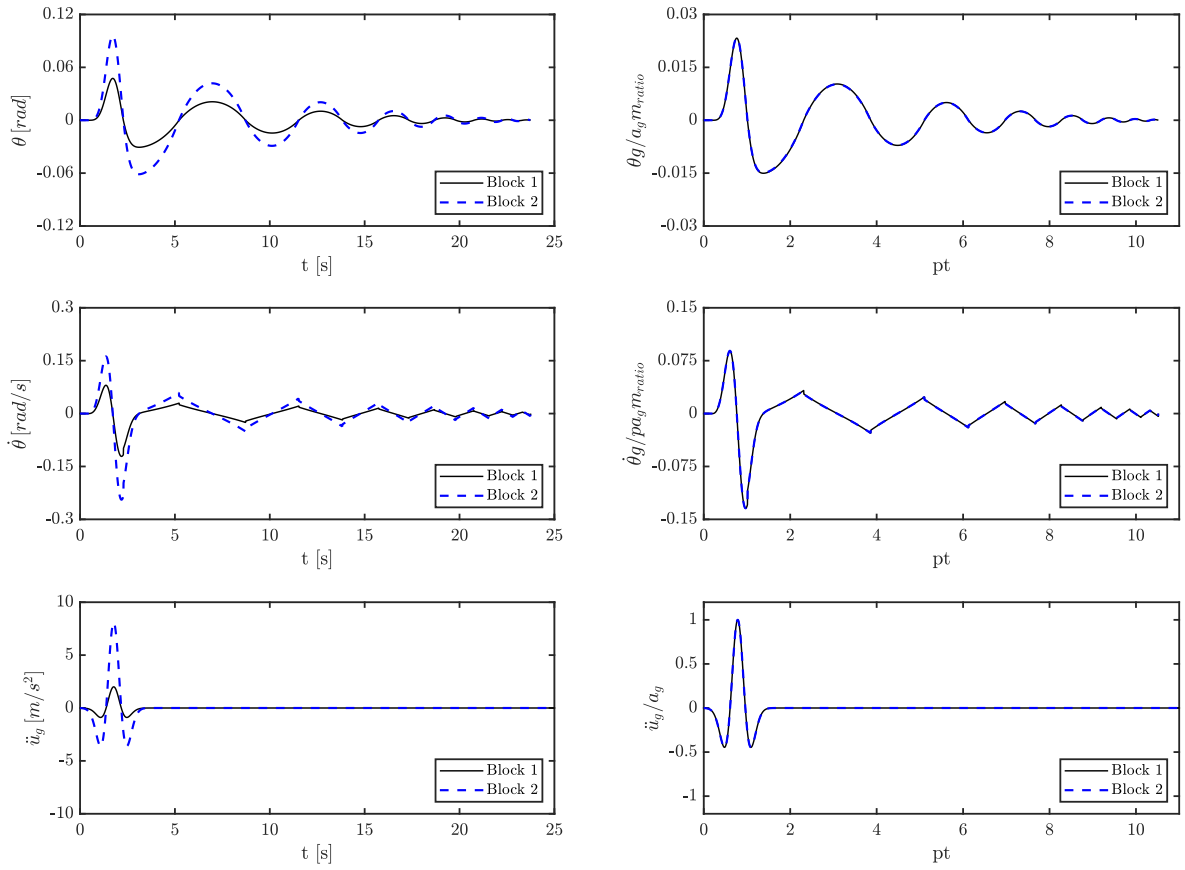

Figure 4.3: Response of two rocking walls of different shape and size but equivalent dimension-orientionless parameters (Block 1: $R_1 = 5[m]$, $\alpha_1 = 5°$ and $m_{ratio,1} = 10$; Block 2: $R_2 = 10[m]$, $\alpha_2 = 10°$ and $m_{ratio,2} = 5$).

4.2.2 Rocking response under pulse excitations

The rocking response of free-standing blocks is usually studied by means of rocking spectra, like the one presented in Figure 4.4a. This representation consist of contour plots of the normalized response variable in the frequency ratio (ω_g/p_w) and acceleration amplitude plane ($a_g\, m_{ratio}/g \tan\alpha$), for a block of a given slenderness α. In this part of the study, symmetric Ricker wavelets [129, 130] (Equation 4.8) are used as pulse excitations. This analytical wavelet has been shown to satisfactorily approximate the coherent pulse of several pulse-like ground

motions [131].

$$\ddot{u}_g(t) = a_g\left(1 - \frac{2\pi^2 t^2}{T_g^2}\right) e^{-\frac{\pi^2 t^2}{T_g^2}} \tag{4.8}$$

where $T_g = 2\pi/\omega_g$ is the period that maximizes the Fourier spectrum of the symmetric Ricker wavelet, and a_g is the acceleration amplitude.

As noted in the previous section, the mass ratio has two competing effects on the dynamic response of the wall. On the one hand it reduces the frequency parameter, p_w, improving the global stability of the system (size effect of rocking behaviour [3]), while on the other hand it amplifies the ground acceleration. These effects can be examined with reference to Figure 4.4. Figure 4.4b shows the maximum rotation response of a given block ($R = 5[m]$ and $\alpha = 10°$) subjected to a symmetric Ricker pulse of acceleration amplitude $a_g = g\tan\alpha$ and frequency $\omega_g = 2.8[rad/s]$ for different values of mass ratio. The path followed by the block on the frequency ratio-acceleration amplitude plane is indicated with a white dashed line in Figure 4.4a.

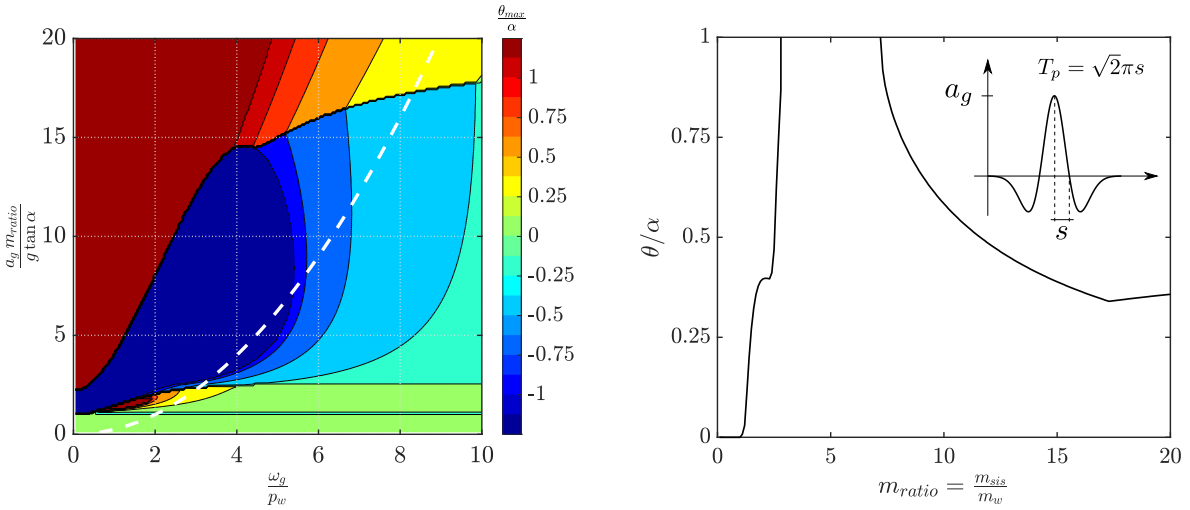

(a) Rocking spectrum for $\alpha = 10°$.

(b) Effect of m_{ratio} for a given block.

Figure 4.4: Rocking spectra under symmetric Ricker pulse ground motions.

The low mass ratio area of the spectrum shown in Figure 4.4b (or low frequency ratio according to Equation 4.4) shows that small increments in the seismic mass cause the response to swiftly change from no-uplifting to overturning. As the mass ratio keeps increasing, the shift in the frequency parameter, p_w, takes the block outside of the overturning regions (indicated in blue and red in Figure 4.4a) and into the safe rocking area. The maximum rotation response then keeps decreasing until it starts surging again in the high mass ratio region (or high frequency ratio), although without reaching the overturning condition. In real rocking building structures, the mass ratio usually ranges from 1 (Housner's rocking block) to well over 10 in cases where the rocking element is only used as a lateral resistant system and the gravity loads are supported by secondary elements.

4.3 Dynamics of post-tensioned rocking walls

In post-tensioned rocking walls, the structural member is free to uplift and rock while post-tensioned tendons are incorporated to increase the lateral resistance and re-centring capabilities of the building. Additional energy dissipation can be introduced by adding unbonded steel bars or external dissipation devices. This type of structures can be studied considering the model presented in Figure 4.5, where the rocking wall analysed in the previous section has been connected to the base through an elastic tendon passing through its middle. When the system of Figure 4.5 rotates the weight, W, and the force in the vertical tendon, F_{pt}, exert a restoring moment, M_r.

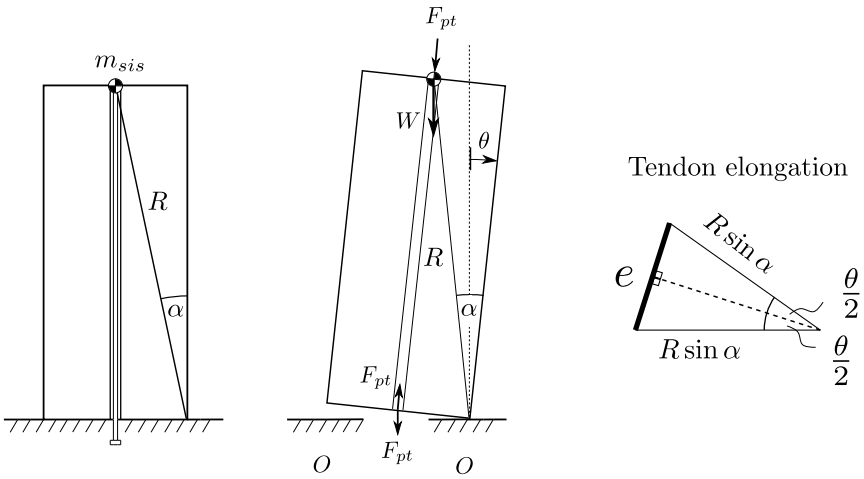

Figure 4.5: Post-tensioned rigid rocking wall under a horizontal ground excitation.

The post-uplifting stiffness of a free-standing wall (as the one studied in Section 4.2) is negative, since the line of action of the weight approaches the pivot point as rotation increases, reducing the lever arm of the restoring moment. By contrast, when elastic tendons are incorporated, the rotation of the wall increases the re-centring elastic force, providing a positive stiffness that is added to the negative stiffness of the rocking block. The elongation of the tendon, e, can be expressed as a function of the rotation θ (Figure 4.5):

$$e = R\sin\alpha\sqrt{2}\sqrt{1-\cos\theta} \tag{4.9}$$

and the force in the post-tensioned tendon is:

$$F_{pt} = \frac{EA\,e}{R\cos\alpha} + P_0 = EA\tan\alpha\sqrt{2}\sqrt{1-\cos\theta} + P_0 \tag{4.10}$$

where $EA/R\cos\alpha$ is the axial stiffness of the vertical tendon and P_0 is the initial post-tensioning force. For a positive rotation ($\theta > 0$), the total restoring moment is given by:

$$M_r(\theta) = WR\sin(\alpha-\theta) + F_{pt}\,R\sin\alpha\cos\frac{\theta}{2} \tag{4.11}$$

Replacing Equation 4.10 into Equation 4.11 yields:

$$M_r(\theta) = WR\sin(\alpha-\theta) + R\sin\alpha\left(EA\tan\alpha\,\sin\theta + P_0\sqrt{\frac{1+\cos\theta}{2}}\right) \tag{4.12}$$

which can be rearranged as:

$$\frac{M_r(\theta)}{WR} = \sin\alpha\left(\cos\theta + \frac{P_0}{W}\sqrt{\frac{1+\cos\theta}{2}} + \sin\theta\left(\frac{EA}{W}\tan\alpha - \cot\alpha\right)\right) \tag{4.13}$$

If small rotations are considered (small θ), Equation 4.13 can be linearized such that:

$$\frac{M_r(\theta)}{WR} = \sin\alpha\left(1 + \frac{P_0}{W} + \theta\left(\frac{EA}{W}\tan\alpha - \cot\alpha\right)\right) \tag{4.14}$$

The term multiplying θ in Equation 4.14 corresponds to the stiffness of the system after uplifting. Therefore, the linearized condition to obtain a positive post-uplift stiffness is:

$$\frac{EA}{W} > \frac{1}{\tan^2\alpha} \tag{4.15}$$

This condition is equivalent to the expression obtained by Vassiliou and Makris [53] for vertically restrained classic rocking blocks. Figure 4.6 compares the moment-rotation response of post-tensioned rocking walls for different levels of normalized elastic force (EA/W) and initial post-tension force (P_0/W). As expected, the axial stiffness of the tendon only modifies the slope of the response after uplifting. On the other hand, the initial post-tensioning force increases the uplift threshold and therefore shifts the curves in Figure 4.6b vertically.

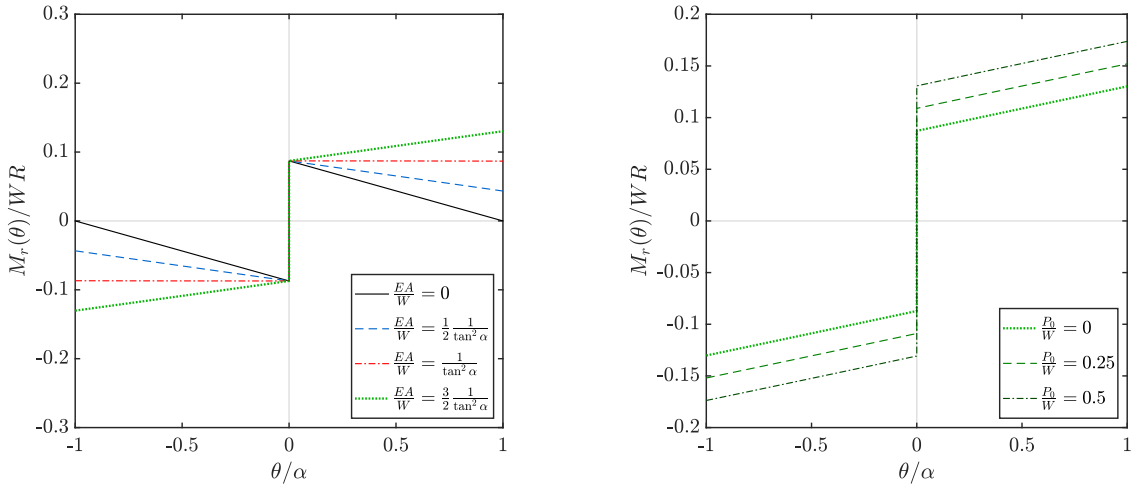

(a) No initial pre-stress ($P_0/W = 0$).

(b) Constant tendon stiffness: $\frac{EA}{W} = \frac{3}{2}\frac{1}{\tan^2\alpha}$.

Figure 4.6: Effect of a) the tendon stiffness, EA/W, and b) initial post-tensioning force, P_0/W, on the moment rotation relation of the rocking wall.

4.3.1 Free vibrations response of post-tensioned rocking walls

With reference to Figure 4.5, the evaluation of the rotational equilibrium about the rocking pivot point gives:

$$m_{sis}\, R^2\, \ddot{\theta} + W R \sin(\alpha - \theta) + R \sin\alpha \left(EA \tan\alpha \, \sin\theta + P_0 \sqrt{\frac{1+\cos\theta}{2}} \right) = 0 \qquad (\theta > 0) \tag{4.16}$$

Introducing the frequency parameter, $p_w = \sqrt{g/R\, m_{ratio}}$, and rearranging leads to:

$$\ddot{\theta} = -p_w^2 \left(\sin(\alpha - \theta) + \sin\alpha \left(\frac{EA}{W} \tan\alpha \sin\theta + \frac{P_0}{W} \sqrt{\frac{1+\cos\theta}{2}} \right) \right) \tag{4.17}$$

Equation 4.17 can be linearized if slender blocks are considered ($\alpha \leq 20°$), such that:

$$\ddot{\theta} - p_w^2 \left(1 - \frac{EA}{W}\alpha^2 \right) \theta = -p_w^2 \alpha \left(1 + \frac{P_0}{W} \right) \tag{4.18}$$

If the post-uplift stiffness of the wall is null ($EA\alpha^2/W = 1$), the second term of the left-hand side of Equation 4.18 becomes zero, as the restoring moment is independent from the rotation amplitude. Therefore, for a wall released from rest ($\dot{\theta}(0) = 0$) with an initial rotation θ_0, the solution of Equation 4.18 is defined by parts as:

$$\theta(t) = \begin{cases} \frac{\alpha\left(1+\frac{P_0}{W}\right)}{1-\frac{EA}{W}\alpha^2} - \left(\frac{\alpha\left(1+\frac{P_0}{W}\right)}{1-\frac{EA}{W}\alpha^2} - \theta_0 \right) \cosh\left(p_w\, t \sqrt{1-\frac{EA}{W}\alpha^2} \right), & \left(EA\alpha^2/W \neq 1\right) \\ \\ \frac{-\alpha^2\, p_w^2\, t^2 \left(1+\frac{P_0}{W}\right)}{2} + \theta_0, & \left(EA\alpha^2/W = 1\right) \end{cases} \tag{4.19}$$

Equation 4.19 describes the motion of the wall as it rotates back to the vertical position. If there is no energy dissipation during impact, the block will then rotate in the negative direction ($-\theta$) reaching a maximum amplitude of $-\theta_0$, and fall back to reach its initial position. The time required to complete this cycle of oscillation is the period of free vibration. Following Housner's [3] reasoning, the time needed to go from $\theta = \theta_0$ to $\theta = 0$ corresponds to T/4. Therefore:

$$Tp_w = \phi\left(\frac{\theta_0}{\alpha}, \frac{EA\alpha^2}{W}, \frac{P_0}{W} \right) = \begin{cases} \frac{4}{\sqrt{1-\frac{EA}{W}\alpha^2}} \cosh^{-1} \left\{ \frac{1}{1-\frac{\theta_0\left(1-\frac{EA}{W}\alpha^2\right)}{\alpha\left(1+\frac{P_0}{W}\right)}} \right\}, & \left(EA\alpha^2/W \neq 1\right) \\ \\ 4\sqrt{\frac{2\,\theta_0}{\alpha\left(1+\frac{P_0}{W}\right)}}, & \left(EA\alpha^2/W = 1\right) \end{cases} \tag{4.20}$$

Equation 4.20 shows that for a post-tensioned block of a given mass ratio and geometry (p_w and α), the period of oscillation, T, depends on the initial rotation, θ_0, the dimensionless elastic force, EA/W, and the dimensionless post-tension force, P_0/W. Figure 4.7 plots this expression for fixed values of θ/α, P_0/W and $EA\alpha^2/W$. As expected, Figure 4.7a shows that the period of oscillation decreases for higher values of initial post-tension and elastic forces. This effect is more significant closer to the origin ($P_0/W \leq 2$ and $EA\alpha^2/W \leq 1$) and becomes less important for higher values of vertical forces. On the other hand, Housner's early study already identified that the period of oscillation of a rocking body strongly depends on the initial rotation amplitude [3]. The plots presented in Figure 4.7b and Figure 4.7c are consistent with this finding, showing that higher values of θ_0/α correspond to longer periods of oscillation. Moreover, the influence of the post-tensioned tendon is more important for initial rotations close to α, and becomes insignificant for small values of θ_0/α.

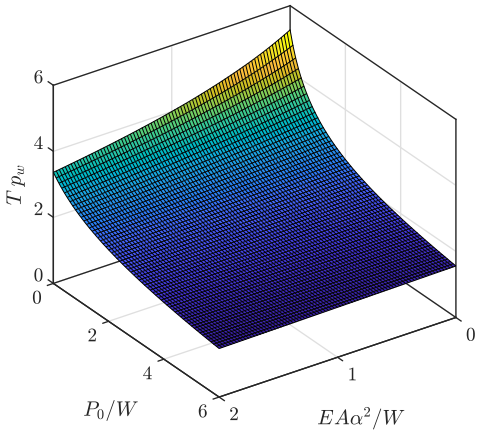

(a) Initial rotation, $\theta_0/\alpha = 0.5$.

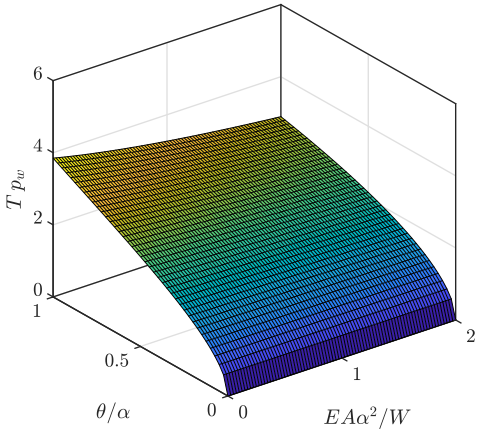

(b) Post-tensioning force $P_0/W = 2$.

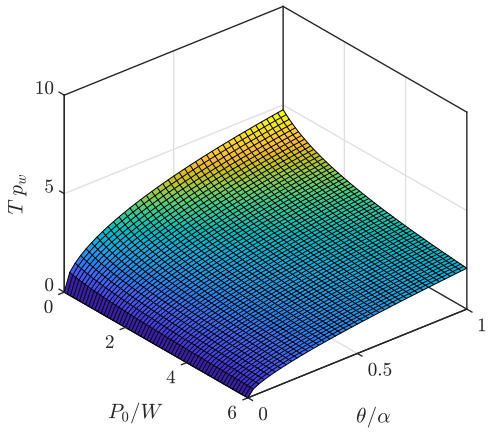

(c) Elastic force $EA\alpha^2/W = 1.5$ (positive stiffness after uplifting).

Figure 4.7: Effect of the initial rotation (θ/α), elastic force (EA/W), and initial post-tensioning force (P_0) on the period of oscillation of a post-tensioned rocking wall.

4.3.2 Seismic response of post-tensioned structural walls

When subjected to a horizontal ground excitation, $\ddot{u}_g$, the post-tensioned rigid wall shown in Figure 4.5 uplifts and starts rocking when

$$\ddot{u}_g \geq \left(\frac{P_0}{W} + 1\right) \frac{g}{m_{ratio}} \tan\alpha \tag{4.21}$$

Evaluating the rotational equilibrium of the post-tensioned wall about the pivot points (positive and negative directions) gives:

$$m_{sis}\, R^2\, \ddot{\theta} + WR\, \sin(\alpha\, sgn(\theta) - \theta) + sgn(\theta)\, F_{pt}\, R\, \sin\alpha \cos\frac{\theta}{2} = \\ - m_{sis}\, \ddot{u}_g R\, \cos(\alpha\, sgn(\theta) - \theta) \tag{4.22}$$

Combining Equations 4.10 and 4.22, and introducing the frequency parameter, $p_w = \sqrt{g/R\, m_{ratio}}$, yields:

$$\ddot{\theta} = -p_w^2 \Bigg(\sin(\alpha\, sgn(\theta) - \theta) + m_{ratio}\, \frac{\ddot{u}_g}{g} \cos(\alpha sgn(\theta) - \theta) \\ + \sin\alpha \left(\frac{EA}{W} \tan\alpha \sin\theta + sgn(\theta)\, \frac{P_0}{W} \sqrt{\frac{1+\cos\theta}{2}} \right) \Bigg) \tag{4.23}$$

which is equivalent to the expression derived by Vassiliou and Makris [53] for vertically restrained rigid blocks. Again, this equation of motion can be linearized if slender walls are considered ($\alpha \leq 20°$), such that:

$$\ddot{\theta} = -p_w^2 \left(\alpha\, sgn(\theta) \left(1 + \frac{P_0}{W}\right) + \theta \left(\frac{EA\alpha^2}{W} - 1 \right) + m_{ratio}\, \frac{\ddot{u}_g}{g} \right) \tag{4.24}$$

Figure 4.8 compares the seismic demands (peak rotation and angular acceleration) for slender walls with different levels of elastic and initial post-tensioning force, subjected to symmetric Ricker pulses of acceleration amplitude $a_g = 2\, g \tan\alpha / m_{ratio}$. The analyses presented in Figure 4.8 consider dimensionless elastic forces that result in post-uplifting stiffnesses varying from negative to positive values, while the maximum post-tensioning force is limited by the rocking-triggering condition (Equation 4.21). The response of a free-standing rocking block is also included in Figure 4.8 for comparative purposes.

The results depicted in Figure 4.8 show that the elastic force improves the stability of the wall when $\omega_g / p_w < 2$ (small structures), but has very little effect on the maximum rotation and acceleration response for larger structures. This behaviour is related to the increase in the post-uplifting stiffness, which allows the block to withstand rotations greater than α and still return to its vertical position. Nevertheless, higher rotational accelerations are observed for some small to medium-sized walls ($\omega_g / p_w < 4$) in comparison with free-rocking walls.

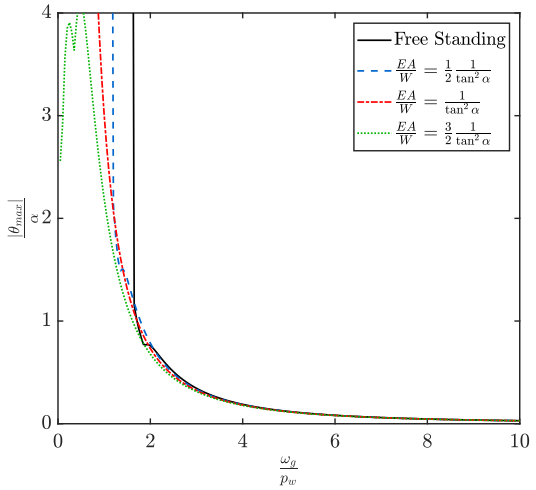

(a) Rotation spectra, $P_0 = 0$.

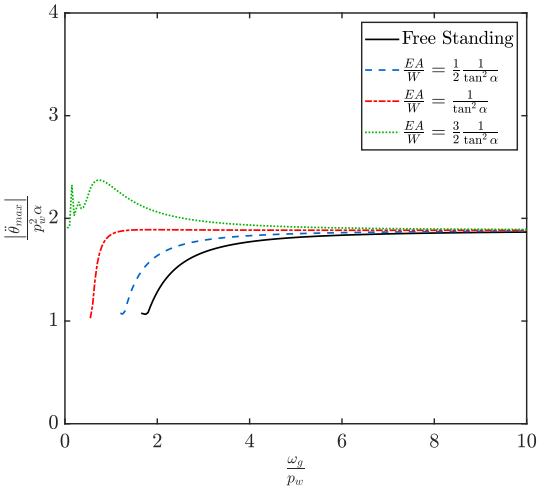

(b) Acceleration spectra, $P_0 = 0$.

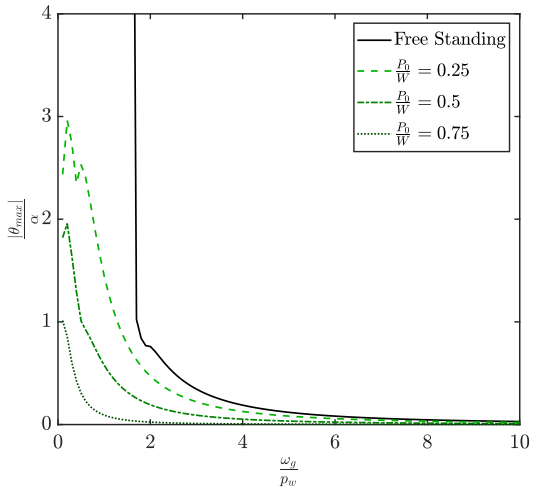

(c) Rotation spectra, $\frac{EA}{W} = \frac{3}{2}\frac{1}{\tan^2\alpha}$.

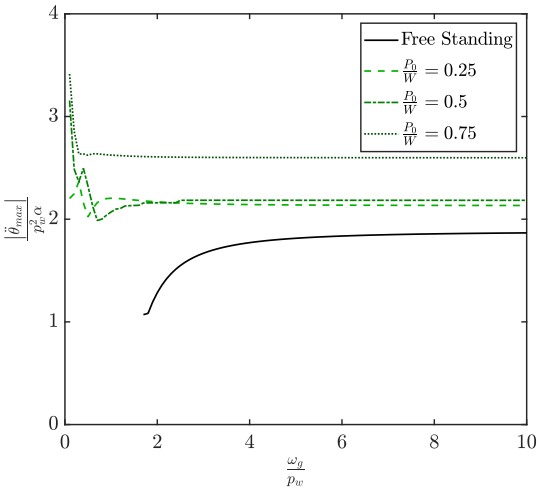

(d) Acceleration spectra, $\frac{EA}{W} = \frac{3}{2}\frac{1}{\tan^2\alpha}$.

Figure 4.8: Effect of the dimensionless elastic force, EA/W, and dimensionless initial post-tensioning force, P_0/W, on the rotation and angular acceleration demands for slender walls subjected to Ricker pulses of acceleration amplitude $a_g = 2\,g\,\tan\alpha/m_{ratio}$.

Moreover, the larger the elastic force the higher the relative acceleration at lower frequency ratios ($\omega_g/p_w < 4$).

On the other hand, the level of initial post-tensioning force has a more significant effect on the maximum rotation response of both, small and large structures. While an improved stability can be observed for $\omega_p/p_w < 4$, reductions in the maximum rotations for greater frequency ratios (larger walls) are also obtained. Importantly, the response enhancement becomes more significant the higher the level of initial post-tensioning. However, these improvements happen at the expense of inducing higher rotational accelerations over the full range of frequency ratios studied.

The results presented in Section 4.2.1 show that regardless of the acceleration amplitude of a ground motion, the intensity dimensionless parameter, $a_g m_{ratio}/g \tan\alpha$, can be significantly amplified by the ratio between the seismic and gravitational masses. Consequently, high effective acceleration amplitudes that are usually not relevant for the study of classic free-standing blocks, need to be considered when dealing with post-tensioned rocking walls. Figure 4.9 compares the peak seismic demands (rotation and angular acceleration) for different post-tensioned rocking walls subjected to acceleration pulses of amplitude $a_g = 20\, g \tan\alpha/m_{ratio}$. The results of the analyses suggest that the use of post-tensioned tendons becomes less advantageous when pulses of higher acceleration amplitude are considered. Although the elastic force slightly reduces the overturning cases, the initial post-tensioning force can increase the rotation and acceleration demands in some cases. This behaviour is studied in more detail in Figure 4.10, where the maximum response of a block with $\omega_p/p_w = 4$ to symmetric Ricker pulses of different acceleration amplitude is plotted as a function of the dimensionless initial post-tensioning force.

It can be observed from Figure 4.10a that for low ground acceleration amplitudes, larger initial post-tensioning forces are related to proportionally lower maximum rotations with the potential to suppress the rocking response altogether (Equation 4.21). As previously observed in Figure 4.8, this reduction is accompanied by an important increase in the maximum peak accelerations. For the post-tensioned wall considered in the analysis ($\alpha \leq 20°$, $\omega_p/p_w = 4$) and with reference to the response of a free-standing block, a reduction of 50% in the maximum rotation would be associated with a 25% increase in the peak angular acceleration. This acceleration magnification becomes even more significant for higher levels of initial post-tensioning force.

On the other hand, when ground motions of higher acceleration amplitudes are considered (Figure 4.10b), a spectral region where the rotation and acceleration are simultaneously amplified can be identified. For small values of dimensionless initial post-tensioning force ($P_0/W < 6$), rotation demands are significantly amplified, reaching a peak of more than twice the maximum rotation of the benchmark free-standing block at around $P_0/W \approx 4$. A similar trend is observed for rotational acceleration demands, although with a smaller amplification

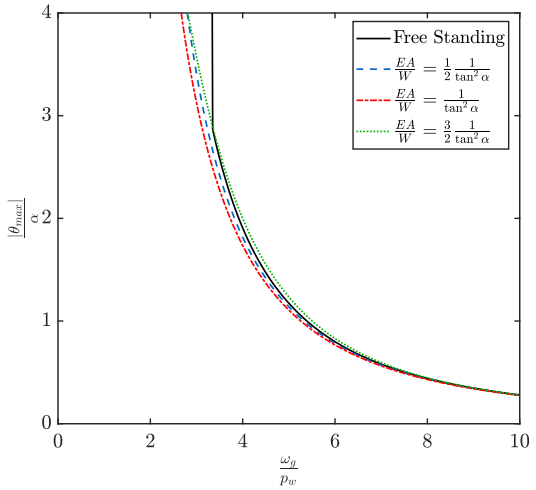

(a) Rotation spectra, $P_0 = 0$.

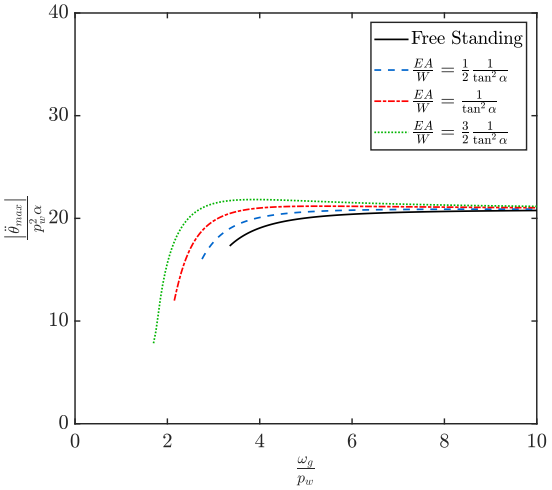

(b) Acceleration spectra, $P_0 = 0$.

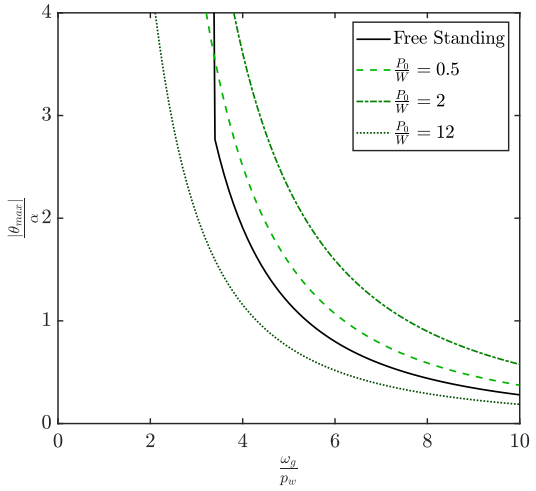

(c) Rotation spectra, $\frac{EA}{W} = \frac{3}{2}\frac{1}{\tan^2\alpha}$.

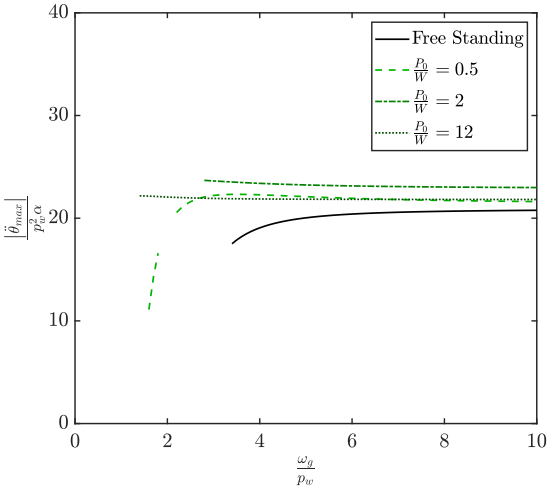

(d) Acceleration spectra, $\frac{EA}{W} = \frac{3}{2}\frac{1}{\tan^2\alpha}$.

Figure 4.9: Effect of the dimensionless elastic force, EA/W, and dimensionless initial post-tensioning force, P_0/W, on the peak rotation and angular acceleration demands for slender walls subjected to Ricker pulses of acceleration amplitude $a_g = 20\,g\,\tan\alpha/m_{ratio}$.

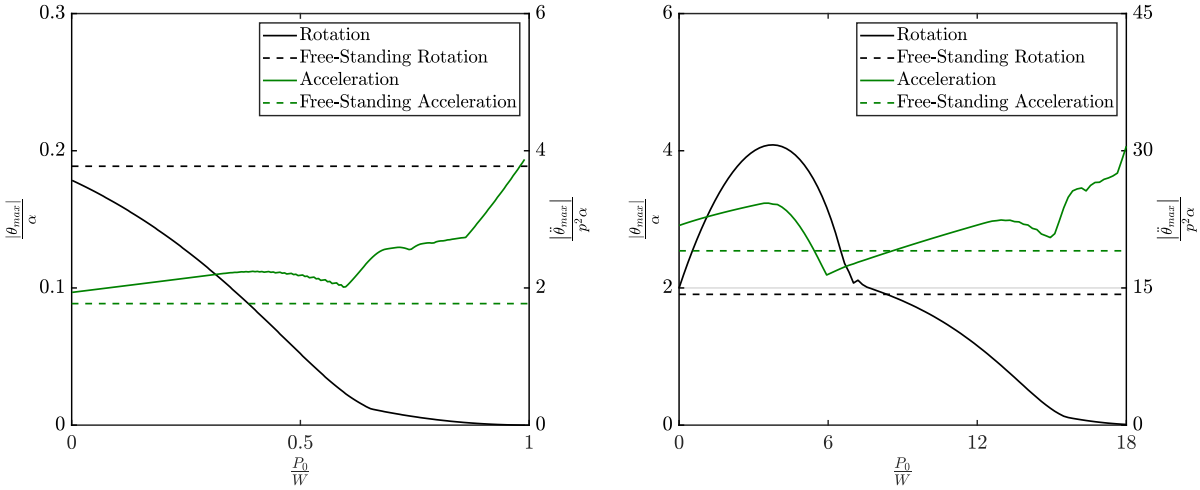

(a) $a_g = 2\,g\,\tan\alpha/m_{ratio}$. (b) $a_g = 20\,g\,\tan\alpha/m_{ratio}$.

Figure 4.10: Effect of the dimensionless initial post-tensioning force, P_0/W, on the rotation and angular acceleration demands of a slender wall with $\frac{EA}{W} = \frac{3}{2}\frac{1}{\tan^2\alpha}$, subjected to a symmetric Ricker pulse of frequency ratio $\omega_p/p_w = 4$.

ratio. This observation is particularly relevant, as it happens at levels of initial post-tensioning force ratios that are most commonly observed in practice. For higher magnitudes of initial post-tensioning forces, the behaviour of the seismic demands resembles the trends observed in Figure 4.10a for smaller ground acceleration amplitudes, with maximum rotations reducing progressively and peak accelerations being amplified.

4.4 Seismic control of post-tensioned walls with inerters

Although post-tensioned systems have been shown to be effective in controlling structural damage, high rotations and accelerations associated with the rocking motion can cause significant non-structural and contents damage. The analyses conducted in the previous chapter have shown that the use of supplemental rotational inertia can help to significantly reduce these seismic demands. This control strategy can also be applied to post-tensioned walled buildings by connecting the inerter directly to the rocking elements or rigid diaphragm of the structure, as shown in Figure 4.11. For low-rise buildings, the wall element can be assumed to behave as a rigid block, and the dynamic behaviour of the system can be studied simply incorporating the contribution of the inerter to the models examined in previous sections. Herein, an inerter connected to the top of the wall (Point C) is considered for simplicity.

Rocking motion initiates when the overturning moment due to the ground excitation exceeds the restoring moment exerted by the self-weight and the vertical tendon (Equation 4.21). Until this instant, the resisting force in the inerter is zero, since there is no relative acceleration between its terminals. Once the block uplifts, point C in Figure 4.11 follows a circular path.

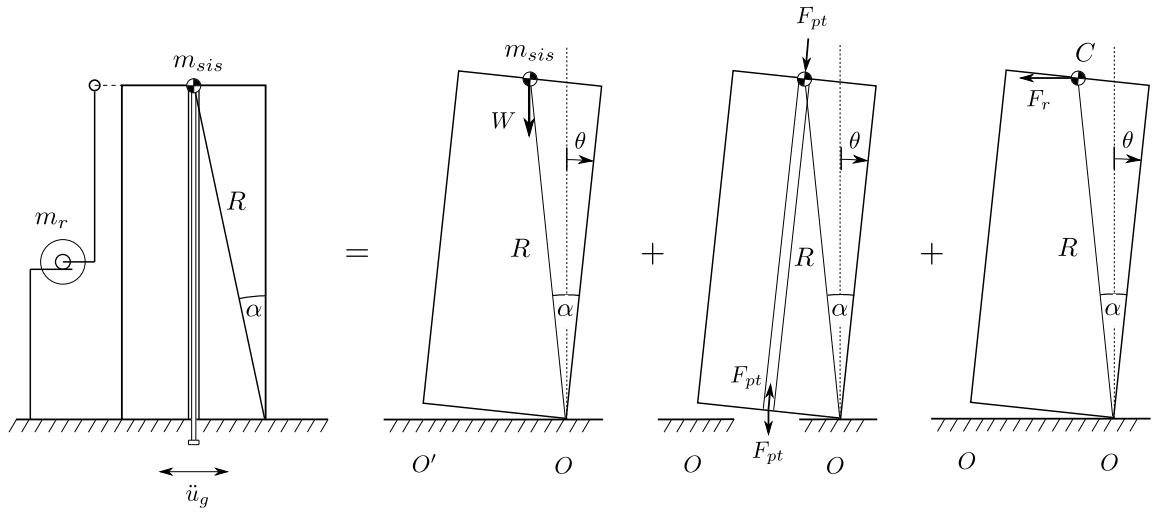

Figure 4.11: Single-degree-of-freedom system representing a post-tensioned rocking wall equipped with an inerter.

Neglecting the contribution of the centripetal acceleration, the resisting force in the inerter is:

$$F_r = m_r\, R\, \ddot{\theta} \cos(\alpha sgn(\theta) - \theta) \tag{4.25}$$

where m_r is the inertance or apparent mass of the inerter. Evaluating the rotational equilibrium around the rocking pivot point gives:

$$\begin{aligned} \left(m_{sis}R^2 + m_r R^2 \cos^2(\alpha\, sgn(\theta) - \theta)\right)\ddot{\theta} \\ + WR \sin(\alpha\, sgn(\theta) - \theta) + sgn(\theta)\, F_{pt}\, R \sin\alpha \cos\frac{\theta}{2} \\ = -m_{sis}\, \ddot{u}_g R \cos(\alpha\, sgn(\theta) - \theta) \end{aligned} \tag{4.26}$$

Combining Equations 4.10 and 4.26, and rearranging:

$$\begin{aligned} \ddot{\theta} = -p_{w,\sigma}^2 \Bigg(\sin(\alpha\, sgn(\theta) - \theta) + m_{ratio}\, \frac{\ddot{u}_g}{g} \cos(\alpha sgn(\theta) - \theta) \\ + \sin\alpha \left(\frac{EA}{W} \tan\alpha \sin\theta + sgn(\theta)\, \frac{P_0}{W} \sqrt{\frac{1+\cos\theta}{2}} \right) \Bigg) \end{aligned} \tag{4.27}$$

with

$$p_{w,\sigma} = \sqrt{\frac{g}{m_{ratio}\, R \left(1 + \sigma \cos^2(\alpha\, sgn(\theta) - \theta)\right)}} \tag{4.28}$$

where σ is the aparent mass ratio defined as: $\sigma = m_r/m_{sis}$. Equations 4.27 and 4.28 are analogous to the equation of motion obtained in Chapter 3 for free-rocking bodies equipped with inerters. These expressions show that the inclusion of the inerter effectively reduces

the frequency parameter, p_w, of the post-tensioned rocking element. This reduction generally results in enhanced stability and lower seismic demands due to the well-known size effect of the rocking behaviour [3]. Importantly, the frequency parameter of a rocking wall depends only on the size, R, and the mass ratio of the structure (Equation 4.4). Consequently, it cannot be modified without altering the elevation (R) or the plan distribution of the building (m_{ratio}). This highlights the significance of inerter-based control strategies as they open the door for an expedient modification of the dynamic response of a rocking system without altering its geometry.

As mentioned previously, in most practical cases the wall elements can be considered to be slender ($\alpha < 20°$), and Equation 4.27 can be linearized such that:

$$\ddot{\theta} = -p_{w,\sigma}^2 \left(\alpha \, sgn(\theta) \left(1 + \frac{P_0}{W} \right) + \theta \left(\frac{EA\alpha^2}{W} - 1 \right) + m_{ratio} \frac{\ddot{u}_g}{g} \right) \tag{4.29}$$

with

$$p_{w,\sigma} = \sqrt{\frac{g}{m_{ratio} \, R \, (1+\sigma)}} \tag{4.30}$$

The analysis presented in Chapter 3 demonstrated that the effect of the inerter on impact is very small when slender structures are considered (see Figure 3.7). Accordingly, in the following sections the coefficient of restitution, r_σ, is assumed to be a constant and independent parameter of the structural system equal to $r_\sigma = 0.85$.

4.4.1 Structural demands under single pulse excitations

In order to thoroughly assess the effectiveness of the proposed system, the response of a wide range of post-tensioned rocking walls subjected to symmetric Ricker pulses was examined. Walls of positive post-uplift stiffness ($EA/W = 3/2 \tan^2 \alpha$) and initial post-tensioning force equal to $P_0/W = 5$ are selected as representative of typical design configurations. Additionally, two apparent mass ratios, $\sigma = 0.5$ and $\sigma = 1$, are considered for the structures equipped with inerters. It is important to note that, although the apparent mass ratios are relatively high, the actual gravitational masses can be kept several orders of magnitude lower by using amplifying mechanisms such as ball-screws [7] or geared wheels [6]. The results presented below correspond to acceleration pulses with amplitude $a_g = 9\,g \, \tan\alpha / m_{ratio}$, representing to 1.5 times the amplitude required to trigger the rocking motion (Equation 4.21).

Figure 4.12 presents the results of the analyses in terms of rotation and acceleration spectra. As noted above, the introduction of post-tensioning reduces the maximum rotation of the walls, although in this case it has a negligible effect on the acceleration demands. The inerter on the other hand, further reduces the peak rotations while at the same time it significantly diminishes the angular accelerations. Moreover, while the reduction in rotations becomes less

significant for higher frequency ratios, the decrease in accelerations is almost constant along all frequency ratios, reaching reductions of around 50% for $\sigma = 1$.

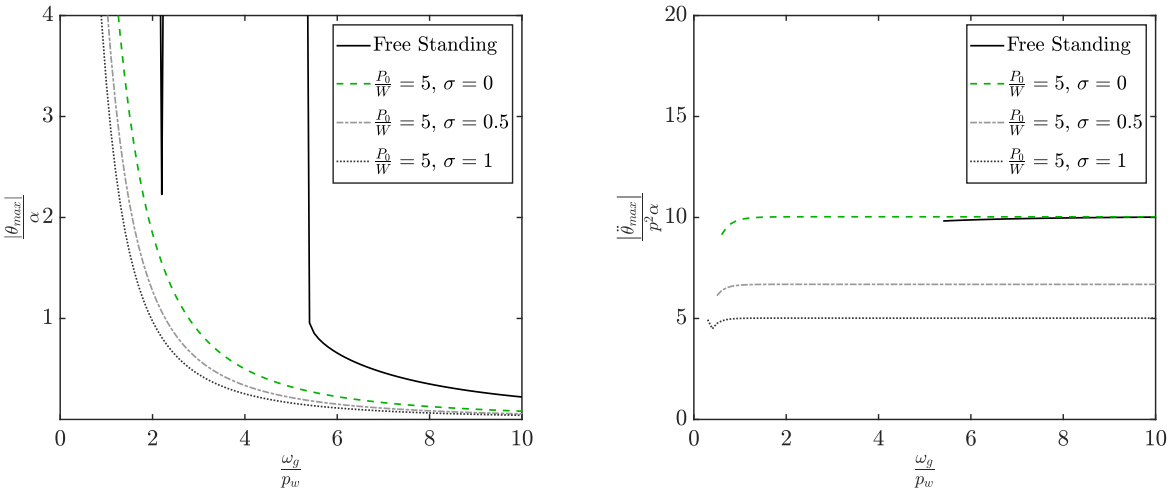

(a) Rotation spectra, $\frac{EA}{W} = \frac{3}{2}\frac{1}{\tan^2\alpha}$.

(b) Acceleration spectra, $\frac{EA}{W} = \frac{3}{2}\frac{1}{\tan^2\alpha}$.

Figure 4.12: Peak rotation and acceleration demands of post-tensioned rocking walls with and without inerters subjected to symmetric Ricker pulses of acceleration amplitude $a_g = 9\,g\,\tan\alpha/m_{ratio}$.

Another parameter of great interest for the seismic design of post-tensioned buildings is the base shear, V_b. Considering that the slender wall element behaves approximately as a rigid block, this can be obtained as:

$$V_b(\theta) = \frac{M_r(\theta)}{R} \tag{4.31}$$

where M_r is the restoring moment exerted by the weight, W, and the post-tensioned tendon. Figure 4.13a shows the base shear corresponding to the same structures analysed above. As expected, for the case of negative stiffness (free-standing wall), the maximum shear force is constant and determined by the uplifting condition. The introduction of the initial post-tensioning force significantly increases this lower limit (Equation 4.21), amplifying also the base shear of the post-tensioned structures. Since the positive stiffness of the rocking walls is relatively low, the reduction in rotations brought about by the inerter does not translate in a significant reduction of the restoring moment, and therefore the base shear is mainly controlled by the uplift resistance.

Figure 4.13b shows the resisting force developed in the inerter for the protected structures under consideration. Forces of around 58% and 85% of the weight supported by the wall, W, were registered for $\sigma = 0.5$ and $\sigma = 1$ respectively. Although this values can seem high, they are lower than the vertical post-tensioning load considered in the analyses, and therefore should be accommodated by adequate detailing.

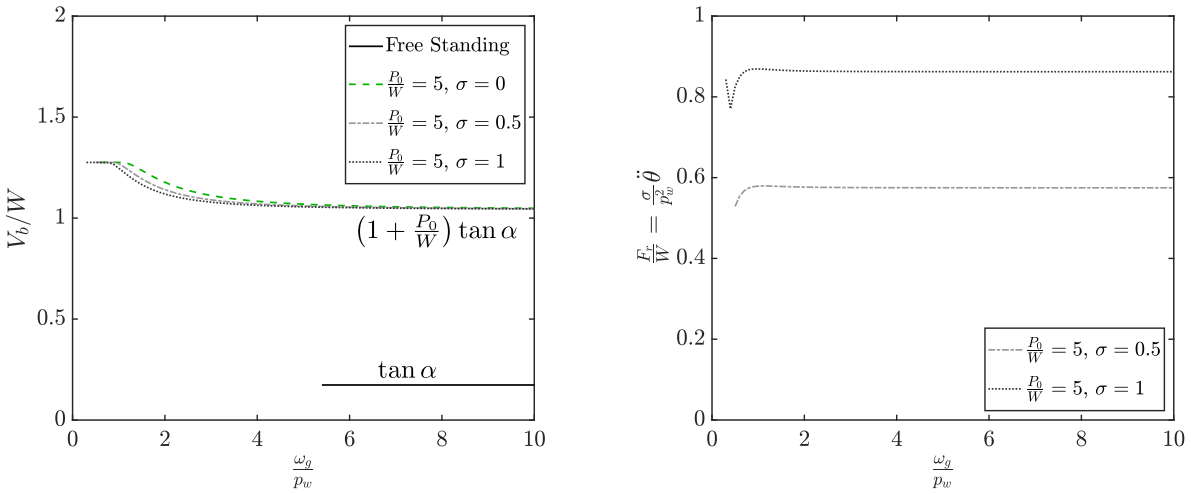

(a) Normalized base shear.

(b) Normalized force in the inerter.

Figure 4.13: Base shear and inerter force in post-tensioned rocking walls with and without inerters subjected to symmetric Ricker pulses of acceleration amplitude $a_g = 10 \tan \alpha / m_{ratio}$.

4.4.2 Seismic demands under real pulse-like ground motions

In the previous section, the dynamic behaviour of post-tensioned rocking walls equipped with inerter devices was studied using single Ricker pulse excitations. In real seismic events, structures are subjected to an acceleration history that can be represented as a series of individual pulses with different frequencies. The early work of Housner [3] already identified that the action of these successive pulses can increase the structural demands and overturn free-standing blocks for smaller acceleration amplitudes than a single pulse excitation. In this section, the effectiveness of the inerter for the control of the seismic response of rocking structures is assessed considering the same set of 202 pulse-like ground motion records used in Chapter 3 (Table 3.1). The ground motion database includes records from 21 earthquakes with magnitudes M_w ranging from 5.4 to 7.9.

A 3-storey rigid-wall system ($R = 9[m]$ and $\alpha = 10°$) with positive post-uplift stiffness ($EA/W = 3/2 \tan^2 \alpha$), $m_{ratio} = 5$ and $P_0/W = 5$ was selected as a realistic case study, while an inerter of apparent mass ratio $\sigma = 1$ was considered. Figure 4.14 compares the rotation and acceleration response histories of the buildings subjected to the 90° component of the 1986 San Salvador earthquake. Three cases are assessed in this figure: i) a free-rocking building, ii) a building with a post-tensioned wall and iii) the same post-tensioned building equipped with an inerter of apparent mass $\sigma = 1$. The rotation is presented in radians whereas accelerations are presented as the linear acceleration at Point C (Figure 4.11), obtained as the product of the angular acceleration, $\ddot{\theta}$, and the size parameter of the wall, R - in g.

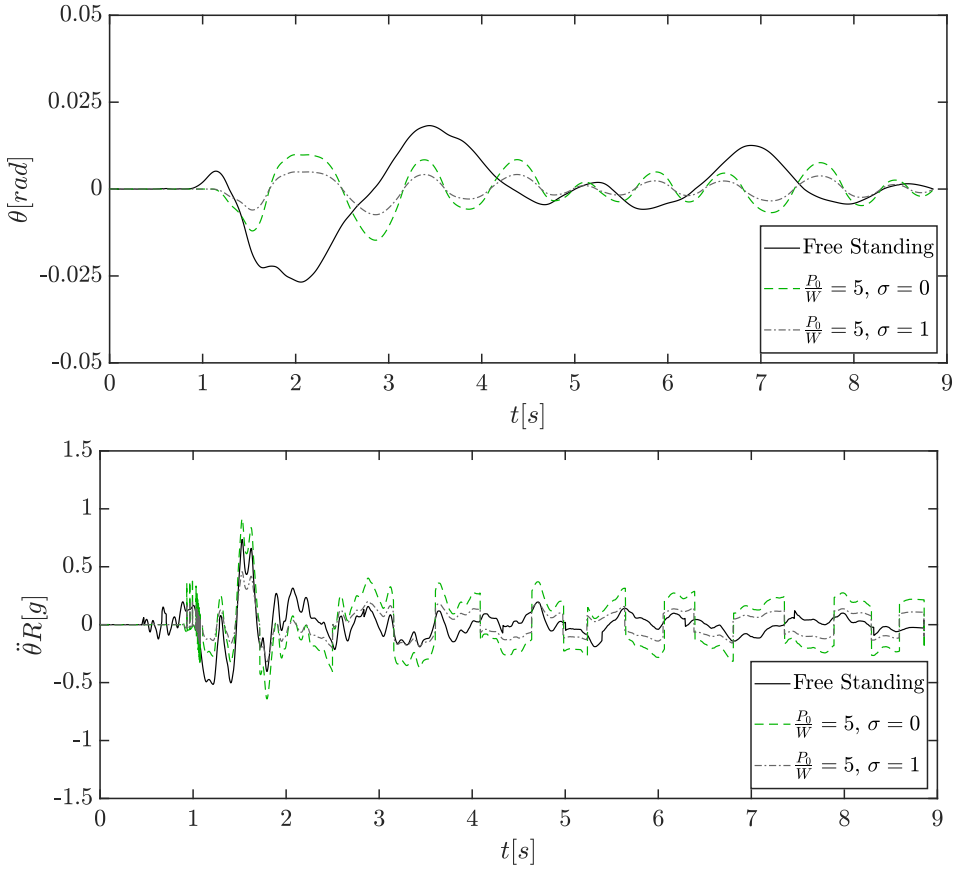

Figure 4.14: Rotation and acceleration response of post-tensioned rocking walls with and without inerters subjected to real pulse-like ground motion.

The results plotted in Figure 4.14 are consistent with the observations made in previous sections for single pulse excitations. The addition of the post-tensioned tendons reduced the maximum rotation of the wall but increased the peak acceleration. Nevertheless, the introduction of the inerter efficiently offsets this effect, further diminishing the rotation response and significantly reducing accelerations to levels even lower than those of the benchmark free-standing structure.

A cloud analysis considering the earthquake database described in Table 3.1 was conducted in order to compare the seismic performance of the post-tensioned structures with and without inerters. The uniform duration, t_{uni}, which corresponds to the sum of the time intervals during which the ground acceleration exceeds the limit to cause uplifting (Equation 4.21), was selected as the intensity measure, as recommended by Dimitrakopoulos et al. [42]. As done in the assessment performed in Chapter 3, a power law is assumed to relate the median estimated demand $\overline{D}_m$ and the intensity measure IM [42, 132]

$$\overline{D}_m = a\, IM^b \tag{4.32}$$

When plotted on a $ln(\overline{D}_m) - ln(IM)$ plane, Equation 4.32 becomes a straight line

$$\ln(\overline{D}_m) = \ln a + b \ln(IM) \tag{4.33}$$

where a and b are regression coefficients. Figure 4.15 presents the results of the cloud analysis and the corresponding fitted seismic demand models for the protected and unprotected structures. The results of the regression analyses show a strong correlation between the selected intensity measure, t_{uni}, and the seismic demands, validating the estimation model proposed in Equation 4.32.

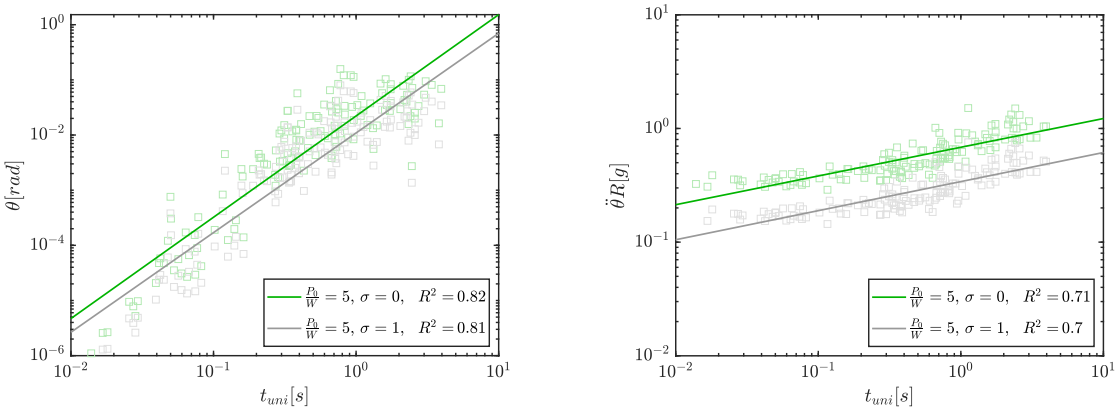

(a) Peak rotations.

(b) Peak accelerations.

Figure 4.15: Peak rotation and acceleration demands of post-tensioned rocking walls with and without inerters subjected to the earthquake database shown in Table 3.1.

In general, the structure equipped with inerter devices shows significantly smaller seismic demands for the whole range of IMs considered. Mean reductions of around 50% are observed in both peak rotations and peak accelerations (note the logarithmic scale). These conclusions are consistent with observations made in Figure 4.14 and the results obtained in Section 4.4.1 for single pulse excitations.

As discussed previously, post-tensioned systems have proved to be highly effective in controlling structural damage. Nevertheless, economic losses during seismic events are usually controlled by damage to non-structural components, which is often triggered at response intensities that are smaller than those required to produce structural damage [133]. Performance-based assessment of non-structural building components requires the identification of drift and acceleration sensitive elements and the definition of their corresponding limits [93]. Design codes typically specify these limits as a function of the non-structural component typology. With the aim of comparing the overall performance of post-tensioned walled structures with and without ineters, the limit defined in Eurocode 8 [134] for buildings having ductile non-structural components, $\theta \leq 0.75\%$, is adopted in this study. Figure 4.16a shows the fragility functions associated to this limit state obtained for the protected and unprotected structures considered

in the previous analyses. The cloud-to-IDA procedure proposed by Miano et al. [135] was used to minimize the number of analyses and amount of scaling.

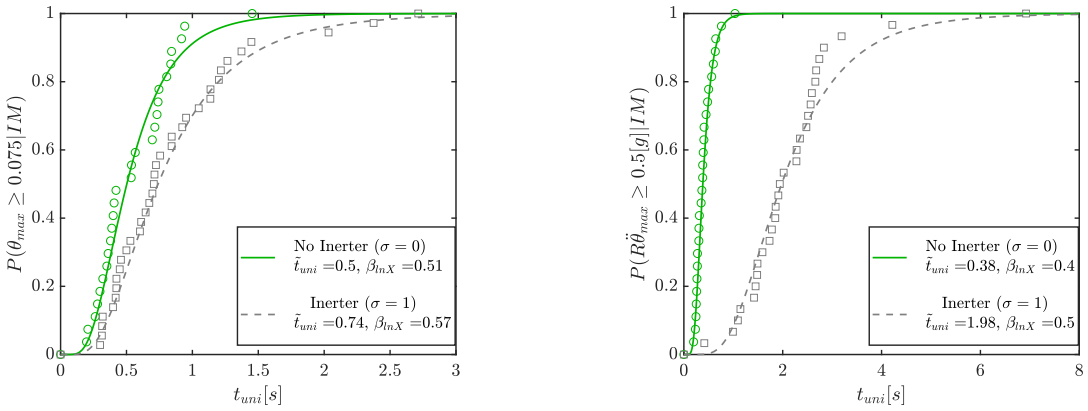

(a) Rotation limit: $\theta_{max} = 0.75\%$.

(b) Acceleration limit: $R\ddot{\theta}_{max} = 0.5[g]$.

Figure 4.16: Fragility functions for post-tensioned rocking walls with and without inerters.

On the other hand, the design of acceleration-sensitive non-structural components traditionally entails the computation of floor response spectra [136]. Nonetheless, the peak floor acceleration can be used as a first proxy in order to assess the performance of the proposed seismic control strategy. Figure 4.16b presents the fragility functions associated to an acceleration limit of $R\ddot{\theta} = 0.5[g]$.

The fragility functions depicted in Figure 4.16 demonstrate the significant improvement in the performance of post-tensioned rocking structures brought about by the inerter. In terms of rotations, the estimated median IM associated with the selected drift limit state is $\tilde{t}_{uni} = 0.5[s]$ for the unprotected structure, whereas this parameter increases to $\tilde{t}_{uni} = 0.74[s]$ when the inerter is introduced. Moreover, the response enhancement becomes more important for higher probabilities of exceedance. Similar trends are observed in the case of peak floor accelerations, with an even greater increase (nearly four-fold) in the median IM. On the other hand, smaller variations were obtained on the logarithmic standard deviation, β_{lnX}. The results presented in Figure 4.16 are in line with the demand reductions observed in the previous sections and allow to conclude that the use of of supplemental rotational inertia devices configures a practical alternative to improve the dynamic response and boost the overall seismic performance of rocking building structures.

4.5 Concluding remarks

This chapter has examined the basic dynamic behaviour of post-tensioned rocking structures and assessed the feasibility of using supplemental rotational inertia to reduce their structural demands and improve their overall seismic performance. Firstly, a modified rigid block representative of rocking building structures was defined. Importantly, this model considers

the possibility of having different seismic and gravitational masses through the introduction of an m_{ratio} parameter. Based on a formal dimensional-orientational assessment of the system, this mass ratio was incorporated into the existing Π-parameters without introducing a new dimensionless group.

In a second stage, a vertical post-tensioned tendon was introduced to the model. After deriving the equations of motion, the free-vibration response of the system was examined. Additionally, the structural demands under Ricker pulse excitations were studied in terms of maximum rotations and peak angular accelerations. The results of these analyses showed that the elastic force can help to improve the stability of smaller rigid blocks, but has little effect on larger structures. This behaviour is related to the increase in the post-uplift stiffness which allows the block to survive rotations greater than its slenderness, α, and still return to the vertical position. On the other hand, the initial post-tensioning force had a more significant effect on the maximum rotations of both, smaller and larger structures. Moreover, the improvement in the response becomes more important the higher the level of initial force. Nevertheless, these rotation reductions are accompanied by a significant increase on the peak angular accelerations at low frequency ratios for un-stressed rocking walls and over the full spectral range in the case of structures with non-zero levels of initial post-tensioning.

The introduction of the mass ratio parameter, m_{ratio}, implies that regardless of the acceleration amplitude of a ground motion, the intensity dimensionless parameter, $a_g m_{ratio}/g \tan\alpha$, can assume significantly high values. Consequently, the consideration of high effective acceleration amplitudes, which are usually not relevant for classic free-standing blocks, becomes important when studying post-tensioned rocking walls. The results obtained suggest that the use of post-tensioned tendons becomes less advantageous when pulses of higher acceleration amplitude are considered, as the initial post-tensioning force can significantly amplify rotation and acceleration demands for initial force ratios that are common in practical applications ($P_0/W \leq 6$).

Finally, the alternative of using supplemental rotational inertia for the seismic control of post-tensioned rocking buildings was assessed. The equation of motion of the system showed that the inclusion of the inerter effectively reduces the frequency parameter of the wall resulting in lower seismic demands due to the well-known size effect of rocking behaviour. This result was then reasserted by the rocking spectra obtained for structures with typical post-uplift stiffness and initial post-tensioning force values subjected to Ricker acceleration pulses. The analyses showed that the introduction of the inerter further lowers the rotation response, while at the same time it significantly reduces the building accelerations levels. Nevertheless, this response enhancement does not translate into a significant reduction of the lateral forces, as the positive stiffness of the rocking walls is relatively low and the

base shear is mainly controlled by the uplift resistance. Lastly, a probabilistic assessment of the seismic performance of protected and unprotected structures was conducted using a set of 202 real pulse-like acceleration records. The results of this assessment confirmed the behavioural trends observed under single pulse excitations, allowing to conclude that the use of supplemental rotational inertia devices configures a practical alternative for modifying the dynamic response and reducing seismic demands in post-tensioned rocking building structures.

The first two chapters of this thesis have examined the response of rocking structures equipped with inerters considering simplified models based on rigid blocks. It is recognized, however, that in many cases the flexibility of the structural systems cannot be ignored and must be considered in the assessment of the proposed seismic control strategy. This problem is addressed in the following chapter, where the analysis of rocking structures equipped with inerters is extended to single-mass flexible oscillators.

Chapter 5

Effect of the oscillator flexibility on the efficiency of the inerter

5.1 Introduction

In the previous chapters, the alternative of using inerters to improve the seismic response of free-standing and post-tensioned rocking structures was assessed considering simplified models of rigid blocks. However, in some practical applications, the degree of flexibility of the rocking body cannot be neglected. Moreover, some of the underlying assumptions of the analytical models used to study rigid bodies imply that the structures are slender, and therefore more likely to deform during the rocking motion. These instances highlight the need for a rigorous assessment of the dynamics of flexible uplifting structures equipped with inerters and a detailed quantification of the effects of flexibility on the efficiency of the system.

In this chapter, an original analytical model is proposed based on the expressions developed by Oliveto et al. [43] by considering the effects of grounded supplemental rotational inertia devices. Additionally, two previously proposed impact formulations are implemented and compared. The newly formulated model is then used to examine the structural demands and overturning response of the system under coherent pulses. The response of flexible rocking structures under high frequency excitations is also considered, while the possibility of using inerters to control their elastic deformation at uplifted resonance is examined. Finally, the conclusions obtained under coherent cycloidal pulses are extended to real ground motions by evaluating the response of rocking structures to a set of recorded acceleration series.

5.2 Analytical Formulation

The concept of using a two-terminal supplemental inertia device to enhance the rocking performance of uplifting elastic structures is illustrated in Figure 5.1. Figure 5.1a shows a hori-

zontal inerter supported by a stiff chevron frame [95] and connected to the centre of mass of a rocking structure, while two alternative vertical-inerter configurations are depicted in Figures 5.1b and 5.1c.

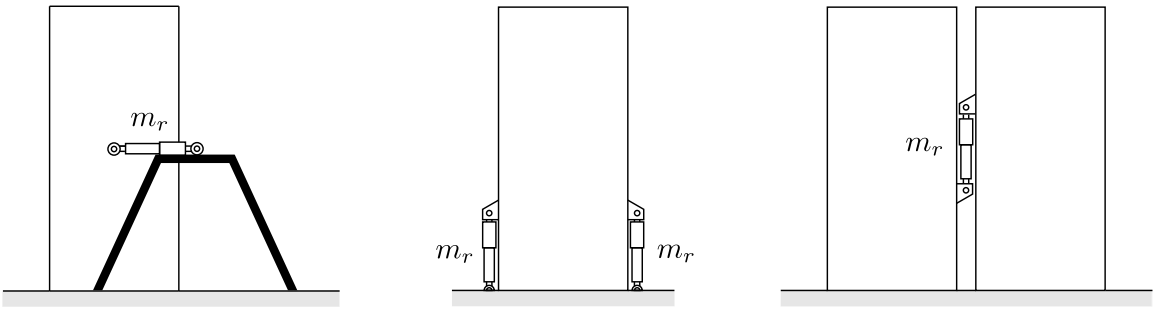

(a) Horizontal inerter. (b) Pair of vertical inerters. (c) Coupling inerter.

Figure 5.1: Examples of inerter configurations for the seismic protection of flexible rocking structures.

The fundamental dynamic behaviour of these structures can be studied with reference to the system shown in Figure 5.2. This model consists of a lumped mass, m, supported by a deformable column of flexural stiffness, k, and damping coefficient, c, attached to a rigid base allowed to uplift freely about points O and O'. A horizontal grounded inerter of apparent mass, m_r, is connected to the structure at point C. The geometry of the structure is characterized by its slenderness, α, and its diagonal, R_0. It is assumed, for convenience of the formulation, that the underlying soil is infinitely rigid and the coefficient of friction is large enough to prevent sliding.

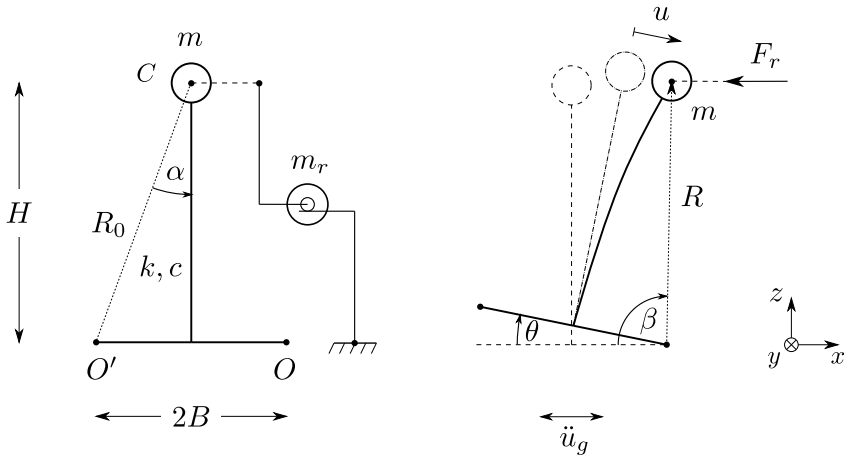

Figure 5.2: Idealized analytical model of a flexible rocking structure connected to an inerter.

At any given time, the position of the mass, m, is defined by the distance to the pivot point, R, and the Lagrangian rotation, β. It should be noted that although these generalized coordinates simplify the derivation of the equations of motion, they do not provide direct information for the engineering assessment of the structure's performance. Alternatively, the response of the system can be described by the relative lateral deformation of the column, u, and the rigid

body rotation of the base, θ. This latter set of parameters provides information that can be easily visualized and interpreted by engineers, and therefore is used for the presentation of the results. By considering small deformations in the oscillator and large rotations at the base, the two set of parameters can be related according to:

$$\begin{aligned} \theta &= \beta \mp \sin^{-1}(H/R) \\ u &= \pm B \mp \sqrt{R^2 - H^2} \end{aligned} \tag{5.1}$$

On the other hand, the relative horizontal displacement of C is given by:

$$x = \pm B \mp R\cos\beta \tag{5.2}$$

5.2.1 Equations of motion

The dynamic response of the structure shown in Figure 5.2 can be divided into two phases: i) a full contact phase, where there is no base rotation; and ii) a rocking phase, where the base uplifts and the system rocks and oscillates simultaneously. An elastic structure whose motion starts from rest will respond initially in the full contact phase until uplift ensues. After base uplifting, the structure will transition into a rocking motion and experience both rotational and translational deformations.

Full contact phase

The initial dynamic response of an inerter-equipped flexible rocking structure starting from rest can be described by the equation of motion of an inerter-equipped fixed base single-degree-of-freedom system [95]:

$$\ddot{u} + \frac{2\,\xi\,\omega_n}{(1+\sigma)}\,\dot{u} + \frac{\omega_n^2}{(1+\sigma)}\,u = -\frac{\ddot{u}_g}{(1+\sigma)} \tag{5.3}$$

where ω_n and ξ are the natural frequency and damping ratio of the fixed base oscillator, and $\sigma = m_r/m$ is the apparent mass ratio of the inerter. When the overturning moment exceeds the resisting moment due to gravitational forces, the base uplifts and the structure starts rocking. This condition is represented by:

$$\mp mH\big(\ddot{u}\,(1+\sigma) + \ddot{u}_g\big) > mg\big(B \mp u\big) \tag{5.4}$$

where the -u condition corresponds to uplift about the right corner and the +u to uplift about the left corner. Considering equations 5.3 and 5.4 , the critical displacement at which uplift occurs can be obtained as [43]:

$$u_{cr} = \pm\,\frac{gB \mp 2H\xi\omega_n\dot{u}}{\omega_n^2 H + g} \tag{5.5}$$

For the rocking motion to begin, the system must reach the critical displacement with non-zero velocity in the direction of uplift. In undamped systems, where $u << B$, Equation 5.5 can be further simplified to [56]:

$$u_{cr,0} = \pm \frac{gB}{\omega_n^2 H} \tag{5.6}$$

It is important to note that although the inerter does not directly affect the magnitude of the critical displacement, it does alter the intensity of the ground motion required to reach it. Makris and Kampas [95] studied the dynamic response of single-degree-of-freedom systems with supplemental rotational inertia and showed that the inerter not only suppresses the level of ground shaking, but also lengthens the period of the structure. In most cases, this results in a reduced deformation response, but there may be instances where the shift in the period takes the structure to a region of higher spectral ordinates and offsets the suppressive effect of the inerter. In such scenario, uplift and the onset of the rocking motion would happen earlier for inerter-protected structures such as those examined herein.

Rocking phase

The equations of motion are derived using Lagrange's equations for the generalized coordinates R and β. Accordingly, the kinetic energy of the flexible rocking structure is given by:

$$T_f = \frac{1}{2} m \left(\dot{R}^2 + R^2 \dot{\beta}^2\right) \tag{5.7}$$

The effects of the inerter are analogous to those of an additional mass that opposes the motion but does not react to the ground acceleration. Consequently, the kinetic energy of the inerter can be expressed as:

$$T_r = \frac{1}{2} m_r \dot{x}^2 = \frac{1}{2} m_r \left(\mp \dot{R} \cos\beta \pm R\dot{\beta} \sin\beta\right)^2 \tag{5.8}$$

or expanding it:

$$T_r = \frac{1}{2} m_r \left(\dot{R}^2 \cos^2\beta - 2R\dot{R}\dot{\beta} \cos\beta \sin\beta + R^2\dot{\beta}^2 \sin^2\beta\right) \tag{5.9}$$

Then, the total kinetic energy of the system is:

$$T = \frac{1}{2} m \left(\dot{R}^2 + R^2 \dot{\beta}^2\right) + \frac{1}{2} m_r \left(\dot{R}^2 \cos^2\beta - 2R\dot{R}\dot{\beta} \cos\beta \sin\beta + R^2\dot{\beta}^2 \sin^2\beta\right) \tag{5.10}$$

On the other hand, the potential energy is given by:

$$V = \pm mgR\sin\beta + \frac{1}{2} k\, u^2 = \pm mgR\sin\beta + \frac{1}{2} k \left(\pm B \mp \sqrt{R^2 - H^2}\right)^2 \tag{5.11}$$

The Lagrange function is defined as:

$$L = T - V \tag{5.12}$$

Replacing Equation 5.10 and Equation 5.11 into Equation 5.12 gives:

$$L = \frac{1}{2} m \left(\dot{R}^2 + R^2\dot{\beta}^2\right) + \frac{1}{2} m_r \left(\dot{R}^2 \cos^2\beta - 2R\dot{R}\dot{\beta}\cos\beta\sin\beta + R^2\dot{\beta}^2\sin^2\beta\right) \mp mgR\sin\beta - \frac{1}{2} k \left(\pm B \mp \sqrt{R^2 - H^2}\right)^2 \tag{5.13}$$

Since a viscous damping model is considered for the elastic oscillator, the associated dissipative force can be included as a Rayleigh's dissipation function:

$$D = \frac{1}{2} c\,\dot{u}^2 = \frac{c\,R^2\dot{R}^2}{2(R^2 - H^2)} \tag{5.14}$$

Finally, the non-conservative generalized forces are given by:

$$Q_k = \frac{\partial W}{\partial q_k} = -m\ddot{u}_g \frac{\partial x}{\partial q_k} \tag{5.15}$$

where q_k represents the $k\text{-}th$ generalized coordinate. During the rocking motion, the system must satisfy Lagrange's equation:

$$\frac{d}{dt}\left(\frac{\partial L}{\partial \dot{q}_k}\right) - \frac{\partial L}{\partial q_k} + \frac{\partial D}{\partial \dot{q}_k} = Q_k \tag{5.16}$$

Starting with the generalized coordinate R:

$$\frac{\partial L}{\partial R} = mR\dot{\beta}^2 + m_r\left(R\dot{\beta}^2\sin^2\beta - \dot{R}\dot{\beta}\cos\beta\sin\beta\right) \mp mg\sin\beta - kR\left(1 - \frac{B}{\sqrt{R^2 - H^2}}\right) \tag{5.17}$$

$$\frac{\partial L}{\partial \dot{R}} = m\dot{R} + m_r(\dot{R}\cos^2\beta - R\dot{\beta}\cos\beta\sin\beta) \tag{5.18}$$

$$\frac{d}{dt}\left(\frac{\partial L}{\partial \dot{R}}\right) = m\ddot{R} + m_r\left(\ddot{R}\cos^2\beta - 2\dot{R}\dot{\beta}\cos\beta\sin\beta - \dot{R}\dot{\beta}\cos\beta\sin\beta - R\ddot{\beta}\cos\beta\sin\beta + R\dot{\beta}^2\sin^2\beta - R\dot{\beta}^2\cos^2\beta\right) \tag{5.19}$$

$$\frac{\partial D}{\partial \dot{R}} = \frac{cR^2\dot{R}}{R^2 - H^2} \tag{5.20}$$

and

$$Q_R = \pm m\,\ddot{u}_g\cos\beta \tag{5.21}$$

Replacing Equations 5.17 to 5.21 into Equation 5.16 yields:

$$m\ddot{R} + m_r\big((\ddot{R} - R\dot{\beta}^2)\cos^2\beta - (2\dot{R}\dot{\beta} + R\ddot{\beta})\cos\beta\sin\beta\big) = kR\left(\frac{B}{\sqrt{R^2 - H^2}} - 1\right) - \frac{cR^2\dot{R}}{R^2 - H^2} + mR\dot{\beta}^2 \pm m\ddot{u}_g\cos\beta \mp mg\sin\beta \quad (5.22)$$

Introducing the apparent mass ratio, $\sigma = m_r/m$, and rearranging:

$$\ddot{R} + \sigma\big((\ddot{R} - R\dot{\beta}^2)\cos^2\beta - (2\dot{R}\dot{\beta} + R\ddot{\beta})\cos\beta\sin\beta\big) = \omega_n^2 R\left(\frac{B}{\sqrt{R^2 - H^2}} - 1\right) - \frac{2\,\xi\,\omega_n\,R^2\dot{R}}{R^2 - H^2} + R\dot{\beta}^2 \pm \ddot{u}_g\cos\beta \mp g\sin\beta \quad (5.23)$$

Repeating the same procedure for β:

$$\frac{\partial L}{\partial \beta} = m_r\big(-\dot{R}^2\cos\beta\sin\beta - R\dot{R}\dot{\beta}(\cos^2\beta - \sin^2\beta) + R^2\dot{\beta}^2\cos\beta\sin\beta\big) \mp mgR\cos\beta \quad (5.24)$$

$$\frac{\partial L}{\partial \dot{\beta}} = mR^2\dot{\beta} + m_r\big(-R\dot{R}\cos\beta\sin\beta + R^2\dot{\beta}\sin^2\beta\big) \quad (5.25)$$

$$\frac{d}{dt}\left(\frac{\partial L}{\partial \dot{\beta}}\right) = m\big(R^2\ddot{\beta} + 2R\dot{R}\dot{\beta}\big) + m_r\big(-\dot{R}^2\cos\beta\sin\beta - R\ddot{R}\cos\beta\sin\beta - R\dot{R}\dot{\beta}\cos^2\beta + R\dot{R}\dot{\beta}\sin^2\beta + 2R\dot{R}\dot{\beta}\sin^2\beta + R^2\ddot{\beta}\sin^2\beta + 2R^2\dot{\beta}^2\cos\beta\sin\beta\big) \quad (5.26)$$

$$\frac{\partial D}{\partial \dot{\beta}} = 0 \quad (5.27)$$

and

$$Q_\beta = \mp m\,\ddot{u}_g R\sin\beta \quad (5.28)$$

Replacing Equations 5.24 to 5.28 into Equation 5.16 yields:

$$m\big(R^2\ddot{\beta} + 2R\dot{R}\dot{\beta}\big) - m_r\big(R\ddot{R}\cos\beta\sin\beta - 2R\dot{R}\dot{\beta}\sin^2\beta - R^2\ddot{\beta}\sin^2\beta - R^2\dot{\beta}^2\cos\beta\sin\beta\big) = \mp mgR\cos\beta \mp m\ddot{u}_g R\sin\beta \quad (5.29)$$

Introducing the apparent mass ratio, $\sigma = m_r/m$, and rearranging:

$$\ddot{\beta} - \frac{\sigma}{R}\big((\ddot{R} - R\dot{\beta}^2)\cos\beta\sin\beta - (2\dot{R}\dot{\beta} + R\ddot{\beta})\sin^2\beta\big) = -\frac{2\dot{R}\dot{\beta}}{R} \mp \frac{g}{R}\cos\beta \mp \frac{\ddot{u}_g}{R}\sin\beta \quad (5.30)$$

Therefore, the equations that describe the motion of the uplifted flexible rocking structure shown in Figure 5.2 are:

$$\ddot{R} + \sigma\big((\ddot{R} - R\dot{\beta}^2)\cos^2\beta - (2\dot{R}\dot{\beta} + R\ddot{\beta})\cos\beta\sin\beta\big) = \omega_n^2 R\left(\frac{B}{\sqrt{R^2 - H^2}} - 1\right) - \frac{2\,\xi\,\omega_n\,R^2\dot{R}}{R^2 - H^2} + R\dot{\beta}^2 \pm \ddot{u}_g\cos\beta \mp g\sin\beta \quad (5.31)$$

$$\ddot{\beta} - \frac{\sigma}{R}\big((\ddot{R} - R\dot{\beta}^2)\cos\beta\sin\beta - (2\dot{R}\dot{\beta} + R\ddot{\beta})\sin^2\beta\big) = -\frac{2\dot{R}\dot{\beta}}{R} \mp \frac{g}{R}\cos\beta \mp \frac{\ddot{u}_g}{R}\sin\beta \quad (5.32)$$

5.2.2 Natural frequency and damping ratio of the uplifted system

Once the base uplifts, the structure becomes a mechanism and its dynamic parameters change. Assuming that the amplitude of the displacement and rotation responses were small, Chopra and Yim [30] developed analytical expressions for the uplifted fundamental frequency and damping ratio of a rocking oscillator. Replicating this reasoning for the system presented in Figure 5.2, the corresponding uplifted dynamic parameters can be obtained. Accordingly, the lateral equilibrium condition under free oscillations gives:

$$\left(m + m_r\right)\left(\ddot{u} + H\ddot{\theta}\right) + c\dot{u} + ku = 0 \quad (5.33)$$

Rearranging:

$$\left(1 + \sigma\right)\left(\ddot{u} + H\ddot{\theta}\right) + 2\xi\omega_n\dot{u} + \omega_n^2 u = 0 \quad (5.34)$$

Likewise, rotational equilibrium yields:

$$\left(m + m_r\right)H\ddot{u} + mR_0^2\ddot{\theta} + m_r H^2\ddot{\theta} = \mp mgB \quad (5.35)$$

and rearranging:

$$\left(1 + \sigma\right)\ddot{u} + \left(H\ddot{\theta}\right)\left(\frac{R_0^2}{H^2} + \sigma\right) = \mp g\frac{B}{H} \quad (5.36)$$

Eliminating $(H\ddot{\theta})$ from Equation 5.36:

$$\left(1 + \sigma\right)\ddot{u} - \left(\frac{R_0^2}{H^2} + \sigma\right)\left(\ddot{u} + \frac{2\xi\omega_n}{1+\sigma}\,\dot{u} + \frac{\omega_n^2}{1+\sigma}\,u\right) = \mp g\frac{B}{H} \quad (5.37)$$

and rearranging:

$$\left(1 - \frac{R_0^2}{H^2}\right)\ddot{u} - \left(\frac{R_0^2}{H^2} + \sigma\right)\left(\frac{2\xi\omega_n}{1+\sigma}\,\dot{u} + \frac{\omega_n^2}{1+\sigma}\,u\right) = \mp g\frac{B}{H} \quad (5.38)$$

Then, introducing $R_0^2 = B^2 + H^2$

$$-\frac{B^2}{H^2}\ddot{u} - \left(\frac{R_0^2}{H^2} + \sigma\right)\left(\frac{2\xi\omega_n}{1+\sigma}\,\dot{u} + \frac{\omega_n^2}{1+\sigma}\,u\right) = \mp g\frac{B}{H} \tag{5.39}$$

and multiplying by -H^2/B^2:

$$\ddot{u} + \left(\frac{R_0^2 + H^2\sigma}{B^2(1+\sigma)}\right)\left(2\xi\omega_n\,\dot{u} + \omega_n^2\,u\right) = \pm g\frac{H}{B} \tag{5.40}$$

Accordingly, the fundamental frequency and damping ratio of the uplifted system are given by:

$$\omega_{n,up} = \sqrt{\frac{R_0^2 + H^2\sigma}{B^2(1+\sigma)}}\;\omega_n \tag{5.41}$$

$$\xi_{up} = \sqrt{\frac{R_0^2 + H^2\sigma}{B^2(1+\sigma)}}\;\xi \tag{5.42}$$

Equations 5.41 and 5.42 show that the inerter does not significantly alter the uplifted frequency and damping ratio of slender oscillators. In a limit case, when $R \approx H$, the amplifying term accompanying the fixed base frequency and damping ratio tends to R/B, the same factor obtained by Chopra and Yim for free-standing rocking oscillators [30]. Accordingly, the increase in the uplifted frequency and damping ratio of inerter-equipped oscillators is also controlled by the slenderness of the structure.

5.2.3 Energy dissipation in the deformable structure

The previous section demonstrated that the addition of viscous damping to rocking models may lead to an overestimation of the energy dissipated in the uplifted state. In order to further examine this, a variable damping coefficient is introduced to the model. Therefore, a prescribed damping ratio, ξ_{fc}, is assigned to the oscillator during the full contact phase. Once the base uplifts, the analysis is halted and the damping ratio is adjusted to ξ_{up} before continuing, in such a way that the resultant uplifted damping agrees with experimental observations [32]. The effect of considering different levels of uplifted damping ratios, ξ_{up}, in single-mass rocking oscillators is assessed in Figure 5.3. Three cases are considered; first, a constant damping ratio of $\xi_{fc} = \xi_{up} = 0.02$ is adopted (black line). In the second case (red line), the uplifted damping ratio is modified as outlined above so that the resultant damping corresponds to 2% of the critical value of the damped oscillator. In the third case (blue line), no damping is considered during the rocking phase ($\xi_{up} = 0$).

The results presented in Figure 5.3 confirm that the use of a constant damping ratio (black line) results in higher dissipative forces which quickly attenuate the oscillations in the uplifted state. This, in turn, leads to a smoother rotation response, as it can be observed in the detailed view of Figure 5.3b. Nevertheless, the differences between the maximum rotation and

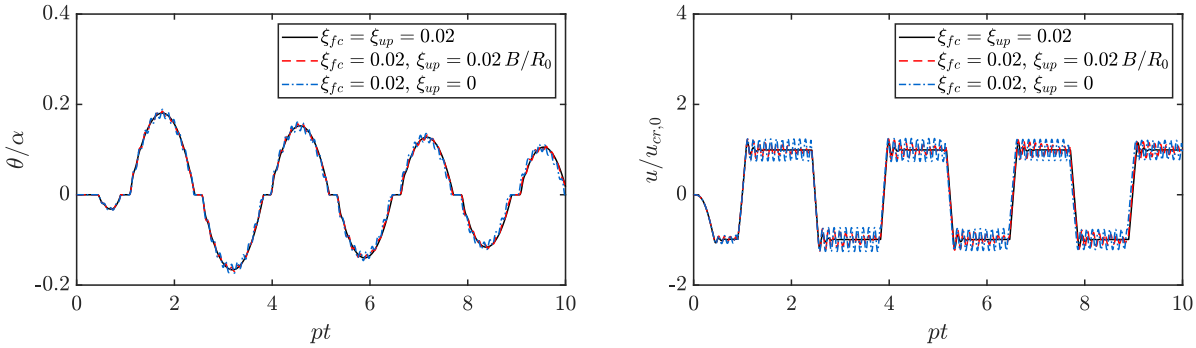

(a) Rotation and deformation responses for different levels of damping ratio.

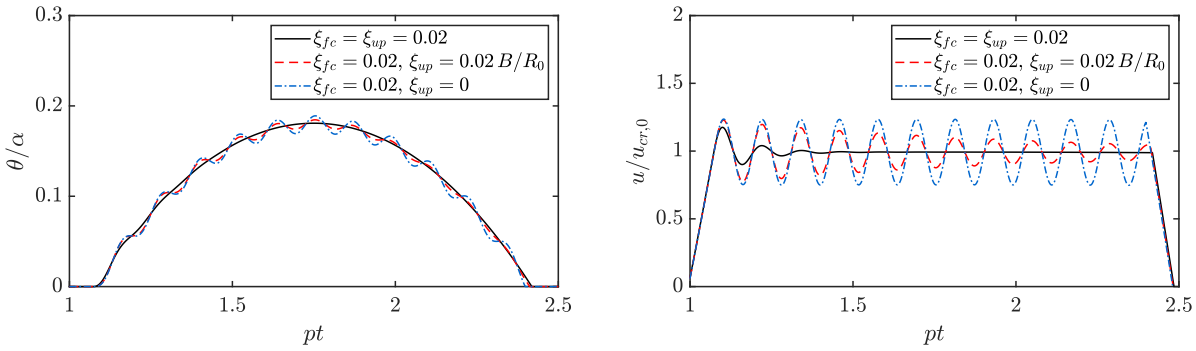

(b) Detailed view of the rotation and deformation responses during a rocking cycle.

Figure 5.3: Response of a single-mass rocking structure of $\omega_n/p = 5$, $\alpha = 0.1$, $\sigma = 0$ and different values of damping ratio, subjected to a single sine pulse of $\omega_g/p = 5$ and $a_g = g\tan\alpha$.

the elastic deformation responses of the three cases under consideration are not significant. Consequently, a conservative assumption of no damping during the rocking phase is adopted in this study, unless otherwise stated.

5.2.4 Modelling of a pair of parallel clutched inerters

When the structure-inerter system is subjected to a ground excitation, part of the energy is transferred to the inerter and accumulated in it as angular momentum. As the translating mass of the structure slows down, the energy accumulated in the rotating flywheels might drive the mass and induce undesirable deformations. To ensure that the inerter can only oppose the motion of the structure, the clutch mechanism previously introduced in Chapter 3 is also implemented in the current analytical model. The sequential engagement of the two parallel inerters is again modelled mathematically through a redefinition of the inertance, m_r, after each time step according to:

$$F_r(t) = \begin{cases} m_r\ \ddot{x} & \left[\frac{\ddot{x}}{\dot{x}}\right] > 0 \\ \\ 0, & \left[\frac{\ddot{x}}{\dot{x}}\right] < 0 \end{cases} \tag{5.43}$$

5.3 Transition upon impact

When the rocking base impacts the foundation, energy is dissipated mainly due to radiation damping on the underlying media [137]. Housner [3] used conservation of angular momentum to take into account this energy loss by assuming instantaneous impact with forces concentrated at the pivoting corner, thereby obtaining a coefficient of restitution that suggests that the energy lost after each impact is a function of the block's geometry alone, and independent of the angular velocities or the mechanical properties of the contact surfaces. Although Housner's approach rightly identifies the slenderness, α, as the main parameter affecting impact, several experimental studies have demonstrated the inaccuracy of his assumptions [28,29]. Consequently, many researchers have considered the coefficient of restitution as an independent parameter of the problem [122] or have set-out to develop different impact formulations [35, 138].

Acikgoz and DeJong [44] extended Housner's impact model to a flexible rocking structure with a lumped mass on its top. Their formulation assumes that, upon impact, the system either stays on the ground and starts a new full contact phase or immediately uplifts about the opposite corner and continues the rocking motion. Accordingly, the two phases discussed above were postulated and their initial conditions were obtained through conservation of angular momentum. The current response phase was to be determined by considering the principle of minimum energy. An alternative model was introduced by Vassiliou et al. [31] who extended Chopra and Yim's [30] Vertical Velocity Energy Loss assumption. In this formulation, impact was idealized as a perfectly inelastic collision which completely dissipates the vertical velocity of the structural mass. In the following sections both approaches, referred to as Adapted ADJ and VVEL respectively, are compared incorporating the effects of supplemental rotational inertia devices.

5.3.1 Adapted ADJ impact model

With reference to Figure 5.4, the pre-impact momentum of the translational mass can be decomposed into Lagrangian coordinates as:

$$\begin{aligned} J_{R_1} &= m\dot{R}_1 \\ J_{\beta_1} &= mR_1\dot{\beta}_1 \end{aligned} \tag{5.44}$$

On the other hand, the linear momentum associated to the apparent mass of the inerter is given by:

$$J_{m_r} = m_r \left(\mp \dot{R}_1 \cos\beta_1 \pm R_1\dot{\beta}_1 \sin\beta_1 \right) \tag{5.45}$$

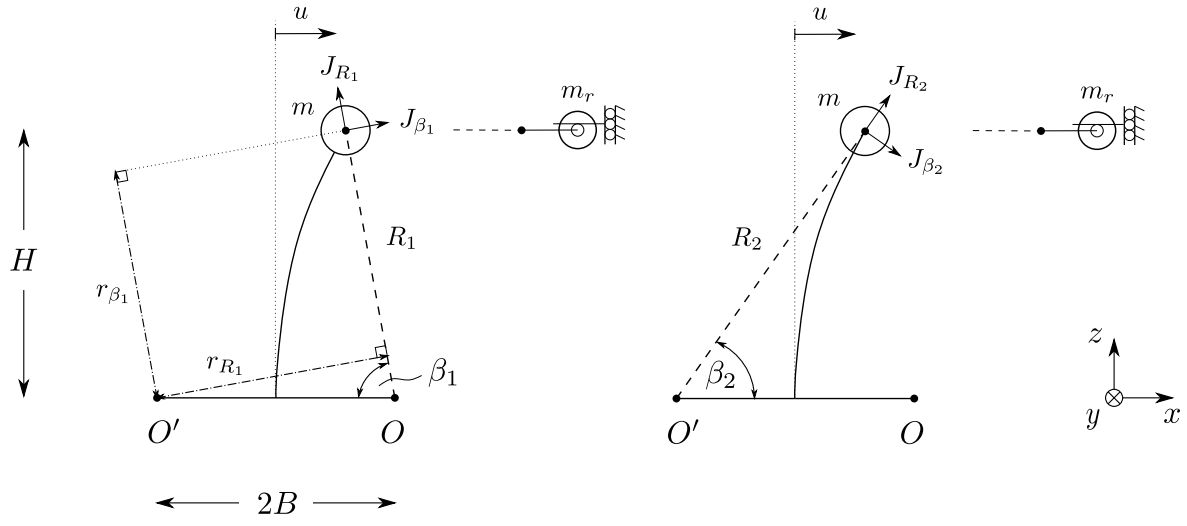

(a) Impact on left corner, O'.

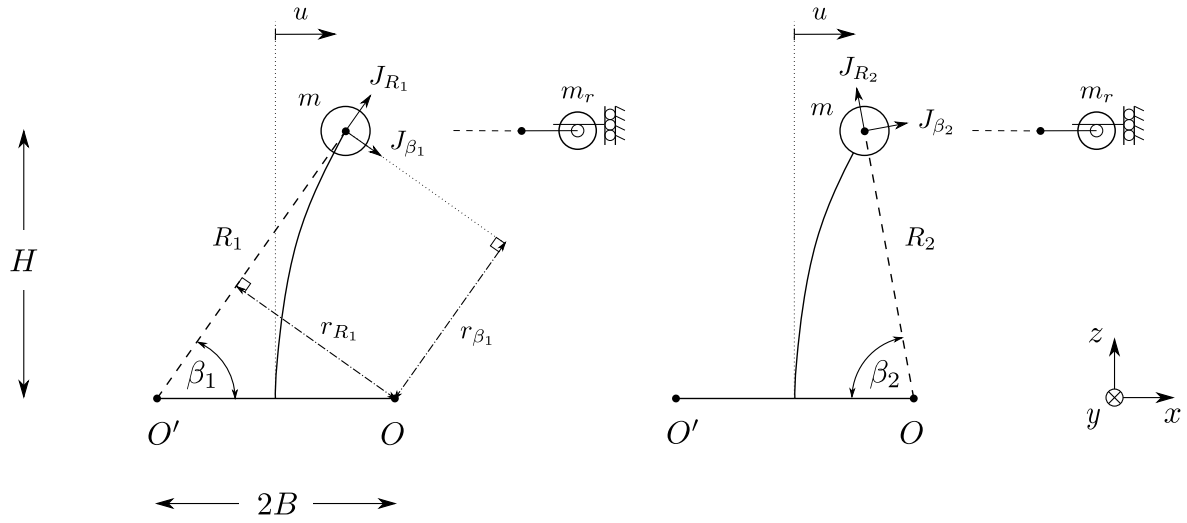

(b) Impact on right corner, O.

Figure 5.4: Moment of momentum of the system about the impacting corner before and after impact (subscript 1 and 2 respectively).

where the upper and lower signs indicate impact on the left and right corners respectively. The moment of momentum about the impacting corner is then obtained as:

$$\Lambda_1 = \pm\, 2\, m\, \dot{R}_1 B \frac{H}{R_1} - m R_1 \dot{\beta}_1 \Big(R_1 - 2B\, \frac{(B \mp u)}{R_1} \Big) - m_r\, H \big(\mp\, \dot{R}_1 \frac{(B \mp u)}{R_1} + H \dot{\beta}_1 \big) \qquad (5.46)$$

5.3.1.1 Fictitious full contact phase

Assuming that, upon impact, the base does not uplift and the structural mass continues moving on a purely translational motion, the moment of momentum of the system about the impacting

corner is given by:

$$\Lambda_2 = -(m + m_r)H\dot{u}_2 \tag{5.47}$$

Conservation of moment of momentum before and after impact ($\Lambda_1 = \Lambda_2$) yields:

$$\dot{u}_2 = \mp\frac{2B\dot{R}_1}{R_1(1+\sigma)} + \frac{H\dot{\beta}_1}{1+\sigma}\left(1 - \frac{B^2 - u^2}{H^2}\right) + \frac{\sigma}{1+\sigma}\left(\mp\dot{R}_1\frac{(B \mp u)}{R_1} + H\dot{\beta}_1\right) \tag{5.48}$$

where the subscripts denote pre (1) and post impact (2) parameters. The deformation of the oscillator, u, before and after impact is assumed to remain constant ($u_1 = u_2$). Since the potential energy of the system does not vary during impact, the change of the total energy can be described by the variation of the kinetic energy of the masses. Thus, the kinetic energy of the fictitious full contact phase can be obtained as:

$$E_{fc} = \frac{1}{2}(m + m_r)\,\dot{u}_2^2 \tag{5.49}$$

5.3.1.2 Fictitious rocking phase

On the other hand, if the base uplifts about the opposite corner and continues rocking, the moment of momentum of the system about the impacting corner is given by:

$$\Lambda_2 = -mR_2^2\dot{\beta}_2 - m_r\,H\big(\pm\dot{R}_2\frac{(B \pm u)}{R_2} + H\dot{\beta}_2\big) \tag{5.50}$$

and conservation of moment of momentum before and after impact ($\Lambda_1 = \Lambda_2$) yields:

$$\dot{\beta}_2 = \frac{1}{R_2^2 + \sigma H^2}\Bigg(\big(H^2 - B^2 + u^2\big)\dot{\beta}_1 \mp \frac{2HB}{R_1}\dot{R}_1 + \sigma H\big(\mp\dot{R}_1\frac{(B \mp u)}{R_1} + H\dot{\beta}_1 \mp \dot{R}_2\frac{(B \pm u)}{R_2}\big)\Bigg) \tag{5.51}$$

Acikgoz and DeJong's approach assumes that the pre and post impact translational velocity remains the same ($\dot{u}_1 = \dot{u}_2$). This gives the second equation for post-impact velocity $\dot{R}_2$:

$$\dot{R}_2 = -\dot{R}_1\left(\frac{R_1}{R_2}\right)\left(\frac{B \pm u}{B \mp u}\right) \tag{5.52}$$

Then, the kinetic energy of the fictitious rocking phase is given by:

$$E_r = \frac{1}{2}m\big(R_2^2\dot{\beta}_2^2 + \dot{R}_2^2\big) + \frac{1}{2}m_r\big(\mp\dot{R}_2\cos\beta_2 \pm R_2\dot{\beta}_2\sin\beta_2\big)^2 \tag{5.53}$$

The corresponding phase of motion after impact is determined comparing Equation 5.49 and Equation 5.53. If $E_{fc} < E_r$, a full contact phase begins with initial conditions defined by Equation 5.48. On the other hand, if $E_r < E_{fc}$, the structure continues rocking about the opposite corner with post impact velocities defined by Equation 5.51 and Equation 5.52.

As noted by Vassiliou et.al [53], in certain occasions, the proposed formulation may lead to an increase in the total energy of the system after impact. In order to enforce energy dissipation in these cases, Acikgoz and DeJong changed the Hounser-like angular momentum conservation to a horizontal momentum conservation approach, leading to:

$$\dot{u}_2 = H\dot{\theta}_1 + \dot{u}_1 \tag{5.54}$$

5.3.2 Vertical Velocity Energy Loss (VVEL) model

The kinetic energy associated with the horizontal component of the pre-impact velocity is given by:

$$E_{1,h} = \frac{1}{2}(m + m_r)\left(H\dot{\theta}_1 + \dot{u}_1\right)^2 \tag{5.55}$$

As suggested by Meek [139], it is appropriate to idealize impact as a perfectly inelastic collision that completely dissipates the kinetic energy associated with the vertical components of the velocity, so that:

$$\dot{\theta}_2 = 0 \tag{5.56}$$

This condition implies that after every impact a full contact phase will always follow. Therefore, the post-impact kinetic energy of the system is:

$$E_2 = \frac{1}{2}(m + m_r)\dot{u}_2^2 \tag{5.57}$$

And equating equation 5.55 and 5.57 yields:

$$\dot{u}_2 = H\dot{\theta}_1 + \dot{u}_1 \tag{5.58}$$

The structure will continue in this full contact phase until the uplift condition (Equation 5.4) is reached again. In cases where the initial velocity, $\dot{u}_2$, is high enough, this can happen almost instantaneously after impact. An example of this situation can be observed in Figure 5.5, where the responses of both impact models are compared for two flexible rocking structures subjected to sinusoidal pulses of frequency $\omega_g/p = 5$ and acceleration amplitude $a_g = 1.5\, g \tan\alpha$. The response obtained with a numerical model implemented in OpenSees (described later in Chapter 6) is also included in the plots.

Very good agreement is observed between the VVEL and Opensees models for both structures analysed. The small difference obtained mainly in the deformation response, u, arises from the corrotational transformation used in the numerical model. On the other hand, the adapted ADJ model dissipates a comparatively higher amount of energy in each impact. These observations are consistent with the experimental results obtained by Truniger el al. [32], who observed that Acikgoz and DeJong's approach tended to overestimate the energy dissipated

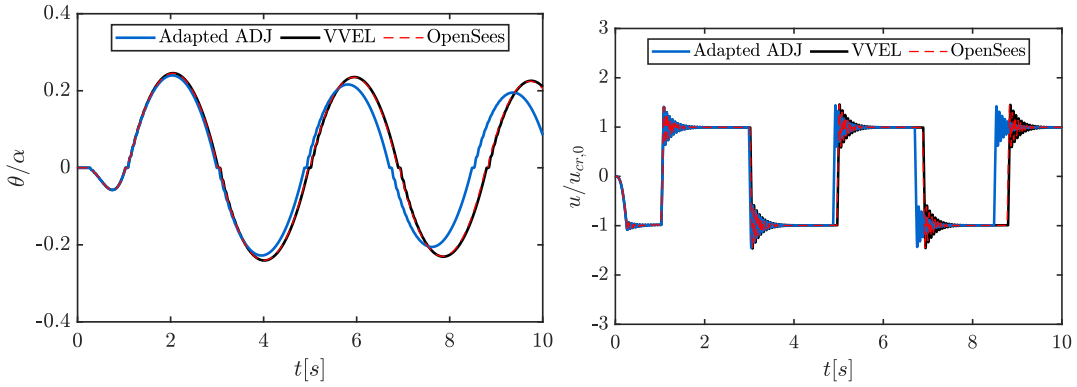

(a) Slender structure ($\alpha = 0.1$)

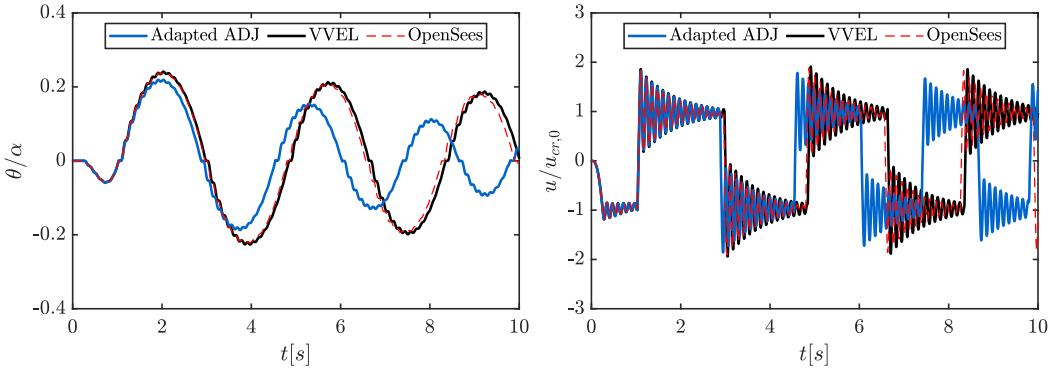

(b) Non-slender structure ($\alpha = 0.2$)

Figure 5.5: Comparison of impact models on a flexible rocking structure of $\omega_n/p = 10$ and $\xi = \xi_{rp} = 0.005$, equipped with an inerter of apparent mass ratio $\sigma = 0.5$, subjected to sinusoudal pulses of frequency $\omega_g/p = 5$ and acceleration amplitude $a_g = 1.5\, g \tan\alpha$.

during impact. In light of the above, the VVEL model is used for the analyses presented in the following sections.

5.4 Dynamic response under coherent pulses

5.4.1 Physically similar dimensionless response

Pulse-type records, which typically contain high ground velocities and low-frequency content, have been shown to be particularly demanding for rocking structures [140, 141]. The fundamental impulsive characteristics of these ground motions can be adequately described by trigonometric pulses [142]. When subjected to such excitations, the dynamic response of the system shown in Figure 5.2 is a function of 10 parameters:

$$[\theta, u] = \phi\left(R_0\,, \alpha\,, m\,, k\,, \xi\,, m_r\,, \omega_g\,, a_g\,, g\,, t\right) \tag{5.59}$$

where ω_g and a_g are the pulse's frequency and acceleration amplitude, respectively, while

the other parameters have been defined previously. Equation 5.59 involves 3 fundamental dimensons and according to Vaschy-Buckingham's Π-theorem [120, 121], the response of the system can be described by $10 - 3 = 7$ dimensionless parameters:

$$\left[\frac{\theta}{\alpha}, \frac{u}{u_{cr,0}}\right] = \phi\left(\frac{\omega_n}{p}, \frac{\omega_g}{p}, \xi, \alpha, \frac{a_g}{g\tan\alpha}, \sigma, pt\right) \tag{5.60}$$

where $p = \sqrt{g/R_0}$ is the frequency parameter of the rocking structure. Figure 5.6 shows the response of rocking structures of $\omega_n/p = 10$, $\alpha = 0.2$ and $\xi = 0.02$, connected to inerters of apparent mass ratio $\sigma = 0.5$, when subjected to a single sine pulse of frequency $\omega_g/p = 8$ and acceleration amplitude $a_g = 1.5g\tan\alpha$. The selected parameters have been chosen to represent a range of structures such as museum artefacts ($R_0 = 2\,[m]$ and $f_n = 3.5\,[Hz]$), bridge piers or rocking buildings ($R_0 = 10\,[m]$ and $f_n = 1.6\,[Hz]$). The responses of the corresponding bare and fixed-base oscillators are also included in Figure 5.6 for comparison purposes.

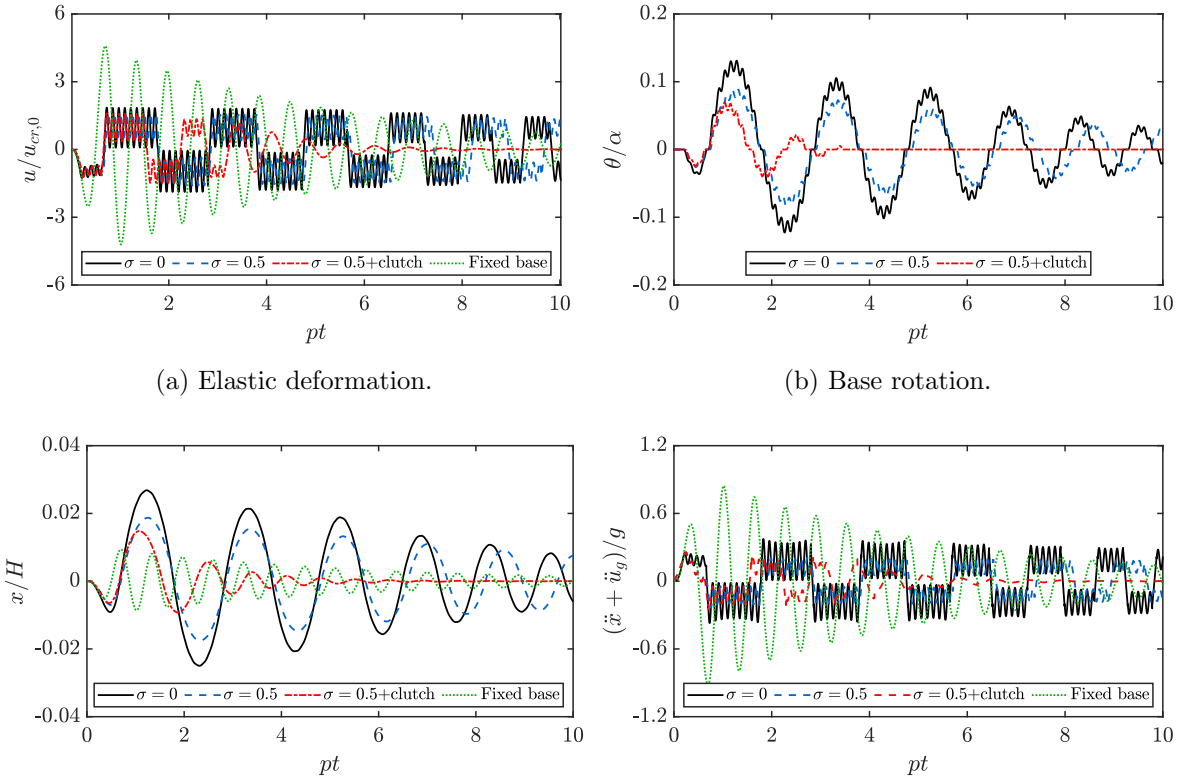

(a) Elastic deformation.

(b) Base rotation.

(c) Drift.

(d) Absolute acceleration.

Figure 5.6: Response of fixed base and rocking flexible structures of $\omega_n/p = 10$, $\alpha = 0.2$, $\xi = 0.02$, with and without inerters, subjected to a sine pulse of $\omega_g/p = 8$ and $a_g = 1.5g\tan\alpha$.

The total lateral drift of a rocking structure, x/H in Figure 5.6, is obtained as the sum of the rotation and structural deformation contributions (Equation 5.2). It can be seen from Figure 5.6 that although the rocking motion limits the deformation of the column to values close to the critical displacement, the base rotation can significantly increase the lateral drift of the structure. Figures 5.6a and 5.6c show an example of this situation. In this particular case,

the maximum structural deformation is reduced to almost a third of the corresponding fixed-base value, whereas the lateral drift is more than doubled. It is also known that under strong ground-motions, SDOF oscillators allowed to uplift experience lower magnitudes of lateral forces. Accordingly, Figure 5.6d shows a significant reduction of the horizontal accelerations in the rocking structures in comparison with fixed-based ones. It should be noted that the impact formulation employed ensures that the horizontal velocity response is smooth, so the lateral acceleration history remains defined.

Figure 5.6a demonstrates that the inerter has a small effect on the elastic deformation of the structural element, u. However, the base rotation, θ, is significantly reduced, which leads to a considerably smaller total horizontal displacement, x. An important further reduction in the peak horizontal acceleration is also observed in Figure 5.6d, with the clutched inerter system experiencing the lower acceleration levels of the set. Importantly, the peak resisting force developed in the inerter remains below 20% of the structure's weight and can be accommodated with adequate detailing. Moreover, similar levels of apparent mass ratios and inerter-forces have been considered in analytical and experimental studies on fixed-base structures [8,95,96]. Overall, the results presented in Figure 5.6 suggest that the combination of rocking and inerters can be an efficient mechanism to reduce deformation and stresses, while at the same time controlling high drifts and accelerations, all of which are conductive to damage.

As noted above, the introduction of the clutch significantly improves the efficiency of the inerter in reducing the base rotation response. The effect of the clutch can be further examined by inspecting the total energy of the structure-inerter system, given by:

$$E_T = \frac{1}{2}m\left(\dot{R}^2 + R^2\dot{\theta}^2\right) + mg(\pm R\sin\beta - H) + \frac{1}{2}ku^2 + \frac{1}{2}\,m_r\,\dot{x}^2 \tag{5.61}$$

where $\dot{x}$ is the horizontal velocity of point C (see Figure 5.2). Figure 5.7 shows the total energy of the same set of structures analysed above. The total energy is normalized by $E_{ref} = mgR_{cg}(1-\cos\alpha_{cg})$, where E_{ref} represents the difference in potential energy of a rigid rocking structure between its unstable ($\theta = \alpha_{cg}$) and stable ($\theta = 0$)) equilibrium positions [31]. It is clear from Figure 5.7 that the inclusion of the inerter limits the total energy absorbed by the system, while at the same time it reduces the amount of energy dissipated during each impact. This results in the lower peak rotations observed in Figure 5.6b, with similar amplitudes in the later cycles of the rocking response. Such increase in the coefficient of restitution was also predicted by angular momentum equations in Chapter 3.

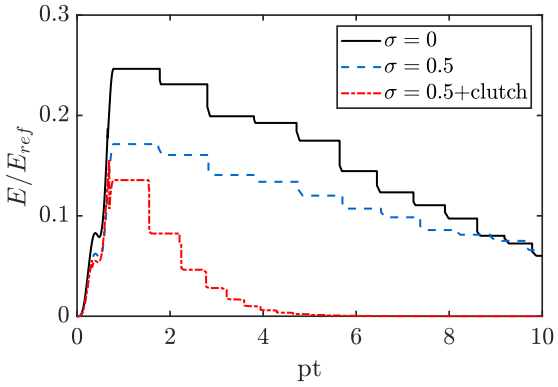

Figure 5.7: Total Energy of the structure-inerter systems.

Part of the total energy absorbed by the system is stored in the inerter device, as shown in the close-up view of Figure 5.8a. As the structure rocks and oscillates this energy is transferred back and forth, and the single inerter (without clutch) alternates between opposing and driving the motion. If a clutch is introduced, the inerter disengages from the structure when $\ddot{x}/\dot{x} < 0$ (marked by the unshaded areas in Figure 5.8b) and the energy stored in it is not transferred back to the oscillator. If the inerter is then able to dissipate this energy, every engagement-disengagement cycle removes energy from the structural system, increasing the rate at which the rotation and deformation responses are attenuated. Experimental analyses conducted by Málaga-Chuquitaype et al. [105] suggest that friction within the inerter can effectively dissipate part of the energy, while additional energy dissipation can be ensured by means of additional viscous fluids [95, 104].

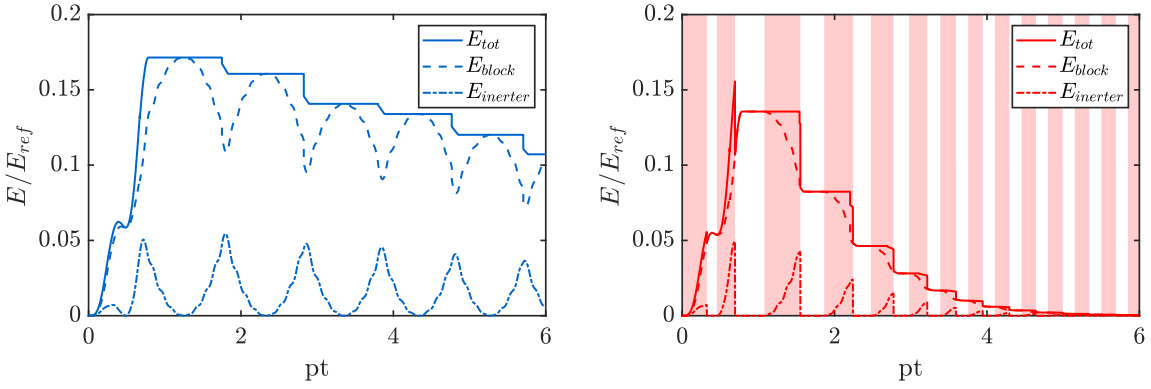

(a) Single inerter without clutch.

(b) Pair of clutched inerters.

Figure 5.8: Effect of the clutch on the energy transfer between the inerters and the structures.

5.4.2 Effect of flexibility on the efficiency of the inerter

The observations presented and discussed above refer to a particular value of the ω_n/p ratio. This section extends those findings to a family of flexible oscillators with a wide range of frequency ratios (ω_n/p). In particular, the effect of flexibility on the efficiency of the inerter

is assessed. To this end, Figure 5.9 and 5.10 summarize the response of flexible rocking structures subjected to trigonometric pulses of frequency $\omega_g/p = 8$ and acceleration amplitude $a_g = 1.5g\tan\alpha$.

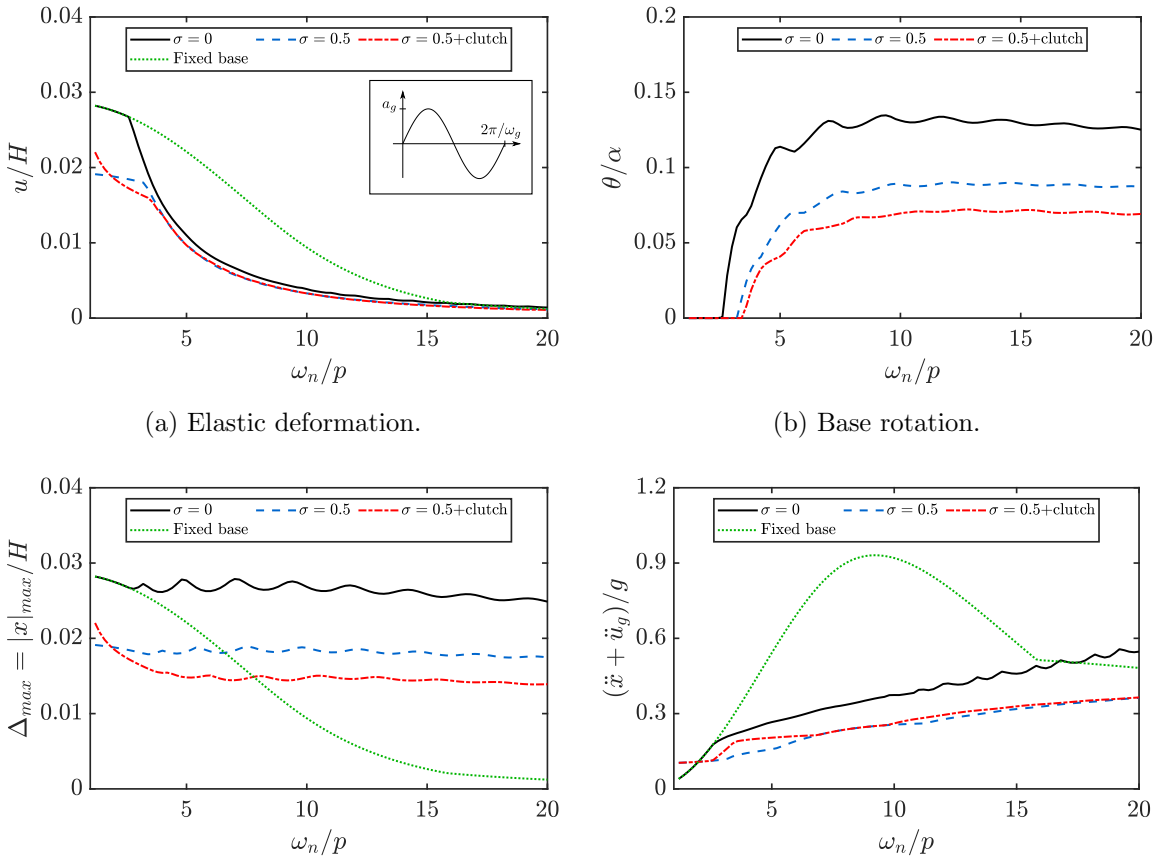

(a) Elastic deformation.

(b) Base rotation.

(c) Drift.

(d) Absolute acceleration.

Figure 5.9: Effect of flexibility on the response of structures with $\alpha = 0.2$, $\xi = 0.02$, with and without inerters, subjected to sine pulses of $\omega_g/p = 8$ and $a_g = 1.5g\tan\alpha$.

Equation 5.6 has evidenced that the critical displacement required to uplift the structure and initiate the rocking motion increases rapidly as the natural frequency, ω_n, decreases. Consequently, very flexible oscillators tend to respond as fixed-base single-degree-of-freedom structures. The effect of the inerter on the elastic deformation of the oscillator, u, is highly influenced by the occurrence or not of the rocking motion. For very flexible oscillators (small ω_n/p) the uplift condition is not reached, and the response approximates that of fixed-base inerter-equipped single-degree-of-freedom systems already studied by Makris and Kampas [95]. However, the onset of rocking, clearly identifiable as a crest in the elastic deformation response of Figure 5.9a and 5.10a, significantly alters the behaviour of the system. Once rocking motion is triggered, the effect of the inerter on the elastic deformation of the oscillator is very limited, and no significant gains are observed as the clutch is introduced although the benefits of the clutch become more relevant as the oscillator's stiffness increases. Nevertheless, the overall effect of the inerter on total drifts, Δ_{max}, is still appreciable after uplift due to the important

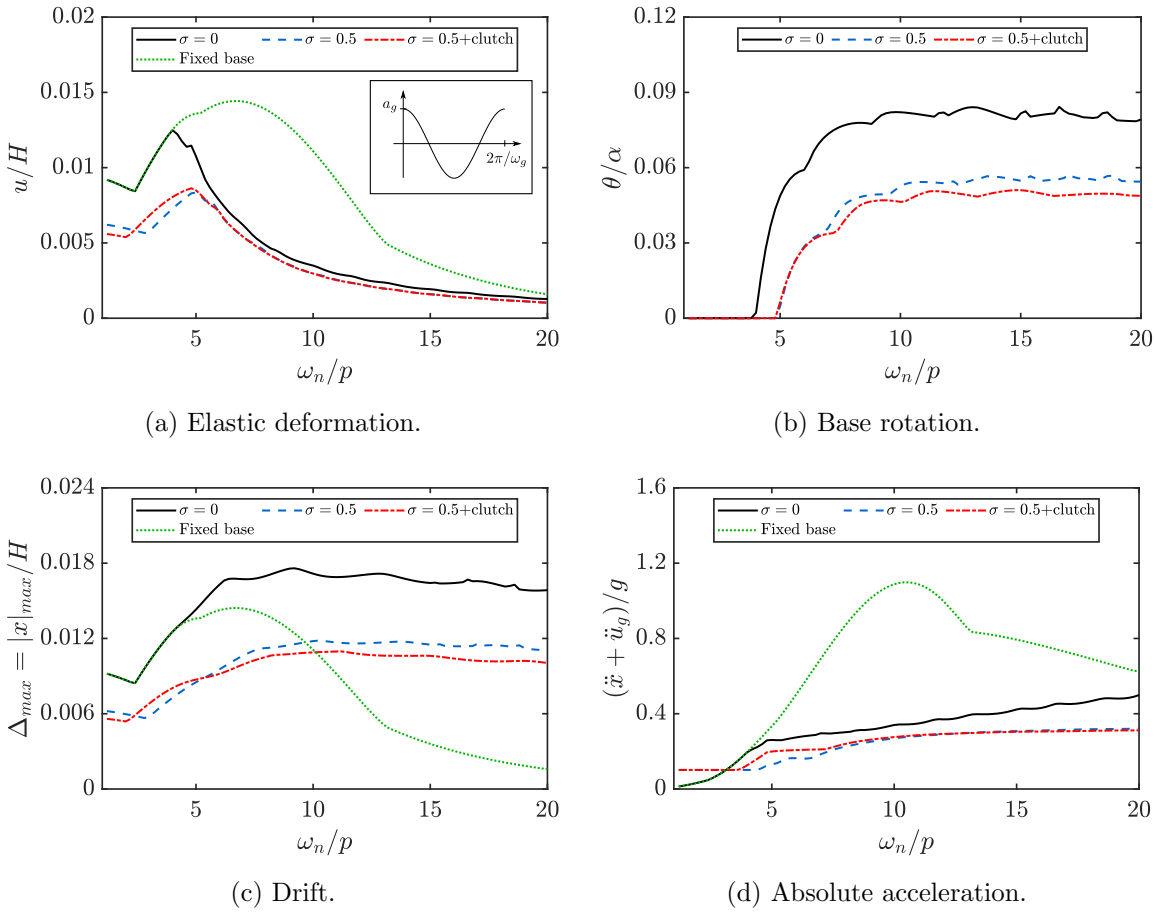

(a) Elastic deformation.

(b) Base rotation.

(c) Drift.

(d) Absolute acceleration.

Figure 5.10: Effect of flexibility on the response of structures with $\alpha = 0.2$, $\xi = 0.02$, with and without inerters, subjected to cosine pulses of $\omega_g/p = 8$ and $a_g = 1.5g\tan\alpha$.

rotational reductions brought about by the supplemental inertia (Figures 5.9b and 5.9b). On the other hand, the absolute horizontal acceleration exhibits different trends depending on the spectral region of interest. For very flexible oscillators that do not uplift, the inerter has a disadvantageous impact on the acceleration, an aspect that has already been identified by Makris and Kampas [95]. In contrast, protected structures that undergo rocking motion experience smaller levels of absolute accelerations, even though the introduction of the clutch does not necessarily result in further reductions in the accelerations.

5.4.3 Effect of the inerter on the overturning response

The global stability of rocking structures is usually studied by means of overturning plots. These graphs represent the areas in the frequency-acceleration amplitude space that result in safe rocking or toppling of the oscillator. Figure 5.11 compares the overturning response of flexible rocking structures of $\omega_n/p = 10$ with and without inerters when subjected to cycloidal pulses. The area above the upper curves represent overturning without impact (Region 1), whereas the areas enclosed by the lower curves correspond to overturning taking place after

impact at the base (Region 2). The remaining regions of the plot are associated with safe rocking (Region 3).

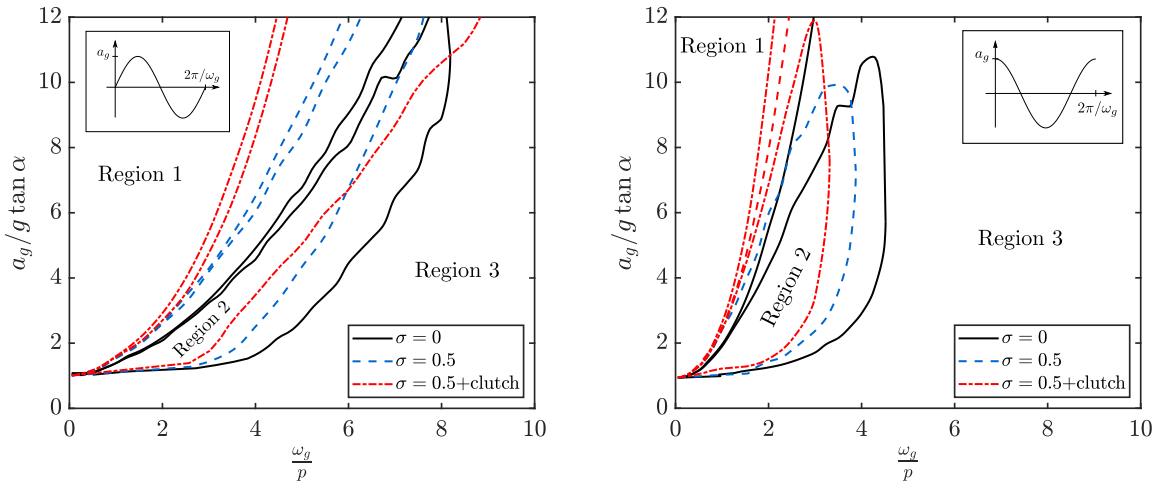

(a) Sine Pulses

(b) Cosine Pulses

Figure 5.11: Overturning response of flexible rocking structures of $\omega_n/p = 10$, slenderness $\alpha = 0.2$ and $\xi = 0.02$ under trigonometric acceleration pulses.

The results presented in Figure 5.11 are consistent with the trends previously observed for rigid rocking bodies. In both cases the inclusion of the inerter reduces the areas of overturning (Regions 1 and 2) and translates them to the lower frequency region. This frequency shift, which is otherwise beneficial, is particularly relevant for the case of overturning after impact (Region 2), as certain structures that would rock safely without the inerter, may overturn when the protective device is incorporated. The introduction of the clutch, on the other hand, further shifts the overturning regions and expands the overturning after impact area (Region 2) to higher acceleration magnitudes, a potential drawback that was also identified for rigid bodies in Chapter 3. Nevertheless, this adverse effect occurs in a frequency-acceleration region of limited practical relevance.

Of particular interest in stability analyses are smaller structures ($\omega_g/p < 4$), which are known to be more vulnerable to overturning during strong ground motions [3]. In these cases, the effect of the inerter becomes less significant, and higher levels of inertances may be required to considerably improve the stability of the oscillator. In this regard, the actual mass of the inerter can be reduced in several orders of magnitude by using amplification mechanisms such as ball-screws [7] or gear systems [6]. Alternatively, the incorporation of a clutch can also enhance the performance of the inerter device in smaller unstable structures.

5.4.4 Response under high frequency excitations

High frequency excitations can cause oscillations in the rocking response that can excite the uplifted structure at its resonance frequency. Since both responses are coupled, the increasing

magnitude of the elastic deformations induces short pounding-like rocking cycles, which can reach significant rotation amplitudes and even overturn the structure [44]. Figure 5.12 shows an example of this behaviour, where a rocking oscillator of flexibility $\omega_n/p = 5$ is subjected to a harmonic excitation of frequency equal to the structure's uplifted frequency, $\omega_g/p = \omega_n/(p \sin\alpha)$, and acceleration amplitude $a_g = 13.7\, g \tan\alpha$. A comparatively more flexible oscillator is chosen in this section, since the uplifted frequencies of stiff structures are usually higher than the frequency content of practical excitations. The response of an inerter-protected structure and the corresponding bare fixed-base and rigid rocking oscillators are also included in the plots for comparison purposes.

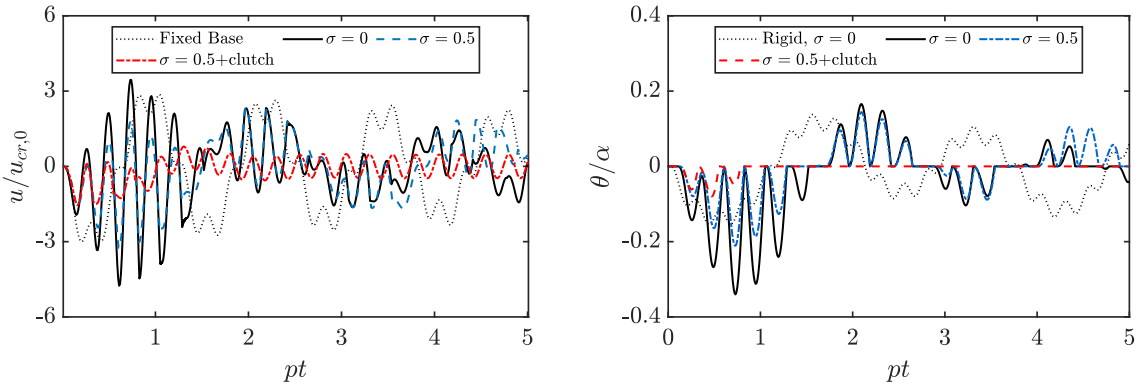

(a) Elastic deformation.

(b) Base rotation.

Figure 5.12: Response of fixed-base and flexible rocking structures of $\omega_n/p = 5$, slenderness $\alpha = 0.2$ and $\xi = 0.02$, with and without inerters, subjected to a harmonic ground motion of frequency $\omega_g = \omega_n/\sin\alpha = 25.1\, p$, and acceleration amplitude $a_g = 13.7\, g \tan\alpha$.

Figure 5.12a shows that the elastic deformation of the bare rocking structure exceeds the deformation of the corresponding fixed-base oscillator. As previously discussed, this magnified response induces short rocking cycles of high rotation amplitude which also exceed the demand associated with the rigid rocking structure (Figure 5.12b). When the inerter is introduced, on the other hand, the elastic deformation of the column falls considerably, leading to an ever more significant reduction of the rotation response.

The effects of uplifted resonance on the response of a wider range of flexible rocking structures can be better analysed if an additional dimensionless term is introduced: $\nu = u_{f,max}/u_{cr,0}$, where $u_{f,max}$ is the maximum displacement of a fixed-base oscillator of the same dynamic properties under the same ground excitation. This term, proposed by Psycharis [143], defines the minimum ground motion intensity required to generate a given displacement in the fixed base structure. Figure 5.13 compares the deformation and rotation response spectra of the flexible rocking structures studied in Figure 5.12 for a wide range of excitation frequencies. The acceleration amplitude of each ground motion is obtained by setting $\nu = 3$.

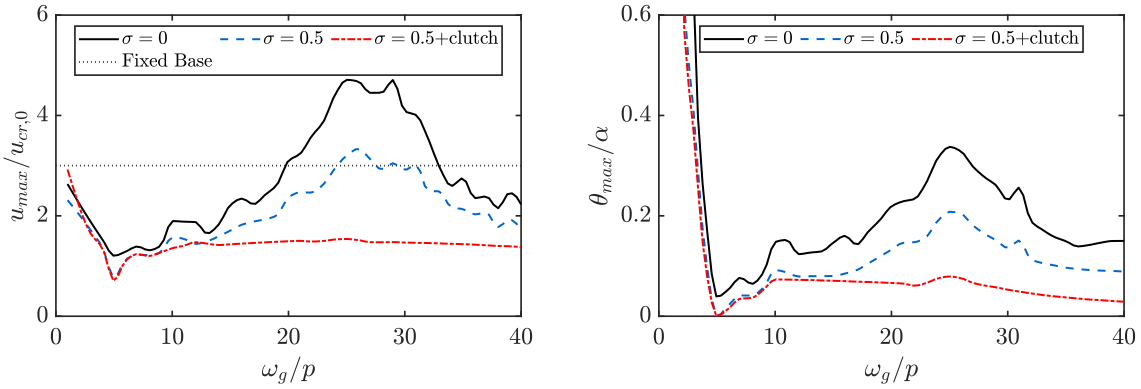

(a) Elastic deformation.

(b) Base rotation.

Figure 5.13: Response of flexible rocking structures of $\omega_n/p = 5$, slenderness $\alpha = 0.2$ and $\xi = 0.02$, with and without inerters, subjected to a harmonic ground motion of variable frequency and acceleration amplitude defined by $\nu = 3$.

The results presented in Figures 5.12 and 5.13 show that the efficiency of the inerter in reducing the elastic deformation of the structure is significantly higher for frequencies neighbouring the uplifted resonance region. On the other hand, a more uniform reduction factor is observed for the rotation response across the range of frequencies considered in the analysis. It is worth noting that these beneficial effects are not a-priori obvious and not wholly caused by the effective period elongation brought about by the inerter. This is demonstrated in Figure 5.13 where such improvements are evident for the full range of frequencies under consideration. Importantly, the introduction of the clutch completely suppresses the uplifted-resonance peak in both response parameters. In light of the above, it is possible to conclude that the use of inerters constitutes an efficient strategy for controlling the response of flexible rocking structures subjected to high frequency excitations.

5.5 Response under non-coherent pulse-like ground motions

Near-source seismic ground motions can contain long velocity pulses that may induce large rotations in rocking structures. Besides the main pulse, they also contain non-coherent frequency components that can amplify the peak ground acceleration [144]. Makris and Roussos [141] examined the stability of free-standing rigid blocks subjected to pulse-like records and showed that the rocking response of smaller structures is mainly governed by these short acceleration pulses, whereas larger blocks are more sensitive to the incremental ground velocity. In this context, it is reasonable to assume that most small rocking structures equipped with inerters will behave as rigid blocks, a problem that has been studied by the authors in a previous publication [145]. Consequently, this section focuses on the response of larger structures, or those where the effect of flexibility cannot be ignored. A rocking structure of $p = 1[Hz]$, $\alpha = 0.15$, and $\xi = 0.02$, representative of a $2B = 3[m]$ by $H = 10[m]$ wall building system, is selected as

a typical case study for the analyses presented herein.

Figure 5.14a and 5.14b show the acceleration and velocity histories recorded at the North Palm Springs station during the 1986 North Palm Springs Earthquake. A long-duration pulse is evident in the velocity history, whereas significant high-frequency spikes are observed in the acceleration series. These features have the potential of causing both large drifts and acceleration demands. The main velocity pulse can be approximated by a sinusoidal pulse of $T_p = 1.4[s]$ and $v_p = 0.6[m/s]$, resulting in a cosinusoidal acceleration of amplitude $\omega_g v_p = 0.27[g]$ [141]. The elastic deformation and base rotation responses of bare and protected rocking structures of $\omega_n = 10[rad/s]$ and apparent mass ratio of $\sigma = 0.5$ to this earthquake are presented in Figures 5.14c and 5.14d.

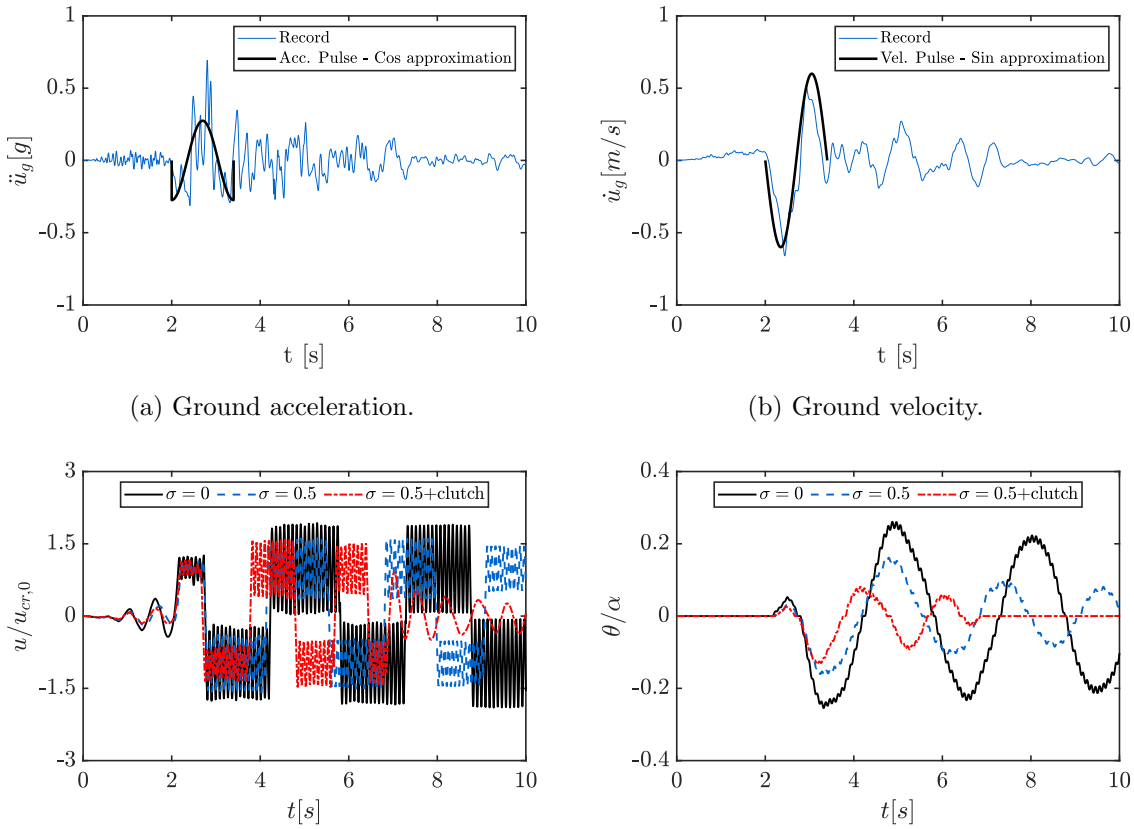

(a) Ground acceleration.

(b) Ground velocity.

(c) Elastic deformation.

(d) Base rotation.

Figure 5.14: Rocking response of a structure of $p = 1[Hz]$, $\alpha = 0.15$, $\omega_n = 10[rad/s]$ and $\xi = 0.02$ to the acceleration history of North Palm Springs, 1986.

The smooth rotation responses observed in Figure 5.14d indicate that rocking is mainly governed by the coherent pulse, and is not significantly affected by the high frequency non-coherent content. This lends credence to the wider applicability of the findings of the previous sections related to the response improvements observed under cycloidal pulses. The beneficial effects of the inerter are also evident in Figure 5.14. In order to generalize these conclusions to a wider range of flexibilities and ground motions, the response of several bare and inerter-

equipped structures to a set of 5 earthquake records is obtained and compared in the form of rocking spectra. The ground motions, summarized in Table 5.1, are selected from the pulse-like database previously described in Table 3.1 and include records with pulses ranging from 1.2[s] to 5.1[s] and peak ground velocities of up to 1.67[m/s]. The listed records were selected in light of their strong coherent and non-coherent components that are able to cause important drift and acceleration demands in flexible uplifting structures of the type considered herein.

No.	**Event**	**Year**	**Station**	T_p **[s]**	**PGV [m/s]**	M_w
1	Landers	1992	Lucerne	5.1	1.4	7.3
2	Northridge-01	1994	Rinaldi	1.2	1.67	6.7
3	Imperial Valley-06	1979	El Centro Diff Array	5.9	0.6	6.5
4	Superstition Hills-02	1987	Parachute Test Site	2.3	1.07	6.5
5	N. Palm Springs	1986	N. Palm Springs	1.4	0.67	6.1

Table 5.1: Pulse-like ground motion records used in the analyses

Figure 5.15 summarizes the response of structures with the same geometry as above ($p = 1[Hz]$ and $\alpha = 0.15$) but with different levels of flexibility (characterized by ω_n), when subjected to the ground motions described in Table 5.1. The figure shows the maximum rotation, elastic deformation, drift and absolute acceleration of bare and protected elastic rocking oscillators with single and clutched inerters. When the maximum rocking angle reaches an arbitrarily large rotation ($\theta \to \infty$), the structure topples. A value of $\theta/\alpha = 1$ is assigned to the ordinate of the rotation spectrum and the values of elastic deformation, drift and absolute acceleration are not reported, as they are not deemed relevant when the structure overturns.

Figure 5.15a shows an important reduction in the number of overturning cases when the inerter is incorporated. The addition of the clutch, on the other hand, leads to a safe low-amplitude rocking response in all cases. Importantly, the rotation reduction factor is considerably higher for the ground motions associated with larger demands like the Parachute and Lucerne records. The peak elastic deformations, presented in 5.15a, show a much smaller effect, in line with the findings presented in the previous sections. It is also worth noting the significant reduction in the dispersion associated with clutched systems indicating a better control of the dynamic response.

As previously discussed, the total peak lateral drift of uplifting structures is mainly controlled by the base rotation. Accordingly, Figure 5.15c exhibits the same trends observed in the base rotation response of Figure 5.15a. On the other hand, Figure 5.15d demonstrates that the inerter also reduces the peak lateral accelerations, specially for the more demanding ground motions. However, the introduction of the clutch does not significantly improve the acceleration demands, with the Rinaldi record showing even higher acceleration magnitudes in the case of clutched inerters in comparison with a single inerter implementation. This partic-

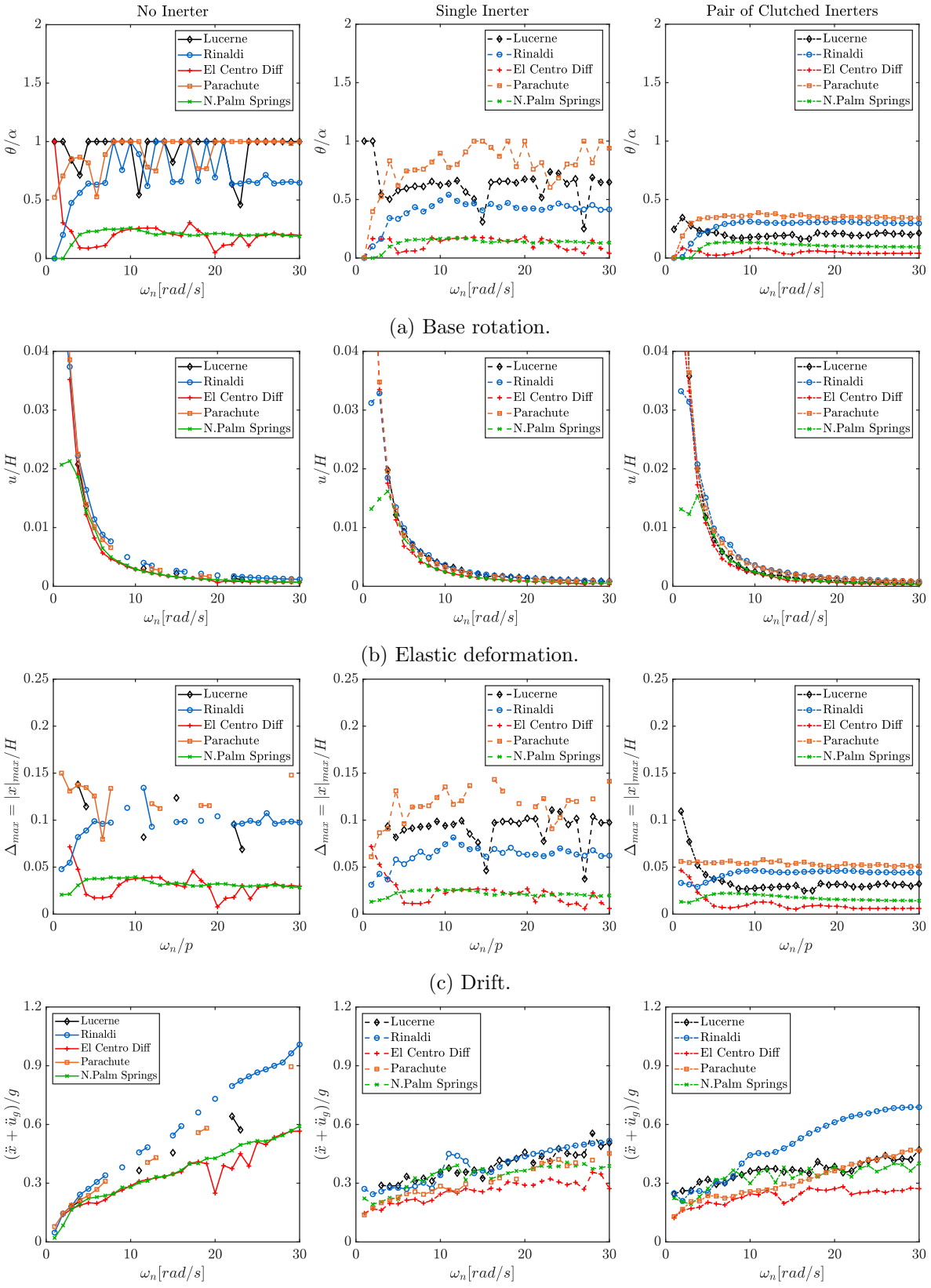

(a) Base rotation.

(b) Elastic deformation.

(c) Drift.

(d) Absolute acceleration.

Figure 5.15: Rocking spectra for a structure of $p = 1[Hz]$, $\alpha = 0.15$, and $\xi = 0.02$ to the pulse-like ground motion set described in Table 5.1.

ular situation is studied in detail in Figures 5.16 and 5.17, where the rotation and acceleration response of oscillators of $\omega_n = 20\,[rad/s]$ is examined. The Rinaldi record, shown in Figure 5.16, contains a distinctive smooth pulse with very few high frequency fluctuations and high acceleration amplitude. Figure 5.17a shows that in the bare and single inerter cases, impact takes place close to the end of the main pulse ($t = 2.8[s]$) meaning that the second half of the excitation, after reversal of acceleration, can effectively help to restrain the motion of these structures. The introduction of the clutch, however, leads to an earlier impact, causing most of the second half of the pulse to exacerbate the rotation after uplift in the opposite direction. This phenomenon was not observed in the other earthquake records because their high frequency non-coherent content causes acceleration reversals within the main pulse (see Figure 5.14a). A similar effect was identified in Figures 5.9d and 5.10d, where cycloidal excitations were considered. This is also evident in Figures 5.17c and 5.17d, which plots the rotation and acceleration response of the same oscillators to a cosine pulse of $T_p = 1\,[s]$ and $a_g = 0.83\,[g]$, representative of the coherent pulse of the Rinaldi record.

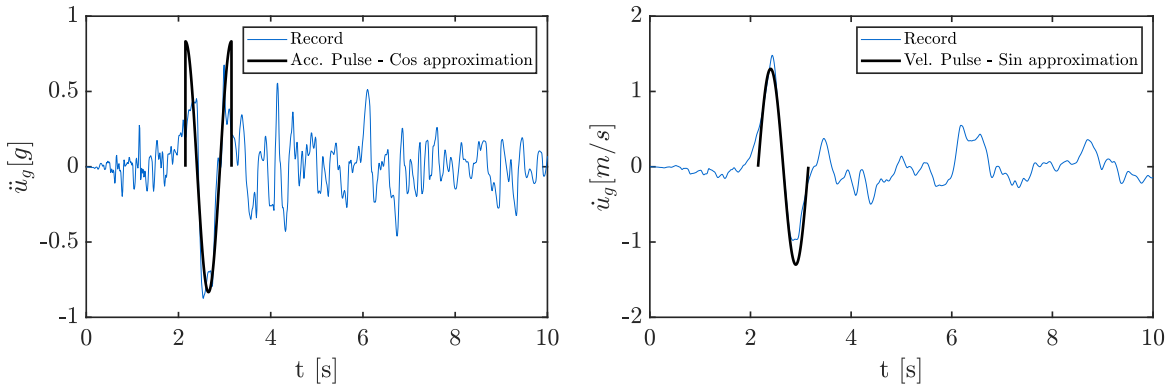

(a) Ground acceleration.

(b) Ground velocity.

Figure 5.16: Coherent pulses in the acceleration and velocity records obtained at Rinaldi station during the 1994 Northridge earthquake.

5.6 Concluding remarks

The dynamic response of deformable rocking structures equipped with inerters was investigated in this chapter. Firstly, analytical expressions that take into account the inerter's effect on the motion of flexible uplifting structures were presented. This model was subsequently used to assess the response of practice-representative structures to coherent single-pulse excitations. The results of the analyses showed that while the incorporation of inerters leads to a pronounced reduction in peak lateral deformations in elastic structures where full base contact is maintained, it has a small effect on the elastic deformation of uplifting oscillators. However, significant reductions were observed in the maximum rotations, resulting in considerably lower overall drift demands. Likewise, similar reductions in the peak lateral accelerations were

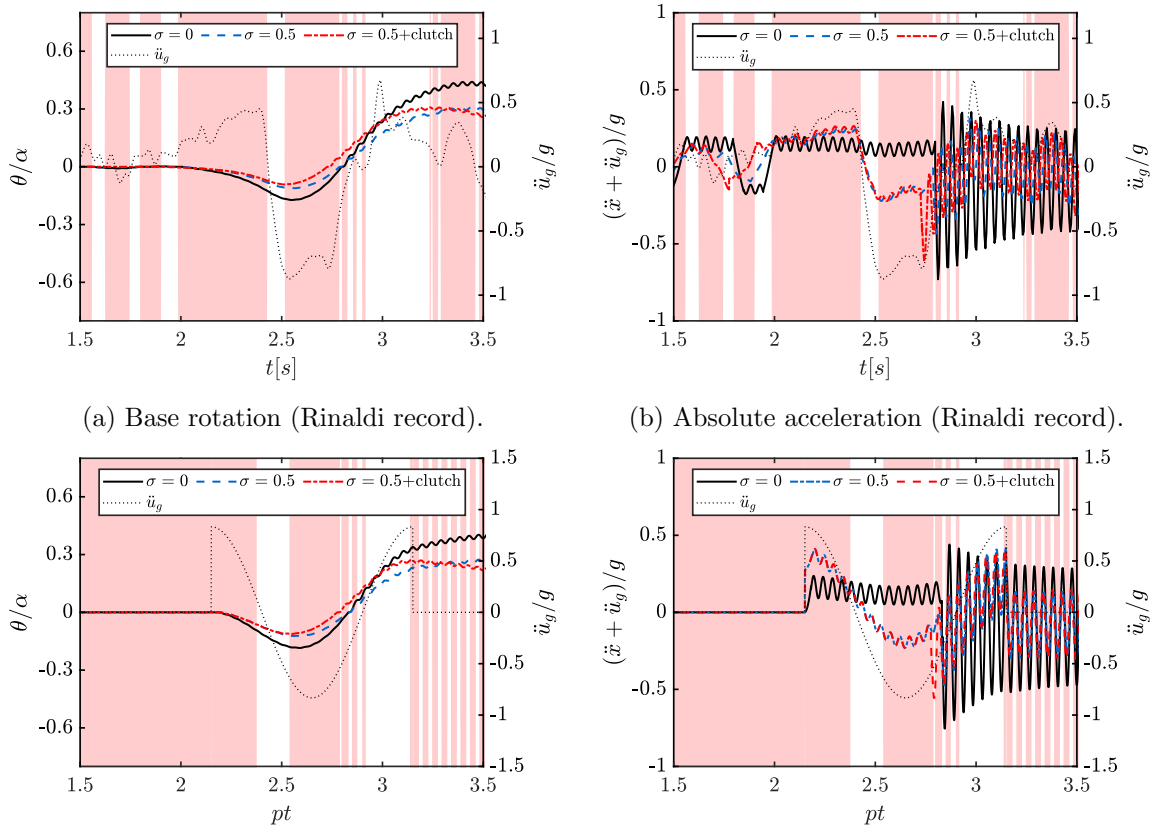

(a) Base rotation (Rinaldi record).

(b) Absolute acceleration (Rinaldi record).

(c) Base rotation (Cosine pulse).

(d) Absolute acceleration (Cosine pulse).

Figure 5.17: Rotation and acceleration response of rocking oscillators of $\omega_n = 20[rad/s]$, $\alpha = 0.2$, $\xi = 0.02$, with and without inerters, when subjected to the Rinaldi record and a cosinusoidal acceleration pulse. Shaded areas indicate engagement of the clutched inerter.

obtained for mid to high stiffness ratios (ω_n/p). These results suggest that combining rocking with inerters can be an efficient strategy to control structural stresses and deformations in flexible structures, while at the same time offsetting the increase in the lateral drifts brought about by the base rotation. Importantly, the analyses reported herein also showed that the efficiency of the inerter is not significantly affected by the level of flexibility of the oscillator.

Examination of the total energy of the system showed that the inerter alternately opposes and drives the motion of the structure as the kinetic energy accumulated in it is transferred back and forth during the rocking response. Assuming that the disconnected clutched-inerter is then able to dissipate this energy, every engagement-disengagement cycle removes energy from the structural system, increasing the rate at which the rotation and deformation responses are attenuated. The introduction of the clutch, however, leads to earlier impact, a phenomenon that can sometimes exacerbate the lateral acceleration demands.

The overall effect of the inerter on the overturning response of flexible structures is

qualitatively similar to the behaviour observed for rigid rocking blocks. The inclusion of the inerter reduced the areas of overturning and translated them to the lower frequencies region. This translation is particularly important for the region of overturning after impact, as certain unprotected structures that would have survived the ground motion, overturn when the inerter is incorporated. The introduction of the clutch, on the other hand, was shown to be particularly attractive for the protection of smaller vulnerable structures. Nevertheless, an expansion of the overturning after impact region was also obtained, but this potential drawback occurred in a frequency-acceleration region of limited practical relevance.

Additionally, the phenomenon of uplifted resonance was examined confirming that the efficiency of the inerter in reducing the elastic deformation grows significantly in the region around the uplifted frequency. Furthermore, consistent reductions on the maximum rotation response were also obtained, while the incorporation of a clutch was shown to fully suppress the uplifted resonance peaks in both elastic deformations and rotations.

Finally, the observations presented above were extended to real ground motions by considering the response of a case of study structure to a set of real pulse-like records. Close examination of the rotation history showed that the rocking drift is mainly governed by the coherent velocity pulse. Accordingly, the response improvements previously observed under analytical pulses were also verified for real pulse-like records. Importantly, the efficiency of the inerter in controlling the structural demands was considerably higher for the more demanding ground motions. Although, in general, inerter protected structures exhibited lower acceleration demands than bare rocking oscillators, the introduction of the clutch did not always result in lower peak accelerations. Overall, it is possible to conclude that the use of inerters constitutes an effective strategy to control the dynamic response of flexible rocking structures under a wide range of dynamic loadings.

All the structural systems considered so far involve inerters connected directly to the lumped mass or centre of mass of the rocking element. Although this simplification has allowed to examine the fundamental dynamics of rocking systems equipped with supplemental rotational inertia, in many real applications this configuration would be impractical. In the following chapter, the alternative of connecting the inerter at a lower level is investigated. Importantly, this analysis will require the introduction of multi-mass rocking elements.

Chapter 6

Seismic control of multi-mass rocking structures with inerters

6.1 Introduction

In the previous chapters the seismic response of rocking structures equipped with inerters has been examined using simplified models of rigid blocks and single-mass oscillators. In these models, the inerter has been connected directly to the lumped mass or centre of mass of the rocking bodies. Although this simplification has allowed the analysis of the fundamental dynamics of inerter-rocking systems, many practical applications cannot be adequately represented by this configuration. Moreover, the analysis of more complex structural systems, such as building or civil structures, requires the incorporation of multi-degree-of-freedom rocking oscillators. In this chapter, a more practical configuration is presented by considering the response of multi-mass rocking structures equipped with inerters connected at the first mass level. To this end, the finite element model developed by Vassiliou et al. [88] is implemented in OpenSees [10] and extended to incorporate the effects of grounded supplemental rotational inertia devices. The full structural model is subsequently validated against previous experimental and analytical results, and used to examine the effect of the inerter on the rotation and elastic deformation demands of a set of 3, 6 and 9-storey structures. Additionally, the interaction between impact forces and higher vibration modes is examined, while the effectiveness of the inerter for controlling the associated acceleration demands and increased bending moments is also evaluated. Finally, the conclusions obtained for analytical pulses are extended to real earthquakes by evaluating the response of the structural systems to a set of pulse-like ground motion records.

6.2 Definition of the numerical models

6.2.1 Model parameters

The dynamic response of multi-mass rocking structures equipped with inerters can be studied considering the system illustrated in Figure 6.1a. In this model, the rocking body is represented by n lumped masses, m_i, connected by elastic beam-column elements of flexural stiffness EI_i, and supported by a rigid base allowed to uplift. Two degrees of freedom per level are considered, namely, lateral displacement and rotation. The geometry of the structure is characterized by the radial distance between the pivot points and the masses, R_i, and the corresponding slenderness angle, α_i. Accordingly, the frequency parameter of the multi-mass structure can be defined as [34]:

$$p_n = \sqrt{\frac{\underline{1}^t [M] \underline{H}\, g}{J_p}} \tag{6.1}$$

where $[M]$ corresponds to the mass matrix, $\underline{H}$ to the vector of mass heights and J_p is the rotational inertia of the system defined as:

$$J_p = \underline{R}^t \, [M] \, \underline{R} \tag{6.2}$$

with $\underline{R}$ being the radial distances vector. Finally, a grounded inerter of inertance $m_{r,1}$ is connected to the horizontal degree of freedom of the first level mass. The apparent mass ratio is defined as $\sigma = m_r / \sum_{i=1}^{n_{levels}} m_i$. For simplicity reasons, a uniform distribution of stiffness and masses along the height of the oscillator is considered for all the structures examined in this study.

6.2.2 Numerical model of the rocking structure

The modelling strategy adopted in this study is based on the finite element modelling approach for flexible rocking structures proposed by Vassiliou et al. [88]. To this end, three components are considered (Figure 6.1b): the deformable body, the rocking surface and the underlying soil. Linear-elastic beam-column elements are used to represent the flexible structure, whereas a zero-length fibre section is considered for the rocking surface. A linear-elastic non-dissipative compression-only material is assigned to the rocking section, so the system is free to rotate about the pivot points. It is assumed that appropriate arrangements to prevent slipping (such as shear keys) have been considered, so the horizontal displacement of node b is constrained to that of node a. Importantly, the inverted T section at the base of the rocking body is assumed to be perfectly rigid. Alternatively, flexibility in the rocking interface is modelled through the stiffness of the vertical zero-length fibres. Unless otherwise stated, the stiffness of these fibres is set at very high values in order to represent a rigid surface. In these cases, 2 fibres

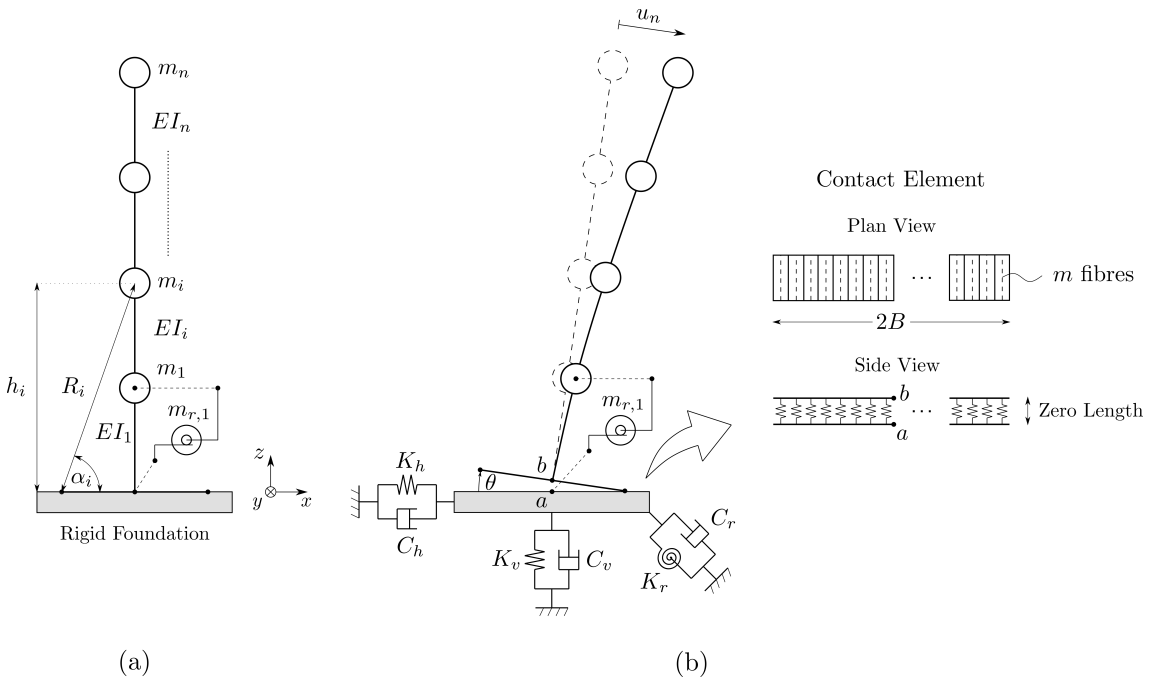

Figure 6.1: Schematic diagram of the numerical model of the rocking structure-inerter system.

are sufficient to simulate the rocking motion [88]. The effects of base flexibility and inelastic deformations in the rocking interface have been further investigated in [146].

As demonstrated in the previous chapter, the incorporation of viscous damping into rocking models may lead to a significant overestimation of the energy dissipated in the uplifted state [30, 32, 44]. In order to address this shortcoming, the variable damping ratio described in Section 5.2.3 is also introduced in the numerical model. Inherent structural damping during the full contact phase is modelled using Rayleigh's classical damping, assigning a prescribed damping ratio, ξ_{fc}, to the first and third vibration modes of the fixed base structure [9] representing at least 90% of the modal mass in the full-contact case. Once the base uplifts, the analysis is halted and the damping ratio is adjusted before continuing so that the resultant uplifted motion agrees with experimental observations. Truniger et al. [32] conducted a series of tests on single-mass oscillators and observed an uplifted damping ratio of the same order of magnitude as the fixed-base value. Moreover, the analytical analyses presented in Section 5.2.3 showed that, for low damping levels, the uplifted damping ratio does not significantly affect the peak rocking and deformation responses. In light of the above, a conservative assumption of no damping during the rocking phase is adopted in this study ($\xi_{up} = 0$).

Energy loss during impact is incorporated by taking into account the energy radiated into the underlying ground. Accordingly, the structure is assumed to rest on a rectangular rigid foundation of length $2B$ and width e, while the soil underneath is represented by a set of vertical, horizontal and rotational springs and dashpots whose mechanical properties are

determined according to machine vibration theory [147]:

$$K_v = \frac{4\,\rho\,V_s^2\,R_0}{1-\nu}\,J_v\Big(\frac{B}{e}\Big), \qquad K_h = \frac{8\,\rho\,V_s^2\,R_0}{2-\nu}\,J_h\Big(\frac{B}{e}\Big), \qquad K_r = \frac{8\,\rho\,V_s^2\,R_0^3}{3(1-\nu)}\,J_r\Big(\frac{B}{e}\Big) \tag{6.3}$$

and

$$\xi_v = \frac{0.425}{\sqrt{\overline{m}_v}}, \qquad \xi_h = \frac{0.29}{\sqrt{\overline{m}_h}}, \qquad \xi_r = 0 \tag{6.4}$$

with

$$\overline{m}_v = \frac{m_t(1-\nu)}{4\rho R_0^3}, \qquad \overline{m}_h = \frac{m_t(2-\nu)}{8\rho R_0^3} \tag{6.5}$$

where m_t is the effective mass of the system, R_0 is the equivalent circular radius of the foundation [147], $J(B/e)$ is the shape correction factor given in [147–149], and ρ, ν and V_s correspond to the density, Poisson's ratio , and shear wave velocity of the supporting soil, respectively. The damping coefficients are then obtained from the damping ratio as $C = 2\xi\sqrt{K m_t}$, where K and ξ are defined in Equations 6.3 and 6.4. It should be noted that while the damping ratio depends on the assumed effective mass of the system, m_t, the damping coefficients used to model the underlying ground depend only on the properties of the soil. On the other hand, Vassiliou et al. [88] demonstrated that the adopted model is not sensitive to the value of the damping coefficient, as long as the properties of the underlying ground correspond to stiff soils or rock. Consequently, the mechanical properties of the soil model are obtained considering $V_s = 1000\,[m/s]$, $\rho = 2\,[ton/m^3]$ and $\nu = 0.3$.

It is well known from machine vibration theory that the spring stiffness and damping coefficients that represent the elastic halfspace under the foundation depend on the frequency of the excitation. Moreover, it has been demonstrated that the dynamic modifications factors, k and c, are a function of the dimensionless frequency factor $\alpha_0 = 2\pi f B/V_s$ [147]. Crucially, if stiff soils are considered, this parameter remains reasonably small for the range of frequencies relevant for the impact phenomenon. For example, for a foundation of $B = 1\,[m]$ and a soil of $V_s = 1000\,[m/s]$, α_0 remains lower than 0.2 for frequencies of up to 30[Hz]. The results for rectangular foundations presented in [147] show that the dynamic modification factors $k_v \approx k_h \approx k_r \approx 1$ for this range of α_0 values, thus justifying the adoption of the constant static stiffness presented in Equation 6.3. Similarly, the damping factors remain reasonably constant for the relevant excitation frequencies.

6.2.2.1 Validation of the structural model

The structural model described in the previous section is implemented in the open-source finite element framework OpenSees [10] and validated against experimental data published in [32]. Newmark's integration method was used considering a constant time step dt. Convergence of the base rotation and elastic deformation response histories was assessed for different time steps, concluding that a $dt = 10^{-4}[s]$ yields reasonable accuracy within practical computation times. Four single-mass rocking oscillators of natural frequencies ranging from 1[Hz] to 4[Hz] are selected for the validation process. In order to accurately represent the experimental specimens, a uniformly distributed mass was assigned to the column elements of the model, whereas a lumped mass and rotational inertia were defined at the base node. The properties of the structures are summarized in Table 6.1. For further details about the specimens and the experimental program, the reader is referred to [32].

Specimen	f_{fix} $[Hz]$	ξ [%]	α $[rad]$	p $[Hz]$
1 Hz Short Base	1.00	0.16	0.081	3.24
2 Hz Long Base	2.07	0.28	0.160	3.23
3 Hz Short Base	3.12	0.35	0.081	3.25
4 Hz Long Base	3.84	1.32	0.081	3.24

Table 6.1: Description of the single-mass rocking specimens selected for the validation process (Truniger et al. [32]).

Figure 6.2 presents the predicted base rotation responses and elastic deformations at the top of the specimens obtained with the numerical model and compares them with the experimental and analytical results obtained by Truniger et al. [32]. One of the main difficulties in the prediction of rocking time history responses is related to the fact that small errors in the rotation amplitude can lead to accumulative errors in the phase. This has been acknowledged in [32] and can be clearly observed in the response of the 1[Hz], 3[Hz] and 4[Hz] specimens. Nevertheless, very good agreement is observed in the amplitude of the base rotation for the whole range of flexibilities under consideration. On the other hand, accurate predictions of the maximum elastic deformation response are also obtained for the more flexible oscillators. However, results show that both the numerical and analytical [32] models tend to overestimate the elastic deformation as the structures become more rigid.

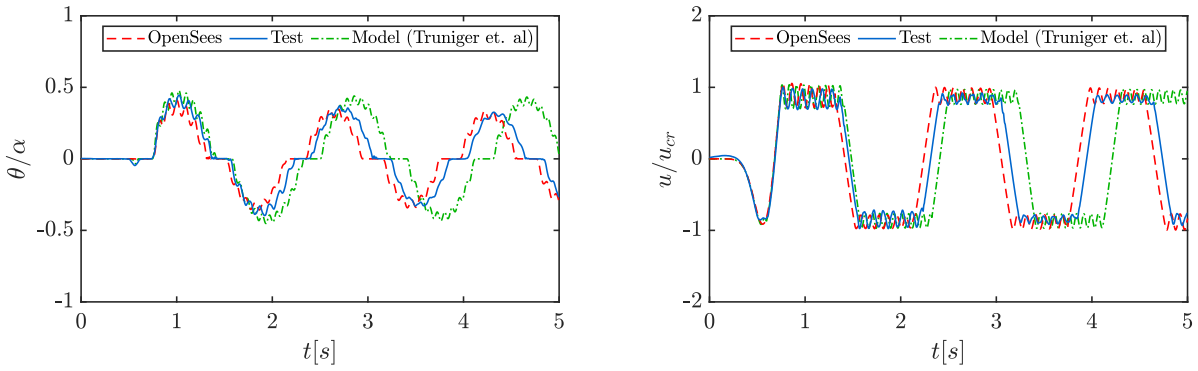

(a) 1 [Hz] Short Base (Test 10)

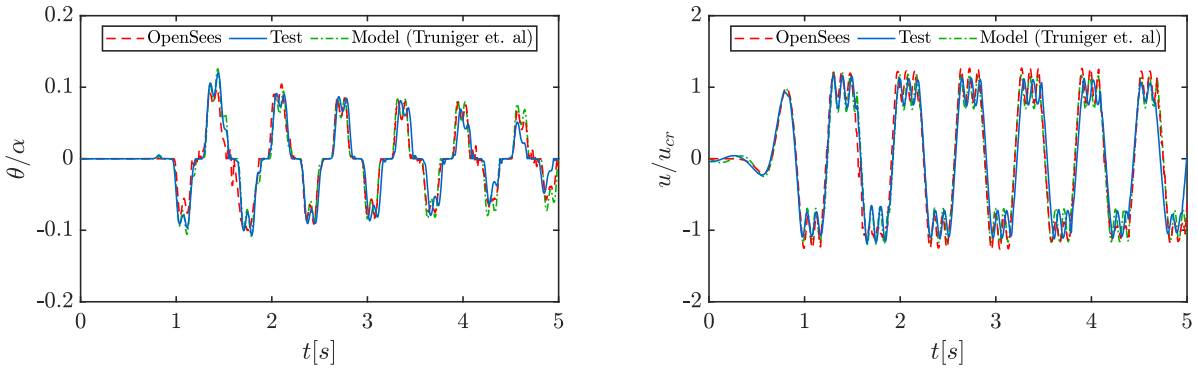

(b) 2 [Hz] Long Base (Test 14)

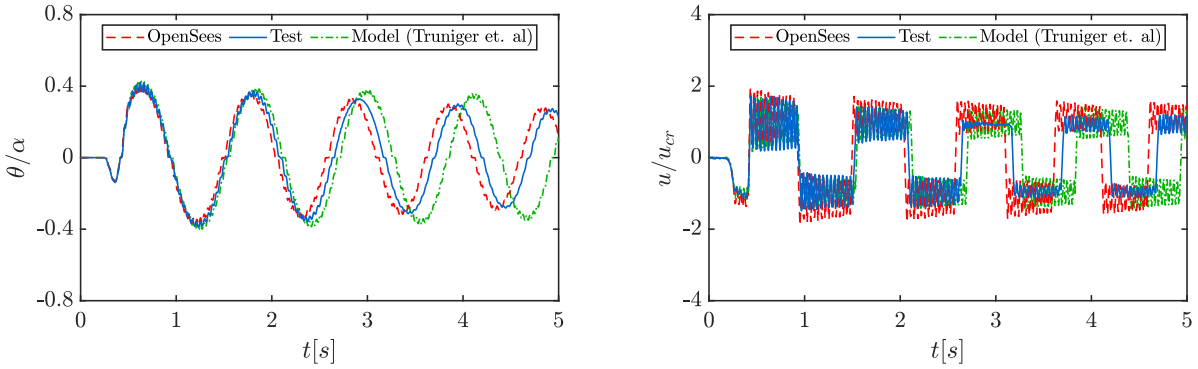

(c) 3 [Hz] Short Base (Test 47)

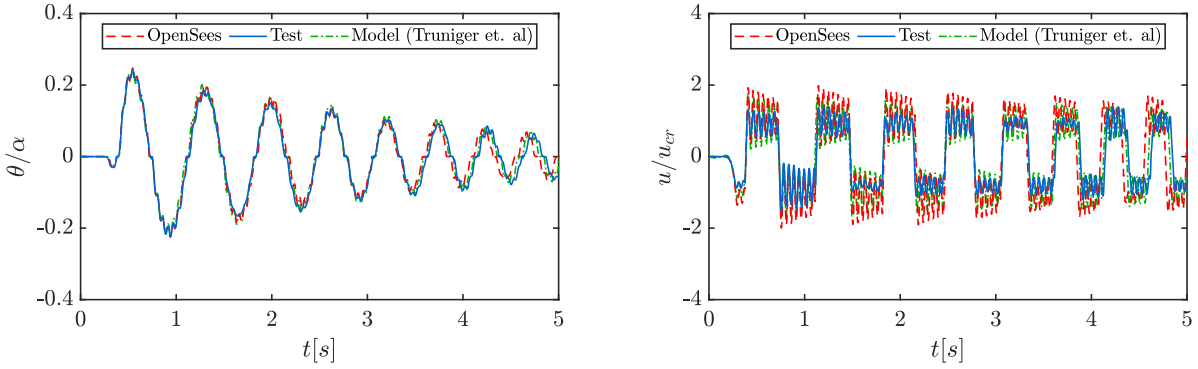

(d) 4 [Hz] Long Base (Test 52)

Figure 6.2: Comparison of the OpenSees numerical model with experimental and analytical results from Truniger et al.

6.2.3 Numerical model of the inerter and clutch

The numerical model of the inerter is schematized in Figure 6.3 and consists of two nodes connected through a rigid link, and an angular mass, J, assigned to the rotational degree of freedom at Node 1. In this way, the relative lateral displacement between the nodes is transformed into a rotation in Node 1.

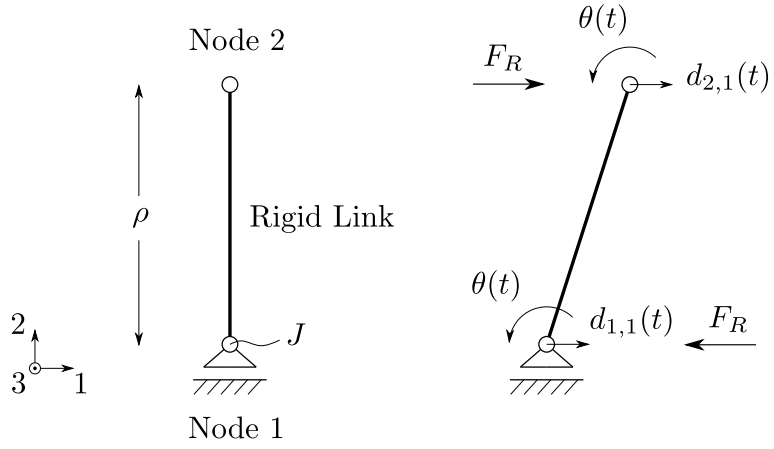

Figure 6.3: Schematic diagram of the numerical model of the inerter

Since a linear geometric transformation is considered for the link element, the relative displacement and rotation of the system are related according to:

$$d_r = d_{2,1}(t) - d_{1,1}(t) = -\rho\theta \tag{6.6}$$

The force couple required to impose this relative displacement, $F_R(t)$, can then be obtained evaluating the rotational equilibrium about Node 1:

$$F_R(t) = \frac{J\ \ddot{d}_r(t)}{\rho^2} = m_r\ \ddot{d}_r(t) \tag{6.7}$$

Therefore the reactive force developed by the model is proportional to the horizontal relative acceleration between Nodes 1 and 2. The parameters of the model, J and ρ, are then defined in terms of the inertance, m_r, according to Equation 6.7.

When the structure-inerter system is subjected to a ground excitation, part of the energy is transferred to the inerter and accumulated as angular momentum. As the translating mass of the structure slows down, the rotating flywheels might drive the mass and induce undesirable deformations. As mentioned before, Makris et al. [95] proposed the use of a clutch mechanism in order to ensure the system can only resist the motion of the structure. As conventional clutches can only act in one direction of motion, a parallel pair of inerters is necessary for this configuration. Additionally, a dissipative mechanism may be needed to decelerate the flywheels once disengaged [95,104]. The sequential engagement of the two parallel inerters can

be modelled mathematically through a redefinition of the inertance, m_r, after each time step according to:

$$F_R(t) = \begin{cases} m_r\ \ddot{d}_r, & \left[\frac{\ddot{d}_r}{\dot{d}_r}\right] > 0 \\ \\ 0, & \left[\frac{\ddot{d}_r}{\dot{d}_r}\right] < 0 \end{cases} \tag{6.8}$$

This formulation can be easily implemented in a TCL script as shown in Listing 6.1.

Listing 6.1: TCL script for simulating the transmission in the clutch mechanism in OpenSees

```
for {set i 1} {$i <= $Nsteps} {incr i} {
  set ok [analyze 1 $DtAnalysis];
  set Acc_i [expr [nodeAccel $top_node 1]];
  set Vel_i [expr [nodeVel   $top_node 1]];
  set ver [expr $Acc_i/$Vel_i];

  if {$ver>=0} {
    set aux 1.;
  } else {
    set aux 0.;
  }
  mass $bottom_node $Mass $Mass [expr $J*$aux];
}
```

6.2.3.1 Validation of the inerter model

The proposed numerical model was implemented in OpenSees [10] and validated against the analytical model developed by Makris et al [95]. The responses obtained with the numerical model and the corresponding solution of the equation of motion for a fixed-base SDOF structure of period $T = 1[s]$ and $\sigma = 0.5$, subjected to a single sinusoidal pulse, are presented in Figure 6.4.

Excellent agreement between the two models is observed in all the plots shown in Figure 6.4. Moreover, the modelling strategy presented in this section has been subsequently validated against experimental results by Málaga-Chuquitaype et al. [105].

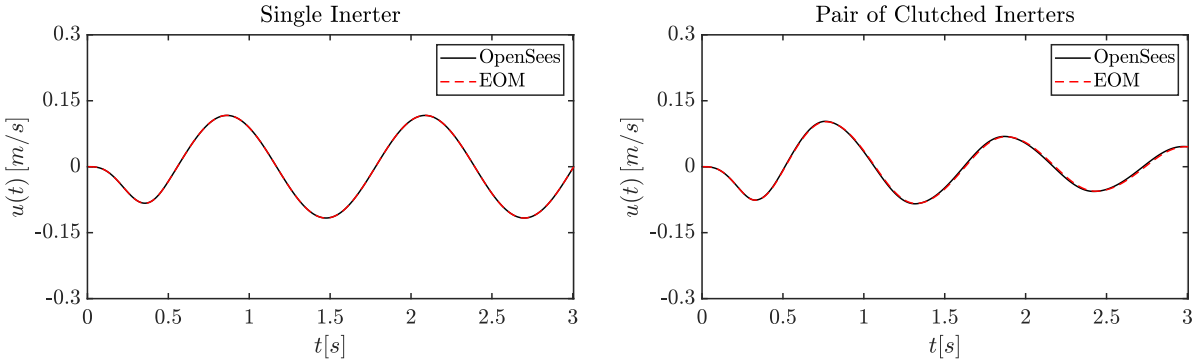

(a) Displacement response.

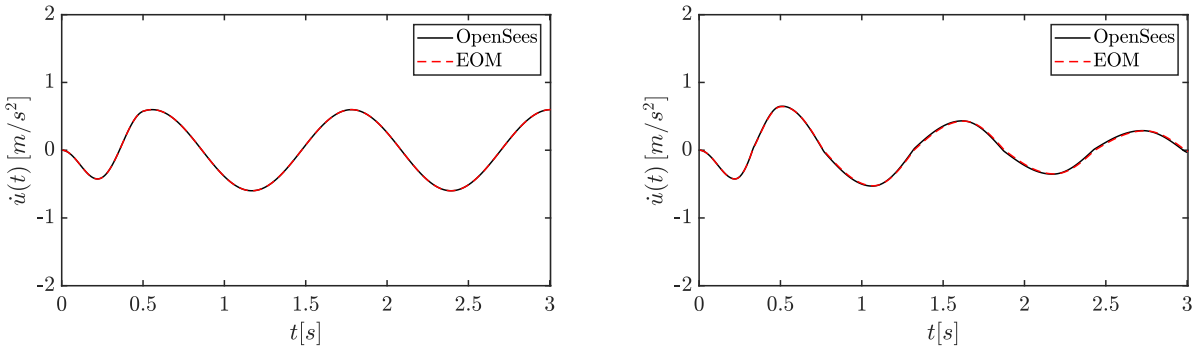

(b) Velocity response.

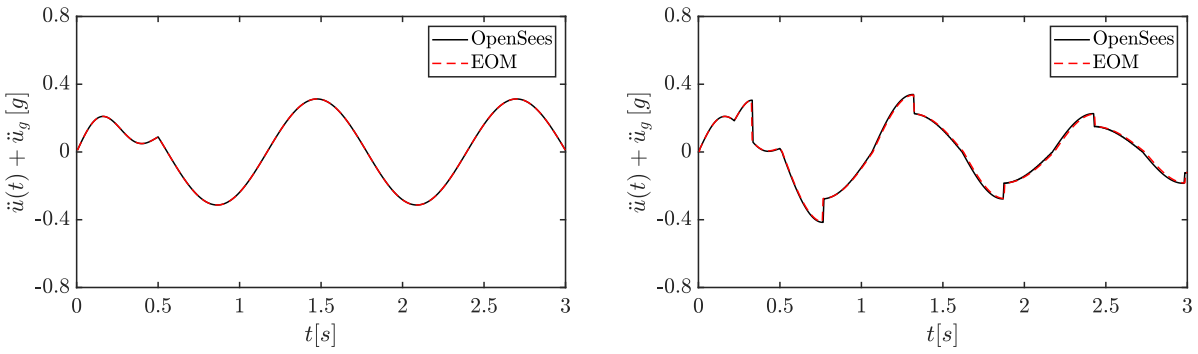

(c) Absolute acceleration response.

Figure 6.4: Comparison of the inerter numerical model and the solution of the equation of motion for a SDOF structure equipped with inerters of $\sigma = 0.5$, subjected to a single sine pulse of $T_0/T_g = 2$ and acceleration amplitue $a_g = 0.5\,[g]$.

6.2.4 Validation of the rocking structure-inerter model

In light of the dearth of available experimental results on multi-mass rocking systems equipped with grounded inerters, the numerical models described in the previous sections are combined and compared with the analytical model for single-mass rocking structures with inerters developed in Chapter 5. This formulation considers large rotations for the base and small deformations for the oscillator. The numerical model, on the other hand, considers a corrotational transformation for the rocking body. In order to make both formulations comparable, the natural frequency of the OpenSees model is obtained considering P-Δ effects in the lateral stiffness of the system.

$$\omega_{n,OS} = \sqrt{\frac{3EI/h^3 - N/h}{m}} \tag{6.9}$$

Figure 6.5 compares the responses obtained for three structures of different flexibility levels and apparent mass ratios, subjected to single sine pulses of frequency ω_g and acceleration amplitude a_g.

Excellent agreement between the two models is observed for the stiffer structures equipped with both single and clutched inerters. However, some small differences emerge in the amplitude of the rotation and elastic deformation responses as the oscillators become more flexible. These differences are partially explained by the variation of the axial load on the flexible column, N, during the rocking motion which alters the lateral stiffness of the oscillator in the numerical model, an effect that becomes more significant in more flexible structures.

6.3 Base rotation and elastic deformation demands

A first assessment of the potential benefits of employing inerters for the seismic control of multi-mass rocking structures is presented in this section by considering the response of a set of oscillators to a wide range of cycloidal pulses. These analytical excitations have been shown to adequately describe the fundamental impulsive characteristics of realistic pulse-like ground motions [142], which can be particularly demanding for rocking structures [140, 141].

Figure 6.6 compares the response histories of structures representative of a 3-storey walled rocking system, with and without inerters, when subjected to a single sine pulse of frequency $\omega_g/\omega_{n1} = 0.6$ and acceleration amplitude $a_g = 3g\tan\alpha_{cg}$, where ω_{n1} is the fundamental frequency of the structures. The response of the buildings is examined in terms of the base rotation, θ, and the elastic deformations at the different mass levels, u_i. The geometry and stiffness of the structures is characterized by their frequency parameter, $p_n = 1.17\,[Hz]$, the slenderness of the centre of gravity, $\alpha_{cg} = 0.165$, and the frequency of the first mode of vibration, $\omega_{n1} = 40.95\,[rad/s]$ (or $T_{n1} = 0.15\,[s]$). These values correspond to a rocking wall of dimensions $2B = 2\,[m]$ by $H = 9\,[m]$. A damping ratio of $\xi_{fc} = 0.01$ is considered for the full contact phase, while no viscous damping is assigned to the uplifted phase of the

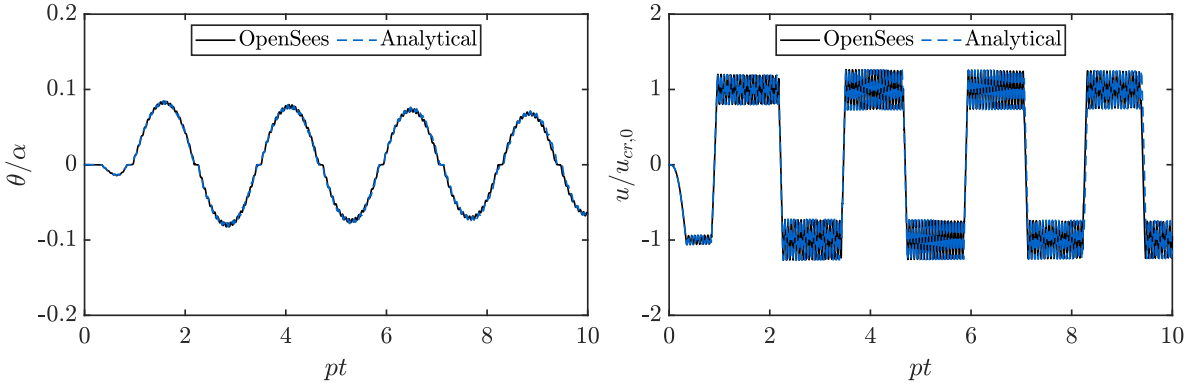

(a) $\omega_n/p = 10$, $\omega_g/p = 5$, $a_g = g\tan\alpha$, $\alpha = 0.1$, $\xi_{fc} = 0.01$, $\xi_{up} = 0$ and $\sigma = 1$ (single inerter).

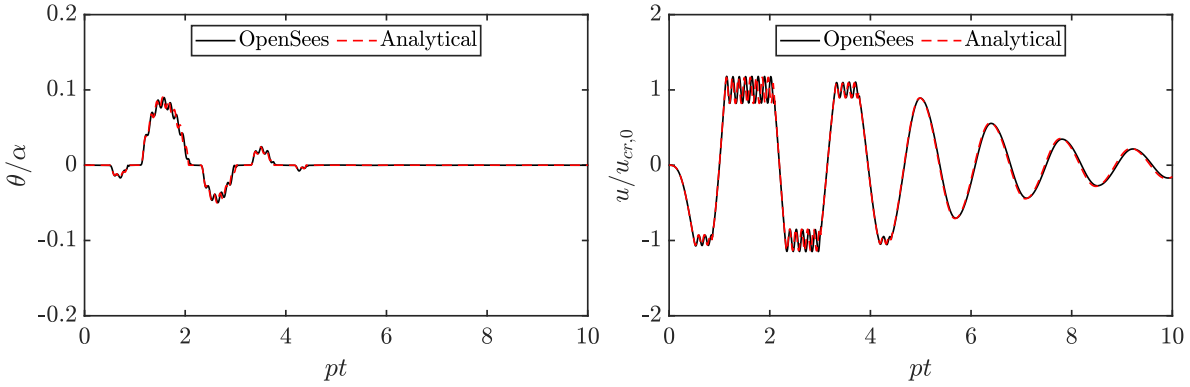

(b) $\omega_n/p = 5$, $\omega_g/p = 5$, $a_g = g\tan\alpha$, $\alpha = 0.1$, $\xi_{fc} = 0.01$, $\xi_{up} = 0$ and $\sigma = 0.5$ (pair of clutched inerters).

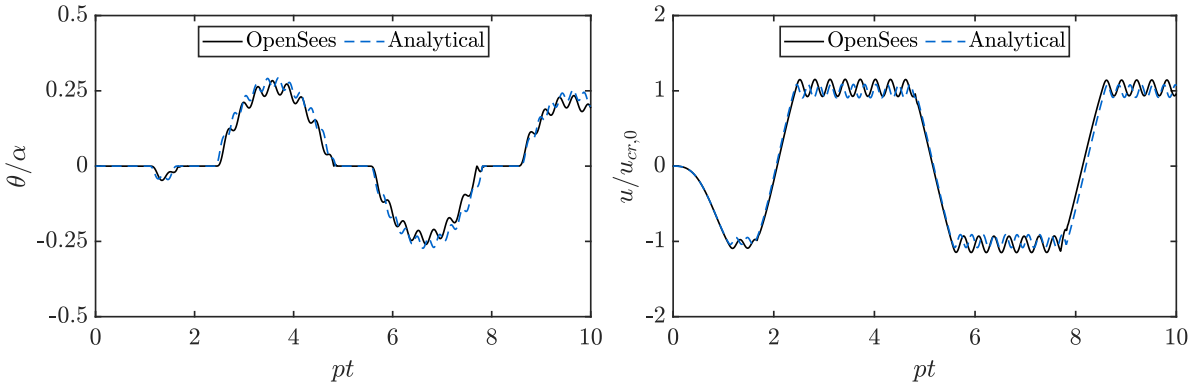

(c) $\omega_n/p = 2$, $\omega_g/p = 3$, $a_g = g\tan\alpha$, $\alpha = 0.1$, $\xi_{fc} = 0.01$, $\xi_{up} = 0$ and $\sigma = 0.5$ (single inerter).

Figure 6.5: Comparison of the numerical (OpenSees) and analytical models for rocking structures equipped with inerters.

response ($\xi_{up} = 0$) as discussed above. Finally, an apparent mass ratio of $\sigma = 1$ is used for the inerter-equipped structures. The response of a fixed-base bare structure is also included for comparison purposes.

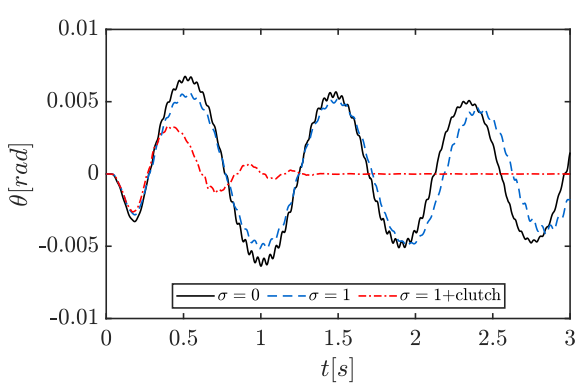

(a) Base rotation.

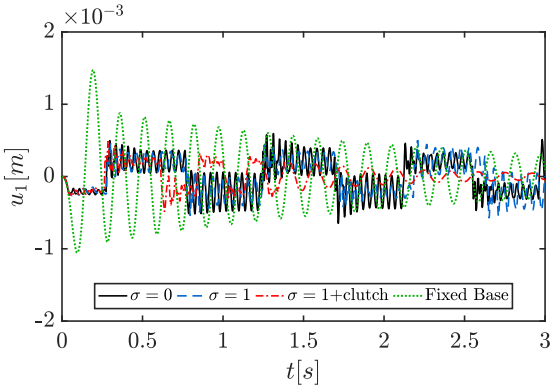

(b) Elastic deformation level 1.

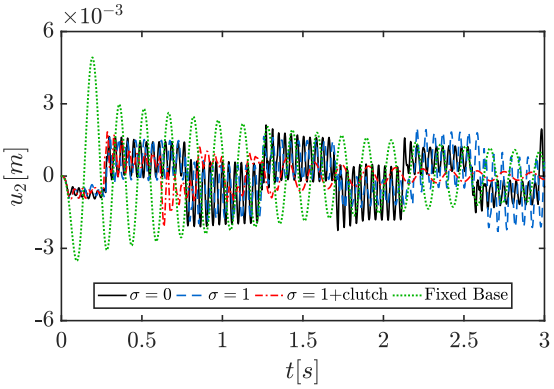

(c) Elastic deformation level 2.

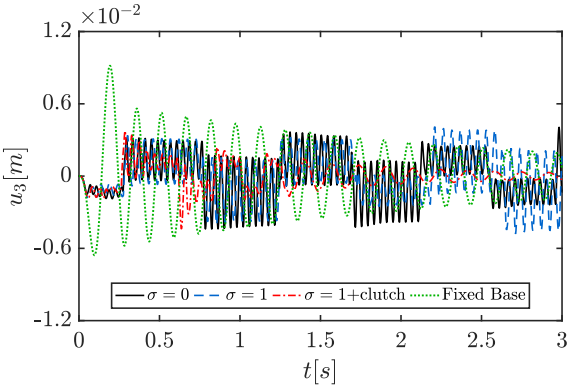

(d) Elastic deformation level 3.

Figure 6.6: Response of 3-storey rocking structures of $p_n = 1.17\,[Hz]$, $T_{n1} = 0.15\,[s]$, $\alpha_{cg} = 0.165$ and $\xi_{fc} = 0.01$, with and without inerters, to a sine pulse of frequency $\omega_g/\omega_{n1} = 0.6$ and acceleration amplitude $a_g = 3g \tan \alpha_{cg}$.

Figure 6.6 shows that, although the inclusion of the single inerter reduces the maximum base rotation, it can also cause slight increases in the amplitude of the elastic deformations of higher storeys with respect to the non-inerter case ($\sigma = 0$). This detrimental outcome stems from the backstay effect caused by the connection of the inerter in the first level, as it will be seen later in Section 6.5. Nevertheless, in all three storeys the peak deformation remains considerably smaller than in the fixed base case. The introduction of the clutch, on the other hand, significantly improves the efficiency of the inerter in reducing the rotation response, although it does not translate into a significant alteration of the amplitude of the structural deformations.

The response spectra presented in Figures 6.7, 6.8 and 6.9 extend the previous analyses to a wider range of pulse frequencies and rocking structures. Figure 6.7 summarizes the response of the same 3-storey systems described above to single sine pulses of varying frequency and

acceleration amplitude $a_g = 3g\tan\alpha_{cg}$, while Figure 6.8 presents the maximum response of 6-level structures of $p_n = 0.86\,[Hz]$, $\alpha_{cg} = 0.142$, and $\omega_{n1} = 21.54\,[rad/s]$ (or $T_{n1} = 0.3\,[s]$). These parameters represent a 6-storey rocking wall of dimensions $2B = 3\,[m]$ by $H = 18\,[m]$. Finally, Figure 6.9 describes the maximum response of 9-level structures of $p_n = 0.72\,[Hz]$, $\alpha_{cg} = 0.1$, and $\omega_{n1} = 14.4\,[rad/s]$ (or $T_{n1} = 0.45\,[s]$) subjected to the same acceleration pulses. This last set of parameters correspond to a 9-storey rocking structure of dimensions $2B = 3\,[m]$ by $H = 27\,[m]$.

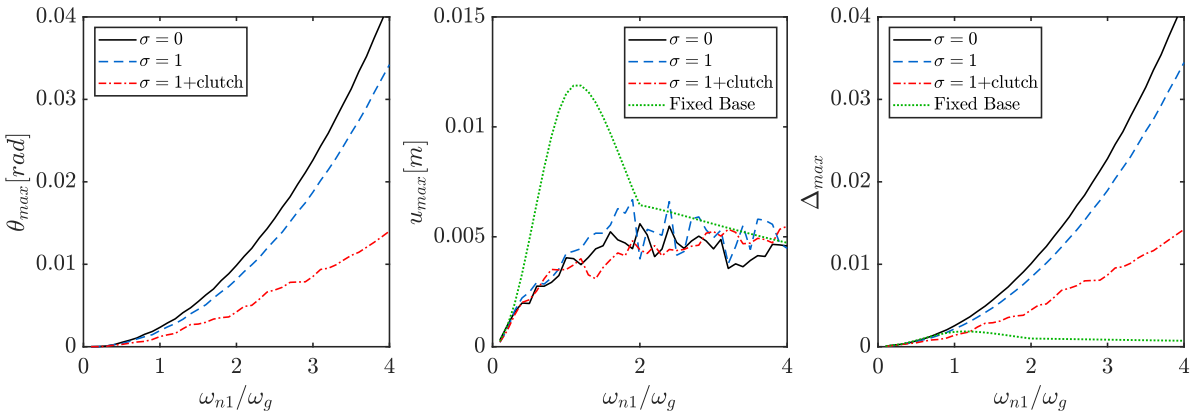

(a) Base rotation. (b) Elastic deformation. (c) Inter-storey drift.

Figure 6.7: Response spectra for 3-storey rocking structures of $p_n = 1.17\,[Hz]$, $T_{n1} = 0.15\,[s]$, $\alpha_{cg} = 0.165$ and $\xi_{fc} = 0.01$, with and without inerters, subjected to sine pulses of acceleration amplitude $a_g = 3\tan\alpha_{cg}$.

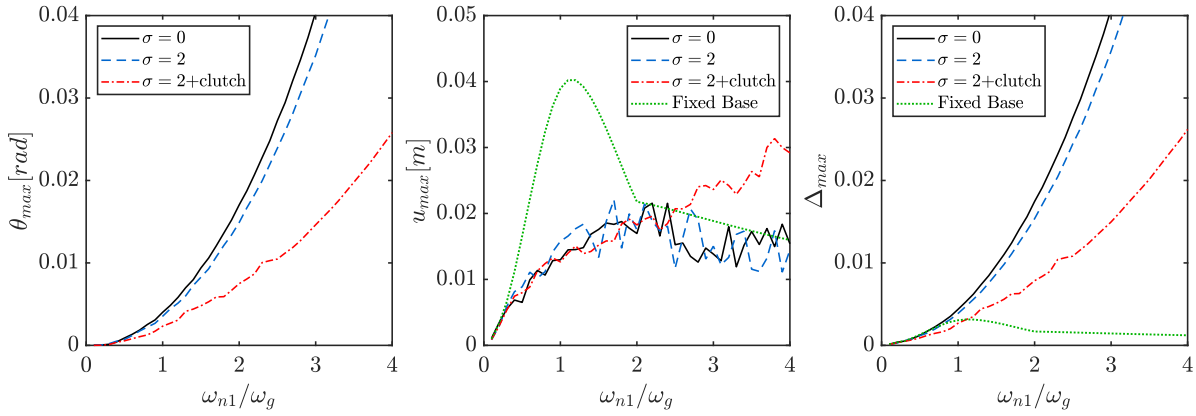

(a) Base rotation. (b) Elastic deformation. (c) Inter-storey drift.

Figure 6.8: Response spectra for 6-storey rocking structures of $p_n = 0.86\,[Hz]$, $T_{n1} = 0.3\,[s]$, $\alpha_{cg} = 0.142$ and $\xi_{fc} = 0.01$, with and without inerters, subjected to sine pulses of acceleration amplitude $a_g = 3\tan\alpha_{cg}$.

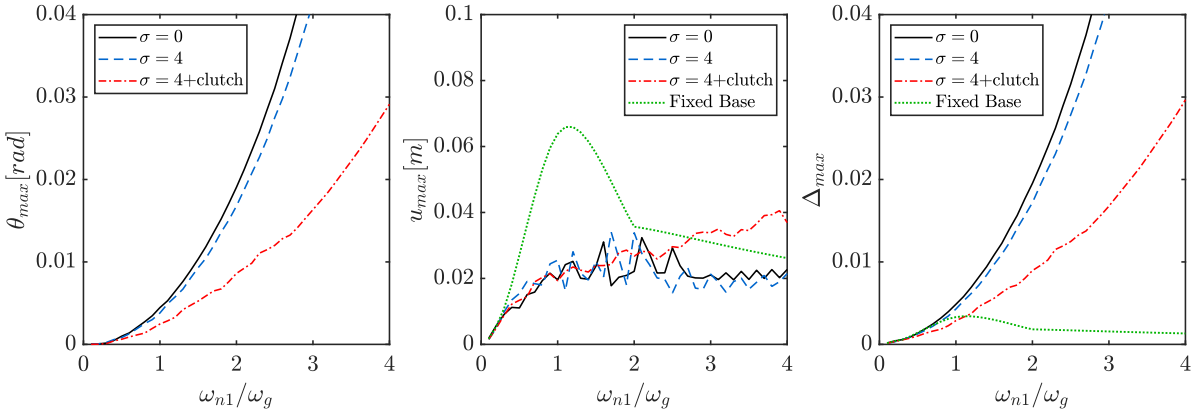

(a) Base rotation. (b) Elastic deformation. (c) Inter-storey drift.

Figure 6.9: Response spectra for 9-storey rocking structures of $p_n = 0.72\,[Hz]$, $T_{n1} = 0.45\,[s]$, $\alpha_{cg} = 0.1$ and $\xi_{fc} = 0.01$, with and without inerters, subjected to sine pulses of acceleration amplitude $a_g = 3\tan\alpha_{cg}$.

In all three cases, the addition of the inerter has very little effect on the rotation and elastic deformation responses for high frequency excitations ($\omega_{n1}/\omega_g < 1$). As the duration of the pulses increases, the rotation demands grow and the effect of the single inerter becomes more significant, reaching reductions between 15% and 20% in the peak rotations of the three structures for $\omega_{n1}/\omega_g > 3$. Although this improvement happens at the expense of inducing slightly larger elastic deformations, this drawback does not translate into higher drifts, since the total lateral deformation is mainly controlled by the base rotation. Likewise, the horizontal motion of the point of connection of the inerter is governed by the rocking action. Consequently, when the clutch is introduced, the disengagement condition defined in Equation 6.8 ensures that the inerter only opposes the rocking motion of the system, hence reducing the rotation amplitudes even further. However, these engagement-disengagement cycles can happen at unfavourable times with respect to the elastic deformations, causing the inerter to arbitrarily oppose and drive the deformation response. This results in the increased elastic deformations observed for the structures equipped with a pair of clutched inerters. It is also important to note that, as the structures become taller, higher levels of inertances are required to obtain similar levels of response suppression. However, the actual mass of the inerter can be reduced thousands of times using amplification mechanisms such as ball-screws [7] or gear systems [6].

6.4 Impact and acceleration demands

In the numerical model presented above, impact is modelled as a vertical contact force which quickly changes the rotational and linear velocities of the system, $\dot{\theta}$ and $\dot{u}$, thus dissipating energy and inducing large accelerations in the oscillator. In this case, variations in the magnitude of the vertical force at the pivot point, F_0, ensure conservation of angular momentum during impact. A simplified representation of this formulation is shown in Figure 6.10, where

a rectangular pulse function is used to represent the impulsive nature of impact on a rocking SDOF oscillator connected to a grounded inerter.

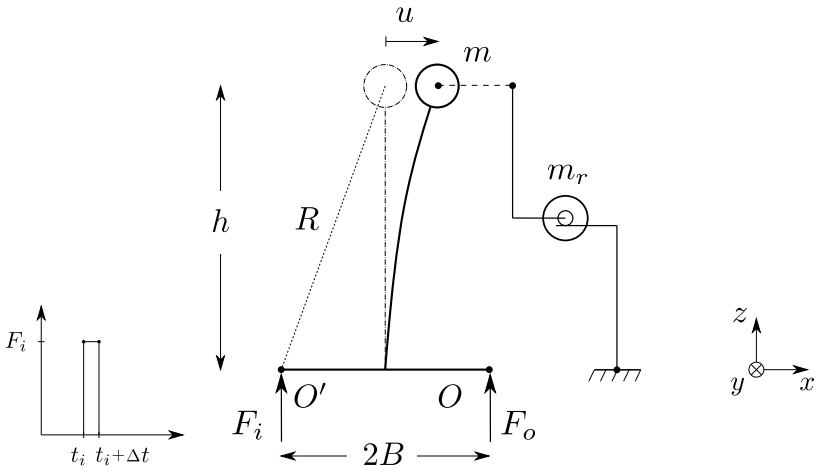

Figure 6.10: Impact force in a SDOF oscillator.

At $t = t_i$, a short duration high amplitude force acts on the impacting corner of the base. Assuming that the amplitudes of the displacement and rotation responses are small, the equations that describe the motion of the system for $t_i \leq t \leq t_i + \Delta t$ are:

$$\left(m + m_r\right)\left(\ddot{u} + h\ddot{\theta}\right) + c\dot{u} + ku = 0$$

$$\left(m + m_r\right)h\ddot{u} + mR^2\ddot{\theta} + m_r h^2\ddot{\theta} = \mp mgB \pm 2F_iB$$

Introducing the apparent mass ratio $\sigma = m_r/m$ and rearranging:

$$\left(1 + \sigma\right)\left(\ddot{u} + h\ddot{\theta}\right) + 2\xi\omega_n\dot{u} + \omega_n^2 u = 0 \tag{6.10}$$

$$\left(1 + \sigma\right)\ddot{u} + \left(h\ddot{\theta}\right)\left(\frac{R^2}{h^2} + \sigma\right) = \mp g\frac{B}{h} \pm \frac{2F_iB}{mh} \tag{6.11}$$

where the upper and lower signs represent impact about the left and right corners, respectively. Eliminating $(h\ddot{\theta})$ algebraically from Equation 6.11:

$$\left(1 + \sigma\right)\ddot{u} - \left(\frac{R^2}{h^2} + \sigma\right)\left(\ddot{u} + \frac{2\xi\omega_n}{1+\sigma}\,\dot{u} + \frac{\omega_n^2}{1+\sigma}\,u\right) = \mp g\frac{B}{h} \pm \frac{2F_iB}{mh}$$

and rearranging:

$$\left(1 - \frac{R^2}{h^2}\right)\ddot{u} - \left(\frac{R^2}{h^2} + \sigma\right)\left(\frac{2\xi\omega_n}{1+\sigma}\,\dot{u} + \frac{\omega_n^2}{1+\sigma}\,u\right) = \mp g\frac{B}{h} \pm \frac{2F_iB}{mh}$$

Introducing $R^2 = B^2 + h^2$

$$-\frac{B^2}{h^2}\ddot{u} - \left(\frac{R^2}{h^2} + \sigma\right)\left(\frac{2\xi\omega_n}{1+\sigma}\,\dot{u} + \frac{\omega_n^2}{1+\sigma}\,u\right) = \mp g\frac{B}{h} \pm \frac{2F_iB}{mh}$$

Multiplying by -h^2/B^2:

$$\ddot{u} + \left(\frac{R^2 + h^2\sigma}{B^2(1+\sigma)}\right)\left(2\xi\omega_n\,\dot{u} + \omega_n^2\,u\right) = \pm g\frac{h}{B} \mp \frac{2F_i h}{mB}$$

Similarly, combining Equations 6.10 and 6.11 to eliminate $\ddot{u}$:

$$-\left(1+\sigma\right)h\ddot{\theta} - 2\xi\omega_n\,\dot{u} - \omega_n^2\,u + h\ddot{\theta}\left(\frac{R^2}{h^2} + \sigma\right) = \mp g\frac{B}{h} \pm \frac{2F_i B}{mh}$$

then:

$$\frac{B^2}{h^2}h\ddot{\theta} - 2\xi\omega_n\,\dot{u} - \omega_n^2\,u = \mp g\frac{B}{h} \pm \frac{2F_i B}{mh}$$

Multiplying by h^2/B^2:

$$h\ddot{\theta} = 2\frac{h^2}{B^2}\xi\omega_n\,\dot{u} + \frac{h^2}{B^2}\omega_n^2\,u \mp g\frac{h}{B} \pm \frac{2F_i h}{mB} \tag{6.12}$$

It is reasonable to assume that the duration of impact, Δt, is very small so no significant deformations occur during this time lapse. Then, conservation of momentum immediately before and after impact yields:

$$\Delta\ddot{u} = \mp\frac{2F_i h}{mB} \tag{6.13}$$

$$\Delta\ddot{\theta} = \pm\frac{2F_i}{mB} \tag{6.14}$$

Equations 6.13 and 6.14 show that significant acceleration spikes can develop in the deformation and rotational coordinates. Morever, the inerter does not affect the magnitudes of these demands. On the other hand, the total horizontal acceleration during impact is given by:

$$\Delta\ddot{x} = \Delta\ddot{u} + h\Delta\ddot{\theta} = 0 \tag{6.15}$$

Equation 6.15 implies that there is no change in the total horizontal velocity of a SDOF rocking oscillator during impact, a result that stems from the vertical impulse assumption underlying the model. It is important to note that the same assumptions underline the Vertical Velocity Energy Loss (VVEL) model adopted in several related studies [30, 31, 150]. This is illustrated in Figure 6.11, where the numerically obtained base rotation and horizontal acceleration responses of a single-mass rocking structure of $p = 1[Hz]$, $\omega_n = 15[rad/s]$, $\alpha = 0.2$, $\xi = 0.01$ and $\sigma = 0$, subjected to a sine pulse of $\omega_g/p = 15$ and $a_g = 2g\tan\alpha$ are plotted. Additionally, the temporal evolution of the energy of the system, defined by Equation 6.16, is also presented in Figure 6.11c.

$$E_T = \frac{1}{2}\sum_{i=1}^{n_{levels}} m(\dot{x_i}^2 + \dot{y_i}^2) + \sum_{i=1}^{n_{levels}} mg(y_i - h_i) + \int_0^H \frac{M(y)^2}{2EI}dy + \frac{1}{2}\,m_r\,\dot{x_i}^2 + \frac{1}{2}\,k_{rs}\,y_{rs}^2 \tag{6.16}$$

where $\dot{x}_i$ and $\dot{y}_i$ are the horizontal and vertical velocities of the mass at the ith-level, $M(y)$ corresponds to the bending moment at a height equal to y, and k_{rs} and y_{rs} are the stiffness and vertical deformation of the fibres used to model the rocking surface.

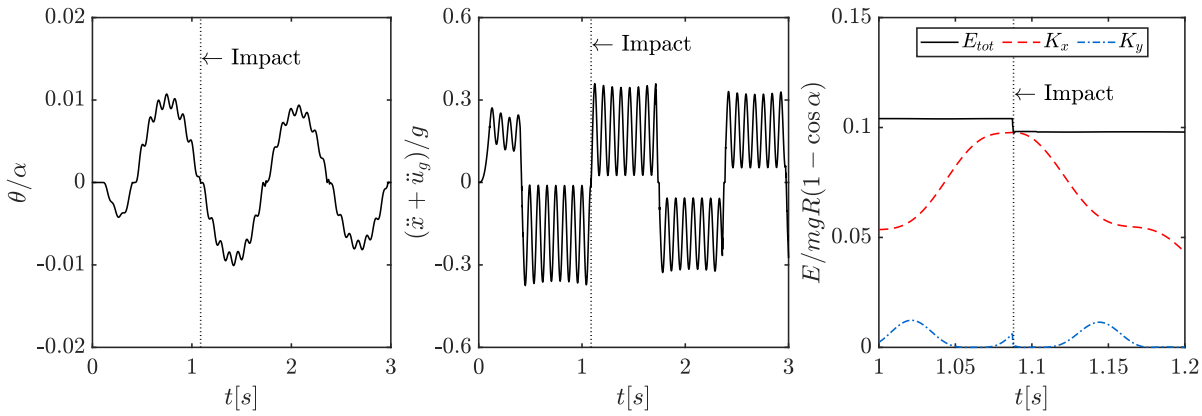

(a) Base rotation. (b) Horizontal abs. acceleration. (c) Energy.

Figure 6.11: Energy dissipation and acceleration response during impact of a single-mass rocking structure of $p = 1[Hz]$, $\omega_n = 15[rad/s]$, $\alpha = 0.2$, $\xi = 0.01$ and $\sigma = 0$, subjected to a sine pulse of $\omega_g/p = 15$ and $a_g = 2g\tan\alpha$.

Figure 6.11c clearly shows that the vertical component of the kinetic energy, K_y, is quickly dissipated at impact, whereas no significant change is observed in the horizontal component, K_x. Accordingly, a smooth horizontal acceleration response is observed in Figure 6.11b, even though sharp changes in the rocking response indicate high rotational acceleration spikes during impact. It is important to note that this is not imposed, but a result of the numerical model adopted in the analysis.

When multi-mass structures are considered, conservation of horizontal kinetic energy during impact does not necessarily ensure a smooth acceleration response, as sudden and opposite changes in the velocity of the masses can generate significant acceleration spikes while keeping the associated energy constant. An example of this is presented in Figure 6.12, where the response of the bare 3-storey structure considered in the previous section to a sine pulse of $\omega_g/\omega_{n1} = 0.3$ and $a_g = 1.5g\tan\alpha_{cg}$ is presented.

Figure 6.12d confirms that the vertical component of the kinetic energy, K_y, is entirely dissipated during impact. Moreover, even though the total horizontal kinetic energy, K_x, remains constant, the individual energies of each mass, $K_{x,i}$, do vary during this time lapse, resulting in the sharp increases in accelerations observed in Figure 6.12c. Interestingly, however, the peak horizontal accelerations happen after impact has ended. The latter observation indicates that the maximum accelerations are not caused by direct action of the impact force, but by the high frequency vibrations induced by it. This interaction between impact and higher modes of the response was also analytically and experimentally identified by Acikgoz and DeJong [34].

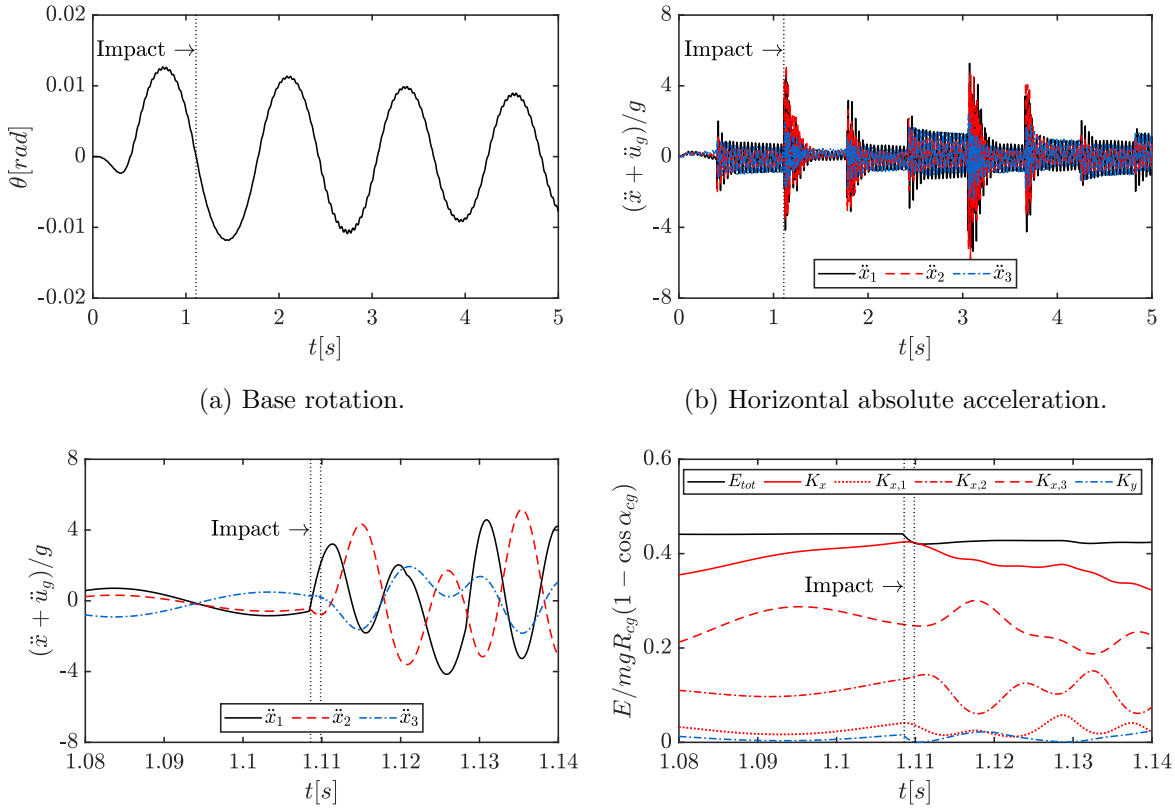

(a) Base rotation.

(b) Horizontal absolute acceleration.

(c) Close-up of the horizontal absolute acceleration.

(d) Energy.

Figure 6.12: Energy dissipation and acceleration response during impact of a 3-storey rocking structure of $p_n = 1.17\,[Hz]$, $T_{n1} = 0.15\,[s]$, $\alpha_{cg} = 0.165$, $\xi_{fc} = 0.01$ and $\sigma = 0$, subjected to a sine pulse of $\omega_g/\omega_{n1} = 0.3$ and $a_g = 1.5g\tan\alpha$.

6.5 Effect of the inerter on the higher-mode response

6.5.1 Floor acceleration demands

The previous section demonstrated that, even when subjected to low frequency pulses, impact forces can excite higher vibration modes of the uplifted system and generate significant acceleration demands. Figure 6.13 shows the first-level acceleration response of the 3-storey structure examined in Figure 6.12. In this case, structures equipped with a single inerter and a pair of clutched inerters have also been included in the plots. Simple inspection of Figure 6.13a reveals that the inerter-equipped structures experience significantly lower acceleration demands. A more detailed view of the response history before and after the second impact (indicated with a vertical dashed line) is presented in Figure 6.13b. It is clear from this plot that the inclusion of the single inerter efficiently controls the amplitude of the high frequency oscillations generated by the impact forces. The implementation of the clutch, on the other hand, undermines the ability of the inerter to control the acceleration demands. According to Equation 6.8, the inerter disengages when the mass at the first floor begins the decelerate

($\ddot{x}_1/\dot{x}_1 < 0$). The sudden disconnection of the inerter (represented as unshaded areas in Figure 6.13b) increases the magnitude of this deceleration, quickly reducing the velocity of the mass and improving the rotation response as a consequence. Nevertheless, the peak acceleration response remains considerably lower than the bare rocking case.

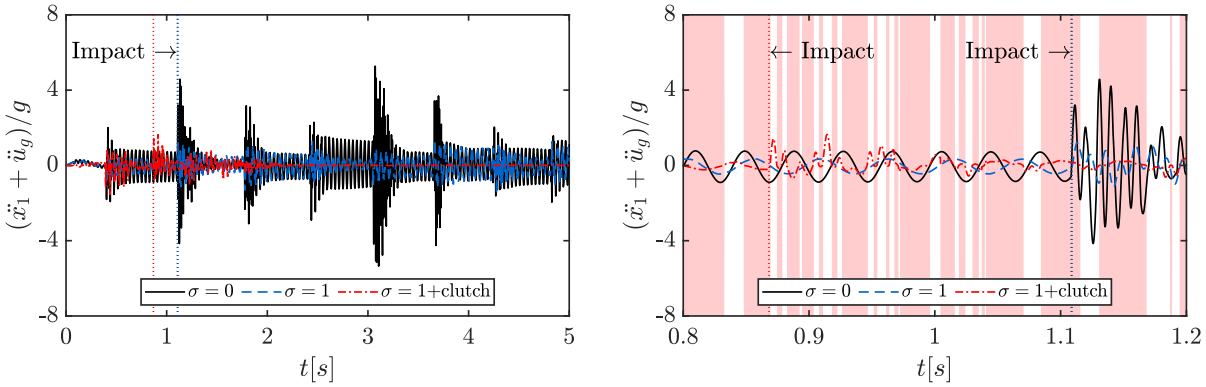

(a) Absolute horizontal acceleration of the first level.

(b) Close-up of the horizontal absolute acceleration.

Figure 6.13: Effect of the inerter on the acceleration demands on the first level of a 3-storey rocking structure of $p_n = 1.17\,[Hz]$, $T_{n1} = 0.15\,[s]$, $\alpha_{cg} = 0.165$, $\xi_{fc} = 0.01$ and $\sigma = 0$, subjected to a sine pulse of $\omega_g/\omega_{n1} = 0.3$ and $a_g = 1.5g\tan\alpha$.

The effect of the inerter on the acceleration demands of the 3, 6 and 9-storey structures described in the previous sections is examined in Figures 6.14, 6.15 and 6.16. The influence of the stiffness of the rocking surface on the peak accelerations and the efficiency of the inerter in controlling them is also assessed in the graphs. Since the foundation is assumed to be rigid, the deformations on the rocking interface are governed by the flexibility of the rocking element material. In order to represent typical construction materials, different elasticity moduli are used in the analysis: Steel (200[GPa]), Concrete (25[GPa]) and Timber (10[GPa]). On the other hand, when a flexible contact zone is considered, uplift occurs gradually, and a higher number of fibres is required to capture the migration of the neutral axis. Accordingly, the number of fibres used to model the contact section in these cases was increased to 2048 [88].

Figures 6.14, 6.15 and 6.16 confirm that structures that undergo rocking motion can experience higher lateral accelerations than their fixed-base counterparts and that those increments are larger for stiffer rocking systems or longer pulses. As shown before, these increased demands are related to high frequency vibrations induced by the impact forces. Moreover, the results summarized in the response spectra show that stockier structures and more rigid rocking surfaces are associated with larger floor accelerations. The inclusion of the inerter consistently reduces these demands, although the introduction of the clutch can offset these improvements to some extent. In very limited cases, however, protected structures subjected to high frequency excitations (or very flexible oscillators) may experience peak accelerations of slightly higher magnitude than the unprotected ones. On the other hand, the relative efficiency of the

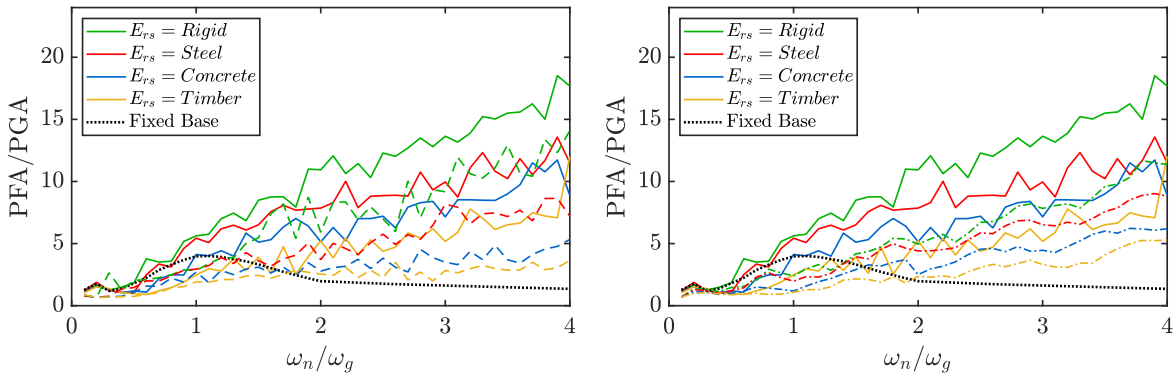

(a) Single inerter. (b) Pair of clutched inerters.

Figure 6.14: Effect of the rocking surface stiffness on the peak floor accelerations in a 3-storey building of $p_n = 1.17\,[Hz]$, $T_{n1} = 0.15\,[s]$, $\alpha_{cg} = 0.165$, $\xi_{fc} = 0.01$ and $a_g = 3g\tan\alpha_{cg}$ with and without inerters (dashed and continue lines, respectively).

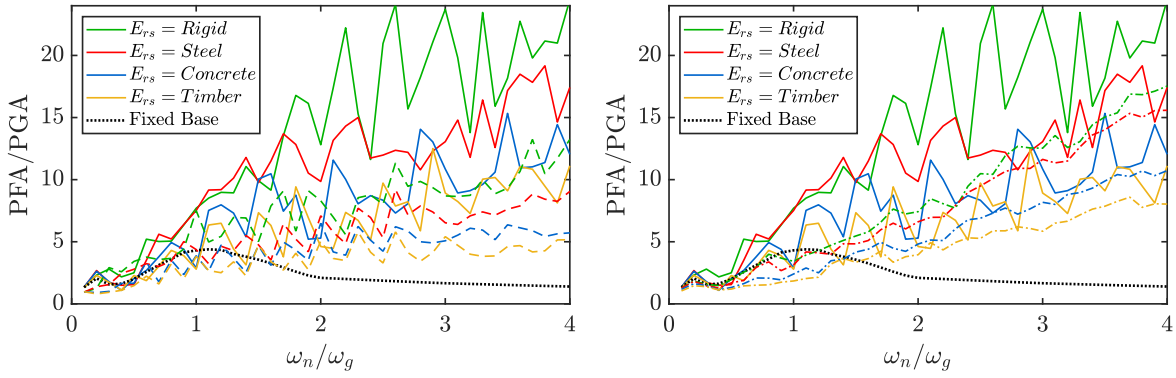

(a) Single inerter. (b) Pair of clutched inerters.

Figure 6.15: Effect of the rocking surface stiffness on the peak floor accelerations in a 6-storey building of $p_n = 0.86\,[Hz]$, $T_{n1} = 0.3\,[s]$, $\alpha_{cg} = 0.142$, $\xi_{fc} = 0.01$ and $a_g = 3g\tan\alpha_{cg}$ with and without inerters (dashed and continue lines, respectively).

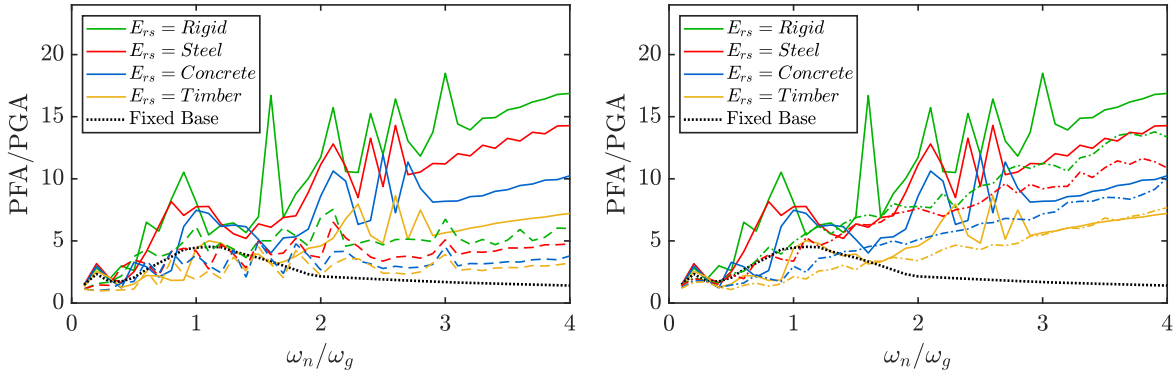

(a) Single inerter. (b) Pair of clutched inerters.

Figure 6.16: Effect of the rocking surface stiffness on the peak floor accelerations in a 9-storey building of $p_n = 0.72\,[Hz]$, $T_{n1} = 0.45\,[s]$, $\alpha_{cg} = 0.1$, $\xi_{fc} = 0.01$ and $a_g = 3g\tan\alpha_{cg}$ with and without inerters (dashed and continue lines, respectively).

inerter in reducing peak floor accelerations is not significantly affected by the flexibility of the rocking surface.

6.5.2 Bending moments distribution

When subjected to lateral excitations, the moment that can develop at the base of a rocking system is limited by the uplift threshold. It is well known, however, that bending moments above the base and shears throughout the structure can increase significantly after base uplift due to the response of higher modes [89,151]. This is further examined with reference to Figure 6.17 which shows the peak responses along the height of the 9-storey structures studied in the previous sections, when subjected to sinusoidal pulses of different frequencies and acceleration amplitude $a_g = 10 \tan \alpha_{cg}$. Firstly, a pulse matching the frequency of the first mode of vibration of the fixed base oscillator, $\omega_g = \omega_{n1}$, is considered in Figure 6.17a. In this case, the total lateral drift is strongly governed by the base rotation, with the elastic deformation contributing only a small percentage of the total horizontal displacement. Examination of the vertical distribution of bending moments reveals that the increase in the structural deformation, u, identified in Section 6.3 is related to the backstay effect caused by the connection of the inerter. The increase in the bending moment at the first floor is also associated with higher shear forces, specially in the clutched inerter case. This is evidenced by the steep slopes of the moment diagram between the base and the first storey in these cases. Importantly, however, these demands remain significantly lower than in the fixed-base structure.

The influence of other modes higher than the first on the response of the bare rocking structure is evident in the envelope of the bending moment diagram, as the highest demands are obtained around the third and fourth levels. Similarly, the approximately uniform distribution of accelerations along the height of the rocking structures indicate that these demands are related to high frequency vibrations associated with impact. The introduction of inerters, on the other hand, helps to control the high frequency response, causing an appreciable reduction of the horizontal acceleration demands and an approximately linear vertical decrease of the bending moments from the critical section at the first level. Once again, the addition of the clutch significantly improves the lateral drift response, although at the expense of reducing the inerter's efficiency to control higher-mode effects.

Figure 6.17b summarizes the response of the same set of structures subjected to high frequency acceleration pulses of $\omega_g = 4\omega_{n1}$. Under this excitation, the rocking structures experience significantly lower rotation demands, while their elastic deformations reach levels comparable to the fixed-base oscillator. The influence of higher modes in the response of the bare structures is clearly evidenced in the bending moments distribution, where values higher than the base moment are observed up to the seventh storey. Similarly, high floor accelerations are obtained along the whole height of the bare rocking building. The inerter-equipped structures, on the other hand, exhibit a linearly decreasing bending moment diagram

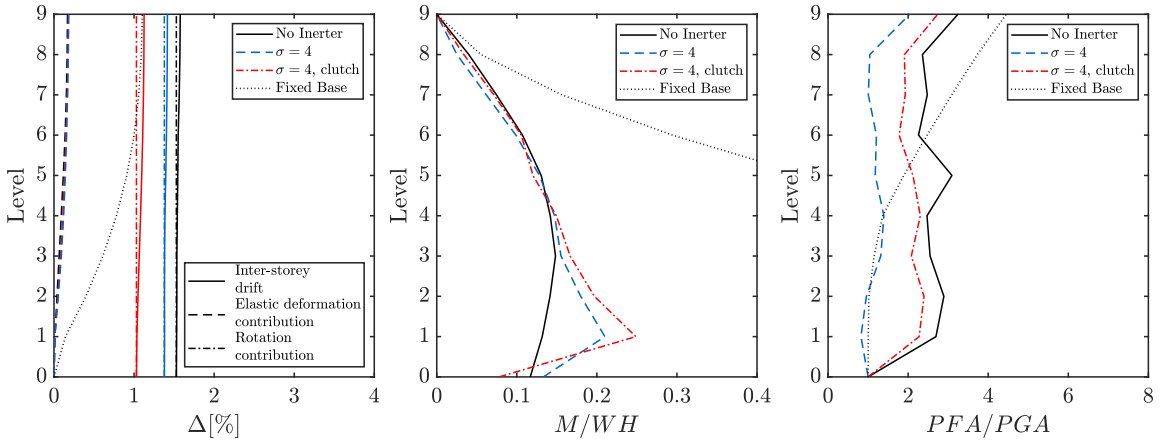

(a) $\omega_g = \omega_{n1}$.

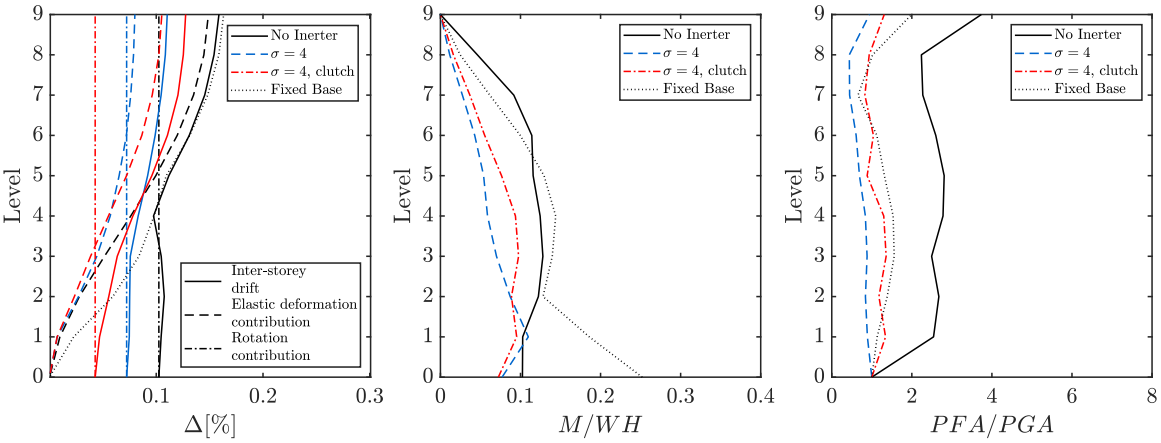

(b) $\omega_g = 4\omega_{n1}$.

Figure 6.17: Effect of higher modes on the response of 9-storey rocking structures of $p_n = 0.72\,[Hz]$, $T_{n1} = 0.45\,[s]$, $\alpha_{cg} = 0.1$ and $\xi_{fc} = 0.01$, with and without inerters, when subjected to sinusoidal pulses of $a_g = 10\tan/\alpha_{cg}$

and significantly lower floor acceleration magnification ratios, indicating an effective control of the higher-mode response.

6.6 Response under real pulse-like ground motions

In order to extend the conclusions obtained in the preceding sections to a wider range of ground motions, the response of bare and inerter-equipped rocking structures to a set of 5 earthquake records is compared and contrasted in Figure 6.18. The structural systems correspond to the same 9-storey rocking structures considered in the previous sections. The same ground motions used in Chapter 5, summarized in Table 5.1, are selected for the analysis. This sub-set contains records with pulses ranging from 1.2[s] to 5.1[s] and peak ground velocities of up to 1.67[m/s]. The listed records were selected in light of their strong coherent and non-coherent components that are able to cause important drift as well as acceleration demands in flexible

uplifting structures.

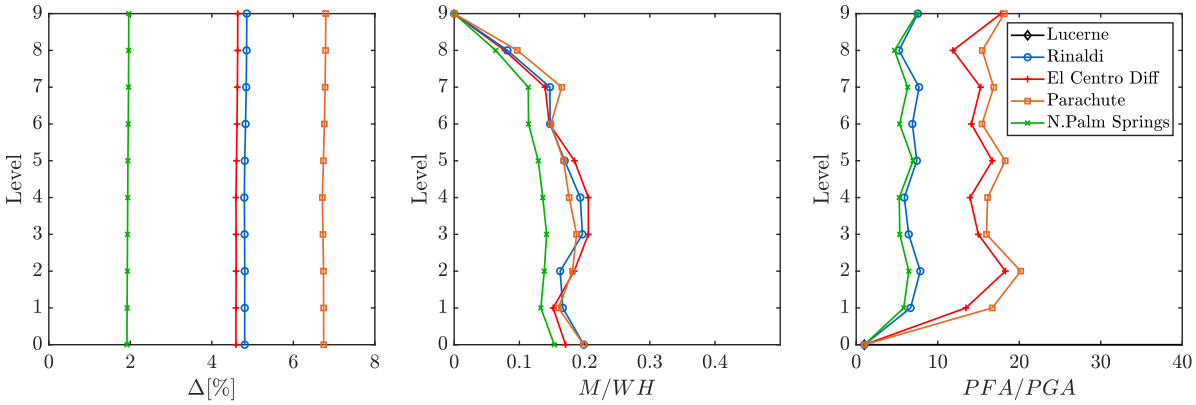

(a) No Inerter.

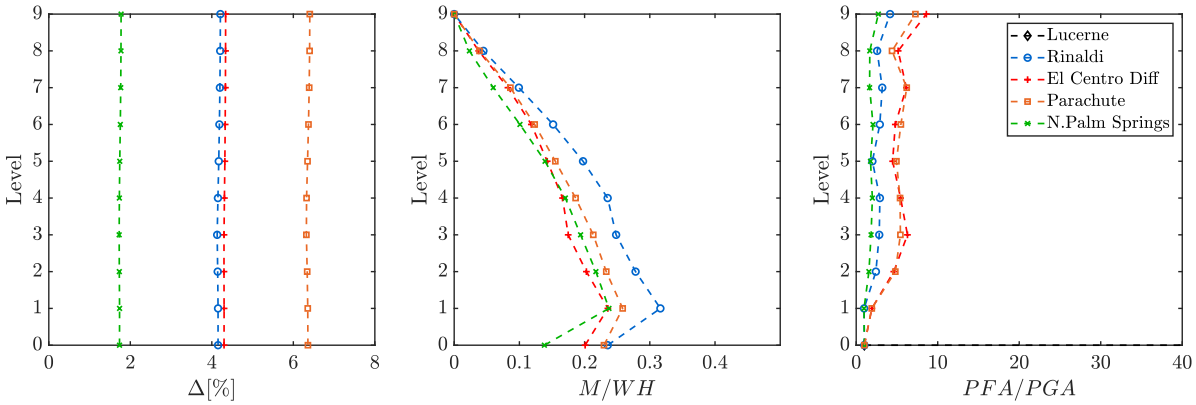

(b) Single Inerter.

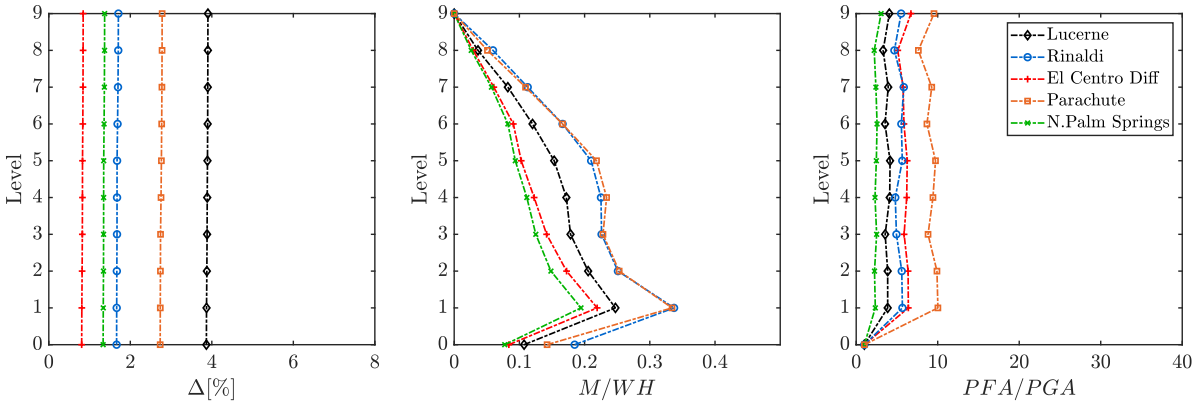

(c) Pair of clutched inerters.

Figure 6.18: Seismic response of 9-storey rocking structures of $p_n = 0.72\,[Hz]$, $T_{n1} = 0.45\,[s]$, $\alpha_{cg} = 0.1$ and $\xi_{fc} = 0.01$, with and without inerters, to the pulse-like ground motion set described in Table 5.1.

The approximately uniform vertical distribution of lateral drifts indicates that the response of the systems is strongly governed by the base rotation. While smaller but appreciable improvements are observed when the single inerter is added, the introduction of the clutch significantly reduces the drift demands. Notably, both the bare and single inerter-equipped

structures topple under the Lucerne 1992 record, whereas the clutched inerter case rocks safely reaching a peak lateral drift of approximately 4%. On the other hand, the effect of higher modes on the response of the bare rocking structure can be clearly identified in the bending moments distribution and the large floor acceleration amplitudes. Although the connection of the single inerter increases the maximum moment at the first level, it also consistently controls higher-mode effects, ensuring that the bending diagrams decrease almost linearly from the critical section. Nevertheless, special attention must be paid to the shear forces that can develop in the first structural level due to the backstay effect caused by the inerter. The effective control of the higher-mode response is also reflected in the significantly lower floor acceleration demands along the whole height of the structure. As it was recognized in previous analyses under cycloidal pulses, the addition of the clutch offsets part of the benefits of the inerter for the control of bending moments and peak floor accelerations. In general, these observations are in agreement with the results presented above for ideal cycloidal pulses and lend confidence to our findings.

6.7 Concluding remarks

The dynamic response of multi-storey rocking structures equipped with inerters at the ground level was investigated in this chapter. Firstly, the finite element model for rocking structures developed by Vassiliou et al. [88] was adapted in order to account for experimental evidence related to the energy dissipated by the rocking oscillator during the uplifted phase. Additionally, this study proposed and validated a new numerical strategy to represent the inerter in finite element frameworks. Both formulations were combined and implemented in OpenSees and the full structure-inerter model was then validated against an analytical model of a single-mass rocking oscillator. Both analytical and numerical formulations showed very good agreement for different levels of flexibility and excitation frequencies. Subsequently, the response of practice-representative multi-mass structures connected to a grounded inerter at the first storey under coherent single-pulse excitations was assessed. It was shown that the incorporation of inerters leads to an appreciable reduction in the base rotation demands, although they can also induce slightly higher elastic deformations due to the backstay effect generated by the connection of the device at the first level. Nevertheless, this potential drawback does not translate into higher drifts as the lateral deformation response is strongly controlled by the base rotations. Similarly, the horizontal motion of the point of connection of the inerter is governed by the rocking action. Thus, if a clutch is introduced, the disengagement condition defined in Equation 6.8 ensures that the inerter can only oppose the rocking motion of the system, hence significantly reducing further the rotation amplitudes. However, with respect to the elastic deformations, the engagement-disengagement cycles happen at inconvenient times, with the inerter arbitrarily opposing and driving the deformation response. As a consequence, the introduction of a clutch can result in increased elastic deformation demands. The results

of the analyses also showed that increasing levels of apparent mass, m_r, are required as the structures become taller. However, the actual mass of the inerter can be reduced by several orders of magnitude by means of amplification mechanisms such as ball-screws or gear systems.

Examination of the equations of motion of a single-mass rocking system during impact, and the numerical results obtained for multi-storey structures provided additional supporting evidence for the Vertical Velocity Energy Loss (VVEL) impact model. Although conservation of horizontal kinetic energy ensures a smooth horizontal acceleration response in single-mass oscillators, sudden and opposite changes in the velocity of the masses can generate significant acceleration spikes in multi-storey structures while keeping the associated energy constant. Close inspection of the temporal evolution of the kinetic energy and acceleration response of multi-mass rocking structures confirmed this observation, although the peak acceleration amplitudes occurred after impact had ended. This indicates that the maximum accelerations are not caused by direct action of the the impact forces, but by the high frequency oscillations induced by them. This interaction between impact and higher modes was also experimentally and analytically identified by Acikgoz and DeJong [47].

The alternative of using inerters to control higher-mode effects on rocking structures was also assessed in this study. Analyses under single pulse excitations showed that the inerter can consistently control the high frequency vibrations generated at impact, significantly reducing the horizontal acceleration demands. Moreover, the efficiency of the inerter was not affected by practical variations of the stiffness of the rocking surface. Likewise, the proposed strategy successfully controlled bending moments along the height of the structures. Although the connection of the inerter increased the moment at the first level, it also ensured an almost linear vertical decrease from the critical section. These results were also observed under high frequency pulse excitations. The introduction of the clutch, however, reduced the ability of the inerter to control the higher-mode response.

Finally, the observations presented above were extended to real ground motions by considering the response of a case of study structure to a set of real pulse-like records. Overall, these observations allow to conclude that single inerters can efficiently control higher-mode effects on flexible rocking structures. The addition of a clutch, on the other hand, significantly improves the drift response of the system, although at the expense of reducing the inerter's ability to control the higher-mode response.

The analyses presented in the previous chapters have considered generalizable models of rocking structures in order to examine the fundamental dynamic behaviour of uplifting structures equipped with inerters. In the following chapter, the conclusions drawn from these analyses are applied to control the seismic response of post-tensioned timber structures.

Chapter 7

Application to post-tensioned rocking timber buildings

7.1 Introduction

As mentioned before in Chapter 2, traditional seismic design methodologies aim to ensure life safety during a design-level earthquake, typically associated with a 10% probability of exceedance in 50 years. Within such frameworks, specific zones are designed to yield and concentrate the majority of the lateral deformations, thus limiting the forces that the structure can experience during an earthquake. As a consequence, structural damage is permitted, and indeed expected, in these critical sections. In the case of timber structures, ductility is usually provided via steel connectors, while timber members are capacity designed in order to ensure that they respond in the elastic range. Although, in general, this design philosophy has succeeded in preventing structural collapse and protecting lives, recent earthquakes have revealed that in many cases the extent of damage can make repairs infeasible, highlighting the mismatch between social expectations and the observed seismic performance of civil structures [152, 153].

Over the last years, performance-based design objectives have shifted towards damage control and continuity of operation after a design-level earthquake. In this context, the advantages of rocking have been applied to the development of a family of self-centring systems that can sustain large lateral deformations with no significant damage. In the case of walled structures, overturning moments are resisted by gravity loads and the vertical post-tensioning usually provided to ensure that the system has a positive post-uplift stiffness. Once the decompression moment is exceeded, a gap begins to open at the base, concentrating most of the rotation demand. Although uplift and the triggering of the rocking motion limit the moment that can develop at the base, it is well known that bending moments and shear forces throughout the structure can increase significantly due to the effects of higher modes, potentially damaging the

structure [89, 151]. Moreover, modern performance-based methodologies also comprise the assessment of non-structural and contents damage, which can represent a significant proportion of the total losses after a seismic event [154]. Damage Measures (DM), such as timber crushing, partition wall cracks and dropped suspended ceiling tiles, are commonly related to Engineering Demand Parameters (EDP) such as inter-storey drifts and floor accelerations. In this chapter, the ability of the inerter to control the rotation amplitude and suppress higher-mode effects in rocking structures is applied to the seismic protection of post-tensioned timber buildings. To this end, a representative set of three post-tensioned rocking walled structures, comprising 3, 6 and 9 storeys, are designed following direct-displacement based design guidelines. Based on the conclusions obtained in previous chapters, a simplified procedure to pre-dimension the inerter device is proposed and used to design a set of ball-screw and gear inerters, with and without clutches. In a first stage, the performance of bare and protected structures with different levels of apparent mass ratios is assessed and compared considering a set of 7 records consistent with the displacement design spectrum. Special attention is paid to the resisting force developed in the inerter and the mechanism to transfer it to the structural diaphragm. Finally, a performance-based assessment is conducted considering a database of 202 pulse-like ground motion records.

7.2 Description of the structural systems

Three different buildings are considered in order to assess the seismic performance of low to mid-rise post-tensioned timber wall systems. The 3, 6 and 9-storey prototype buildings are formed of rectangular modules of 12x10 meters in plan, and have an inter-storey height of 3 meters. The structural plan consists of a frame in the transverse direction supporting gravity loads, and four post-tensioned CLT walls providing lateral load resistance in each direction. External steel dissipaters are added at the base of each wall to increase the energy dissipation capabilities of the system. The length and width of each wall panel are considered as design parameters. Figure 7.1 shows the typical plan and elevation views of the structural system.

The structures correspond to residential buildings - category A, according to EN 1991 Table 6.1. A permanent load of 3 $[kPa]$, representing the self-weight of the structural elements and non-structural components attached to them, is assigned to each floor. On the other hand, a uniformly distributed variable load of 2 $[kN/m^2]$ is considered for the typical storey (EN 1991/Table 6.2). This value is reduced to 0.4 $[kN/m^2]$ for the roof level, in accordance with EN 1991 Table 6.10.

The seismic masses are determined according to EN 1998-1/3.4.2, considering the full weight of the structure and a fraction of the variable loads defined by the reduction factor $\psi_{Ei} = \phi\,\psi_{2i}$. For residential buildings, $\psi_{2i} = 0.3$ (EN 1990/Table A.1.1), whereas ϕ is 1.0 for the roof level and 0.5 for the remaining storeys (EN 1998-1/4.2.4). The resulting seismic weights, presented in Table 7.1, are computed considering a tributary area of 30 $[m^2]$ per wall

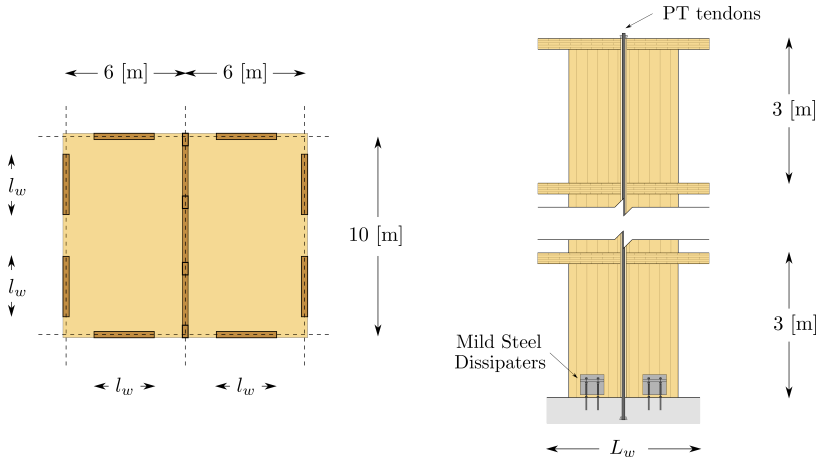

Figure 7.1: Typical plan and elevation views of the case study structures.

system in each direction. On the other hand, the corresponding gravity load is obtained based on simple area relations as one sixteenth of the total weight of the floor.

Floor	**Permanent load** $G_k[kPa]$	**Variable load** $Q_k[kPa]$	**Seismic** $G_k + \psi_{Ei}\, Q_k$ $[kPa]$	**Seismic weight per wall** $[kN]$	**Gravity load per wall** $[kN]$
Typical	3	2	3.3	99	24.75
Roof	3	0.4	3.12	93.6	23.4

Table 7.1: Seismic weight and gravity load per wall system.

7.3 Displacement-based design of the wall systems

Direct Displacement-Based Design (DDBD) [85] is a performance-based methodology where the structural system is designed to achieve, rather than to be bounded by, a specific limit state under a given seismic hazard level. In this method, the nonlinear structure is characterized by a linear single-degree-of-freedom (SDOF) system with an equivalent viscous damping (EVD), whose maximum displacement is approximately equal to the maximum displacement of the original structure [85]. The design process is summarized in Figure 7.2.

The characteristic design displacement of the substitute single-degree-of-freedom (SDOF) system depends on the selected limit state displacement or drift and the deformation profile of the original multi-degree-of-freedom (MDOF) structure:

$$\Delta_d = \frac{\sum_{i=1}^{n} m_i \, \Delta_i^2}{\sum_{i=1}^{n} m_i \, \Delta_i} \tag{7.1}$$

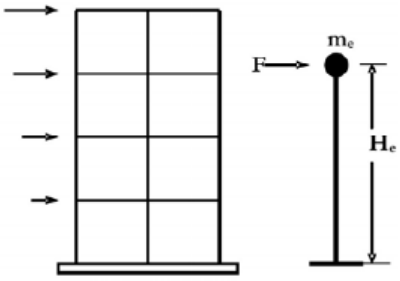

(a) Equivalent SDOF idealization.

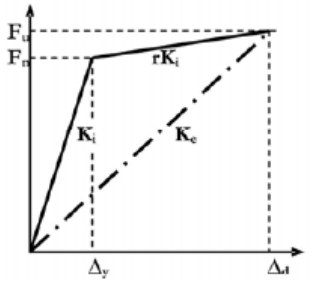

(b) Secant stiffness approximation.

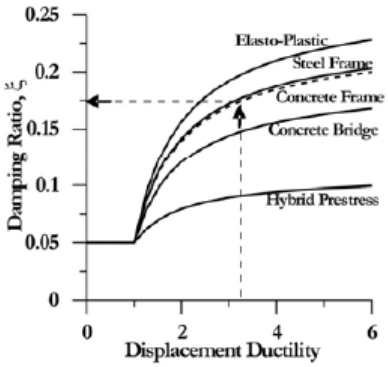

(c) Damping-ductility relationship.

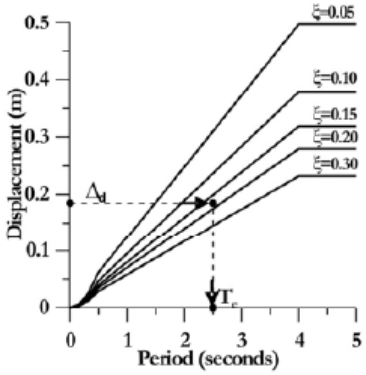

(d) Effective period at maximum response.

Figure 7.2: Direct displacement-based design [85]

where m_i and Δ_i are the mass and displacement of the *i-th* storey, respectively. On the other hand, consideration of the mass participating in the first inelastic mode of vibration gives the effective mass for the substitute structure:

$$m_e = \frac{\sum_{i=1}^{n} m_i \, \Delta_i}{\Delta_d} \tag{7.2}$$

and the effective height:

$$H_e = \frac{\sum_{i=1}^{n} m_i \, \Delta_i \, H_i}{\sum_{i=1}^{n} m_i \, \Delta_i} \tag{7.3}$$

Having determined the design displacement and the corresponding equivalent damping of the substitute structure (see Section 7.3.3), the effective period at maximum response, T_e, can be read from the reduced design spectrum. The effective stiffness, K_e, is then obtained as:

$$K_e = \frac{4\pi^2 \, m_e}{T_e^2} \tag{7.4}$$

and the base shear can be estimated:

$$V_b = K_e \, \Delta_d \tag{7.5}$$

Finally, the base shear is distributed to each floor based on the inelastic mode shape and mass distribution:

$$F_i = \frac{V_b \, m_i \, \Delta_i}{\sum_{i=1}^{n} m_i \, \Delta_i} \tag{7.6}$$

As noted by Newcombe et al. [81], some special considerations are required for the displacement-based design of post-tensioned timber walls, the most important of which are summarized in the following sections.

7.3.1 Displacement profile

The displacement profile defines the effective mass, height and design displacement of the equivalent SDOF system (Figure 7.2a)). In rocking structures, the shape of the displacement profile is defined by the relative importance of the base rotation and the flexural and shear deformations. Although a linear displacement profile can be assumed for the design of post-tensioned concrete walls, this is usually inaccurate for timber members, as shear and flexural deformations can be significant. Based on the results of several numerical analyses, Sarti [61] proposed the following expression for the displacement profile that accounts for the cantilever behaviour of the wall panels:

$$\delta_i = (1 - k_{el})\frac{h_i}{h_n} + k_{el}\left[\frac{3}{2}\left(\frac{h_i}{h_n}\right)^2\left(1 - \frac{h_i}{3h_n}\right)\right] \tag{7.7}$$

with:

$$k_{el} = 0.1 + \frac{0.6}{\mu} \tag{7.8}$$

It is important to note that, as the elastic deformation contribution factor, k_{el}, depends on the ductility of the system, μ, the procedure to determine the displacement profile is iterative.

7.3.2 Yield displacement

In order to compute the displacement profile and the equivalent viscous damping of the substitute SDOF system, the ductility demand of the structure must be determined first. Since the target displacement is set at the beginning of the design procedure, the yield displacement defines the ductility demand of the system (Figure 7.2b). In post-tensioned walls equipped with external steel dissipaters, the yield displacement depends on the base rotation and the elastic deformation of the wall element at the instant of activation of the dissipation devices [81]:

$$\Delta_{y,e} = \theta_y H_e + \Delta_{w,e} \tag{7.9}$$

where $\Delta_{y,e}$ = total yield deformation at the effective height, θ_y = base rotation at the instant of first yield in the external dissipaters and $\Delta_{w,e}$ = elastic deformation of the wall at the

effective height. The base rotation at first yield is determined using the cross sectional analysis described later in Section 7.3.4. Newcombe [81] also proposed an expression to conservatively estimate the elastic deformation in the wall member, $\Delta_{w,e}$, accounting for both the shear and flexural contributions.

$$\Delta_{w,e} \approx \gamma_{LS}\left(V_b \frac{(1-\beta_s)H_e^2}{6EI_w} + \frac{\bar{V}_s}{2GA_s}\right) \tag{7.10}$$

where γ_{LS} = 1.0 and 1.25 for serviceability and ultimate limit state design, respectively, V_b = base shear, GA_s = shear stiffness of the wall element, EI_w = flexural stiffness of the wall element, β_s = ratio between moment provided by the external dissipaters and the total OTM, and $\bar{V}_s$ = average inter-storey shear (≈0.85 V_b).

The yield displacement of the post-tensioned timber wall systems considered in this study is obtained analytically using the previous expressions and subsequently verified with a pushover analysis. It must be noted that, unlike monolithic reinforced concrete walls, the yield displacement of post-tensioned timber walls depends on the strength of the system, as the decompression moment is governed by the axial load in the wall.

7.3.3 Equivalent viscous damping

The equivalent viscous damping, ξ_{eq}, is given by the sum of the elastic damping ratio, ξ_{el}, and the hysteretic viscous damping of the structural system, ξ_{hyst}. Based on experimental observations, Marriott [86] suggested the use of a 2% elastic damping ratio for post-tensioned timber walls. On the other hand, the hysteretic damping ratio can be approximated using the area-based equivalent viscous damping defined by Jacobsen [155]:

$$\xi_{hyst} = \frac{A_h}{2\pi F_u \Delta_d} \tag{7.11}$$

where A_h = area enclosed by the hysteresis within one complete cycle, F_u = force at the peak displacement, and Δ_d = peak displacement. The hysteretic damping of each structural system is then computed integrating the area within one cycle of stabilized force-displacement response from a push-pull analysis. Priestley et al. [85] suggest that values obtained from area-based expressions should be corrected to make them consistent with results from inelastic response history analyses, as shown in Figure 7.3.

In a later study, Dwairi et al. [156] developed equivalent damping expressions for post-tensioned rocking systems based on the results of inelastic response-history analyses for a specific set of re-centring ratio and post-uplift stiffness. Since the values used in their analysis do not match the parameters of the case study structures, the original approach suggested by Priestley el al. is considered in this study. Accordingly, the correction factors presented in Figure 7.3 are applied to the area-based hysteric dampings obtained from the push-pull analyses. It is important to note that, since the area of the hysteretic loop depends on the design parameters, the procedure is iterative.

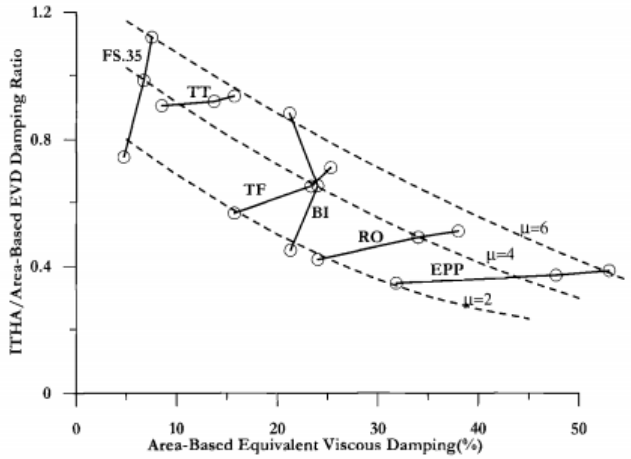

Figure 7.3: Correction factors to be applied to area-based equivalent viscous damping ratio (FS = Flag Shape, TT = Takeda "thin", TF = Takeda "fat", BI = Bi-linear, RO = Ramberg-Osgood, EPP = Elasto-plastic) [85].

The 5% of critical damping elastic displacement spectrum, usually taken directly from seismic codes, is then scaled by R_ξ [134] in order to account for the effect of hysteretic damping:

$$R_\xi = \left(\frac{0.07}{0.02 + \xi_{eq}} \right)^{0.5} \tag{7.12}$$

7.3.4 Cross-sectional analysis

The Direct-Displacement-Based Design procedure described in the previous sections is used to determine the lateral forces acting on the structural system. In order to achieve the target displacement set at the beginning of the process, the base rocking section must be designed to satisfy the moment demand for the imposed base rotation, θ_{imp}. Figure 7.4 shows the forces acting on the rocking section in the deformed configuration. These forces are used for the design of the ductile sections, whereas the rest of the structural elements will be capacity designed.

7.3.4.1 Timber stresses

Since Bernoulli's hypothesis (strain compatibility) is no longer valid after decompression, a different approach is needed to analytically describe the moment-rotation response of rocking connections. The Monolithic Beam Analogy developed by Pampanin [80] has been shown to be appropriate for precast concrete [86] and steel [58], however, it might be inaccurate for softer timber connections [81]. Based on experimental evidence and finite element analyses, Newcombe proposed the following expression to relate the imposed rotation and the compression

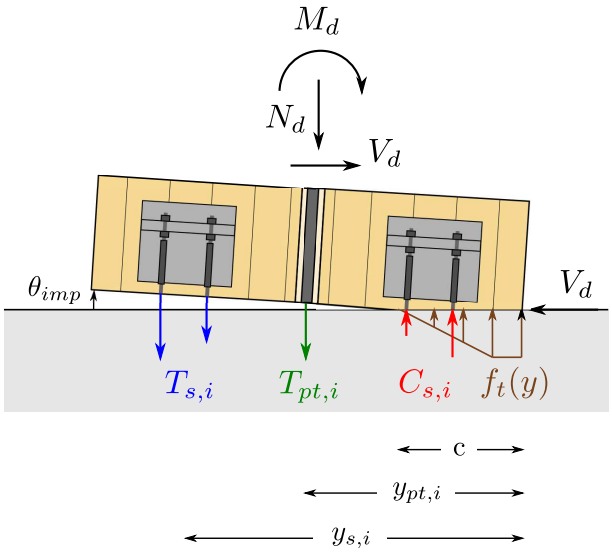

Figure 7.4: Forces acting on the rocking section.

strain at the extreme fiber, ϵ_c, in post-tensioned timber wall-base connections [81]:

$$\epsilon_c = \frac{\theta_{imp}\ c}{L_e} \tag{7.13}$$

$$L_e \approx 65\left(\frac{l_w}{c} - 1\right)\ [\text{mm}] \tag{7.14}$$

where θ_{imp} = imposed rotation in the connection, c = neutral axis depth, and L_e = effective length of an equivalent Winkler spring. According to experimental observations, the strain profile can be assumed to remain approximately linear in both the elastic and inelastic ranges. Additionally, a bilinear or elasto-perfectly-plastic (EPP) stress-strain law can be considered to account for plastic deformations in the timber panel [81]. Integration of the stress distribution along the neutral axis depth gives the resultant compressive force in the timber:

$$C_t = b_b \int_0^c f_t(y)dy \tag{7.15}$$

where b_b = wall panel depth and $f_t(y)$ = compressive stress in the timber panel. On the other hand, the compression centroid is given by:

$$c_c = \frac{b_b \int_0^c f_t(y)ydy}{C_t} \tag{7.16}$$

During the design process, the compressive strain is limited to twice the yield value in order to avoid excessive crushing in the timber.

$$\epsilon_c \leq 2\,\epsilon_{y,t} \tag{7.17}$$

7.3.4.2 Post-tensioned tendons

The elongation of the post-tensioned tendons is given by:

$$\Delta_{pt,i} = \theta_{imp}\big(y_{pt,i} - c\big) \tag{7.18}$$

where $y_{pt,i}$ = distance from the extreme compression fibre to the *i-th* tendon. Then, the variation in the tendon strain caused by the base rotation is:

$$\delta\epsilon_{pt,i} = \frac{\Delta_{pt,i}}{l_{ub}} \tag{7.19}$$

where l_{ub} = unbonded length of the tendons. Accordingly, the total post-tensioning force in each tendon is:

$$T_{pt,i} = E_{pt}\big(\epsilon_{pt0,i} + \delta\epsilon_{pt,i}\big)A_{pt,i} \tag{7.20}$$

where E_{pt} = elastic modulus of the tendons, $\epsilon_{pt0,i}$ = initial strain in the *i-th* tendon, and $A_{pt,i}$ = transverse area of the *i-th* tendon. To ensure the tendons remain elastic, the maximum stress is limited to 90% of the yield value. Additionally, the tendon force should not generate a stress higher than 40% of the compressive strength of the timber under service conditions [157].

7.3.4.3 Mild steel external dissipaters

External fuse-type dissipaters consist of a ductile steel core designed to yield in both tension and compression. To prevent global buckling, the core rod is placed inside a steel case filled with epoxy or grout. Figure 7.5 shows a schematic diagram of one of such devices.

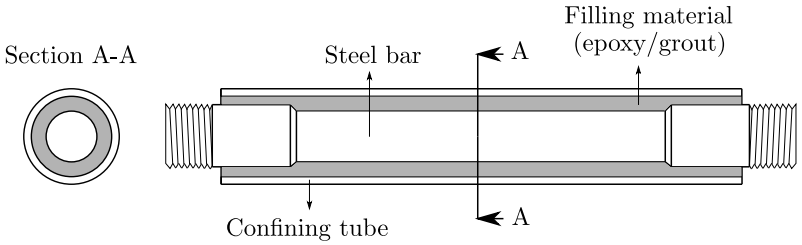

Figure 7.5: Schematic diagram of a mild steel external dissipater.

The elongation of a layer of reinforcement, $\Delta_{s,i}$, can be determined geometrically:

$$\Delta_{s,i} = \theta_{imp}\big(y_{s,i} - c\big) \tag{7.21}$$

where $y_{s,i}$ = distance from the extreme compression fibre to the *i-th* layer of reinforcement. Then, the strain in the external reinforcement is given by:

$$\epsilon_{s,i} = \frac{\Delta_{s,i} - 2\Delta_a}{l'_{ub}} \tag{7.22}$$

where Δ_a = deformation of the dissipater anchorages, and l'_{ub} = unbonded (or fuse) length of the dissipaters. Based on experimental observations from [81], a conservative estimate of 1 [mm] deformation per anchorage is assumed for design. In order to avoid steel fracture due to low cycle fatigue, strain in the dissipaters is limited to 5%. This can be achieved by moving the external dissipaters towards the centreline of the wall or increasing the fuse length of the steel bars. In all cases, adequate compression buckling restraint must be provided [86].

Finally, a perfectly-plastic stress-strain relationship is assumed for design:

$$F_{s,i} = \begin{cases} \epsilon_{s,i}\, E_s\, A_{s,i} & |\epsilon_{s,i}| < \epsilon_{y,s} \\ sign(\epsilon_{s,i})\, E_s\, A_{s,i} & |\epsilon_{s,i}| \geq \epsilon_{y,s} \end{cases} \tag{7.23}$$

where E_s = elastic modulus of the external dissipaters, and $A_{s,i}$ = transverse area of the *i-th* external dissipater. It is important to note, however, that significant levels of strain hardening are expected in the steel dissipaters. Accordingly, the consequent increase in the connection moment needs to be considered when capacity designing the remaining structural elements.

7.3.4.4 Evaluation of sectional equilibrium

As the compression strain in the timber and the forces in the post-tensioned tendons and external dissipaters depend on the neutral axis, iteration is required to determine the neutral axis depth that satisfies vertical equilibrium. Figure 7.6 illustrates the iterative procedure required for the cross-sectional analysis [81].

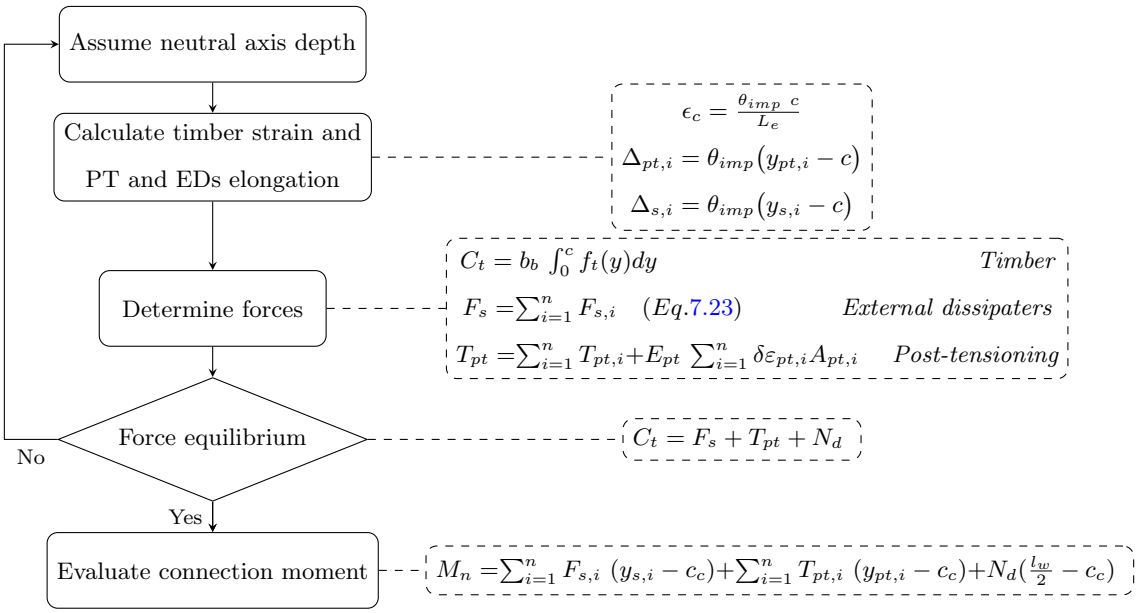

Figure 7.6: Iterative procedure for cross-sectional analysis (adapted from [81]).

7.3.5 Design results

The timber rocking walled buildings were designed as described in the previous sections, considering a top storey drift of 1.2% as target displacement. The properties of the equivalent SDOF structures for the 3, 6 and 9-storey wall systems are shown in Table 7.2.

	Δ_d [m]	m_e [Ton]	H_e [m]	T_e [s]	ξ_{eq}
3-Storey	0.083	25	7.11	0.82	0.13
6-Storey	0.154	47	13.26	1.4	0.11
9-Storey	0.224	69	19.38	2.05	0.11

Table 7.2: Properties of the equivalent SDOF systems

The design spectrum was taken from Eurocode 8 [134], considering high seismic hazard (Type 1), a stiff soil (type B) and a peak ground acceleration of $a_g = 0.4[g]$. As previously discussed, the 5% damping displacement spectrum is reduced to account for the hysteretic damping of the non linear structure. Since the equivalent viscous damping depends on the final design of the walls, the design procedure is iterative. Figure 7.7 shows the final reduced displacement spectra and the effective period of the equivalent SDOF systems. In the case of the 9-storey building, the design displacement determined according to Equation 7.1 exceeds the maximum displacement demand, Δ_D. Although this effectively limits the first mode displacement demands, a minimum level of lateral strength is still required in order to control the length of the structural periods and ensure some mitigation of higher mode effects. Accordingly, the effective period of the 9-storey building was obtained using the approach proposed by Sullivan et al. [158]:

$$T_e = \frac{\Delta_d}{\Delta_{D,\xi}} T_D \tag{7.24}$$

where T_D is the spectral displacement corner period, and $\Delta_{D,\xi}$ is the spectral displacement demand at this period for the anticipated level of equivalent viscous damping. Based on the effective period, effective mass and design displacement, the effective stiffness and base shear of each SDOF oscillator is obtained. The lateral forces are then vertically distributed according to the assumed displacement profile (Section 7.3.1).

The cross-sectional analysis procedure described in Section 7.3.4 is used for the design of the CLT rocking sections. The proportion of the nominal moment provided by the post-tensioning and the external dissipaters is defined by the re-centring ratio:

$$\lambda = \frac{M_{pt} + M_w}{M_s} \tag{7.25}$$

where M_{pt} = moment provided by the post-tensioning, M_w = moment provided by gravity loads, and M_s = moment provided by the external dissipaters. A re-centring ratio of $\lambda = 1.5$

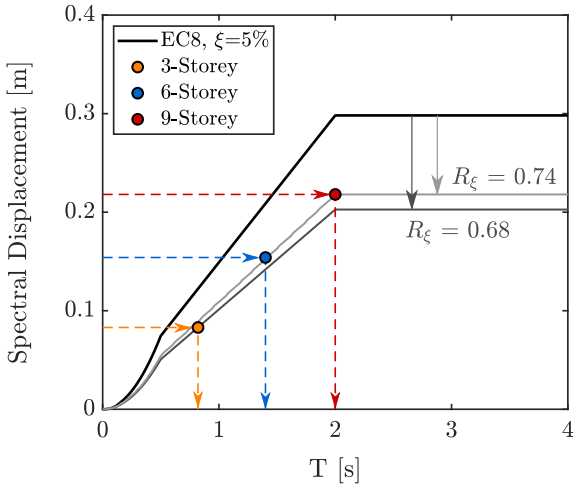

Figure 7.7: Design spectra considered in the DDBD procedure.

is specified in order to ensure full-re-centring of the base connection [81,159]. Accordingly, the moment demands are obtained as:

$$M_s = \frac{M_d}{1+\lambda} \tag{7.26}$$

$$M_{pt} = \lambda M_s - M_w \tag{7.27}$$

where M_d = moment demand from the DDBD procedure. The design forces for the base rocking sections are summarized in Table 7.3.

	V_b [kN-m]	M_d [kN-m]	λ	$M_{pt}+M_w$ [kN-m]	M_s [kN-m]
3-Storey	122	874	1.5	524	349
6-Storey	145	1945	1.5	1167	778
9-Storey	148	2903	1.5	1742	1161

Table 7.3: Design forces for the base rocking sections

The mechanical properties of the materials considered in the design are listed in Table 7.4.

CLT Panel			**PT Tendons**		**Ext. Dissipaters**	
E_{par} [MPa]	G [MPa]	$f_{y,t}$ [MPa]	E_{PT} [MPa]	$f_{y,pt}$ [MPa]	E_s [MPa]	$f_{y,s}$ [MPa]
11000	660	30	190000	1560	200000	320

Table 7.4: Material properties

Finally, Table 7.5 and Table 7.6 summarize the design results for the three structures under consideration. The post-tensioned cables are placed symmetrically around the centreline of

the wall, whereas the external dissipaters are connected at a distance $y_{s,i}$ and $y'_{s,i}$ from the edges of the CLT panel (see Figure 7.4).

	l_w [m]	b_b [m]	N° cables	$A_{pt,i}$ [cm^2]	A_{pt} [cm^2]	$T_{pt,0}$ [kN]
3-Storey	2.5	0.2	2	1.4	2.8	317
6-Storey	3	0.25	5	1.4	7	606
9-Storey	3.5	0.3	5	1.4	7	776

Table 7.5: Post-tensioned walls design results.

	N° of dissip.	ϕ_s [mm]	A_s [cm^2]	A'_s [cm^2]	l'_{ub} [m]	$y_{s,i} = y'_{s,i}$ [m]
3-Storey	2+2	18	5.1	5.1	0.3	0.5
6-Storey	2+2	24	9	9	0.36	0.6
9-Storey	2+2	26	10.6	10.6	0.39	0.6

Table 7.6: External dissipaters design results.

Figure 7.8 shows the base moment-top storey drift response of the wall systems obtained from push-pull analyses conducted with the numerical model presented in Section 7.4. The design points are also indicated on the curves. It can be observed that the sectional design methodology and the numerical model are consistent with the DDBD procedure.

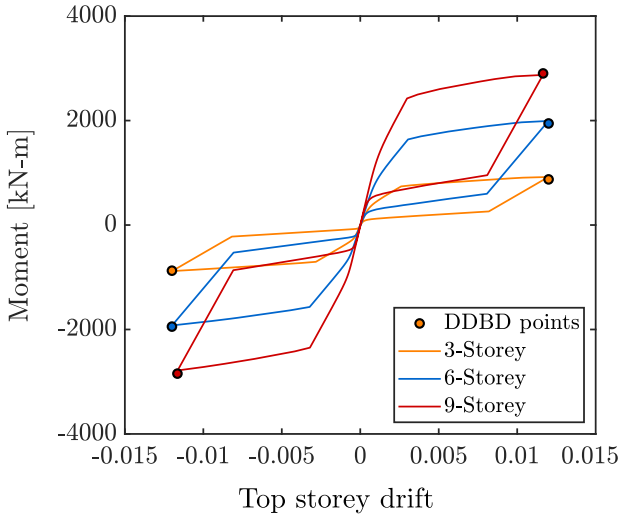

Figure 7.8: Base moment - top storey drift response.

7.4 Numerical model

Finite element models for post-tensioned timber walls have been developed and validated against experimental results [61, 79, 81]. In such models, the elastic deformation of the structural members was captured by means of elastic beam-column elements, while compression-only multi-spring or fibre sections were used to account for rigid-body rotations and moment-axial load interaction in the rocking connections. Axial springs or truss elements were also used to model the post-tensioned tendons and external dissipation devices. The numerical model used in this study builds upon these past investigations. Figure 7.9 shows a schematic diagram of such a model. The soil-foundation formulation previously described in Chapter 6 is also adopted in order to better represent energy dissipation and the forces generated during impact.

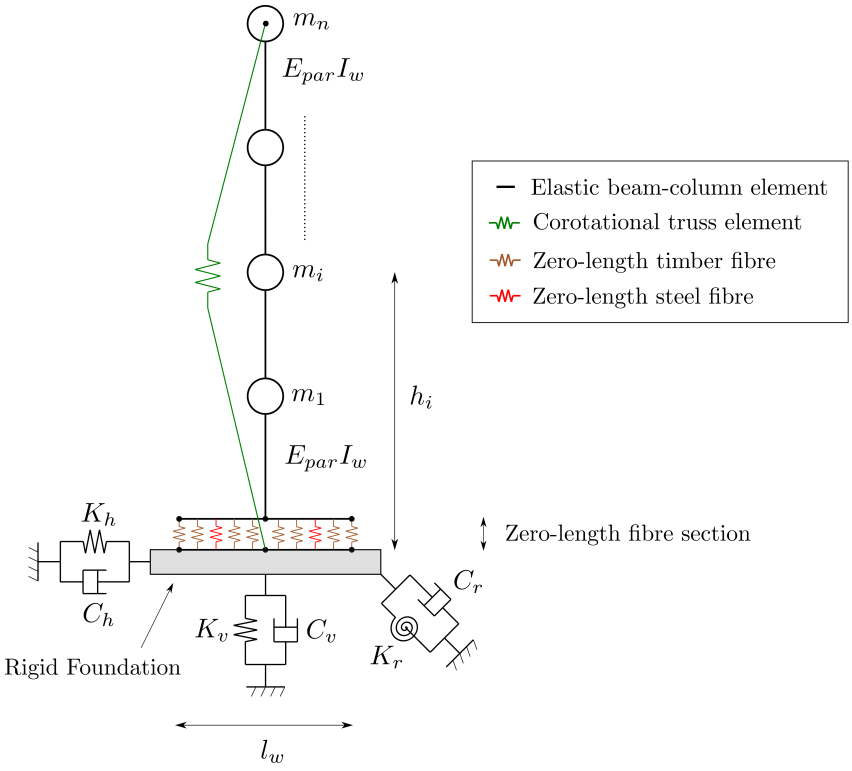

Figure 7.9: Schematic diagram of the numerical model of the post-tensioned timber walls.

The structural model shown in Figure 7.9 is implemented in the open-source finite element framework OpenSees [10]. The CLT wall panels are modelled with a series of Elastic-Timoshenko-Beam elements, which include axial, flexure, and shear deformations. A zero-length fibre section is used to model the CLT-foundation contact zone, consisting of a stack of 32 constant stiffness fibres distributed and weighted through a Lobatto integration method [87]. The overall axial stiffness of the fibre section, K_t, is determined by dividing the axial stiffness

of the timber panels by an effective length, L_e (Equation 7.14).

$$K_t = \frac{E_{par}\ A_w}{L_e} \tag{7.28}$$

where E_{par} = parallel-to-grain elastic modulus of the timber panel, A_w = cross-sectional area of the wall, and L_e = effective length of an equivalent Winkler spring (Equation 7.14). As mentioned earlier, Newcombe [81] conducted several finite elements analyses in order to determine an expression for the effective length, L_e, in timber walls. The analyses showed that the effective length is not constant and varies mainly with the ratio between the wall length and the neutral axis depth (Equation 7.14). The variable nature of the effective length implies that the axial stiffness of the rocking connection changes as the neutral axis shifts, and therefore its moment-rotation response cannot be accurately described using constant stiffness springs. However, in most of the cases analysed in [81] the neutral axis depth reached an asymptote at 10% to 20% of the wall length. Newcombe showed that the axial stiffness of the multi-spring model can be reasonably estimated based on the effective length along this asymptote. This assumption slightly under-estimates the connection moment at small rotations (less than 1%) due to the inability to account for the increase in stiffness when the neutral axis depth is large.

A compression-only elastic perfectly-plastic material (ElasticPPGap material) is assigned to the timber fibres. The yield strength of each fibre is determined applying the corresponding Lobatto weightings [87] to the overall CLT panel axial strength, $F_{y,t}$.

$$F_{y,t} = f_{y,t}\ A_w \tag{7.29}$$

where $f_{y,t}$ = parallel-to-grain yield strength of the timber panel. Vertical zero-length fibres with an elastic perfectly-plastic material are used to model the mild steel external dissipaters. The yield deformation is determined according to Equation 7.22, taking into account the unbonded length, l'_{ub}, and the achorages deformation, Δ_a. Finally, the post-tensioned tendons are modelled using a corotational truss element connected to the fixed base node and the top floor node. A tension only bi-linear material model (ElasticPPGap) is used for the post-tensioning steel. An initial strain is applied to the material model such that the post-tensioned tendon strain is at the target value after accounting for losses due to the axial deformations in the timber wall.

The variable damping ratio introduced in previous chapters is also incorporated in the numerical model of the post-tensioned timber walls. Inherent structural damping during the full contact phase is modelled using Rayleigh's classical damping, assigning a prescribed damping ratio of ξ_{el} = 2% to the first and third vibration modes of the fixed base structure [9] representing at least 90% of the modal mass in the full-contact case. Once the base uplifts, the analysis is halted and the conservative assumption of no damping during the rocking phase is enforced. On the other hand, the effects of diaphragm flexibility and wall-to-diaphragm interaction are beyond the scope of the study and are not considered in the models.

7.5 Seismic design validation

Each wall model was subjected to a set of 7 different earthquake records selected from the ground motion database described in Table 3.1. The records are chosen so the mean spectral displacement demand is consistent with the 2%-damped displacement design spectrum within the period range from 0.1[s] to 2.5[s]. This range of periods was chosen to include at least the first three elastic modes of vibration of the 9-storey building and the effective periods of all the substitute SDOF structures. The mean squared error between the displacement design spectrum and the records mean was used as selection criterion, defining a tolerance of 1% within the range of periods of interest. Figure 7.10 shows the acceleration and displacement spectra of the ground motions sub-set and the spectrum considered during the design procedure.

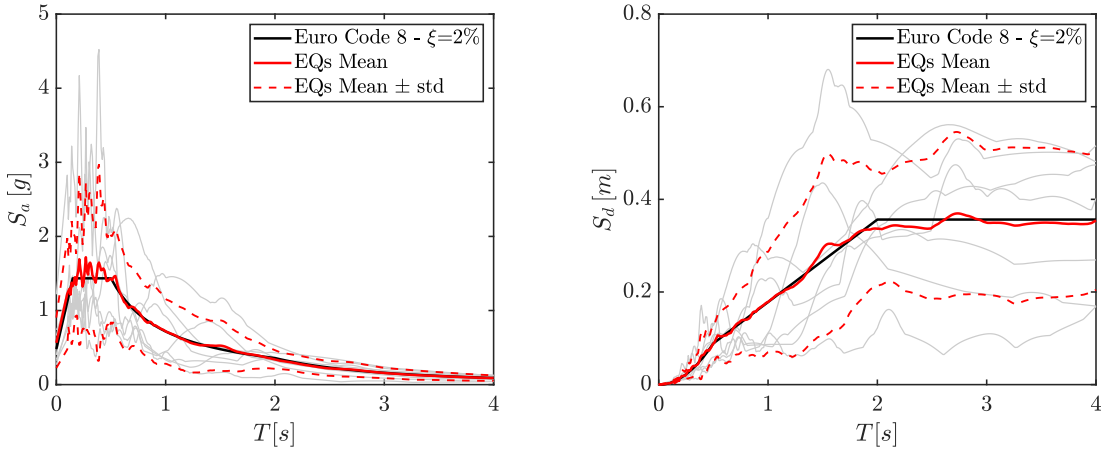

Figure 7.10: Spectra of the suite of 7 records and spectrum used for design.

Figures 7.11 to 7.14 summarize the response of the 3, 6 and 9-storey structures to the set of 7 ground motion records described above. The floor displacement profile, inter-storey shears and inter-storey moments from the response-history analyses are compared with the predicted values from the displacement-based design. The results of the analyses show that the DDBD procedure adequately estimates the mean lateral displacements of the buildings, with differences ranging from 4% to 10%. These small deviations are likely related to a misestimation of the hysteretic damping obtained with the area-based approach. The shape of the displacement profile, on the other hand, is reasonably described by the design assumption.

The moment at the base of the walls is limited by the strength of the rocking section and, therefore, is very similar to the design value. The very small deviations observed in the graphs arise from variations in the imposed base rotation. On the other hand, bending moments above the base and shears throughout the structures are significantly underestimated by the DDBD design procedure. This shear and moment amplification is caused by the response of higher modes of vibration, which were not directly accounted for in the displacement-based design procedure. Although methodologies to incorporate higher mode effects in the design of fixed-base reinforced concrete walls and bridges have been proposed [85, 160, 161], they are

not directly applicable to the design of post-tensioned rocking timber systems. Alternatively, higher-mode effects are considered at the end of the design process, amplifying the design forces along the height of the structure and verifying that they do not substantially reduce the structural performance [61,81]. Importantly, active measures to diminish higher-mode effects, like multiple rocking sections [89], are rarely implemented. The influence of higher modes in the response of the structures is also evident in the peak floor accelerations, where floor acceleration magnification ratios ($FAM = PFA/PGA$) of up to 4 are obtained.

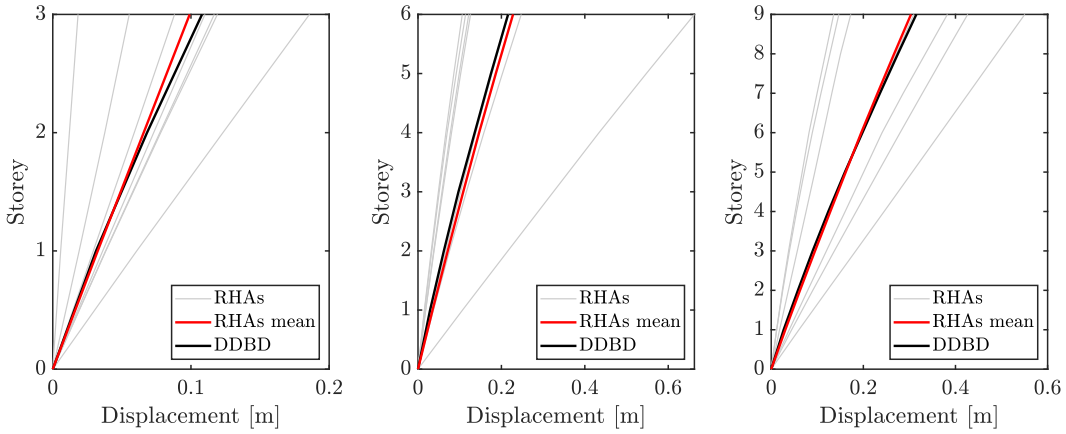

Figure 7.11: Design validation: displacement profiles of the case study structures.

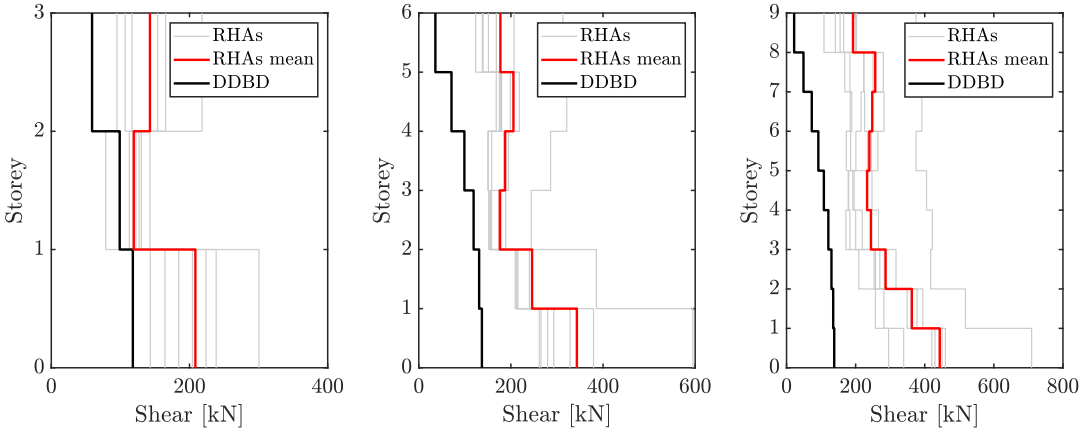

Figure 7.12: Design validation: Maximum shear forces in the wall element.

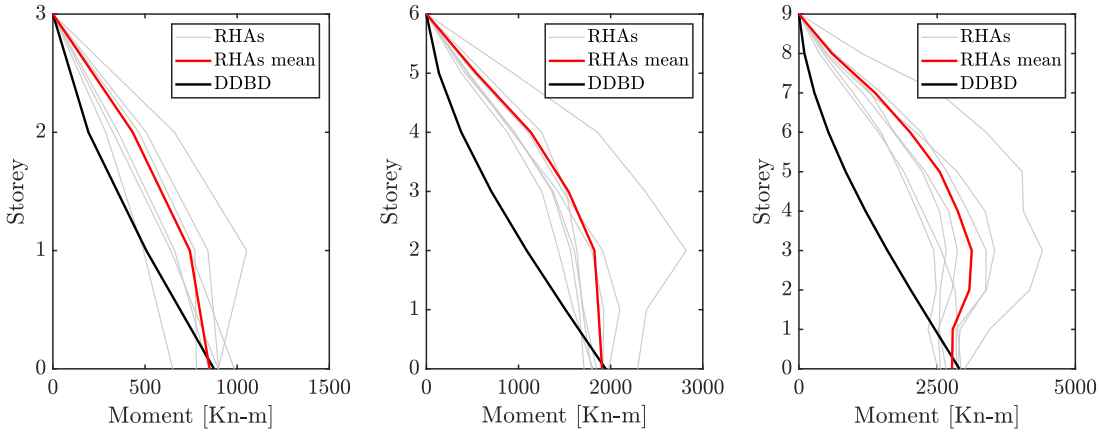

Figure 7.13: Design validation: Maximum bending moments in the wall element.

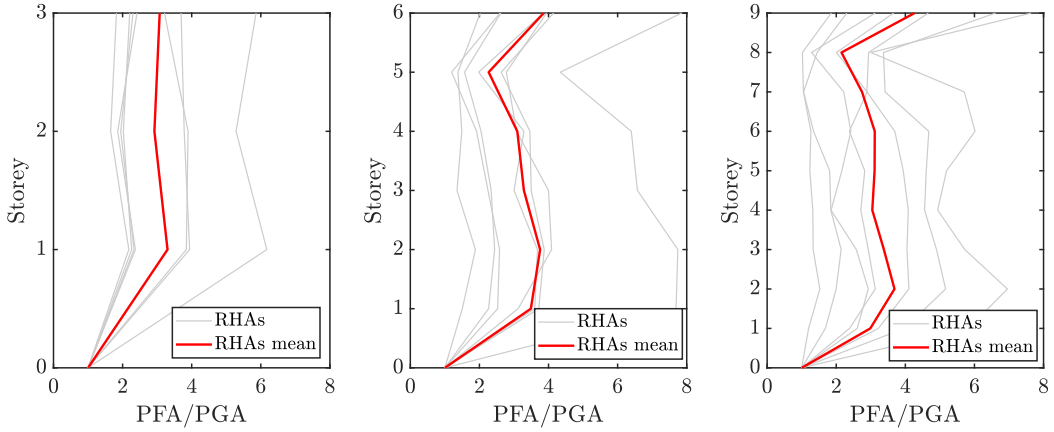

Figure 7.14: Design validation: Floor acceleration magnification factors.

7.6 Design of the inerters

As shown in Chapter 6, supplemental rotational inertia devices can be used to control the rotation amplitude and higher-mode effects in flexible rocking structures. In this section, a set of ball-screw and gear inerters is designed and applied to the seismic protection of the case study structures described above.

7.6.1 Pre-dimensioning procedure

Firstly, a simplified procedure to pre-dimension the inerter device is proposed based on the equal displacement rule [162] and the conclusions obtained from previous chapters. The design concept is illustrated in 7.15, where the response of a bare and an inerter-equipped rocking block is compared in terms of the rigid body rotation, θ, and the top displacement, Δ. The rocking block is characterized by its semidiagonal, R_1, and slenderness α. An inerter of aparent mass m_r is connected to the structure in Figure 7.15b.

It was shown in Chapter 3 that the inclusion of the inerter has an effect equivalent to increasing the size of a rigid rocking block while keeping the associated slenderness constant.

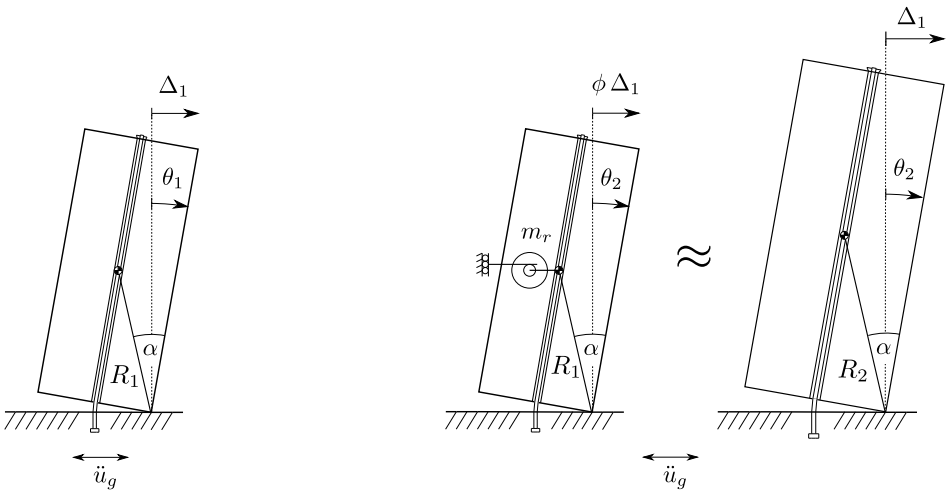

(a) No Inerter. (b) Single Inerter.

Figure 7.15: Simplified pre-dimension procedure for the inerter device.

Moreover, the analytical model of Chapter 4 demonstrated that the effects of post-tensioning can be isolated as two independent dimensionless parameters that do not affect the frequency parameter of the structure. Accordingly, the rotation response of the inerter-equipped structure can be represented by the larger block of Figure 7.15b, whose size parameter, R_2, can be obtained by equating the frequency parameter of both systems, $p_{r1} = p_{r2}$. Considering the more general expression for multi-mass rocking structures (see Section 6.2.1):

$$p_{ri} = \sqrt{\frac{\underline{1}^t [W] \underline{\mathrm{H}}_i}{J_{pi}}} \tag{7.30}$$

where:

$$J_{p1} = \underline{R_1}^t \, [M] \, \underline{R_1} + m_r h_1^2 \tag{7.31}$$

is the rotational inertia of a rocking structure with an inerter of apparent mass m_r connected at the first floor, and

$$J_{p2} = \underline{R_2}^t \, [M] \, \underline{R_2} \tag{7.32}$$

is the rotational inertia of the larger equivalent block.

On the other hand, Reggiani and Vassiliou [162] demonstrated that two blocks of different size but identical slenderness under a given ground motion experience the same top displacement, provided that they are not close to overturn. This implies that the unprotected rocking block (Figure 7.15a) and the inerter-equivalent larger block (Figure 7.15b) experience the same top displacement Δ_1 for the same ground motion demand. The rotation of the larger block can then be obtained as:

$$\theta_2 = \frac{\Delta_1}{2R_2 \cos\alpha} \tag{7.33}$$

Then the rotation reduction factor is given by:

$$\phi = \frac{\theta_2}{\theta_1} = \frac{R_1}{R_2} \tag{7.34}$$

In this way, a first estimation of the response reduction associated with any given apparent mass, m_r, can be obtained for rigid rocking structures.

In the case of flexible structures, the total lateral displacement depends on the base rotation and elastic deformation contributions. According to the results obtained in Chapters 5 and 6, it is reasonable to assume that the inerter does not significantly affect the elastic deformation response of the structures. Thus, if the reduction factor, ϕ, is only applied to the rotation component, the top displacement of an inerter-equipped flexible structure can be obtained as:

$$\Delta_r = \big(\phi\,(1 - k_{el}) + k_{el}\big)\Delta_1 \tag{7.35}$$

where k_{el} is the elastic deformation contribution factor defined in Equation 7.8. Then, the displacement reduction factor for flexible rocking structures equipped with inerters is given by:

$$\phi_{el} = \frac{\Delta_r}{\Delta_1} = \phi\,(1 - k_{el}) + k_{el} \tag{7.36}$$

As in Chapter 6, inerters connected to the first floor diaphragm are employed for practical considerations. In a first stage, the efficiency of the proposed strategy is assessed for three different levels of inertance. For each structural system, apparent mass ratios ranging from $\sigma = 0.5$ to 4 are selected resulting in displacement reduction factors between $\phi_{el} = 0.78$ and 0.98. In the context of displacement-based design, this reductions would translate into smaller wall sections for any target displacement. Importantly, the predicted efficiency of the inerter diminishes as the structures become taller, resulting in very modest displacement reductions in the case of the 9-storey building equipped with inerters of $\sigma = 1$. The results of the preliminary design are summarized in Table 7.7.

7.6.2 Design of the ball-screw and gear inerters

Over the last years, several types of inerters have been proposed employing rack-and-pynion mechanisms [6], ball screws [5], electromagnetic devices [103] and hydraulic components [101]. The realisation considered in this study, depicted in Figure 7.16, is based on the ball-screw an gear inerter proposed by Nakamura et al. [96]. In this configuration, a ball screw mechanism is used to transform the linear motion of a rod into a rotation in a flywheel. A gear system is also included to further amplify the rotational motion, while a clutch can be incorporated to ensure the inerter only opposes the motion of the structure.

	σ	ϕ	k_{el}	ϕ_{el}
	0.5	0.91	0.24	0.93
3-Storey	1	0.83	0.24	0.87
	2	0.71	0.24	0.78
	1	0.94	0.26	0.95
6-Storey	2	0.89	0.26	0.92
	4	0.8	0.26	0.85
	1	0.97	0.26	0.98
9-Storey	2	0.94	0.26	0.96
	4	0.89	0.26	0.92

Table 7.7: Preliminary design of the inerters.

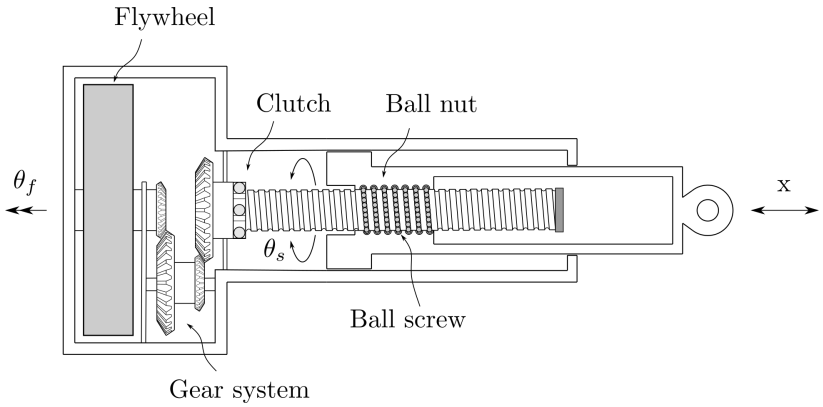

Figure 7.16: Ball-screw and gear inerter.

The rotational angle of the screw, θ_s, can be obtained as a function of the linear displacement:

$$\theta_s = \frac{2\pi}{L_s} x \tag{7.37}$$

where L_s denotes the ball screw lead, which is the linear distance a ball nut travels in one revolution of the ball screw. The rotation of the screw is then amplified by the gear system, so the rotation of the flywheel is given by:

$$\theta_f = \alpha_g \frac{2\pi}{L_s} x \tag{7.38}$$

where α_g denotes the gear amplification ratio. By employing a system of gears in series, Nakamura et al. [96] obtained rotation amplification ratios of $\alpha_g = 5$, while values of up to 10 were used in [98]. On the other hand, the inertial moment exerted by the flywheel is:

$$M_f = I_f \ddot{\theta}_f = I_f \, \alpha_g \frac{2\pi}{L_s} \ddot{x} \tag{7.39}$$

where I_f is the rotational inertia of a flywheel of radius R_f and mass m_f:

$$I_f = \frac{1}{2} m_f R_f^2 \tag{7.40}$$

The axial force in the screw corresponding to this torque is [7]:

$$F_r = \frac{2\pi}{\eta L_s} M_f \tag{7.41}$$

where η indicates the rotary efficiency of the ball-screw mechanism. A representative value of $\eta = 0.95$ is used for the design procedure [96]. Replacing Equations 7.39 and 7.40 into Equation 7.41 the resisting force of the inerter is obtained:

$$F_r = \ddot{x} \, \frac{m_f R_f^2}{2\eta} \left(\alpha_g \frac{2\pi}{L_s} \right)^2 \tag{7.42}$$

Accordingly, the apparent mass of the ball-screw and gear inerter is given by:

$$m_r = 2\, m_f \, R_f^2 \, \frac{\alpha_g^2 \, \pi^2}{\eta \, L_s^2} \tag{7.43}$$

A set of 9 ball-screw and gear inerters is designed considering the apparent mass ratios defined in the previous section (see Table 7.7). A pair of parallel inerters is considered in each case in order to reduce the internal forces in the mechanical components of the devices and to facilitate the implementation of the clutch when required. The thickness of the flywheels, e_f, is determined considering a steel density of $\rho_s = 8\,[Ton/m^3]$. The results of the design process are summarized in Table 7.8.

	$\boldsymbol{\sigma}$ (2 inerters)	$\boldsymbol{L_s}$ [mm]	$\boldsymbol{\alpha_g}$	$\boldsymbol{R_f}$ [m]	$\boldsymbol{e_f}$ [m]	$\boldsymbol{m_f}$ [Kg]	$\boldsymbol{I_f}$ [m^4]	$\boldsymbol{m_r}$ [Ton]
	0.5	12	3	0.05	0.037	2.33	0.003	8
3-Storey	1	12	3	0.06	0.036	3.24	0.006	15
	2	12	3	0.06	0.072	6.48	0.012	30
	1	12	4	0.06	0.04	3.64	0.007	30
6-Storey	2	12	5	0.06	0.052	4.66	0.008	61
	4	12	5	0.065	0.075	7.95	0.017	121
	1	12	4	0.06	0.06	5.46	0.01	45
9-Storey	2	12	5	0.06	0.077	6.99	0.013	91
	4	12	5	0.07	0.083	10.28	0.025	182

Table 7.8: Design of the ball-screw and gear inerters.

7.7 Preliminary assessment of the inerter-equipped structures

A first assessment of the effect of the inerters on the response of the case study structures is conducted considering the set of 7 records described in Section 7.5. The inerter devices connected to the first floor diaphragm are modelled using the same numerical formulation presented in Chapter 6.

7.7.1 Structures equipped with non-clutched inerters

Figure 7.17 to 7.20 compare the mean peak displacement, floor acceleration, inter-storey shear and bending moment demands of the unprotected buildings ($\sigma = 0$) with those of the inerter-equipped ones. The displacement profiles predicted with the simplified pre-dimensioning procedure of Section 7.6.1 are also indicated with a dotted line. Although the use of a rigid block for the representation of a flexible structure inherently introduces a degree of inaccuracy to the methodology, the results of the analyses suggest that the proposed procedure can produce reasonable estimations of displacement response improvements for preliminary design stages. While reductions between 2% and 22% were predicted in Table 7.7, total lateral displacements up to 28% lower are observed in the case of the 3-storey structure. In particular, very good estimations are obtained for the 6 and 9-storey buildings.

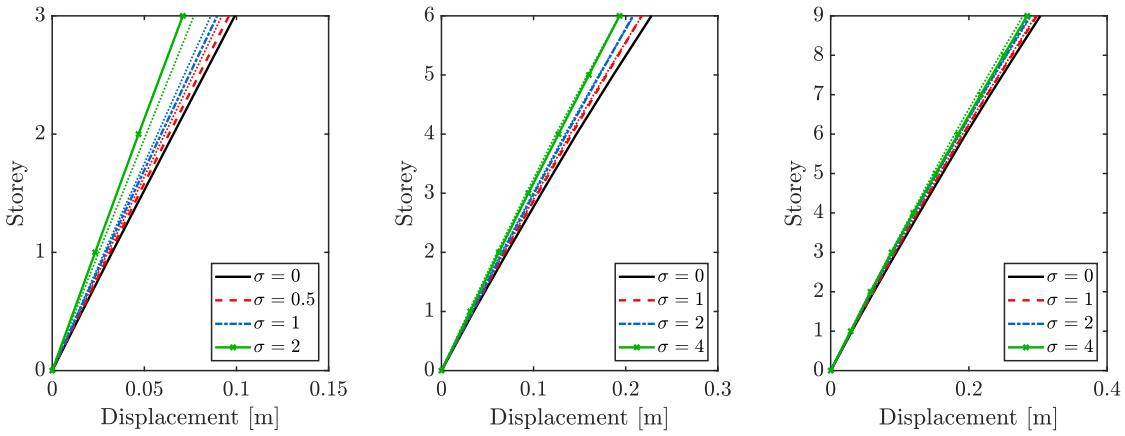

Figure 7.17: Mean peak displacements of the case study buildings equipped with non-clutched inerters subjected to a set of 7 spectrum-compatible accelerograms.

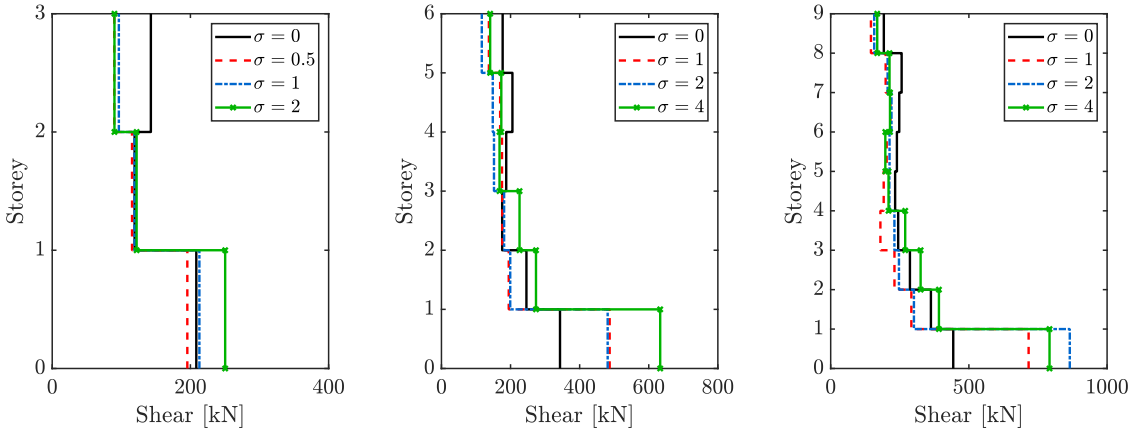

Figure 7.18: Mean peak shear forces of the case study buildings equipped with non-clutched inerters subjected to a set of 7 spectrum-compatible accelerograms.

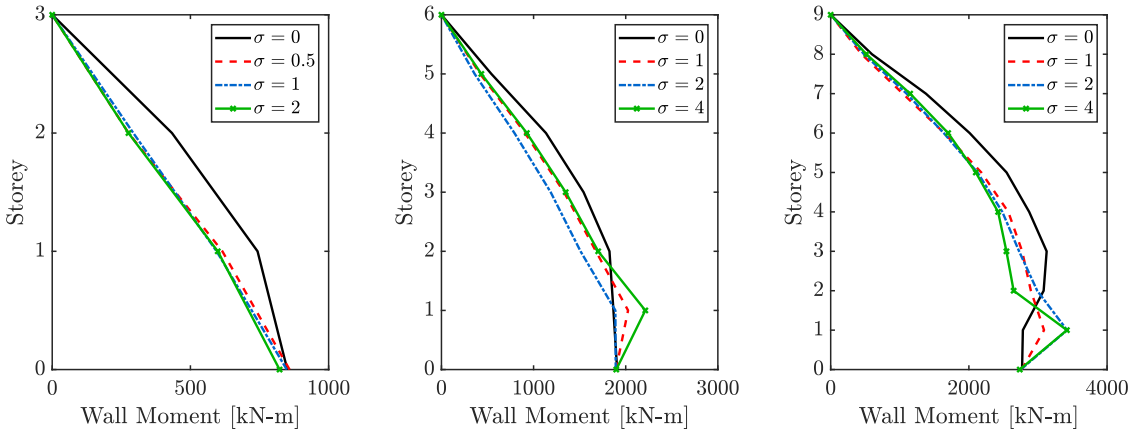

Figure 7.19: Mean peak moments of the case study buildings equipped with non-clutched inerters subjected to a set of 7 spectrum-compatible accelerograms.

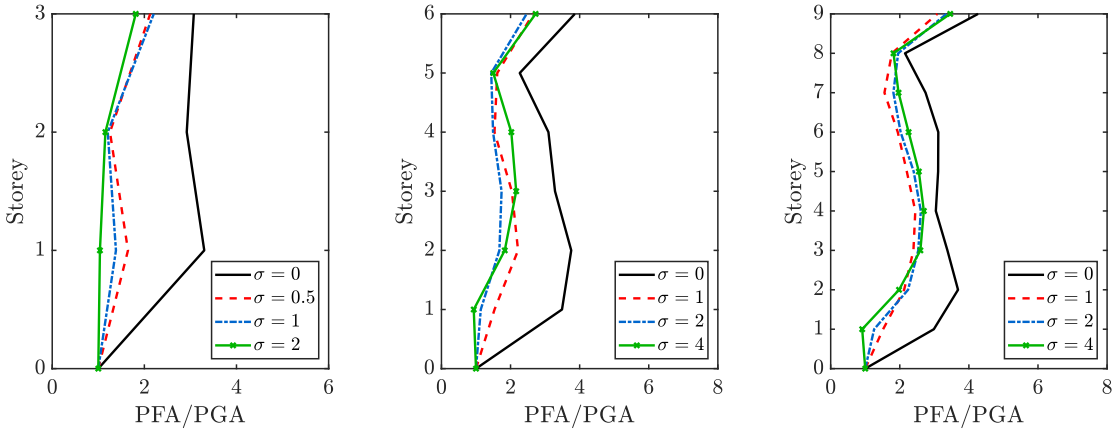

Figure 7.20: Mean peak floor accelerations of the case study buildings equipped with non-clutched inerters subjected to a set of 7 spectrum-compatible accelerograms.

As previously observed in Chapter 6, the introduction of inerters efficiently controls higher-mode effects in flexible rocking structures. This is reflected in significantly lower peak floor accelerations and reduced bending moments above the critical section for the three structural systems under consideration. Although the control of the higher-mode response also reduces inter-storey shears in higher stories, the connection of the inerter to the first storey diaphragm significantly amplifies the shear force in the ground level. This phenomenon is further examined in the following section. Moreover, while increasing levels of apparent mass ratios did not necessarily result in further response improvements, they generally amplified the shear force in the first storey. This points to the existence of optimal inertance values beyond which the device becomes detrimental. It is also important to note that, while the effect of the inerter on the displacement response decreases as the structures become taller, its ability to control higher-mode effects it is not significantly affected by the height of the wall systems.

7.7.2 Structures equipped with clutched inerters

As depicted in Figure 7.16, a clutch can be incorporated into the system to ensure that the inerter can only resist and not drive the motion of the structure. Since a clutched inerter can only oppose one direction of motion, the total apparent mass ratio of the inerters designed in Table 7.8 is divided between the two parallel devices when the clutch is incorporated. Accordingly, the response of structures equipped with clutched inerters is compared with that of the buildings connected to non-clutched inerters of twice the apparent mass ratio. Figures 7.21 to 7.24 present such comparison for the intermediate values of apparent mass ratios considered in the design (i.e. $\sigma = 1$, $\sigma = 2$ and $\sigma = 2$ for the 3, 6 and 9-storey buildings, respectively). The mean response of the unprotected structures ($\sigma = 0$) is also plotted for comparison purposes.

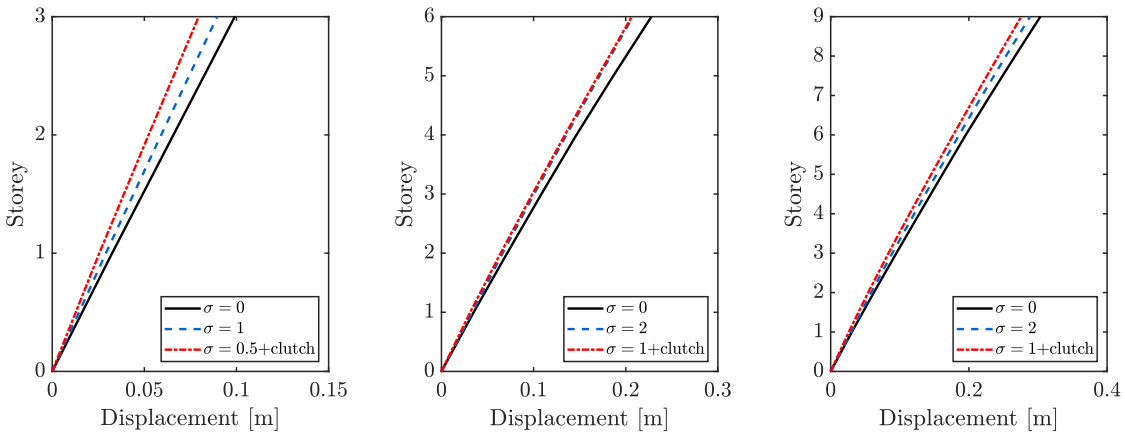

Figure 7.21: Mean peak displacements of the case study buildings equipped with non-clutched and clutched inerters.

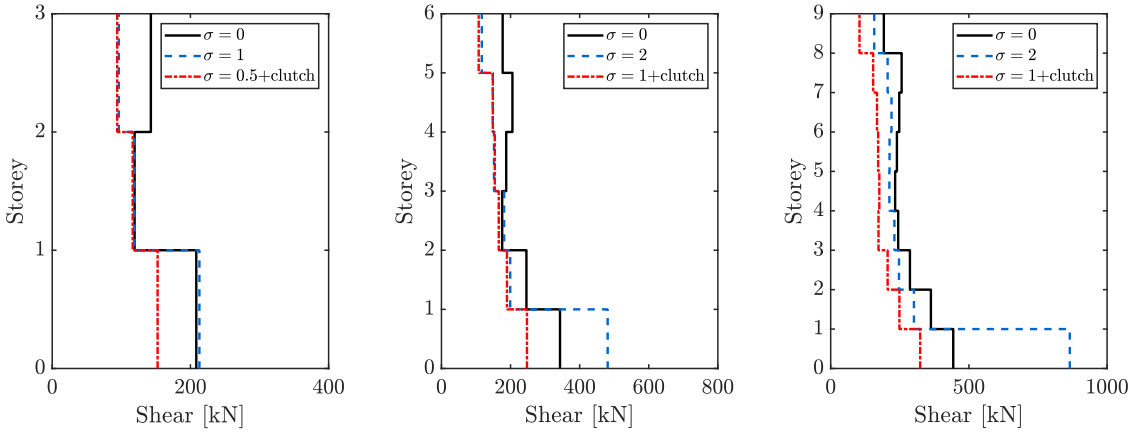

Figure 7.22: Mean peak shear forces of the case study buildings equipped with non-clutched and clutched inerters.

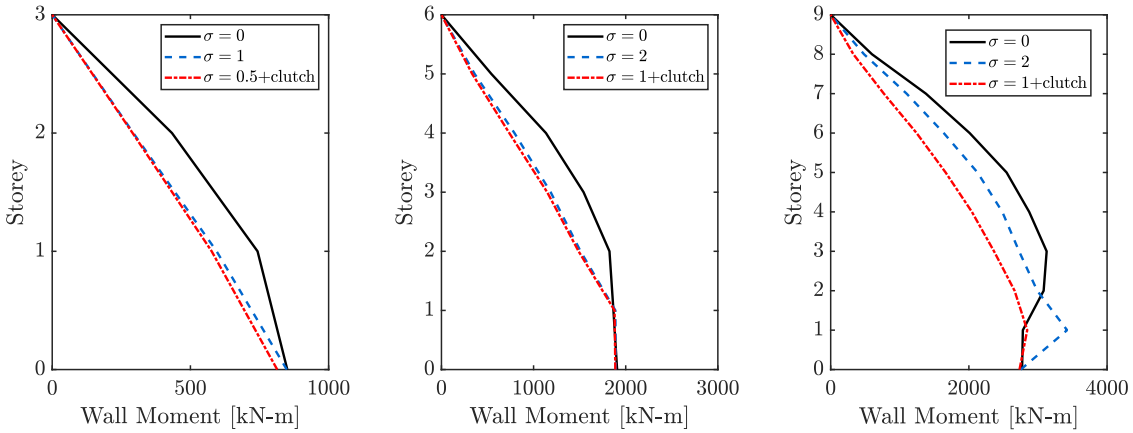

Figure 7.23: Mean peak bending moments of the case study buildings equipped with non-clutched and clutched inerters.

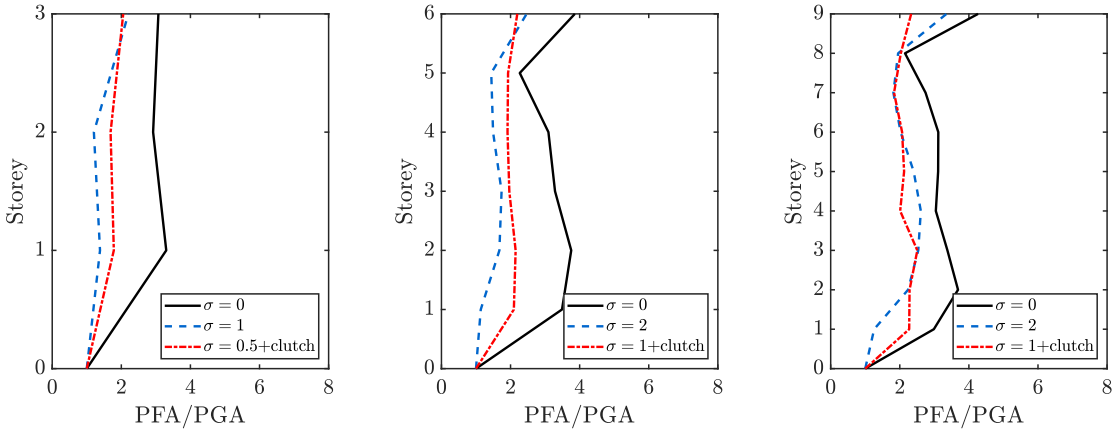

Figure 7.24: Mean peak floor accelerations of the case study buildings equipped with non-clutched and clutched inerters.

Although the introduction of a clutch reduces the total apparent mass ratio of a given pair of parallel inerters, the ability of the system to control the displacement response of rocking structures is not significantly affected. Furthermore, the 3-storey structure equipped with clutched inerters experienced considerably lower mean lateral deformations, while no significant differences are observed in the case of the 6 and 9-storey buildings protected with non-clutched and clutched inerters. A similar trend is observed in the floor accelerations and bending moment distributions of the 3 and 6-storey structures, where peak values of comparable magnitude are obtained along the height of the wall systems for both inerter configurations. The benefits of the clutch become more evident in the 9-storey building, as significant reductions in the maximum floor accelerations and inter-storey moments are obtained. Crucially, a marked reduction in the shear force at the ground level is observed for all of the structures equipped with clutched-inerters, reaching magnitudes even lower than in the unprotected case. This observation suggests that the shear amplification observed in the non-clutched inerter cases is related to a surge in the resisting force as the device drives the structural motion. A closer examination of this phenomenon is presented in Figures 7.25 and 7.26, where the response of the 9-storey structures at the instants of maximum top-storey displacement and maximum base shear is plotted for a single ground motion from the set. The velocity response along the height of the buildings is also included to illustrate the direction of the motion, while the magnitude and direction of the inerter resisting force is indicated in the shear diagram.

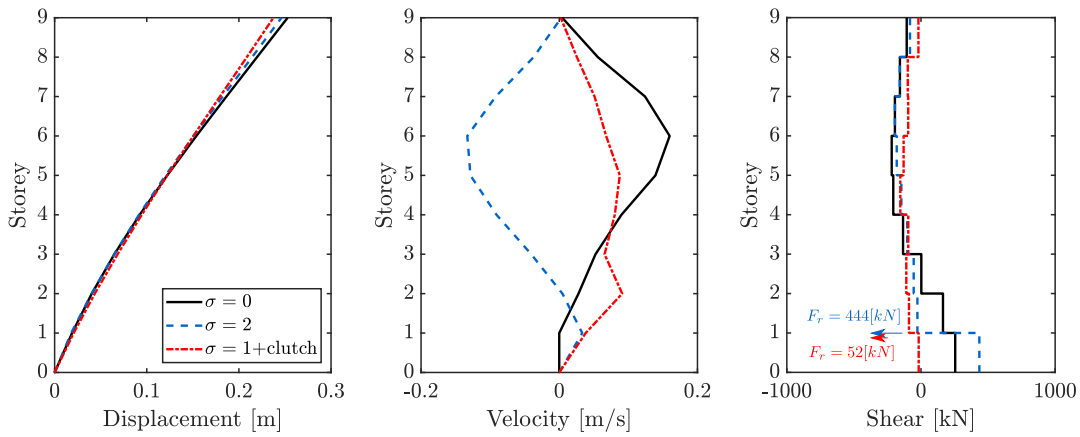

Figure 7.25: Response of the 9-storey buildings with and without inerters to the 1989 Loma Prieta - Gilroy Array #2 record. Instant of maximum top-storey displacement.

Figure 7.25 shows that both inerter configurations oppose the motion of the wall at the instant of maximum roof displacement, increasing the shear forces in the ground floor level. Importantly, the introduction of the clutch considerably reduces the magnitude of the resisting force without compromising the control of the response. Nevertheless, Figure 7.26 demonstrates that the maximum shear at the ground level takes place at smaller lateral deformations, and is highly influenced by the response of higher modes. In the case of the structure equipped

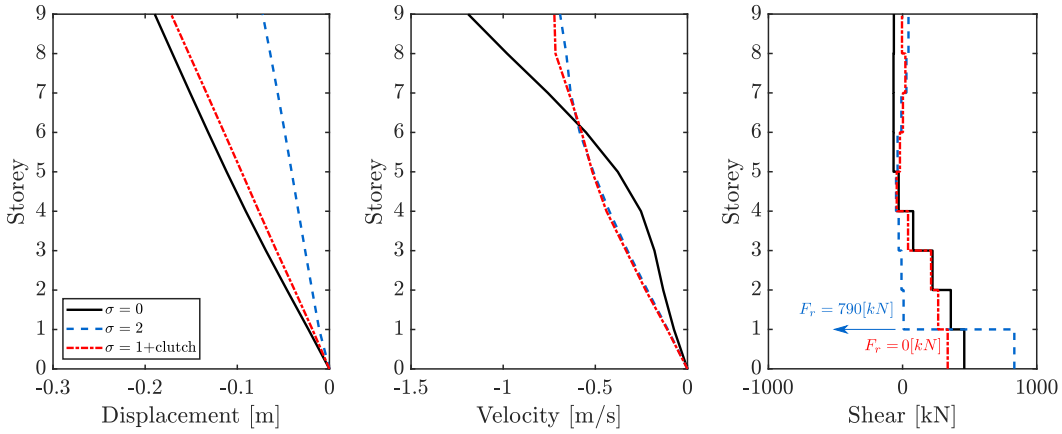

Figure 7.26: Response of the 9-storey buildings with and without inerters to the 1989 Loma Prieta - Gilroy Array #2 record. Instant of maximum shear in the ground level.

with non-clutched inerters, high horizontal accelerations at the first floor generate large inertial forces ($F_r = 790[kN]$) which pull the structure and significantly increase the shear demand. When the clutch is introduced, however, the inerter is not able to drive the motion of the structure and no force is transferred to the wall element. As a result, the peak shear in the structure equipped with clutched inerters is drastically reduced, while no significant increases in the floor accelerations along the height of the buildings is observed (see Figure 7.24).

7.7.3 Resisting force in the inerters

As shown in the previous section, large inertial forces can develop in the inerters during a seismic event. The mechanical components of the devices, as well as the connection to the floor diaphragm, must be designed to resist these demands, potentially limiting the practicality of the proposed strategy. A quantification of the magnitude of such forces is presented in Figure 7.27, where the mean peak total force in the pair of parallel inerters is plotted for the structural systems analysed above.

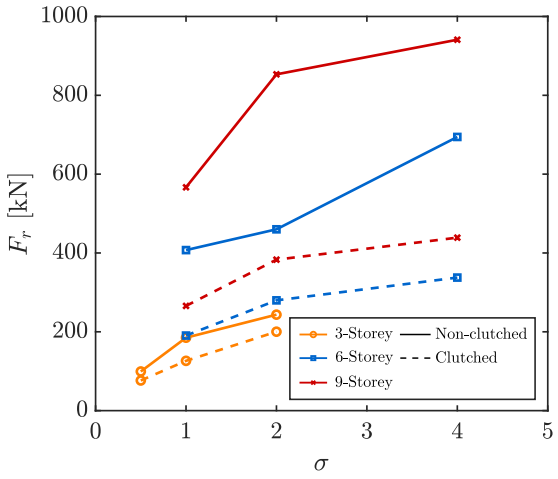

Figure 7.27: Mean total force in the inerter systems (2 parallel devices).

It is important to note that the inertance, m_r, required to achieve any given apparent mass ratio, σ, is directly proportional to the total weight of the structure. This observation explains the pronounced rise in the inerter resisting force as the buildings become taller. Figure 7.27 also shows the trends observed in the previous section, where significantly lower inertial forces were observed when the clutch was introduced. The results summarized in the figure show reductions of up to 60% in the case of the 9-storey building equipped with clutched inerters. Importantly, the observed reduction of the inertial forces does not affect the ability of the inerter to control the seismic response of the structural systems. The relevance of these results is highlighted in the following section, where mechanisms to limit and transfer the force in the inerter to the floor diaphragm are proposed.

7.8 Design of the inerter-diaphragm connection

The resisting force developed in the inerter devices must be transferred to the ground and to the floor diaphragm. Makris and Kampas [95] first proposed the use of a rigid chevron frame for the implementation of a pinion-rack-flywheel inerter in SDOF fixed-base structures. The same concept is applied in Figure 7.28, where the inerter devices designed in the previous sections are supported by a rigid frame and connected to the floor diaphragm through a screwed or bolted steel plate. Replaceable fuse elements are incorporated in order to limit the resisting force that can develop in the inerter and protect its mechanical components and the steel-timber connection. Two alternatives are proposed: (i) Buckling-restrained bars designed to yield in tension and compression at a pre-defined axial load [61,86], and (ii) flexural plates, such as TADAS devices [163], designed to bend and yield thus limiting the force than can be transferred between the inerter and the floor diaphragm.

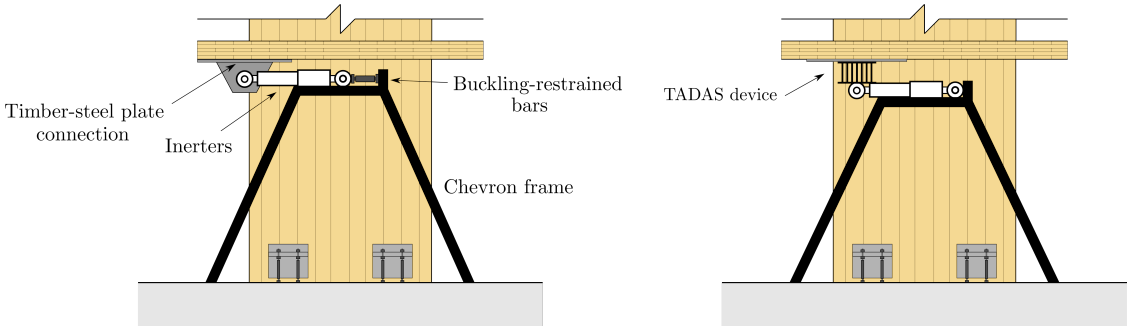

(a) Buckling-restrained bars. (b) TADAS device.

Figure 7.28: Proposed alternatives for the implementation of grounded inerters at the first level.

Based on the response improvements observed in the preliminary assessment of Section 7.7 and practical considerations regarding the magnitude of the associated inertial forces, a single apparent mass ratio is selected for each case study building and inerter configuration (see Table 7.9). The corresponding mean resisting forces presented in Figure 7.27 are considered as

the characteristic seismic demand, E_k. Accordingly, the design demand for the fuse elements is obtained as $E_d = \gamma_I E_k$, where $\gamma_I = 1.0$ for residential buildings (EN1998-1:2004 4.2.5). Buckling-restrained bars are selected as fuse elements considering the same material properties described in Table 7.4. The results of the design procedure are summarized in Table 7.9.

				Buckling-restrained bars		
	Inerter type	$\boldsymbol{\sigma}$	$\boldsymbol{E_d}\,[kN]$	$\boldsymbol{\phi_s}[mm]$	$\boldsymbol{A_s}[cm^2]$	$\boldsymbol{l'_{ub}}[m]$
3-Storey	Non-clutched	1	185	3 ϕ 16	6	0.15
	Clutched	0.5	126	2 ϕ 16	4	0.15
6-Storey	Non-clutched	2	460	3 ϕ 25	14.7	0.15
	Clutched	1	280	3 ϕ 20	9.4	0.15
9-Storey	Non-clutched	2	853	6 ϕ 24	27.1	0.15
	Clutched	1	383	4 ϕ 20	12.6	0.15

Table 7.9: Design of the fuse elements for the inerter connection.

Finally, the timber-steel plate connection is capacity designed considering an over-strength factor for the fuse elements of $\gamma_{ov} = 1.25$. A cross-laminated timber floor of thickness $e_{clt} = 0.2[m]$ and characteristic density $\rho_k = 380[Kg/m^3]$ is assumed for design, while coach screws KOP16200 (Rotho Blaas catalogue [164]) are selected as connector elements. Additionally, a steel plate with a thickness equal to the external diameter of the screws, $e_s = d_1$, is used to distribute and transfer the resisting force from the inerter. The mechanical properties and distancing specifications of the screws are described in Table 7.10.

Nominal diameter	d_1 [mm]	16
Shank diameter	d_s [mm]	16
Effective diameter	d_{eff} [mm]	16
Length	L [mm]	200
Effective length	l_{eff} [mm]	120
Characteristic yield moment	$M_{y,k}$ [Nmm]	138000
Characteristic withdrawal-resistance parameter	$f_{ax,k}$ $[N/mm^2]$	10
Associated density	ρ_a $[kg/m^3]$	360
Minimum distance parallel to grain (pre-drilling holes)	a_1 $[mm]$	64
Minimum distance perpendicular to grain (pre-drilling holes)	a_2 $[mm]$	64

Table 7.10: Mechanical properties and distancing specifications for coach screws KOP16200 [164].

The characteristic strength of the connections is calculated according to Eurocode 5. The penetration depth, t_1, is obtained based on the dimensions of the screws and the thickness of

the steel plate. Thus:

$$t_1 = L - e_s = 184[mm] \tag{7.44}$$

The embedding strength for the screws is calculated using:

$$f_{h,1,k} = 0.082\,(1 - 0.01\,d_{eff})\,\rho_k = 26.2\,[N/mm^2] \tag{7.45}$$

and the characteristic withdrawal capacity:

$$R_{ax,k} = \frac{f_{ax,k}\,d_{eff}\,l_{eff}}{1.2}\left(\frac{\rho_k}{\rho_a}\right)^{0.8} = 17\,[kN] \tag{7.46}$$

Then, the load-carrying capacity per connector is obtained according to Eurocode 5 8.2.3, considering the expressions for thick steel plates in single shear (modes c, d and e):

$$R_k = min\begin{cases} f_{h,1,k}\,t_1\,d_{eff} \\ f_{h,1,k}\,t_1\,d_{eff}\left(\sqrt{2 + \frac{4M_{y,k}}{f_{h,1,k}\,t_1^2\,d_{eff}}} - 1\right) + \frac{R_{ax,k}}{4} \\ 2.3\sqrt{M_{y,k}\,f_{h,1,k}\,d_{eff}} + \frac{R_{ax,k}}{4} \end{cases} = 21.66[kN] \tag{7.47}$$

The design strength per connector is then obtained considering $k_{mod} = 1.1$ (instantaneous action) and $\gamma_m = 1$ (accidental combinations):

$$R_d = \frac{k_{mod}\,R_d}{\gamma_m} = 23.83\,[kN] \tag{7.48}$$

On the other hand, the effective number of screws for one row of n connectors is obtained as:

$$n_{eff} = min\begin{cases} n \\ n^{0.9}\sqrt[4]{\frac{a_1}{13\,d_{eff}}} \end{cases} \tag{7.49}$$

A distance between connectors of $a_1 = a_2 = 64\,[mm]$ is assumed according to the manufacturer specifications. The required effective number of screws is then obtained dividing the over-strength design shear, $V_{d,\gamma}$, by the characteristic strength of each connector. The final design of the timber-steel connections is described in Figure 7.29 and Table 7.11.

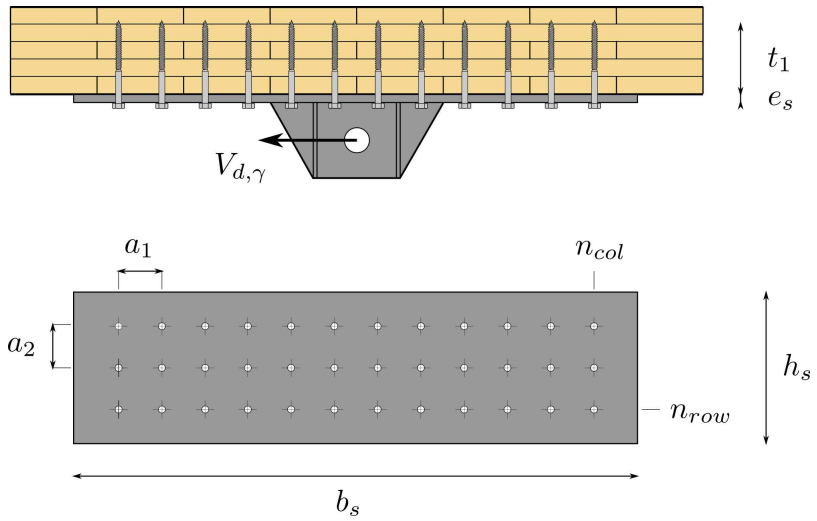

Figure 7.29: Timber floor to inerter connection.

	Inerter type	σ	V_d [kN]	$V_{d,\gamma}$ [kN]	n_{row}	n_{col}	b_s [mm]	h_s [mm]
3-Storey	Non-clutched	1	185	241	3	6	448	256
	Clutched	0.5	126	161	3	4	320	256
6-Storey	Non-clutched	2	460	589	4	11	768	320
	Clutched	1	280	377	3	9	640	256
9-Storey	Non-clutched	2	853	1086	5	17	1152	384
	Clutched	1	383	503	4	9	640	320

Table 7.11: Design of the timber-steel plate connections.

The design results show that increasingly large connections are required as the buildings become taller, an aspect that can potentially limit the applicability of the proposed strategy in high-rise buildings. Nevertheless, the introduction of clutches significantly reduces the magnitude of the shear design force, resulting in considerably smaller and more practical connections.

7.9 Performance-based assessment

Given the uncertainties involved, the evaluation of the performance of inerter-equipped structures ought to be carried out within an explicit probabilistic framework. In this context, the mean annual frequency of exceeding a predefined *Engineering Demand Parameter* EDP (such as peak inter-storey drift, peak floor acceleration, etc.) can be obtained as:

$$\lambda(EDP > edp) = \int P(EDP > edp \,|\, IM = im) \,|d\lambda(im)| \tag{7.50}$$

where IM denotes the ground motion intensity measure (e.g. spectral elastic acceleration at the first-mode period of vibration) and λ_{IM} represents the seismic hazard at the site, measured in terms of mean annual frequency of exceeding a level of intensity im. The first term of Equation 7.50, commonly referred to as the fragility of the structure, expresses the conditional probability of exceeding an specific edp given that the ground motion intensity measure is equal to im. Information regarding the fragility of the structure is generally obtained from non-linear dynamic analyses performed for a specific structure subjected to a set of ground motions scaled to various levels of seismic intensity.

In this section, the performance of the 3, 6 and 9-storey timber buildings described above is assessed and compared within this probabilistic framework, considering the mass ratios for each inerter configuration as defined in Table 7.11. The performance of the structures is compared in terms of maximum inter-storey drifts and floor accelerations, Engineering Demand Parameters (EDPs) that are usually indicative of structural and non-structural damage.

7.9.1 Numerical models and ground motion database

The same set of 202 pulse-like ground motion records used in previous chapters is employed in the assessment. The earthquake catalogue, presented in Table 3.1, contains all the pulse-like records available in the PEER database and covers a range of magnitudes between 5.4 and 7.9, and closest distance-to-ruptured area (R_{rup}) up to 56 [km], as illustrated in the scatter diagram in Figure 7.30a. Figure 7.30b, on the other hand, shows the corresponding 5%-damped elastic acceleration spectra and the associated mean, 16^{th} and 84^{th} percentiles.

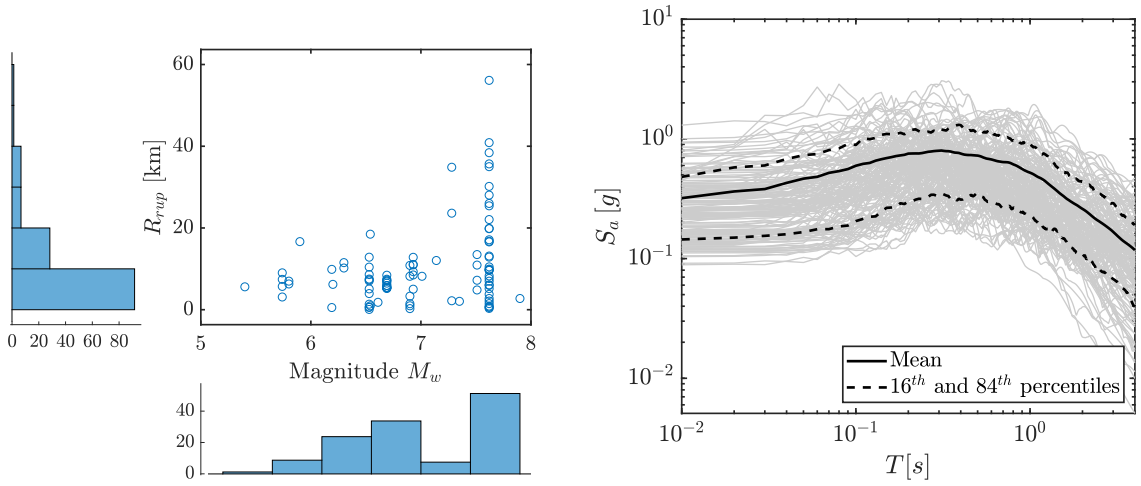

(a) Magnitude-R_{rup} scatter diagram.

(b) Elastic response spectra, $\xi = 5\%$.

Figure 7.30: Magnitude-R_{rup} scatter diagram and 5% damped elastic spectra of the record set used for the performance based assessment.

The buildings are modelled using the numerical formulation described in Section 7.4, incorporating a zero-length element with a perfectly-plastic material to represent the fuse elements.

The steel-timber connection, on the other hand, is assumed to remain fully elastic, as it is capacity designed.

7.9.2 Cloud Analysis

The bare and inerter-equipped case study structures are subjected to the suite of 202 ground motion records described in the previous section. The resulting Cloud data contains pairs of ground motion intensity measures (IM) and their corresponding structural performance variable (EDP). As done in previous chapters, a linear regression in the natural logarithmic scale is applied in order to estimate the statistical properties of the Cloud data. Accordingly, the conditional median demand $\widehat{EDP}$ for a given IM can be predicted as:

$$\ln \widehat{EDP}\,(IM) = \ln a + b \ln(IM) \tag{7.51}$$

where $\ln a$ and b are parameters of the linear regression. This equation is equivalent to fitting a power-law in the original arithmetic scale. The (constant) conditional logarithmic standard deviation of EDP given IM can be estimated as [135]:

$$\beta_{EDP|IM} = \sqrt{\sum_{n=1}^{N} \left(\ln EDP_i - \ln\left(a\, IM_i{}^b\right)\right)^2/(N-2)} \tag{7.52}$$

where EDP_i and IM_i are the corresponding Cloud data for the $i-th$ record in the set and N is the number of records. Based on the results obtained by Giouvanidis et al. [42] and observations from Chapters 3 and 4, four different intensity measures are assessed and compared: uniform time duration (t_{uni}), peak ground velocity (PGV), peak ground acceleration (PGA), and the 5% damped spectral acceleration at the first fixed-base structural period, $S_a(T_1)$. As defined in Chapter 3, the computation of t_{uni} entails the identification of the minimum ground acceleration required to trigger the rocking motion. Although it is recognized that elastic deformations prevent the definition of a unique uplift ground acceleration, the analyses presented in Chapter 4 demonstrated that this value can be reasonable approximated by:

$$\ddot{u}_{g,crit} = \left(\frac{P_0}{W} + 1\right)\frac{g}{m_{ratio}} \tan \alpha_{cg} \tag{7.53}$$

where P_0 corresponds to the initial post-tensioning force, W is the gravity load in the wall, m_{ratio} is the mass ratio defined in Section 4.2 and equal to 4 for buildings at hand, and α_{cg} is the slenderness of the centre of mass of the wall. Table 7.12 and 7.13 describe the goodness of fit of the regression models for the four IMs under consideration.

		t_{uni}		PGV		PGA		$S_a(T_1)$	
N° Storeys	σ	R^2	β	R^2	β	R^2	β	R^2	β
3	0	0.57	0.61	0.34	0.77	0.65	0.56	0.58	0.61
	1	0.56	0.59	0.35	0.73	0.63	0.56	0.55	0.61
	0.5+clutch	0.56	0.68	0.31	0.87	0.76	0.51	0.67	0.6
6	0	0.47	0.54	0.54	0.51	0.52	0.52	0.57	0.49
	2	0.48	0.55	0.55	0.51	0.49	0.55	0.54	0.52
	1+clutch	0.47	0.59	0.54	0.55	0.59	0.52	0.64	0.48
9	0	0.4	0.51	0.67	0.38	0.39	0.52	0.59	0.42
	2	0.4	0.52	0.66	0.39	0.38	0.52	0.59	0.43
	1+clutch	0.39	0.54	0.65	0.4	0.42	0.53	0.65	0.41

Table 7.12: Correlation coefficient, R^2, and standard deviation, β, of the regression models for the maximum inter-storey drift.

		t_{uni}		PGV		PGA		$S_a(T_1)$	
N° Storeys	σ	R^2	β	R^2	β	R^2	β	R^2	β
3	0	0.35	0.38	0.09	0.47	0.28	0.42	0.3	0.41
	1	0.37	0.28	0.12	0.34	0.23	0.32	0.21	0.32
	0.5+clutch	0.59	0.26	0.18	0.39	0.65	0.26	0.64	0.26
6	0	0.44	0.32	0.2	0.38	0.35	0.34	0.38	0.33
	2	0.47	0.26	0.2	0.32	0.37	0.28	0.35	0.29
	1+clutch	0.49	0.28	0.3	0.33	0.66	0.23	0.69	0.22
9	0	0.45	0.31	0.24	0.36	0.39	0.33	0.34	0.34
	2	0.42	0.31	0.2	0.37	0.46	0.3	0.37	0.33
	1+clutch	0.37	0.35	0.31	0.36	0.71	0.24	0.61	0.27

Table 7.13: Correlation coefficient, R^2, and standard deviation, β, of the regression models for the peak floor acceleration.

Table 7.12 shows that $S_a(T_1)$ is consistently the most efficient IM for the prediction of the maximum inter-storey drift, with correlation coefficients close to $R^2 \approx 0.6$ in most cases, even though PGA and PGV show a stronger correlation for the 3 and 9-storey buildings, respectively. On the other hand, none of the proposed intensity measures shows a strong correlation with the peak floor acceleration (PFA) response, presenting R^2 values below 0.5 in all cases. This can be partially explained by the behaviour observed in Chapter 6, where forces developed during impact were shown to excite higher modes of the response, increasing the lateral accelerations regardless of the characteristics of the ground motion. While it is recognized that further research is required for the definition of intensity measures

that can efficiently predict PFAs, the most efficient IM from the set, t_{uni}, is adopted for the seismic demand analysis presented in this section. Figures 7.31 to 7.33 compare the peak inter-storey drift and floor acceleration demands obtained for the bare and inerter-protected structures, considering the regression models described above. The remaining regression plots are presented in Appendix C.

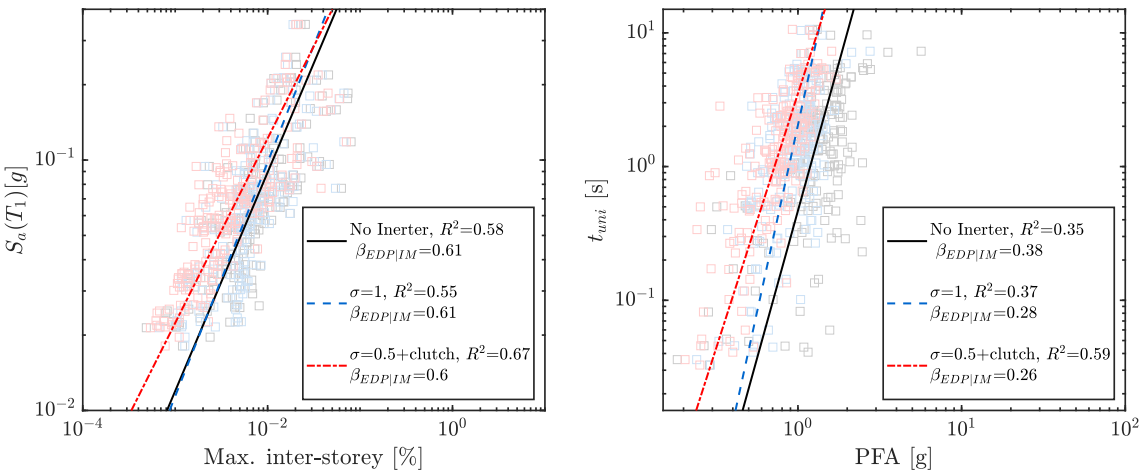

Figure 7.31: Cloud analysis results and seismic demand prediction models for the 3-Storey structures.

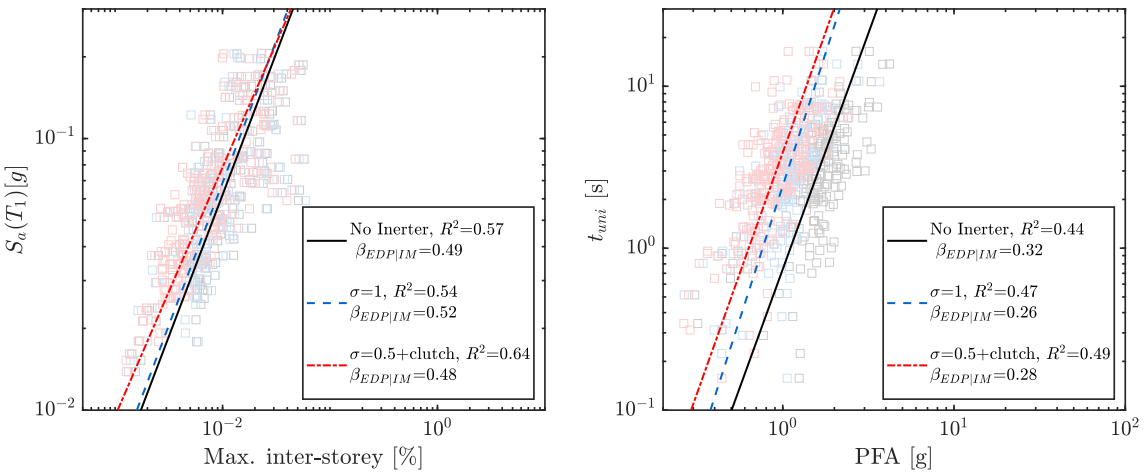

Figure 7.32: Cloud analysis results and seismic demand prediction models for the 6-Storey structures.

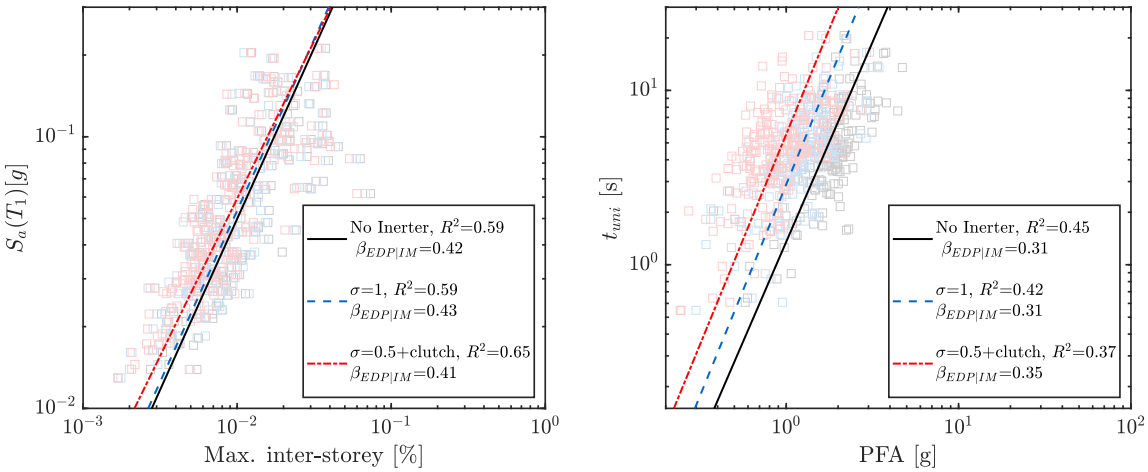

Figure 7.33: Cloud analysis results and seismic demand prediction models for the 9-Storey structures.

The main advantage of the inerter devices is clearly evidenced in the floor acceleration plots, where considerably lower demands are observed across the whole range of intensity levels under consideration. As discussed in Chapter 6, the inclusion of inerters attenuates the high frequency vibrations induced during impact and elongates the vibration periods of the structures, thus shifting them towards lower spectral ordinates (see Appendix B). Moreover, the inclusion of clutches further improves the floor acceleration response. On the other hand, the results of the analyses show that the structures equipped with non-clutched inerters experience slightly smaller drift demands than the unprotected ones. The addition of the clutch, however, further improves the drift response for low to mid IMs, but becomes less effective under higher seismic intensity levels. This behaviour is further examined in Figure 7.34, where the base rotation response and the resisting force in the inerters of the 9-storey structure are compared for ground motions with $S_a(T_1) = 0.08g$ (low intensity) and $S_a(T_1) = 0.15g$ (high intensity). The response histories presented in these plots show that, as the seismic intensity grows, the force in the inerter reaches the capacity of the fuse elements, thus capping the force that can be transmitted to the structure and limiting the effect of the inerter on the response.

7.9.3 Fragility assessment based on Cloud Analysis

The *Cloud to IDA* procedure proposed by Miano et al. [135] is used for the estimation of the structural fragilities. This methodology employs the critical demand to capacity ratio (DCR) as the performance variable, thus facilitating the identification of intensity values at the onset of a desired limit state. In this way, IDA curves can be obtained for a selected group of ground motion records with a minimum amount of scaling, which is known to be particularly problematic when pulse-like records are considered [165, 166]. In this context, DCR_{LS} is defined as the demand to capacity ratio for a given limit state LS:

$$DCR_{LS} = \frac{D_{jl}}{C_{jl}(LS)} \tag{7.54}$$

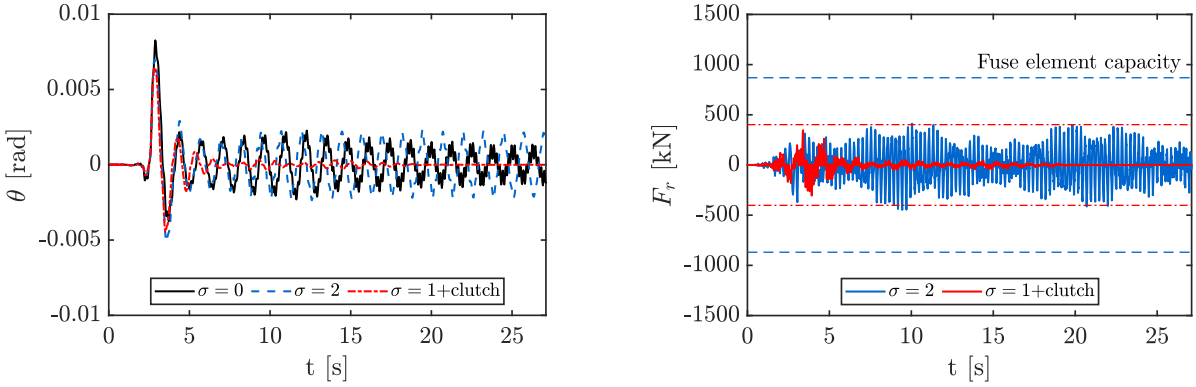

(a) Response to the 1976 Coyote Lake - Gilroy Array #6 record ($S_a(T_1) = 0.08g$).

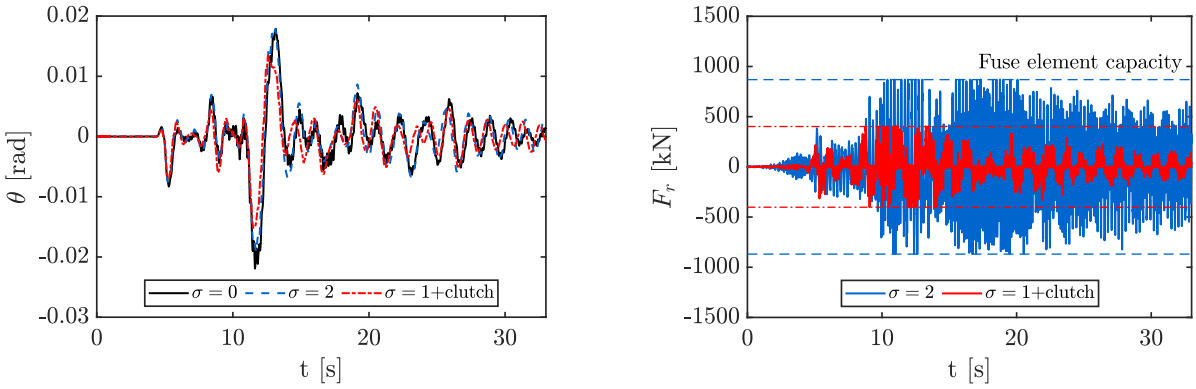

(b) Response to the 1978 Tabas, Iran record ($S_a(T_1) = 0.15g$).

Figure 7.34: Base rotation response and resisting force in the inerters of the 9-storey buildings subjected to ground motion records of low and high $S_a(T_1)$.

where D_{jl} is the demand evaluated for the j^{th} component of the l^{th} mechanism, and $C_{jl}(LS)$ is the limit state capacity for the j^{th} component of the l^{th} mechanism. Accordingly, DCR_{LS} is always equal to unity at the onset of a given limit state LS. In this work, the critical DCR is evaluated for limit states associated with extensive non-structural and contents damage, defined in accordance with current guidelines for seismic performance-based assessment of buildings. The inter-storey drift limit defined in Eurocode 8 [134] for buildings having ductile non-structural components, $\Delta = 0.75\%$, is adopted for displacement-sensitive elements, whereas a floor acceleration limit of $PFA = 1\,g$ is defined for acceleration-sensitive non-structural components [167, 168].

The procedure to derive the IDA-based fragility curves from the Cloud data is illustrated in Figure 7.35 for the drift limit state of the bare 3-storey structure. Firstly, the predicted mean intensity that brings the building to the onset of the considered limit state, $S_{a,CLoud}^{DCR=1}$, is obtained from the regression models presented in the previous section. With this information, the data points can be screened to identify the records with $S_a(T_1)$ close to $S_{a,CLoud}^{DCR=1}$ and DCR_{LS} not too distant from unity. This selection procedure is formalized by defining two confidence bands centred around $S_{a,CLoud}^{DCR=1}$ and $DCR_{LS} = 1$. The logarithmic standard deviation for

DCR_{LS} at $S_{a,CLoud}^{DCR=1}$, estimated by the standard error of regression $\beta_{DCR_{LS}|S_a}$ (Equation 7.52), is used to define the confidence interval around $DCR_{LS} = 1$. Similarly, the logarithmic standard deviation for $S_a(T_1)$ at $DCR_{LS} = 1$, estimated as $\beta_{DCR_{LS}|S_a}/b$, is used to define the confidence bands around $S_{a,CLoud}^{DCR=1}$. Figure 7.35a shows the box-shape area created by the intersection of plus/minus one quarter of the standard deviation from $S_{a,CLoud}^{DCR=1}$ and plus/minus half the standard deviation from $DCR_{LS} = 1$. Importantly, the choice of the width of the confidence bands is qualitative, aiming to encompass at least 20 ground motion records that will be potentially scaled up/down by a factor lower than 1.5.

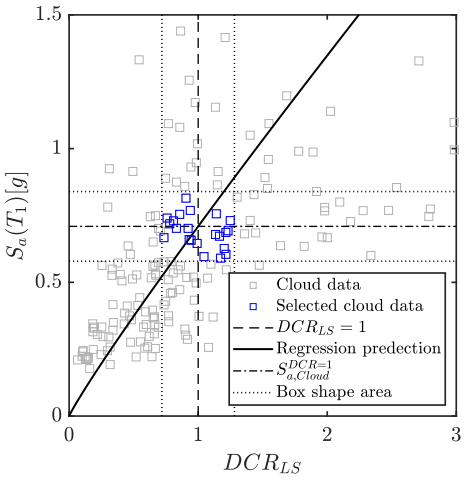

(a) Cloud data selection.

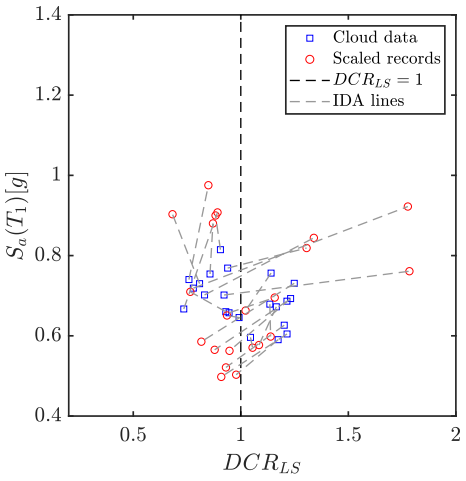

(b) IDA curve segments.

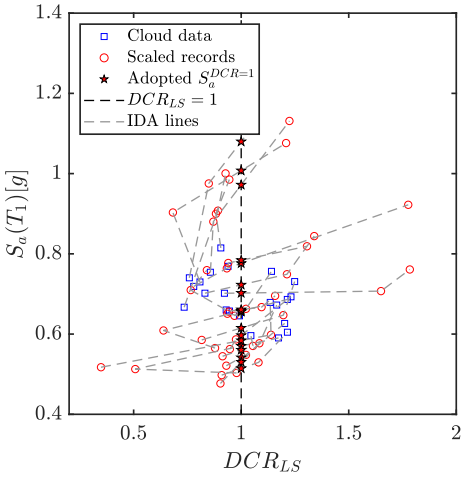

(c) $S_a^{DCR=1}$ estimation.

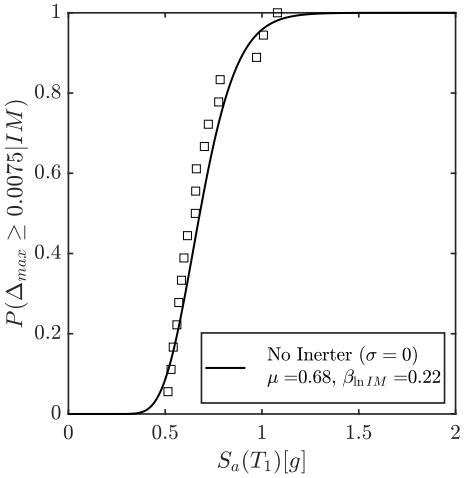

(d) Fragility curve.

Figure 7.35: Cloud to IDA procedure for the drift limit state of the 3-storey structure.

In the next step, the selected ground motions are scaled by a factor equal to $1.0/DCR_{LS,i}$, and the corresponding performance variables obtained from the response history analyses. At this point, a first approximation of the IDA segments is obtained by connecting the two data points for each selected record (Figure 7.35b). The corresponding $S_a^{DCR=1}$ are subsequently interpolated (or projected), and the analyses run once again with the records scaled to this new intensity value. The final $S_a^{DCR=1}$ estimations are ultimately interpolated from this refined IDA segments (Figure 7.35c), and the associated fragilities calculated assuming a log-normal distribution for $S_a^{DCR=1}$ [40] (Figure 7.35d).

Figure 7.36 compares the fragility curves obtained for the different case study structures and limit states under consideration. Additionally, Tables 7.14 and 7.15 summarize the mean and standard deviations of the fitted log-normal distributions in order to facilitate the comparison of trends. Although the previous section showed that the uniform duration, t_{uni}, was the most efficient IM for the prediction of peak floor accelerations, it is recognized that scaling the time scale or frequency content of pulse-like records can bias the expected non-linear response [169, 170]. Alternatively, the peak ground acceleration (PGA), which showed similar levels of correlation, is adopted for the derivation of the PFA fragilities presented below.

The plots show that, in general, the inerter equipped structures have lower probabilities of reaching the defined limit states for any given IM value. In particular, the mean $S_a(T_1)$ required to exceed the assumed drift limit grows considerably when the inerters are incorporated, although this effect becomes less significant as the structures become taller. Moreover, the incorporation of inerters tends to increase the variability of the lateral deformation response. The combination of these effects explain the behaviour observed in the drift fragility plots, where a better response control is obtained for larger probabilities of exceedence, and small differences are observed under lower seismic intensities. Notably, the 9-storey building equipped with non-clutched inerters exhibits slightly higher probabilities of exceeding the assumed drift limit than the unprotected structure under low seismic intensities. On the other hand, the incorporation of clutches improved the drift response in all cases, an observation that is line with the results obtained in the previous section.

Much more significant improvements are observed in the peak floor acceleration response. Estimated mean PGA values of up to 3 times larger are obtained for the buildings equipped with inerters for a limit state of extensive damage. Nevertheless, as the structures become taller, the effect of the inerter on the frequency parameter (Equation 7.31) and the vibration periods of the system (see Appendix B) becomes less significant, thus reducing the efficiency of the protective measure. The introduction of clutches, however, significantly improves the acceleration response of the three structures under consideration. Importantly, the inerters also reduced the variability of the floor acceleration response, indicating an efficient control of higher-mode effects. The conclusions presented above are consistent with results obtained in

preceding chapters, and allow to conclude that the use of inerters constitutes a viable alternative to control seismic demands and higher mode-effects in rocking structural applications.

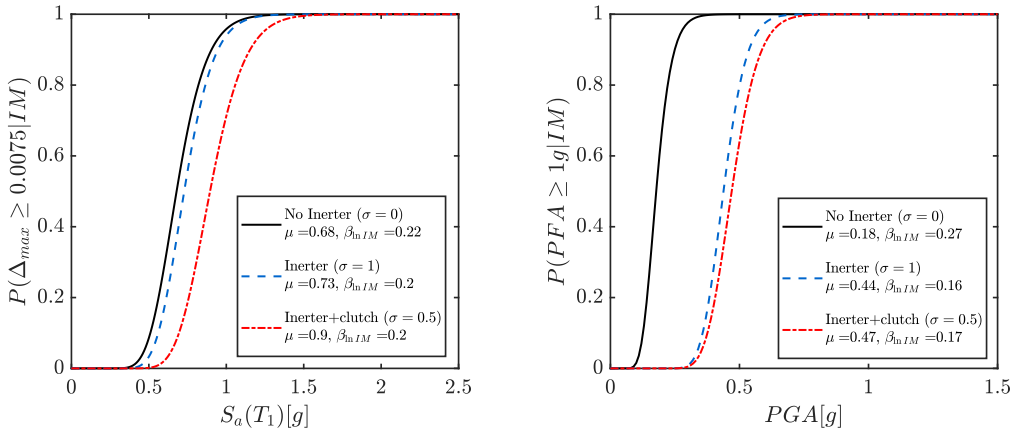

(a) 3-Storey structures.

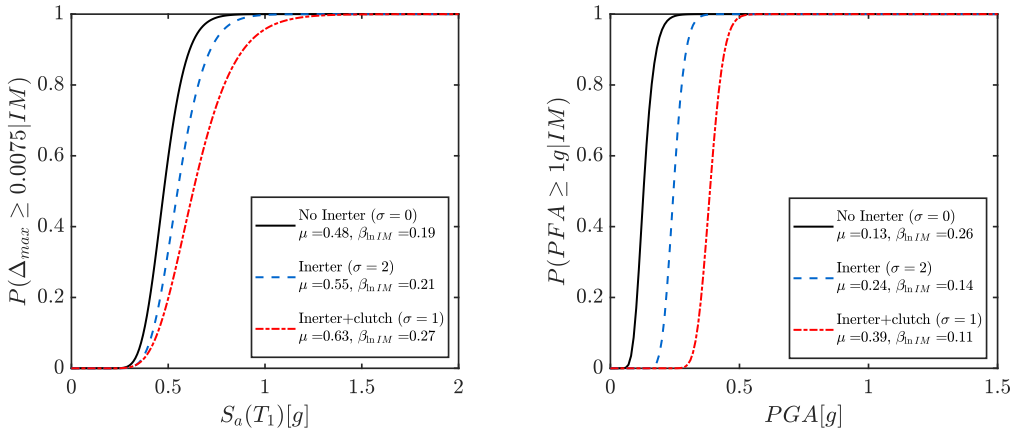

(b) 6-Storey structures.

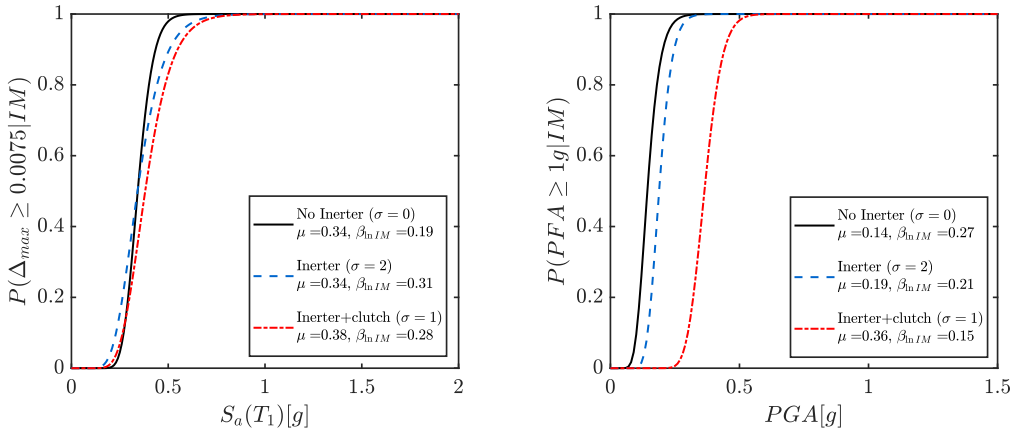

(c) 9-Storey structures.

Figure 7.36: Structural fragilities for the defined limit states of $\Delta = 0.75\%$ and $PFA = 1\,g$.

	3-Storey			6-Storey			9-Storey		
σ	0	1	0.5+clutch	0	2	1+clutch	0	1	1+clutch
μ	0.68	0.73	0.9	0.48	0.55	0.63	0.34	0.34	0.38
$\beta_{\ln\|IM}$	0.22	0.2	0.2	0.19	0.21	0.27	0.19	0.31	0.28

Table 7.14: Parameters of the fitted log-normal distributions for the maximum inter-storey drift.

	3-Storey			6-Storey			9-Storey		
σ	0	1	0.5+clutch	0	2	1+clutch	0	1	1+clutch
μ	0.18	0.44	0.47	0.13	0.24	0.39	0.14	0.19	0.36
$\beta_{\ln\|IM}$	0.27	0.16	0.17	0.26	0.14	0.11	0.27	0.21	0.14

Table 7.15: Parameters of the fitted log-normal distributions for the peak floor accelerations.

7.10 Concluding remarks

This chapter has examined the possibility of employing inerters to improve the seismic performance of post-tensioned timber buildings. In a first stage, a set of three case study structures, comprising 3, 6 and 9 storeys, was designed following Direct-Displacement-Based Design guidelines. The response of the bare structures to a sub-set of 7 ground motion records consistent with the design spectrum was evaluated and compared with the design predictions. While good estimations of peak displacements were obtained, the analyses showed that bending moments and shears throughout the structures can be strongly underestimated due to the influence of higher modes on the response. Moreover, large floor accelerations were also observed, specially in the taller buildings. The results of these analyses were later used as a benchmark for a preliminary assessment of the effect of the inerter devices on the seismic response of the structures.

Based on results and conclusions from previous chapters, a simplified procedure to pre-dimension the inerter devices was put forward in this chapter. The proposed methodology hinges on the observation that the response of an inerter-equipped rigid block is equivalent to that of a larger bare block of the same slenderness. Then, by equating their frequency parameters, the equivalent size of the larger block can be obtained. On the other hand, Reggiani and Vassiliou [162] demonstrated that two blocks of different size but identical slenderness experience the same top displacement, provided that they are not close to overturn. This equal displacement rule facilitates the definition of a relation between the base rotation of the blocks based on their size ratio. In this way, a rotation reduction factor can be defined for any given apparent mass ratio. Moreover, Chapter 6 demonstrated that the inerter has little effect on the elastic deformation response of a flexible rocking structure. Thus, the top displacement reduction factor was obtained by applying the inerter factor only

to the rotation component of the total deformation. The proposed methodology was used to pre-dimension inerters with apparent mass ratios ranging from $\sigma = 0.5$ to 4, resulting in displacement reduction factors between $\phi_{el} = 0.78$ and 0.98. The inerters devices were then designed implementing a ball-screw and gear configuration. Although the use of a rigid block for the representation of flexible structures inherently introduces some degree of inaccuracy to the preliminary design methodology, results from non-linear response history analyses showed that the proposed procedure can produce reasonable estimations of peak displacement reductions.

A first assessment of the effect of the inerters on the response of the case study structures was conducted considering the sub-set of 7 ground motion records used for design. The results of the analyses showed displacement reductions in line with the analytical predictions of the pre-dimension methodology. Additionally, the introduction of inerters efficiently controlled higher-mode effects in the structures. This was reflected in significantly lower peak floor accelerations and reduced bending moments above the critical section. Although the control of the higher-mode response also reduced inter-storey shears in higher floors, the connection of non-clutched inerters to the first level diaphragm significantly amplified the shear force in the ground storey. Closer examination of this phenomenon revealed that the peak shear at this level occurs at lateral deformations smaller than the maximum, with the inerter device driving the motion of the structure. Accordingly, the introduction of a clutch drastically reduced the shear amplification, as it prevents the inerter from pulling the structure. This behaviour also resulted in significantly lower peak resisting forces in the inerter, an aspect that can improve the applicability of the proposed strategy. Importantly, the clutch also further reduced the peak lateral displacements without affecting the ability of the inerter to control the higher-mode response.

For the final design, a single apparent mass ratio was selected for each case study structure and inerter configuration. The corresponding inertances were defined based on the results of the preliminary assessment and practical aspects regarding the magnitude of the associated inertial forces. The ground-inerter-diaphragm load path was designed considering the mean peak force in the inerters from the response history analyses as the seismic demand. Replaceable fuse elements were also incorporated in order to limit the force that can develop in the inerter, thus protecting its mechanical components and the steel-timber connection. The results of the connection design highlighted the advantages of incorporating a clutch into the device, as significantly smaller steel plates were required to transfer the resisting forces of clutched inerters.

Finally, the performance of the bare and protected case study structures was assessed and compared within a probabilistic framework. To this end, the three archetype structures

were subjected to a set of 202 pulse-like ground motion records obtained from 21 different earthquakes. The resulting Cloud data was subsequently used to estimate the median seismic demands and compare the performance of the case study buildings in terms of inter-storey drifts and peak floor accelerations. The results of the analyses showed that the structures equipped with non-clutched inerters experienced slightly smaller drift demands, whereas the addition of a clutch further improved their displacement response. The main advantage of the inerter devices was evidenced in the peak floor acceleration response, where significantly lower demands were obtained across the whole range of intensity levels under consideration. Finally, the results of the Cloud analyses were used to estimate the probability of exceeding drift and acceleration limits typically associated with non-structural and contents damage. The *Cloud to IDA* procedure developed by Miano et al. [135] was implemented in order to estimate the fragility functions associated with the defined limit states. The result of the analysis confirmed that inerter-equipped structures have lower probabilities of exceeding the assumed drift and acceleration limits. Although appreciable increases in the mean IMs were obtained for the drift limit state, much more significant improvements were observed in the peak floor acceleration response. Moreover, unlike the lateral deformation demands, the ability of the inerters to control the lateral accelerations was not significantly affected by the height of the structures. This observation indicates an efficient control of the higher modes response. The results of the design and assessment procedures presented in this chapter have demonstrated the potential applicability of the proposed strategy for the seismic control of rocking building structures.

Chapter 8

Conclusions

8.1 Summary of main findings

As stated in Section 1.2, the main aims of this thesis were to provide a comprehensive and rigorous examination of the dynamic response of rocking structures equipped with supplemental rotational inertia devices, and to explore the alternative of using inerters to improve the seismic performance of post-tensioned buildings. To this end, a series of analytical and numerical methods were employed to conduct a thorough assessment of the proposed seismic control strategy. In the following sections, the main findings of the work are summarized and organized according to these two main objectives.

8.1.1 Dynamics of rocking structures equipped with inerters

- *Fundamental dynamics:* The analytical model developed in Chapter 3 demonstrated that the inclusion of inerters reduces the frequency parameter of a rocking block, thus reducing its seismic demands due to the well-known size effect of rocking behaviour. This finding is particularly interesting as it opens the possibility of modifying the dynamic characteristics of a rigid rocking block without altering its geometry. Importantly, the extended model presented in Chapter 4 showed that the incorporation of vertical post-tensioning or different seismic mass to weight ratios (m_{ratio}), features typically observed in rocking building structures, does not affect the ability of the inerter to control the rocking response. Likewise, the analyses presented in Chapter 5 demonstrated that, although the inerter does not significantly reduce the elastic deformations of flexible rocking bodies, it does control the base rotation response, resulting in considerably lower overall drift demands. However, when taller multi-mass uplifting structures are considered, the effect of an inerter connected at the first-mass level becomes less significant, as its influence on the frequency parameter diminishes (see Equation 7.31). Accordingly, larger apparent mass ratios are required in order to obtain appreciable response improvements in multi-

mass rocking structures. Nevertheless, the actual mass of the inerter can be reduced by several orders of magnitude by means of amplification mechanisms such as ball-screws or gear systems.

- *Implications on the impact transition:* The effect of the inerter on the rotation transition was first evaluated using an extension of Housner's impact formulation. This analysis showed that, in general, the inclusion of the inerter results in higher coefficients of restitution, indicating lower energy dissipation during impact. Importantly, this effect was found not to be significant in slender blocks, although it can affect the efficiency of the proposed strategy when high apparent mass ratios or non-slender structures are considered (Figure 3.7). In particular, the results of a cloud analysis showed that this increase in the coefficient of restitution can cause inerter-equipped structures to experience larger rotation demands under low seismic intensities, as successive acceleration spikes induce rocking cycles of increasing amplitude which can exceed the rotation demand generated by the main pulse (Figure 3.20). When subjected to ground motions of higher intensity, however, the peak rotation response is governed by the velocity pulse and the inclusion of inerters results in consistently lower seismic demands. These observations were later confirmed using alternative impact formulations, such as the Vertical Velocity Energy Loss model (VVEL) and a numerical representation of the energy radiated in the underlying soil.

- *Acceleration response of single-mass oscillators:* The lateral acceleration response of rigid blocks equipped with inerters was first examined considering an extension of Housner's simplified model. Within this classical framework, impact forces are assumed to be instantaneous and concentrated at the pivot corners. Although this model has been shown to provide a good estimation of the amount of energy dissipated during impact, the previous assumptions imply an instantaneous change of velocity and, therefore, an unrealistic infinite acceleration at the transition instant. Using an alternative formulation based on Dirac-Delta forces, it was demonstrated that the infinite acceleration spikes predicted by Housner's model can be ignored under the assumption that impact forces are sufficiently distributed over time as to cause continuous velocity transitions, but sharp enough not to appreciably affect the rotation response. On the other hand, when considering flexible rocking oscillators, experimental studies have shown that Housner's approach tends to overestimate the energy dissipated during impact. Alternatively, the Vertical Velocity Energy Loss (VVEL) was adopted for the study of deformable structures. Since this approach assumes that only the vertical component of the kinetic energy is dissipated during impact, the horizontal acceleration response remains smooth and defined at all times. The above mentioned models were used to examine the response of single-mass rocking systems under coherent pulses and real pulse-like ground motions, demonstrating that structures equipped with inerters experience significantly lower peak accelerations.

The introduction of the clutch, however, leads to earlier impact, a phenomenon that can sometimes exacerbate the lateral acceleration demands.

- *Effects of the clutch:* When subjected to a ground motion, part of the total energy absorbed by the rocking-inerter system is stored in the inerter device. As the structure rocks and oscillates this energy is transferred back and forth, and the single inerter (without clutch) alternates between opposing and driving the motion. If a clutch is introduced, the inerter disengages from the structure and the energy stored in it is not transferred back to the oscillator. If the inerter is then able to dissipate this energy, every engagement-disengagement cycle removes energy from the structural system, increasing the rate at which the rotation and deformation responses are attenuated. Importantly, the addition of the clutch was shown to significantly enhance the rotation response of inerter-equipped structures, although it can also have a detrimental effect on the acceleration demands of rigid and single-mass oscillators.

- *Effects on the overturning response:* As expected, the use of supplemental rotational inertia devices improved the global stability of both rigid and flexible free-standing bodies. Examination of their overturning plots showed that the inerter reduces the areas of overturning in the frequency-acceleration amplitude plane (ω_g/p - $a_g/g \tan\alpha$), and translates them to lower frequency ratios. This frequency shift, which is otherwise beneficial, is particularly relevant for the case of overturning after impact, as certain structures that would rock safely without the inerter, may overturn when the protective device is incorporated. The introduction of the clutch, on the other hand, further shifts the overturning regions and expands the overturning after impact area to higher acceleration magnitudes, a potential drawback that has limited practical implications as it occurs in a frequency-acceleration region of limited practical relevance. Of particular interest in stability analyses are smaller structures, which are known to be more vulnerable to overturning during strong ground motions. In this regard, the results from probabilistic assessments considering a set of 202 pulse-like ground motion showed that small structures equipped with inerters experience reduced probabilities of overturning in comparison with uncontrolled bodies, while the addition of a clutch further improves their seismic stability.

- *Effects on the drift response:* The lateral drift of a rocking structure, is obtained as the sum of the rotation and structural deformation contributions. Although uplift and the triggering of the rocking motion effectively limits the deformation of a SDOF oscillator to values close to the critical displacement, the base rotation can considerably increase the total lateral displacements (Figures 5.6). While the inerter device has only a small effect on the elastic deformation of the column, it significantly reduces the base rotation, leading to considerably smaller drifts. In the case of multi-mass rocking structures,

the backstay effect caused by the connection of the inerter at the first-mass level can slightly increase the deformations in the structural elements. Nevertheless, this potential drawback does not translate into higher drifts as the lateral deformation response is strongly controlled by the base rotation. Similarly, the horizontal motion of the point of connection of the inerter is governed by the rocking action. Thus, if a clutch is introduced, the disengagement condition ensures that the inerter can only oppose the rocking motion of the system, hence significantly reducing further the rotation amplitudes. However, with respect to the elastic deformations, the engagement-disengagement cycles happen at inconvenient times, with the inerter arbitrarily opposing and driving the deformation response. As a consequence, the introduction of a clutch can result in increased elastic deformation demands.

- *Control of higher-mode effects:* Although conservation of horizontal kinetic energy (VVEL model) ensures a smooth horizontal acceleration response in single-mass oscillators, sudden and opposite changes in the velocity of the masses can generate significant acceleration spikes in multi-storey structures while keeping the associated energy constant. Close inspection of the temporal evolution of the kinetic energy and acceleration response of multi-mass rocking structures confirmed this observation, although the peak acceleration amplitudes occurred after impact had ended. This indicates that the maximum accelerations are not caused by direct action of the the impact forces, but by the high frequency oscillations induced by them. Accordingly, higher modes of the response can be excited during impact, even if the ground motion does not contain significant high frequency components.

  Analyses under single pulse excitations showed that the inerter can consistently control the high frequency vibrations generated at impact, significantly reducing the horizontal acceleration demands. Additionally, the inclusion of the inerter elongates the vibration periods of the structure, pushing them towards lower spectral ordinates. Likewise, the proposed strategy successfully controlled bending moments along the height of the structures. Although the control of the higher-mode response also reduced inter-storey shears in higher floors, the connection of non-clutched inerters to the first level diaphragm significantly amplified the shear force in the ground storey. Closer examination of this phenomenon revealed that the peak shear at this level occurs at lateral deformations smaller than the maximum, with the inerter device driving the motion of the structure. Accordingly, the introduction of a clutch drastically reduced the shear amplification, as it prevents the inerter from pulling the structure. This behaviour also resulted in significantly lower peak resisting forces in the inerter, an aspect that can improve the applicability of the proposed strategy. Importantly, the introduction of the clutch did not significantly affect the ability of the inerter to control the higher-mode response.

- *Numerical modelling of the inerter:* A numerical strategy to represent the inerter device

in finite element frameworks was developed and implemented in OpenSees. Additionally, a simplified procedure to model the effect of the clutch was also introduced. The numerical model was successfully validated against analytical models of fixed-base and rocking singe-degree-of-freedom oscillators equipped with inerters.

8.1.2 Application to post-tensioned timber buildings

- *Design of post-tensioned timber walled buildings:* A set of three case study structures, comprising 3, 6 and 9 storeys, was designed following Direct-Displacement-Based Design guidelines and subjected to a sub-set of 7 ground motion records consistent with the design spectrum. While good estimations of peak displacements were obtained, the analyses showed that bending moments and shears throughout the structures can be strongly underestimated due to the influence of higher modes on the response. Moreover, large floor accelerations were also observed, specially in the taller buildings. The results of these analyses were later used as a benchmark for a preliminary assessment of the effect of the inerter devices on the seismic response of the structures.

- *Selection of the apparent mass ratio:* Based on the conclusions obtained from analytical models, a simplified procedure to pre-dimension the inerter devices was developed. The proposed methodology combines the equal displacement rule [162] with the equivalent size-scaling effect of the inerter in order to obtain a base rotation reduction factor. Moreover, recognizing that the inerter has little effect on the elastic deformation response of a flexible rocking structure, a top displacement reduction factor was obtained applying the inerter factor only to the rotation component of the total deformation. The methodology was later validated against results from non-linear response history analyses, showing that the proposed procedure can produce reasonable estimations of peak displacement reductions.

- *Force in the inerter:* The results from response history analyses showed that large inertial forces can develop in the inerters during a seismic event. Moreover, since the inertance required to achieve any given apparent mass ratio is directly proportional to the total weight of the structure, the resisting force in the inerter increases significantly as the building becomes taller. Crucially, the mechanical components of the devices, as well as the connection to the floor diaphragm, must be designed to resist these demands, potentially limiting the practicality of the proposed strategy. In order to limit the force that can develop in the inerter and prevent brittle failures within the device, replaceable fuse elements were implemented in the connection. Yielding in these components, however, affected the efficiency of the inerter under higher seismic intensities. The introduction of the clutch, on the other hand, considerably reduced the inertial forces. Importantly, these improvements did not affect the ability of the inerter to control the seismic re-

sponse of the structural systems. The results of the connection design highlighted the advantages of incorporating a clutch into the device, as significantly smaller steel plates were required to transfer the resisting forces of clutched inerters.

- *Performance-based seismic assessment:* Modern design frameworks generally quantify seismic risk in terms of overall performance, looking at both the structural and non-structural components of a building. Although post-tensioned rocking systems have proved to be highly effective in controlling structural damage, excessive inter-storey drifts or floor accelerations associated with the rocking motion can significantly reduce the overall performance of the structure. In this context, and motivated by the observations drawn from the analytical models, the possibility of employing inerters to control these engineering demand parameters was evaluated within a probabilistic framework. To this end, a Cloud Analysis considering a set of 202 pulse-like ground motion records obtained from 21 different earthquakes was performed. The estimated median demands showed that structures equipped with non-clutched inerters experienced slightly smaller drift demands in comparison with the uncontrolled buildings. The addition of the clutch, however, further improved the drift response for low to mid IMs, but became less effective under higher seismic intensity levels due to yielding in the fuse elements. On the other hand, the main advantage of the inerter devices was evidenced in the peak floor acceleration response, where an efficient control of higher-mode effects resulted in significantly lower demands across the whole range of intensity levels under consideration. Finally, the results of the Cloud analyses were used to estimate the probability of exceeding drift and acceleration limits typically associated with non-structural and contents damage. The resulting fragilities confirmed that inerter-equipped structures have lower probabilities of exceeding the assumed drift and acceleration limits. Although appreciable increases in the mean IMs were obtained for the drift limit state, much more significant improvements were observed in the peak floor acceleration response. Moreover, unlike the lateral deformation demands, the ability of the inerters to control the lateral accelerations was not significantly affected by the height of the structures. Overall, the results of the performance-based assessment demonstrated the potential applicability of the proposed strategy for the seismic control of rocking building structures.

8.2 Limitations and future work

The alternative of employing inerters to improve the seismic performance of rocking structures has been thoroughly examined in this thesis. The studies conducted as part of this work have also highlighted the need for further research in the following areas:

- All the analyses presented in this thesis have treated rocking as a 2-dimensional in-plane motion. Although this simplification allows to study the fundamental dynamics of the problem, it is recognized that planar analysis can only qualitatively describe the behaviour of 3-dimensional rocking structures. Moreover, the analytical models employed in the analyses assume that no bouncing or slippage occurs during impact. Accordingly, further research is required in order to investigate the effects of these assumptions on the efficiency of the inerter.

- The analytical model developed in Chapter 3 predicts an increase in the frequency parameter of rocking blocks equipped with inerters and a reduction of the energy dissipated during impact. Although the basic formulation on which this model is based has been shown to adequately predict the main statistics of the seismic response of rocking blocks, the additional effect of the inerter needs to be experimentally validated.

- Throughout this thesis, the clutch has been modelled as an ideal device that engages and disengages instantaneously. Moreover, it is assumed that the energy stored in the inerter device is completely dissipated before re-engagement. A detailed experimental assessment is required in order to examine the suitability of these assumptions. In particular, the effects of backlash, flywheel damping, clutch stiffness and dry friction need to be explicitly considered. On the other hand, further research is required to investigate the ratcheting effect observed in clutched devices when re-engagement occurs at large driving-mass velocities.

- Although a strong correlation was observed between the uniform time duration, t_{uni}, and the seismic demands in rigid rocking structures, better intensity measures are required to adequately estimate the seismic response of post-tensioned timber buildings. In particular, further work is required to describe the floor acceleration demands, which were shown to be affected by both the ground motion and the forces developed during impact.

- The results from Chapters 6 and 7 demonstrated that higher modes can significantly amplify the seismic forces along the height of rocking structures. Although methodologies to incorporate these effects in the design of fixed-based reinforced concrete systems have been proposed, they are generally not extendible to post-tensioned timber buildings, as uplift and the subsequent rocking motion alter the dynamic parameters of the system.

Moreover, the analyses presented in this thesis showed that impact forces can excite higher modes of the uplifted system even if the ground motion does not contain significant high frequency components. Accordingly, further work is required in order to incorporate these phenomena in the DDBD procedure for rocking timber structures.

Appendices

Appendix A

Rocking spectra of slender rigid blocks

The response of slender rigid blocks to trigonometric pulses is presented in Figures A.1 and A.2 in terms of rocking spectra. This representation consist of contour plots of the normalized response variable in the frequency ratio (ω_g/p) and acceleration amplitude ($a_g/g\tan\alpha$) plane, for a block of a given slenderness α. Accordingly, Figures A.1 and A.2 compare the rotation and acceleration demands for a rigid block of slenderness $\alpha = 10^\circ$ subjected to cosinusoidal and sinusoidal pulses, respectively, of dominant frequency ω_g and acceleration amplitude a_g. Results are offered for three different configurations: (a) no inerter, (b) single inerter ($\sigma = 0.5$), and (c) pair of clutched inerters ($\sigma = 0.5$). Overall, the results presented in Figures A.1 and A.2 are in line with the conclusions obtained in Chapter 3 for non-slender rocking structures, showing considerable reductions in the rotation and acceleration demands when the inerter is incorporated.

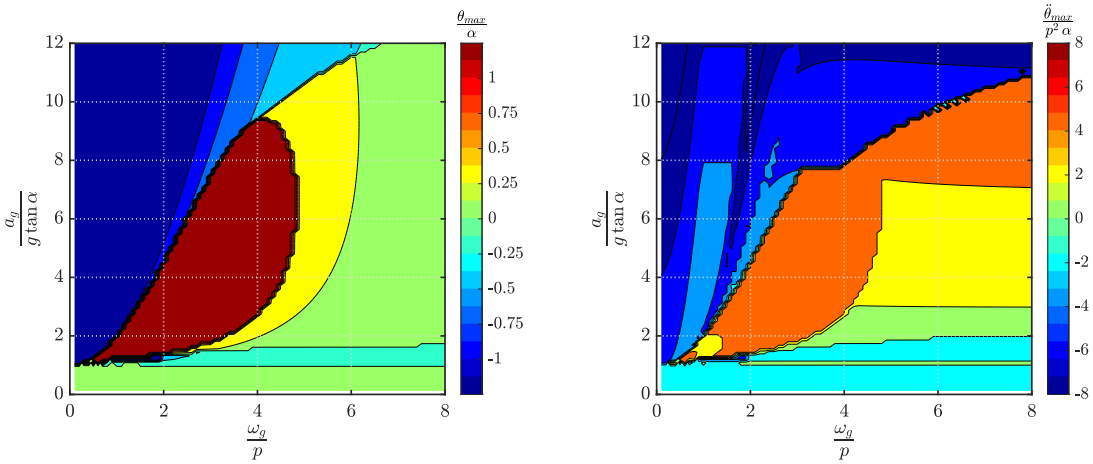

(a) Single rigid block (no inerter).

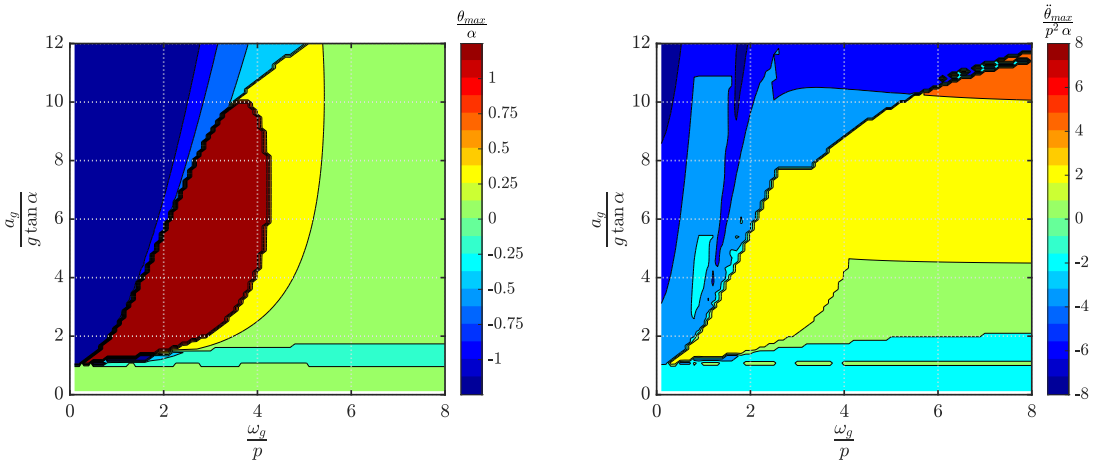

(b) Rigid block connected to a single inerter ($\sigma = 0.5$).

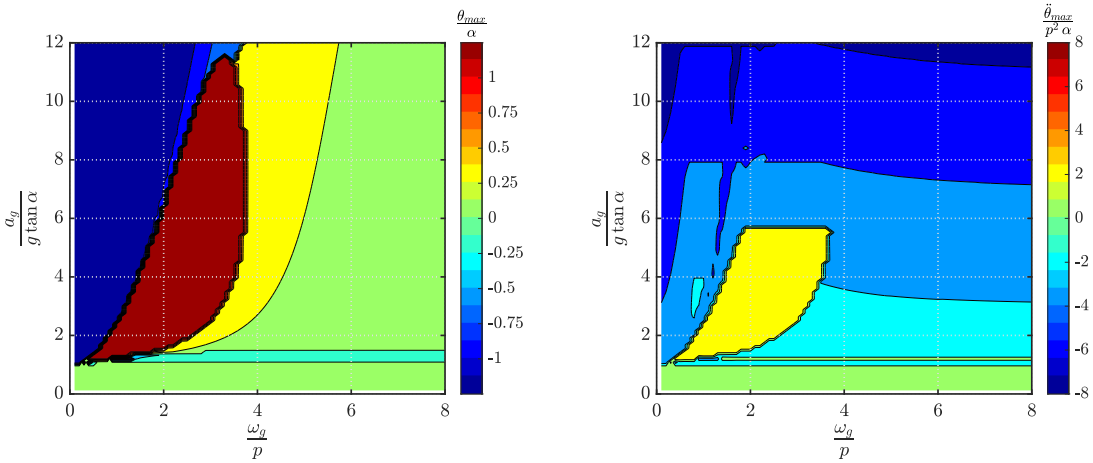

(c) Rigid block connected to a pair of clutched inerters ($\sigma = 0.5$).

Figure A.1: Rocking spectra for a non-slender block ($\alpha = 10°$) subjected to cosine pulse excitations.

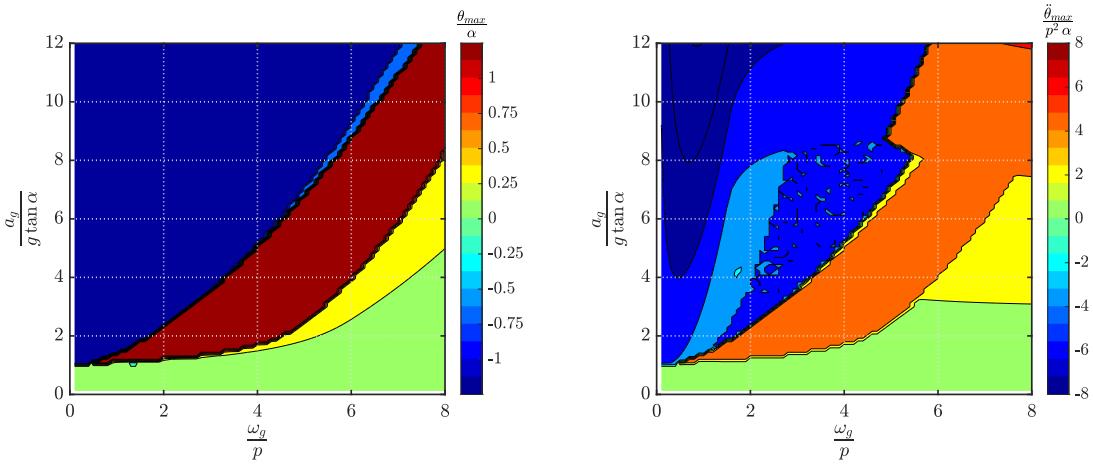

(a) Single rigid block (no inerter).

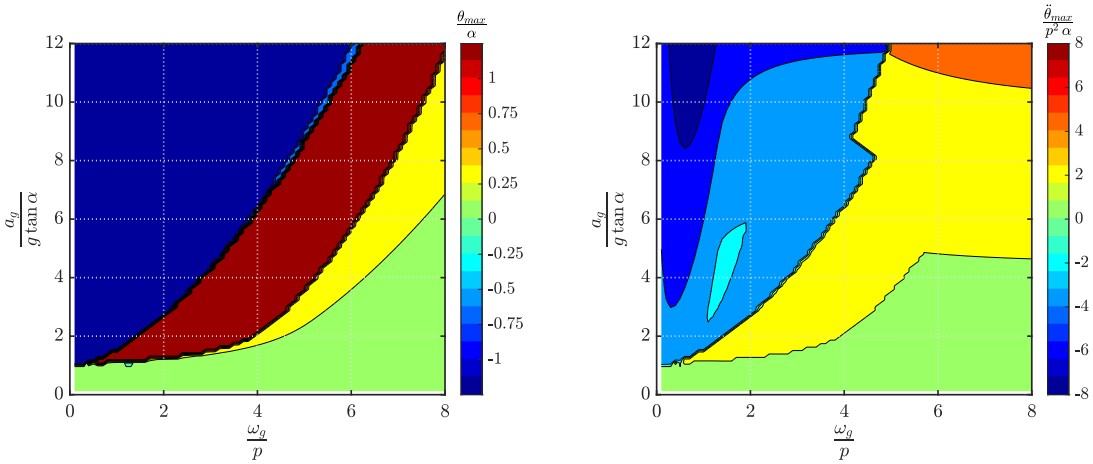

(b) Rigid block connected to a single inerter ($\sigma = 0.5$).

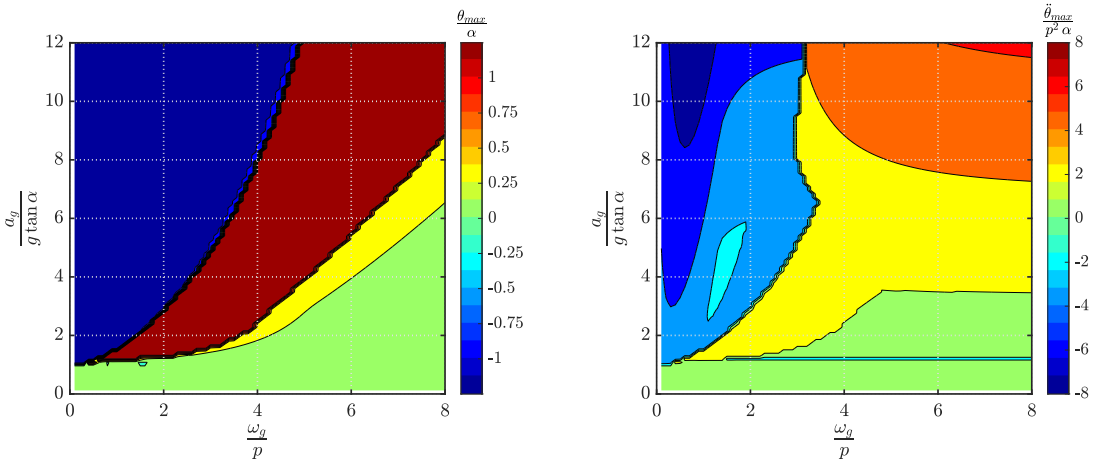

(c) Rigid block connected to a pair of clutched inerters ($\sigma = 0.5$).

Figure A.2: Rocking spectra for a non-slender block ($\alpha = 10°$) subjected to sine pulse excitations.

Appendix B

Fixed-base MDOF structures equipped with inerters

Figure B.1 shows a fixed-base multi-degree-of-freedom structure connected to a grounded inerter at the first mass level. The structural system consists of n lumped masses, m_i, connected by elastic beam-column elements of stiffness k_i.

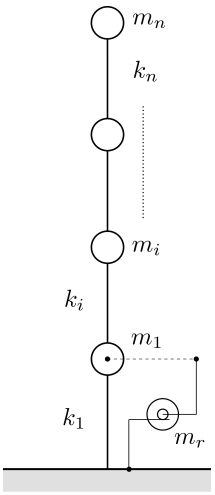

Figure B.1: Fixed-base MDOF structure connected to an inerter at the first-mass level.

Under free vibrations, the equations of motion of the system are:

$$[M]\ddot{x} + [K]x = 0 \tag{B.1}$$

with

$$[M] = \begin{pmatrix} m_1 + m_r & 0 & \cdots & 0 \\ 0 & m_2 & \cdots & 0 \\ \vdots & \vdots & \ddots & \vdots \\ 0 & 0 & \cdots & m_n \end{pmatrix} \tag{B.2}$$

and

$$[K] = \begin{pmatrix} k_1 + k_2 & -k_2 & & \\ -k_2 & k_2 + k_3 & \ddots & \\ & \ddots & \ddots & -k_n \\ & & -k_n & k_n \end{pmatrix} \tag{B.3}$$

On the other hand, it is well known that the free vibration response of the MDOF system can be described by the following eigenvalue problem:

$$([K] - \lambda_j[M])\phi_j = 0 \tag{B.4}$$

where $j = 1, ..., n$, $\omega_{nj} = \sqrt{\lambda_j}$ are the natural frequencies of the system, and ϕ_j is the jth mode shape corresponding to natural frequency ω_{nj}, normalized such that $\phi_j^T[M]\phi_j = 1$. Repeating Chen's et al. reasoning [106], the influence of the inerter on the jth frequency can be studied by obtaining the derivative with respect to m_r:

$$\left(\frac{\partial[K]}{\partial m_r} - \frac{\partial \lambda_j}{\partial m_r}[M] - \lambda_j \frac{\partial[M]}{\partial m_r}\right)\phi_j + ([K] - \lambda_j[M])\frac{\partial \phi_j}{\partial m_r} = 0 \tag{B.5}$$

Pre-multiplying both sides by ϕ_j^T and considering that $\partial[K]/\partial m_r = 0$, $\phi_j^T([K] - \lambda_j[M]) = 0$, and $\phi_j^T[M]\phi_j = 1$ yields:

$$\frac{\partial \lambda_j}{\partial m_r} = -\lambda_j \phi_j^T \frac{\partial[M]}{\partial m_r}\phi_j \tag{B.6}$$

where:

$$\frac{\partial[M]}{\partial m_r} = \begin{pmatrix} 1 & 0 & \cdots & 0 \\ 0 & 0 & \cdots & 0 \\ \vdots & \vdots & \ddots & \vdots \\ 0 & 0 & \cdots & 0 \end{pmatrix} \tag{B.7}$$

Then:

$$\frac{\partial \lambda_j}{\partial m_r} = -\lambda_j \left(\phi_j^{(n)}\right)^2 \tag{B.8}$$

Equation B.8 demonstrates that the inclusion of the inerter shortens the vibration frequencies of the system or, equivalently, elongates its natural periods. Generally, this results in a reduced higher-mode response, as the natural frequencies of the system are shifted towards smaller spectral acceleration ordinates. Moreover, for any given mode shape, ϕ_j, Equation B.8 shows that the effect of the inerter becomes less significant as λ_j decreases. Accordingly, higher levels of inertance are required to obtain similar frequency shifts as the structures become taller or more flexible.

Appendix C

Seismic demand prediction models for post-tensioned rocking timber buildings

Figures C.1 to C.12 present the Cloud data and the seismic demand prediction models examined in Chapter 7. Four different intensity measures are considered as the predictive variable: uniform time duration (t_{uni}), peak ground velocity (PGV), peak ground acceleration (PGA), and the 5% damped spectral acceleration at the first fixed-base structural period, $S_a(T_1)$.

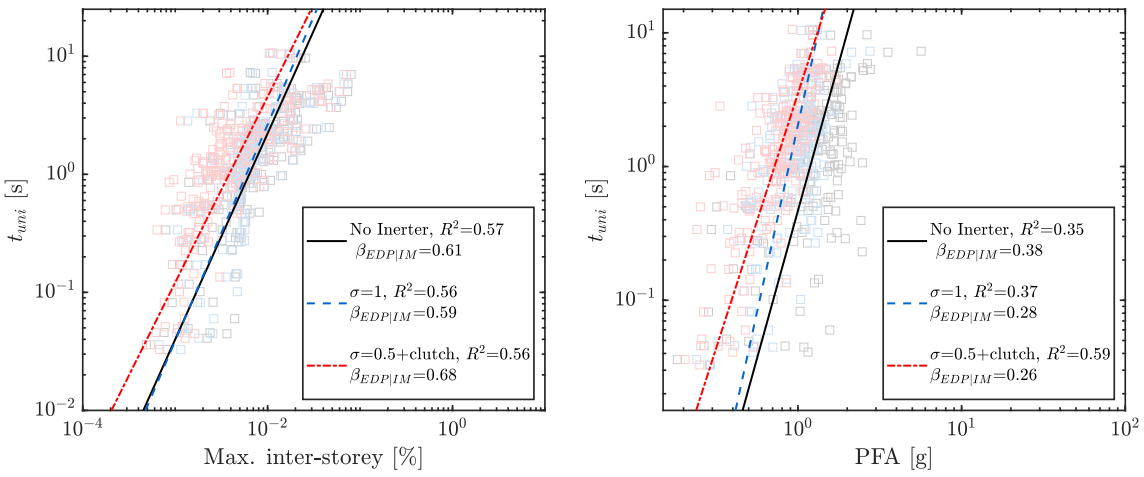

Figure C.1: Seismic demand prediction models for the 3-Storey structures based on t_{uni}.

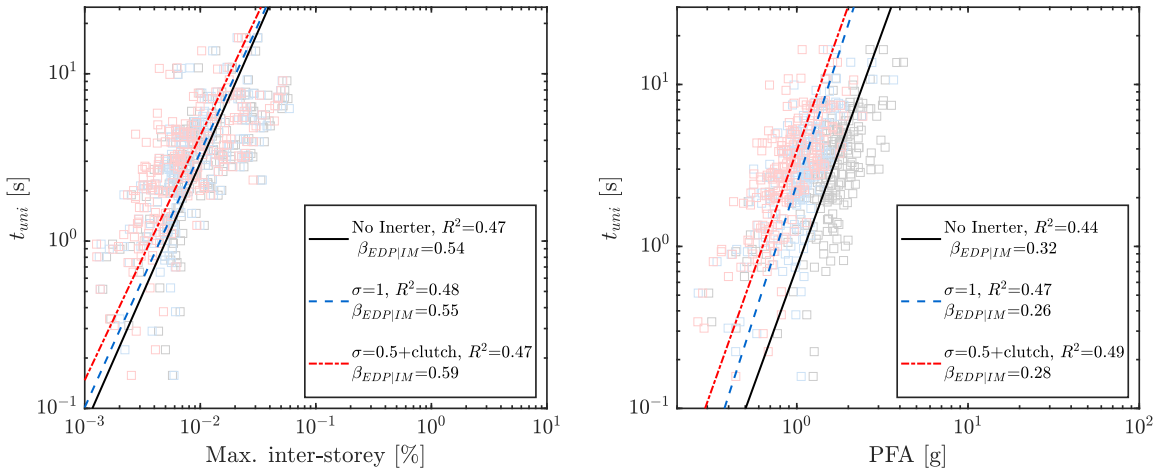

Figure C.2: Seismic demand prediction models for the 6-Storey structures based on t_{uni}.

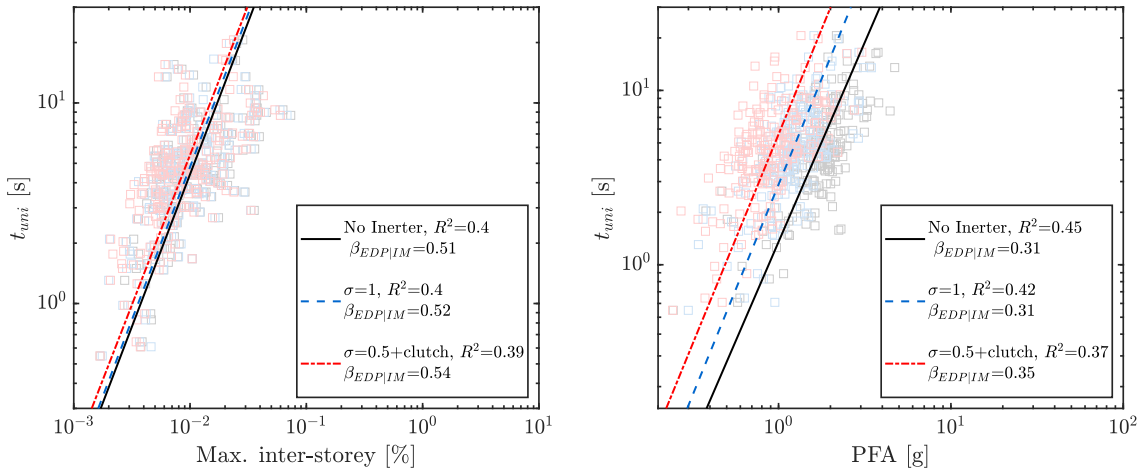

Figure C.3: Seismic demand prediction models for the 9-Storey structures based on t_{uni}.

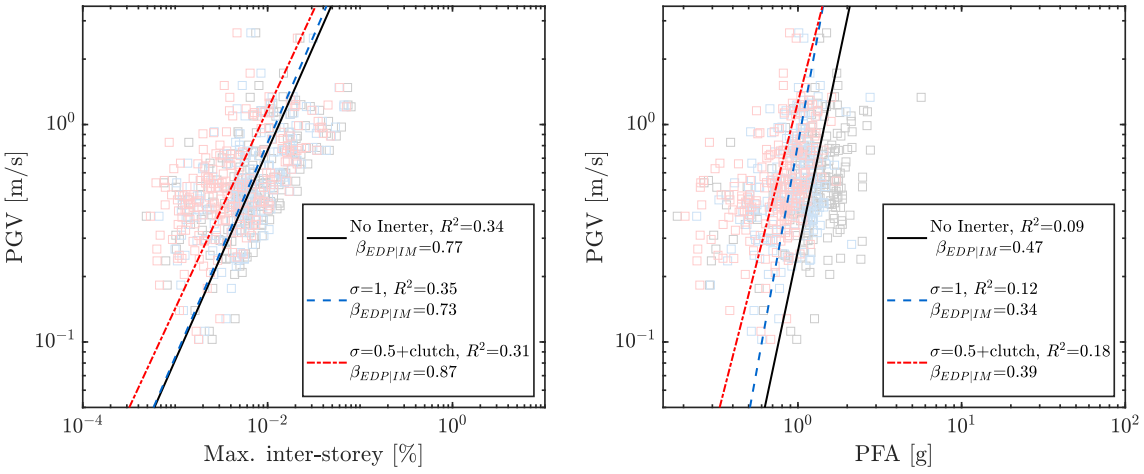

Figure C.4: Seismic demand prediction models for the 3-Storey structures based on PGV.

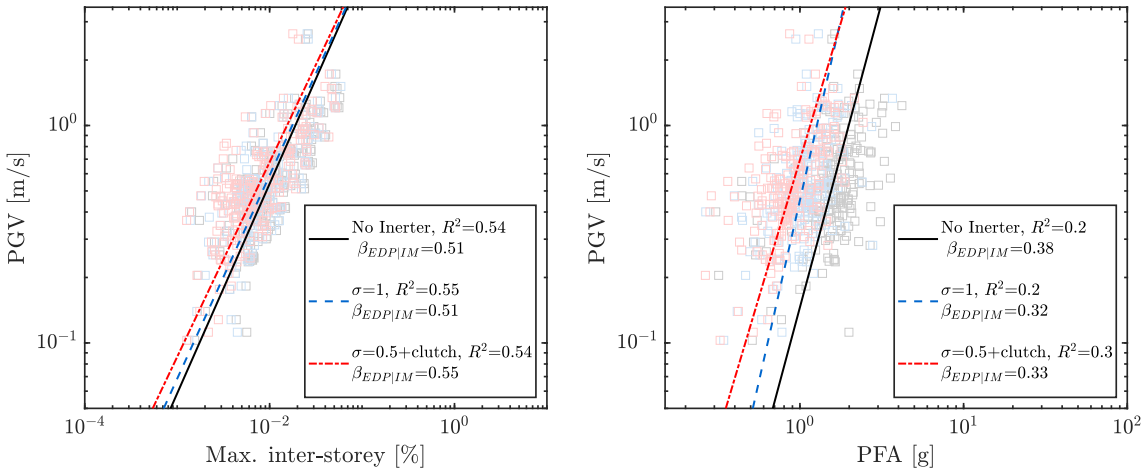

Figure C.5: Seismic demand prediction models for the 6-Storey structures based on PGV.

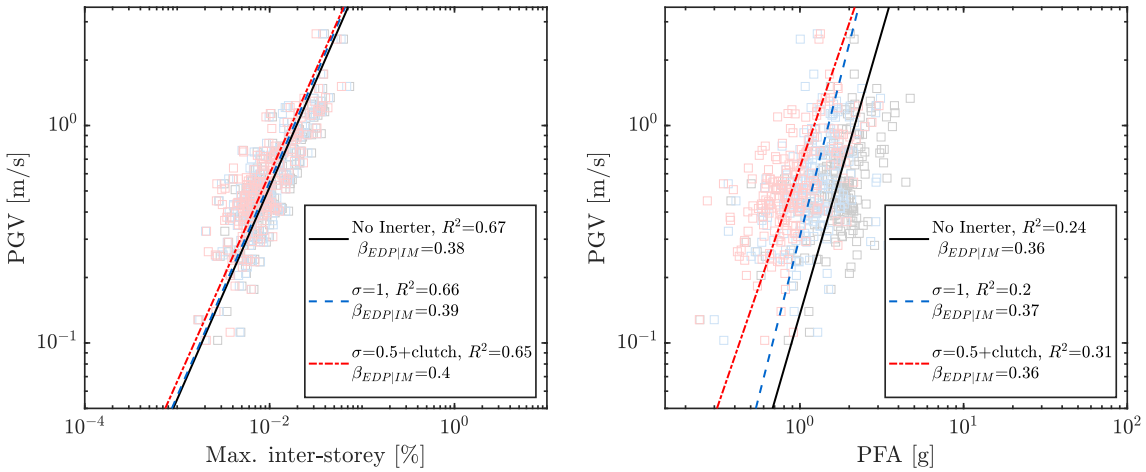

Figure C.6: Seismic demand prediction models for the 9-Storey structures based on PGV.

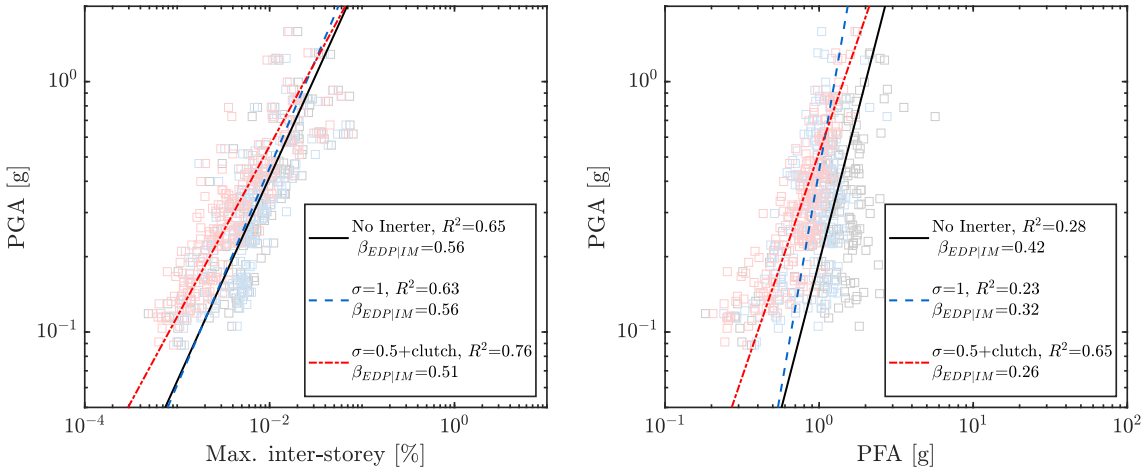

Figure C.7: Seismic demand prediction models for the 3-Storey structures based on PGA.

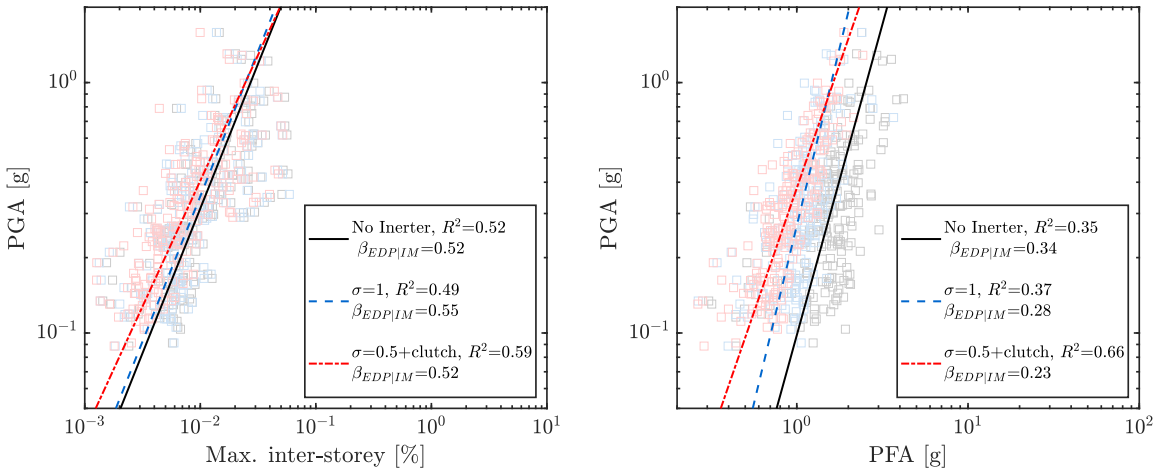

Figure C.8: Seismic demand prediction models for the 6-Storey structures based on PGA.

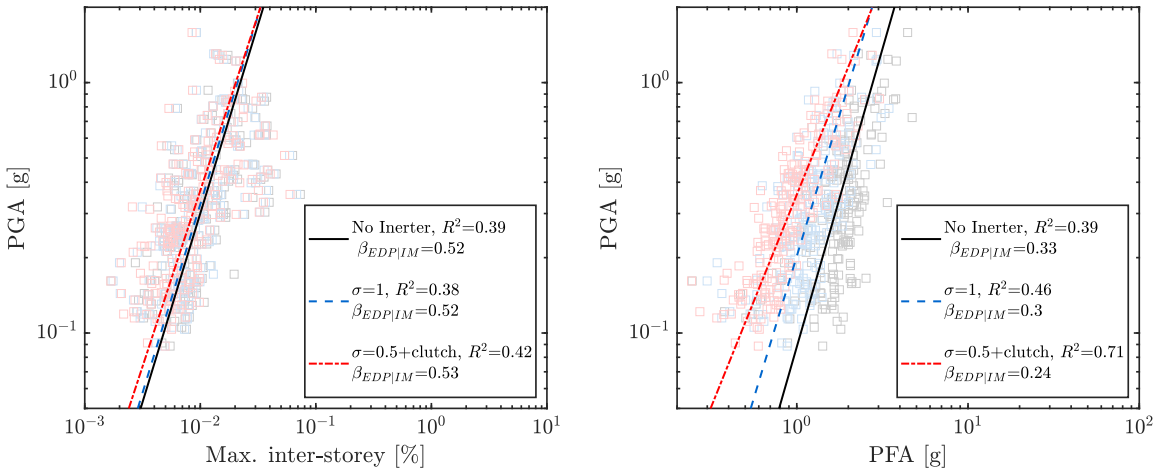

Figure C.9: Seismic demand prediction models for the 9-Storey structures based on PGA.

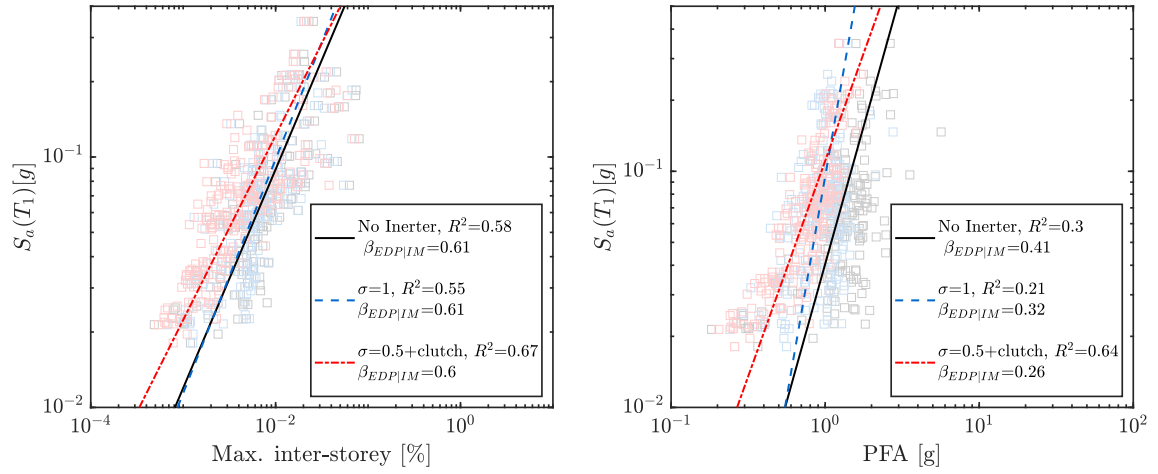

Figure C.10: Seismic demand prediction models for the 3-Storey structures based on $S_a(T_1)$.

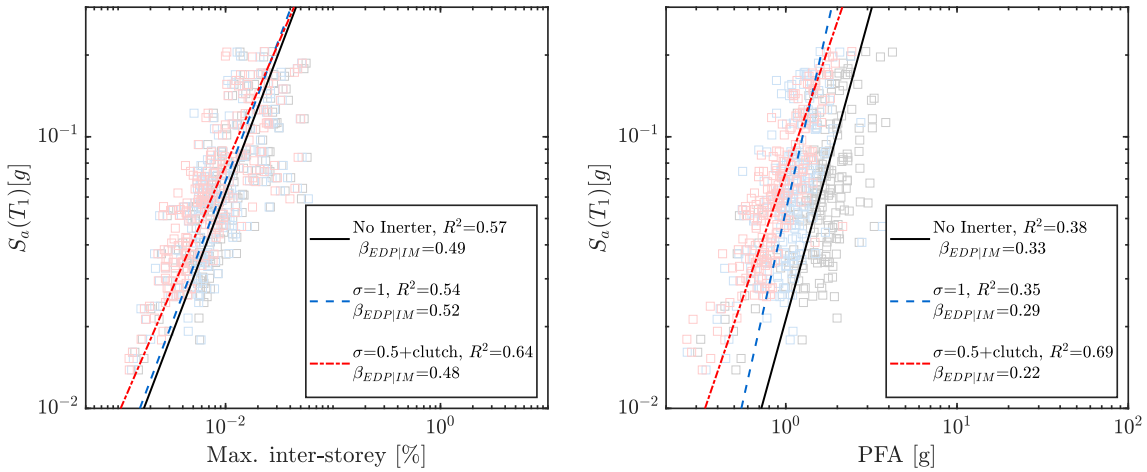

Figure C.11: Seismic demand prediction models for the 6-Storey structures based on $S_a(T_1)$.

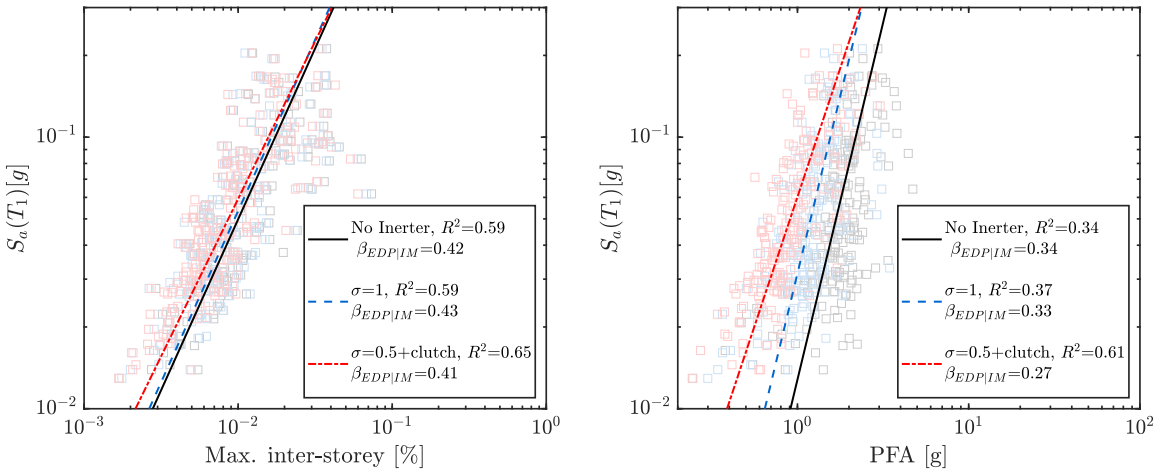

Figure C.12: Seismic demand prediction models for the 9-Storey structures based on $S_a(T_1)$.

References

[1] J. Baker, *The Steel Skeleton, Vol. 2.* Cambridge University Press, 1956.

[2] N. Makris, "A half-century of rocking isolation," *Earthquakes and Structures*, vol. 7, no. 6, pp. 1187–1221, 2014.

[3] G. Housner, "The behavior of inverted pendulum structures during earthquakes," *Bulletin of the Seismological Society of America*, vol. 53, pp. 403–417, 1963.

[4] M. Priestley, "An overview of PRESSS research program," *PCI Journal*, vol. 36(4), 1991.

[5] T. Arakaki, H. Kuroda, F. Arima, Y. Inoue, and K. Baba, "Development of seismic devices applied to ball screw. Part 1: Basic performance of test RD-series," *AIJ J.Technol. Des*, vol. 8, pp. 239–244, 1999.

[6] M. Smith, "Synthesis of mechanical networks: The Inerter," *IEEE Trans. Autom. Control*, vol. 47(10), pp. 1648–1662, 2002.

[7] K. Ikago, K. Saito, and N. Inoue, "Seismic control of single-degree-of-freedom structure using tuned viscous damper," *Earthquake Engineering and Structural Dynamics*, vol. 41, no. 3, pp. 436–474, 2012.

[8] I. Lazar, S. Neild, and D. Wagg, "Using an inerter-based device for structural vibration suppression," *Earthq Eng Struct Dyn*, vol. 43, no. 8, pp. 1129–1147, 2014.

[9] A. Chopra, *Dynamics of structures: Theory and applications to earthquake engineering.* International Series in Civil Engineering and Engineering Mechanics, Prentice Hall, Upper Saddle River, NJ, 2000.

[10] S. Mazzoni, F. McKenna, M. Scott, and G. Fenves, *Open Systems for Earthquake Engineering Simulation User Command-Language Manual - OpenSees version-2.1.0.* Pacific Earthquake Engineering Research Center, University of California, Berkeley, CA, 2009.

[11] D. Konstantinidis and N. Makris, "Seismic response analysis of multidrum classical columns," *Earthq Eng Struct Dyn*, vol. 34, no. 10, pp. 1243–1270, 2005.

[12] I. Psycharis, J. Lemos, D. Papastamatiou, C. Zambas, and C. Papantonopoulos, "Numerical study of the seismic behaviour of a part of the Parthenon Pronaos," *Earthq Eng Struct Dyn*, vol. 32, no. 13, pp. 2063–2084, 2003.

[13] A. Giouvanidis and E. Dimitrakopoulos, "Seismic performance of rocking frames with flag-shaped hysteretic behavior," *JEngMech*, vol. 143, no. 5, pp. 1–13, 2017.

[14] C. Cheng, "Shaking table tests of a self-centering designed bridge substructure," *Eng Struct*, vol. 30, no. 12, pp. 3426–3433, 2008.

[15] K. Solberg, N. Mashiko, J. Mander, and R. Dhakal, "Performance of a damage-protected highway bridge pier subjected to bidirectional earthquake attack," *Journal of Structural Engineering*, vol. 135, no. 5, pp. 469–478, 2009.

[16] D. Dowden, R. Purba, and M. Bruneau, "Behavior of self-centering steel plate shear walls and design considerations," *Journal of Structural Engineering*, vol. 138, no. 1, pp. 11–21, 2012.

[17] A. Dar, D. Konstantinidis, and W. El-Dakhakhni, " Evaluation of ASCE 43-05 seismic design criteria for rocking objects in nuclear facilities," *JStruct Eng*, pp. 1–13, 2016.

[18] A. Contento and A. DiEgidio, "Investigations into the benefits of base isolation for non-symmetric rigid blocks," *Earthq Eng Struct Dyn*, vol. 38, no. 7, pp. 849–866, 2009.

[19] E. Dimitrakopoulos and A. Giouvanidis, "Seismic response analysis of the planar rocking frame," *JEngMech*, vol. 141, no. 7, pp. 3426–3433, 2015.

[20] N. Makris and M. Vassiliou, "Dynamics of the rocking frame with vertical restrainers," *JStructEng*, vol. 141, no. 10, pp. 1–13, 2015.

[21] M. Vassiliou, S. Burger, M. Egger, J. Bachmann, M. Broccardo, and B. Stojadinovic, "The three-dimensional behavior of inverted pendulum cylindrical structures during earthquakes," *Earthq Eng Struct Dyn*, vol. 46, no. 14, pp. 2261–2280, 2017.

[22] M. Vassiliou, "Seismic response of a wobbling 3D frame," *Earthq Eng Struct Dyn*, vol. 47, no. 5, pp. 1212–1228, 2017.

[23] Y. Ishiyama, "Motions of rigid bodies and criteria for overturning by earthquake excitations," *Earthquake Eng Struct Dyn*, vol. 10, no. 5, pp. 635–650, 1982.

[24] H. Shenton and N. Jones, "Base excitation of rigid bodies. i: Formulation," *Journal of Engineering Mechanics*, vol. 117, no. 10, pp. 2286–2306, 1991.

[25] I. Psycharis and P. Jennings, "Rocking of slender rigid bodies allowed to uplift," *Earthquake Engineering & Structural Dynamics*, vol. 11, no. 1, pp. 57–76, 1983.

[26] A. Koh, P. Spanos, and J. Roesset, "Harmonic rocking of rigid block on flexible foundation," *Journal of Engineering Mechanics*, vol. 112, no. 11, pp. 1165–1180, 1986.

[27] A. Palmeri and N. Makris, "Response analysis of rigid structures rocking on viscoelastic foundation," *Earthquake Engineering & Structural Dynamics*, vol. 37, no. 7, pp. 1039–1063, 2008.

[28] M. ElGawady, M. Quincy, J. Butterworth, and J. Ingham, "Effects of interface material on the performance of free rocking blocks," *Earthquake Engineering & Structural Dynamics*, vol. 40, no. 4, pp. 375–392, 2011.

[29] F. Peña, F. Prieto, P. Lourenço, A. C. Costa, and J. Lemos, "On the dynamics of rocking motion of single rigid-block structures," *Earthquake Engineering & Structural Dynamics*, vol. 36, no. 15, pp. 2383–2399, 2007.

[30] A. Chopra and Y. SCS, "Simplified earthquake analysis of structures with foundation uplift," *Journal of Structural Engineering*, vol. 111, no. 4, pp. 906–930, 1985.

[31] M. Vassiliou, R. Truniger, and B. Stojadinović, "An analytical model of a deformable cantilever structure rocking on a rigid surface: development and verification," *Earthquake Engineering & Structural Dynamics*, vol. 44, no. 15, pp. 2775–2794, 2015.

[32] R. T. R, M. Vassiliou, and B. Stojadinovic, "An analytical model of a deformable cantilever structure rocking on a rigid surface: experimental validation," *Earthq Eng Struct Dyn*, vol. 44, no. 15, pp. 2795–2815, 2015.

[33] A. Giouvanidis and E. Dimitrakopoulos, "Nonsmooth dynamic analysis of sticking impacts in rocking structures," *Bull Earthquake Eng*, vol. 15, no. 5, pp. 2273–2304, 2017.

[34] S. Acikgoz and M. DeJong, "Analytical modelling of multi-mass flexible rocking structures," *Earthquake Engineering & Structural Dynamics*, vol. 45, no. 13, pp. 2103–2122, 2016.

[35] F. Prieto, P. Lourenço, and C. Oliveira, "Impulsive dirac-delta forces in the rocking motion," *Earthquake Engineering & Structural Dynamics*, vol. 33, no. 7, pp. 839–857, 2004.

[36] N. Makris and D. Konstantinidis, "The rocking spectrum and the limitations of practical design methodologies," *Earthq Eng Struct Dyn*, vol. 32, no. 2, pp. 265–289, 2003.

[37] M. Chatzis, M. Espinosa, and A. Smyth, "Examining the energy loss in the inverted pendulum model for rocking bodies," *JEngMech*, p. 143:4017013, 2017.

[38] J. Bachmann, M. Strand, M. Vassiliou, M. Broccardo, and B. Stojadinovic, "Is rocking motion predictable?," *Earthquake Engineering and Structural Dynamics*, vol. 47, pp. 535–552, 2018.

[39] E. Dimitrakopoulos and M. DeJong, "Overturning of retrofitted rocking structures under pulse-type excitations," *Journal of Engineering Mechanics*, vol. 138, no. 8, pp. 963–972, 2012.

[40] E. Dimitrakopoulos and T. Paraskeva, "Dimensionless fragility curves for rocking response to near-fault excitations," *Earthquake Eng Struct Dyn*, vol. 44, no. 12, pp. 2015–2033, 2015.

[41] A. Pappas, A. Sextos, F. DaPorto, and C. Modena, "Efficiency of alternative intensity measures for the seismic assessment of monolithicfree-standing columns," *Bull Earthquake Eng*, vol. 15, no. 4, pp. 1635–1659, 2017.

[42] E. Dimitrakopoulos and A. Giouvanidis, "Rocking amplification and strong-motion duration," *Earthquake Engng Struct Dyn*, pp. 1–22, 2018.

[43] G. Oliveto, I. Caliò, and A. Greco, "Large displacement behaviour of a structural model with foundation uplift under impulsive and earthquake excitations," *Earthquake Engineering & Structural Dynamics*, vol. 32, no. 3, pp. 369–393, 2003.

[44] S. Acikgoz and M. DeJong, "The interaction of elasticity and rocking in flexible structures allowed to uplift," *Earthquake Engineering & Structural Dynamics*, vol. 41, no. 15, pp. 2177–2194, 2012.

[45] I. Psycharis, "Dynamics of flexible systems with partial lift-off," *Earthquake Engineering & Structural Dynamics*, vol. 11, no. 4, pp. 501–521, 1983.

[46] S. Yim and A. Chopra, "Simplified earthquake analysis of multistory structures with foundation uplift," *Journal of Structural Engineering*, vol. 111, no. 12, pp. 2708–2731, 1985.

[47] S. Acikgoz, Q. Ma, A. Palermo, and M. DeJong, "Experimental identification of the dynamic characteristics of a flexible rocking structure," *Journal of Earthquake Engineering*, vol. 20, no. 8, pp. 1199–1221, 2016.

[48] I. Calio and M. Marletta, "Passive control of the seismic rocking response of art objects," *Eng. Struct*, vol. 25, no. 8, pp. 1009–1018, 2003.

[49] R. Ceravolo, M. Pecorelli, and L. Z. Fragonara, "Semi-active control of the rocking motion of monolithic art objects," *J. Sound Vib*, vol. 374, pp. 1–16, 2016.

[50] N. Makris and J. Zhang, "Rocking response and overturning of anchored equipment under seismic excitation," *Pacific Earthquake Engineering ResearchCentre, Berkeley*, 1999.

[51] N. Makris and J. Zhang, "Rocking response of anchored blocks under pulse-type motions," *J. Eng. Mech*, vol. 127, pp. 484–493, 2001.

[52] R. Ceravolo, M. Pecorelli, and L. Z. Fragonara, "Comparison of semi-active control strategies for rocking objects under pulse and harmonic excitations," *Mechanical Systems and Signal Processing*, vol. 90, pp. 175–188, 2017.

[53] M. Vassiliou and N. Makris, "Dynamics of the vertically restrained rocking column," *J. Eng. Mech*, vol. 141, no. 12, p. 04015049, 2015.

[54] N. Makris and M. Aghagholizadeh, "Effect of supplemental hysteretic and viscous damping on rocking response of free-standing columns," *Journal of Engineering Mechanics*, vol. 145, no. 5, p. 04019028, 2019.

[55] A. deLeo, G. Simoneschi, C. Fabrizio, and A. DiEgidio, "On the use of a pendulum as mass damper to control the rocking motion of a rigid block with fixed characteristics," *Meccanica*, vol. 51, pp. 2727–2740, Nov 2016.

[56] M. Vassiliou and N. Makris, "Analysis of the rocking response of rigid blocks standing free on a seismically isolated base," *Earthq Eng Struct Dyn*, vol. 41, pp. 177–196, 2012.

[57] X. Pan and C. Málaga-Chuquitaype, "Seismic control of rocking structures via external resonators," *Earthquake Engineering & Structural Dynamics*, vol. n/a, no. n/a, 2020.

[58] C. Christopoulos, A. Filiatrault, C. Uang, and B. Folz, "Post-tensioned energy dissipating connections for moment resisting steel frames," *ASCE Journal of Structural Engineering*, vol. 128 9, pp. 1111–1120, 2002.

[59] Y. Kurama, "Hybrid post-tensioned precast concrete walls for use in seismic regions," *PCI Journal*, vol. 47, pp. 36–59, 09 2002.

[60] T. Holden, J. Restrepo, and J. Mander, "Seismic performance of precast reinforced and prestressed concrete walls," *Journal of Structural Engineering*, vol. 129, no. 3, pp. 286–296, 2003.

[61] F. Sarti, *Seismic Design of Low-Damage Post-Tensioned Timber Wall Systems.* PhD thesis, University of Canterbury, 2015.

[62] A. A. Mesa, *Developments of Advanced Solutions for Seismic Resisting Precast Concrete Frames.* PhD thesis, University of Canterbury, 2010.

[63] J. M. Kelly, R. I. Skinner, and A. J. Heine, "Mechanism of Energy Absorption in Special Devices for Use in Earthquake Resistant Structures," *Bulletin New Zealand Society of Earthquake Engineering*, vol. 5:3, pp. 63–88, 1972.

[64] M. Priestley, S. Sritharan, J. Conley, and S. Pampanin, "Preliminary results and conclusions from the PRESSS five-story precast concrete test-building," *PCI Journal*, vol. 44(6), pp. 42–67, 1999.

[65] Y. Kurama, S. Pessiki, R. Sause, and L. Lu, "Lateral load behavior and seismic design of unbonded post-tensioned precast concrete walls," *ACI Structural Journal*, vol. July-August, pp. 622–632, 1999.

[66] S. Nakaki, J. Stanton, and S. Sritharan, "An overview of the presss five-story precast test building," *PCI Journal*, vol. 44, no. 2, pp. 26–39, 1999.

[67] J. Mander and C. Cheng, "Replaceable hinge detailing for bridge columns," *ACI J.*, vol. 187, pp. 185–204, 1999.

[68] J. Sakai, H. Jeong, and S. Mahin, *Reinforced concrete bridge columns that re-center following earthquakes*, pp. 18–22. 2006.

[69] M. Garlock, J. Ricles, and R. Sause, "Experimental studies of full-scale postensioned steel connections," *Journal of Structural Engineering*, vol. 131, no. 3, pp. 438–448, 2005.

[70] M. Eatherton, J. Hajjar, G. Deierlein, H. Krawinkler, S. Billington, and X. Ma, "Controlled rocking of steel-framed buildings with replaceable energy-dissipating fuses," *14th World Conference on Earthquake Engineering*, 2008.

[71] R. Sause, J. Ricles, D. Roke, N. Chancellor, and N. Gonner, *Large-scale experimental studies of damage-free self-centering concentrically-braced frame under seismic loading*, pp. 1498–1509. 2010.

[72] M. Pollino and M. Bruneau, "Seismic testing of a bridge steel truss pier designed for controlled rocking," *Journal of Structural Engineering*, vol. 136, no. 12, pp. 1523–1532, 2010.

[73] A. Ceccotti, F. Maurizio, L. M. Pio, and S. Carmen, "Results on the Lateral Resistance of Cross-Laminated Wooden Panels. SOFIE Project - Test," *First European Conference on Earthquake Engineering and Seismology, Geneva, Switzerland*, p. pp. 8, 2006.

[74] M. Popovski, J. Schneider, and M. Schwensteiger, "Lateral load resistance of cross-laminated wood panels," *World Conference on Timber Engineering, Trentino, Italy*, 2010.

[75] A. Palermo, S. Pampanin, A. Buchanan, and M. Newcombe, "Seismic design of multi-storey buildings using laminated veneer lumber (LVL)," *New Zealand Society of Earthquake Engineering Conference*, 2005.

[76] A. Palermo, S. Pampanin, and A. Buchanan, "Experimental Invesigations on LVL Seismic Resistant Wall and Frame Subassamblies," *First European Conference on Earthquake Engineering and Seismology*, 2006.

[77] A. Iqbal, S. Pampanin, A. Palermo, and A. Buchanan, "Performance and design of lvl walls coupled with ufp dissipaters," *Journal of Earthquake Engineering*, vol. 19, no. 3, pp. 383–409, 2015.

[78] E. McConnell, D. McPolin, and S. Taylor, "Post-tensioning of glulam timber with steel tendons," *Construction and Building Materials*, vol. 73, pp. 426–433, 2014.

[79] R. Ganey, "Seismic Design and Testing of Rocking Cross Laminated Timber Walls," Master's thesis, University of Washington, 2015.

[80] S. Pampanin, M. Priestley, and S. Sritharan, "Analytical modelling of the seismic behaviour of precast concrete frames designed with ductile connections," *Journal of Earthquake Engineering*, vol. 5, no. 3, pp. 329–367, 2001.

[81] M. P. Newcombe, *Seismic Design of Post-tensioned Timber Frame and Wall buildings*. PhD thesis, University of Canterbury, 2011.

[82] M. Priestley, "Direct Displacement-Based Design of precast/prestressed concrete buildings," *PCI Journal*, 2002.

[83] D. Pennucci, G. Calvi, and T. Sullivan, "Displacement-based design of precast walls with additional dampers," *Journal of Earthquake Engineering*, vol. 13, no. sup1, pp. 40–65, 2009.

[84] A. D. Cesare, F. Ponzo, S. Pampanin, T. Smith, D. Nigro, and N. Lamarucciola, "Displacement based design of post-tensioned timber framed buildings with dissipative rocking mechanism," *Soil Dynamics and Earthquake Engineering*, vol. 116, pp. 317 – 330, 2019.

[85] M. Priestley, G. Calvi, and M. Kowalsky, *Displacement-Based Seismic Design of Structures*. IUSS PRESS, Pavia, Italy, 2007.

[86] D. Marriot, *The Development of High-performance Post-tensioned Rocking Systems for Seismic Design of Structures*. PhD thesis, University of Canterbury, 2009.

[87] H. Spieth, A. Carr, A. Murahidy, D. Arnolds, M. Davies, and J. Mander, "Modelling of post-tensioned pre-cast reinforced concrete frame structures with rocking column connections," *2004 NZSEE Conference*, 2004.

[88] M. Vassiliou., K. Mackie, and B. Stojadinovićr, "A finite element model for seismic response analysis of deformable rocking frames," *Earthquake Engineering & Structural Dynamics*, vol. 46, no. 3, pp. 447–466, 2017.

[89] L. Wiebe and C. Christopoulos, "Mitigation of higher mode effects in base-rocking systems by using multiple rocking sections," *Journal of Earthquake Engineering*, vol. 13, no. sup1, pp. 83–108, 2009.

[90] M. Hasan, D. Roke, and Q. Huang, "Quanti

cation of higher mode responses for steel self-centering concentrically braced frames," *7th International Structural Engineering and Construction Conference*, 2013.

[91] L. Wiebe, C. Christopoulos, R. Tremblay, and M. Leclerc, "Mechanisms to limit higher mode effects in a controlled rocking steel frame. 1: Concept, modelling, and low-amplitude shake table testing," *Eartquake Engineering and Structural Dynamics*, vol. 42, pp. 1053–1068, 2013.

[92] L. Wiebe, C. Christopoulos, R. Tremblay, and M. Leclerc, "Mechanisms to limit higher mode effects in a controlled rocking steel frame. 2: Large-amplitude shake table testing," *Eartquake Engineering and Structural Dynamics*, vol. 42, pp. 1069–1086, 2013.

[93] A. Filiatrault and T. Sullivan, "Performance-based seismic design of nonstructural building components: The next frontier of earthquake engineering," *Earthquake Engineering and Engineering Vibration*, vol. 13, pp. 17–46, Aug 2014.

[94] L. Aragaw and P. Calvi, "Earthquake-induced floor accelerations in base-rocking wall buildings," *Journal of Earthquake Engineering*, pp. 1–29, 2018.

[95] N. Makris and G. Kampas, "Seismic protection of structures with supplemental rotational inertia," *Journal of Engineering Mechanics*, vol. 142, no. 11, pp. 1–11, 2016.

[96] Y. Nakamura, A. Fukukita, K. Tamura, I. Yamazaki, T. Matsuoka, K. Hiramoto, and K. Sunakoda, "Seismic response control using electromagnetic inertial mass dampers," *Earthquake Engineering & Structural Dynamics*, vol. 43, no. 4, pp. 507–527, 2014.

[97] C. Papageorgiou and M. Smith, "Laboratory experimental testing of inerters," *Proc. 44th IEEE Conf. on Decision and Control, IEEE, New York*, pp. 3351–3356, 2005.

[98] C. Papageorgiou, N. Houghton, and M. Smith, "Experimental testing and analysis of inerter devices," *Journal of Dynamic Systems, Measurement, and Control*, vol. 131, 12 2008.

[99] M. Chen, C. Papageorgiou, F. Scheibe, F. Wang, and M. Smith, "The missing mechanical circuit element," *IEEE Circuits and Systems Magazine*, vol. 9, no. 1, pp. 10–26, 2009.

[100] A. Kuznetsov, M. Mammadov, I. Sultan, and E. Hajilarov, "Optimization of improved suspension system with inerter device of the quarter-car model in vibration analysis," *Archive of Applied Mechanics*, vol. 81, pp. 1427–1437, 10 2010.

[101] S. Swift, M. Smith, A. Glover, C. Papageorgiou, B. Gartner, and N. Houghton, "Design and modelling of a fluid inerter," *International Journal of Control*, vol. 86, no. 11, pp. 2035–2051, 2013.

[102] A. Gonzalez-Buelga, I. F. Lazar, J. Z. Jiang, S. A. Neild, and D. J. Inman, "Assessing the effect of nonlinearities on the performance of a tuned inerter damper," *Structural Control and Health Monitoring*, vol. 24, no. 3, p. e1879, 2017.

[103] A. Gonzalez-Buelga, L. Clare, S. Neild, J. Jiang, and D. Inman, "An electromagnetic inerter-based vibration suppression device," *Smart Mater. Struct.*, vol. 24, no. 5, 2015.

[104] J. Hwang, J. Kim, and Y. Kim, "Rotational inertia dampers with toggle bracing for vibration control of a building structure," *Engineering Structures*, vol. 29, pp. 1201–1208, 2007.

[105] C. Málaga-Chuquitaype, C. Menendez-Vicente, and R. Thiers-Moggia, "Experimental and numerical assessment of the seismic response of steel structures with clutched inerters," *Soil Dynamics and Earthquake Engineering*, vol. 121, pp. 200–211, 03 2019.

[106] M. Chen, Y. Hu, L. Huang, and G. Chen, "Influence of inerter on natural frequencies of vibration systems," *Journal of Sound and Vibration*, vol. 333, no. 7, pp. 1874 – 1887, 2014.

[107] K. Ikago, Y. Sugimura, K. Saito, and N. Inoue, "Modal Response Characteristics of a Multi-Degree-of-Freedom Structure Incorporated with Tuned Viscous Mass Dampers," *Journal of Asian Architecture and Building Engineering*, vol. 11, pp. 375–382, 2012.

[108] I. Takewaki, S. Murakami, S. Yoshitomi, and M. Tsuji, "Fundamental mechanism of earthquake response reduction in building structures with inertial dampers," *Structural Control and Health Monitoring*, vol. 19, pp. 590–608, 2012.

[109] J. P. Den Hartog, *Mechanical vibrations*. 4th Ed., McGraw Hill,New York., 1956.

[110] Y. Hu, M. Z. Chen, Z. Shu, and L. Huang, "Analysis and optimisation for inerter-based isolators via fixed-point theory and algebraic solution," *Journal of Sound and Vibration*, vol. 346, pp. 17–36, 2015.

[111] A. Giaralis and A. Taflanidis, "Optimal tuned mass-damper-inerter (tmdi) design for seismically excited mdof structures with model uncertainties based on reliability criteria," *Structural Control and Health Monitoring*, vol. 25, no. 2, p. e2082, 2018.

[112] P. Cacciola, A. Tombari, and A. Giaralis, "An inerter-equipped vibrating barrier for noninvasive motion control of seismically excited structures," *Structural Control and Health Monitoring*, vol. 27, no. 3, p. e2474, 2020.

[113] D. DeDomenico and G. Ricciard, "An enhanced base isolation system equipped with optimal tuned mass damper inerter (tmdi)," *Earthquake Engineering & Structural Dynamics*, vol. 47, no. 5, pp. 1169–1192, 2018.

[114] D. De Domenico and G. Ricciardi, "Improving the dynamic performance of base-isolated structures via tuned mass damper and inerter devices: A comparative study," *Structural Control and Health Monitoring*, vol. 25, no. 10, p. e2234, 2018.

[115] N. Makris, "Basic response functions of simple inertoelastic and inertoviscous models," *Journal of Engineering Mechanics*, vol. 143, no. 11, p. 04017123, 2017.

[116] N. Makris and M. Vassiliou, "Planar rocking response and stability analysis of an array of free-standing columns capped with a freely supported rigid beam," *Earthquake Eng Struct Dyn*, vol. 42, no. 3, pp. 431–449, 2012.

[117] A. I. Motion, "Overrunning clutches application manual," *P-1052-FC by Formsprag Clutch LLC*, 2018.

[118] R. Daniels, "Design and Performance Characteristics of Over-Running Clutches in Gas Turbine Drive Applications," *Journal of Engineering for Power*, vol. 89, no. 2, pp. 207–215, 1967.

[119] MATLAB, *version 7.10.0 (R2010a)*. Natick, Massachusetts: The MathWorks Inc., 2010.

[120] A. Vaschy, " Sur les lois de similitude en physique," *Annales Telegraphiques*, vol. 19, pp. 25–28., 1892.

[121] E. Buckingham, "On physically similar systems; illustrations of the use of dimensional equations," *Phys. Rev.*, vol. 4, pp. 345–376, Oct 1914.

[122] E. Dimitrakopoulos and M. DeJong, "Revisiting the rocking block: closed-form solutions and similarity laws," *Proceedings of the Royal Society A: Mathematical, Physical and Engineering Sciences*, vol. 468, pp. 2294–2318, 2012.

[123] A. Anooshehpoor, T. Heaton, B. Shi, and J. Brune, "Estimates of the ground accelerations at point Reyes station during the 1906 San Francisco earthquake," *Bull. Seismol. Soc. Am*, vol. 89, pp. 845–853, 1999.

[124] C. Petrone, L. DiSarno, G. Magliulo, and E. Cosenza, "Numerical modelling and fragility assessment of typical freestanding building contents," *Bull Earthquake Eng*, vol. 15, no. 4, pp. 1609–1633, 2017.

[125] F. Gelagoti, R. Kourkoulis, I. Anastasopoulos, and G. Gazetas, "Rocking-isolated frame structures: margins of safety against toppling collapse and simplified design approach," *Soil Dyn Earthquake Eng*, vol. 32, no. 1, pp. 87–102, 2012.

[126] C. Málaga-Chuquitaype and K. Bougatsas, "Vector-im-based assessment of alternative framing systems under bi-directional ground-motion," *Engineering Structures*, vol. 132, pp. 188 – 204, 2017.

[127] J. Baker, "Efficient analytical fragility function fitting using dynamic structural analysis," *Earthquake Earthq Spectra*, vol. 31, no. 1, pp. 579–599, 2015.

[128] D. Moroder, S. Pampanin, A. Palermo, T. Smith, F. Sarti, and A. Buchanan, "Diaphragm connections in structures with rocking timber walls," *Structural Engineering International*, vol. 27, no. 2, pp. 165–174, 2017.

[129] N. Ricker, "Further developments in the wavelet theory of seismogram structure," *Bull. Seism. Soc. Am.*, vol. 33, no. 3, pp. 197–228, 1943.

[130] N. Ricker, "Wavelet functions and their polynomials," *Geophysics*, vol. 9, no. 3, pp. 314–323, 1944.

[131] M. Vassiliou and N. Makris, "Estimating time scales and length scales in pulselike earthquake acceleration records with wavelet analysis," *Bull. Seismol. Soc. Am.*, vol. 101, no. 2, pp. 596–618, 2011.

[132] F. Jalayer and C. Cornell, "Alternative non-linear demand estimation methods for probability-based seismic assessments," *Earthquake Engineering & Structural Dynamics*, vol. 38, no. 8, pp. 951–972, 2009.

[133] E. Miranda and S. Taghavi, *A comprehensive study of floor acceleration demands in multi-story buildings*, pp. 616–626. 2009.

[134] C. E. de Normalization, *Eurocode 8 - Design Provisions for Earthquake Resistant Structures, EN-1998-1:2004: E.*

[135] A. Miano, F. Jalayer, H. Ebrahimian, and A. Prota, "Cloud to ida: Efficient fragility assessment with limited scaling," *Earthquake Engineering & Structural Dynamics*, vol. 47, no. 5, pp. 1124–1147, 2018.

[136] T. Sullivan, P. Calvi, and R. Nascimbene, "Towards improved floor spectra estimates for seismic design," *Earthquakes and Structures*, vol. 4, no. 1, pp. 109–132, 2013.

[137] O. Adamidis, G. Gazetas, I. Anastasopoulos, and C. Argyrou., "Equivalent-linear stiffness and damping in rocking of circular and strip foundations," *Bulletin of Earthquake Engineering*, vol. 12, pp. 1177–1200, Jun 2014.

[138] H. Zhang, B. Brogliato, and C. Liu, "Dynamics of planar rocking-blocks with coulomb friction and unilateral constraints: comparisons between experimental and numerical data," *Multibody System Dynamics*, vol. 32, pp. 1–25, Jun 2014.

[139] J. Meek, "Dynamic response of tipping core buildings," *Earthquake Engineering & Structural Dynamics*, vol. 6, no. 5, pp. 437–454, 1978.

[140] S. Acikgoz and M. DeJong, "The rocking response of large flexible structures to earthquakes," *Bull Earthquake Eng*, vol. 12, p. 875–908, 2014.

[141] N. Makris and Y. Roussos, "Rocking response of rigid blocks under near-source ground motions," *Géotechnique*, vol. 50, no. 3, pp. 243–262, 2000.

[142] N. Makris, "Rigidity - plasticity - viscosity: Can electrorheological dampers protect base-isolated structures from near-source ground motions?," *Earthquake Engineering & Structural Dynamics*, vol. 26, no. 5, pp. 571–591, 1997.

[143] I. Psycharis, "Effect of base uplift on dynamic response of sdof structures," *Journal of Structural Engineering*, vol. 117, no. 3, pp. 733–754, 1991.

[144] J. Hall, T. Heaton, M. Halling, and D. Wald, "Near-source ground motion and its effects on flexible buildings," *Earthquake Spectra*, vol. 11, no. 4, pp. 569–605, 1995.

[145] R. Thiers-Moggia and C. Málaga-Chuquitaype, "Seismic protection of rocking structures with inerters," *Earthquake Engng Struct Dyn*, vol. 48, pp. 528–547, 2019.

[146] E. Avgenakis and I. Psycharis, "Modeling of inelastic rocking bodies under cyclic loading," *Journal of Engineering Mechanics*, vol. 146, no. 4, 2020.

[147] G. Gazetas, "Analysis of machine foundation vibrations: state of the art," *International Journal of Soil Dynamics and Earthquake Engineering*, vol. 2, no. 1, pp. 2–42, 1983.

[148] D. Barkan, *Dynamics of bases and foundations*. McGraw- Hill (translated), 1962.

[149] J. Dominguez and J. Roesset, "Dynamic stiffness of rectangular foundations," *Research Report R78-20, MIT*, 1978.

[150] R. Thiers-Moggia and C. Málaga-Chuquitaype, "Seismic response of uplifting flexible structures with inerters," *Manuscript submitted for publication in: Earthquake Engng Struct Dyn*, 2020.

[151] M. Priestley and A. Amaris, "Dynamic amplification of seismic moments and shear forces in cantilever walls," *Research Report ROSE-2002/01, IUSS Press, Pavia, Italy*, 2002.

[152] J. Moehle, R. Riddell, and R. Boroschek, "The mw 8.8 chile earthquake of february 27, 2010," *EERI Special Earthquake Report*, 2010.

[153] S. Pampanin, *Towards the Ultimate Earthquake-Proof Building: Development of an Integrated Low-Damage System*, pp. 321–358. Springer International Publishing, 2015.

[154] H. Aslani and E. Miranda, "Probabilistic earthquake loss estimation and loss disaggregation in buildings," *Report No. 157, John A. Blume Center Earthquake Engineering Center, Stanford, CA*, vol. 157, 2005.

[155] L. S. Jacobsen, "Damping in composite structures," *2nd World Conference on Earthquake Engineering, Tokyo and Kyoto, Japan*, pp. 1029–1044, 1960.

[156] H. Dwairi, M. Kowalsky, and J. Nau, "Equivalent damping in support of direct displacement-based design," *Journal of Earthquake Engineering*, vol. 11, no. 4, pp. 512–530, 2007.

[157] M. Davies and M. Fragiacomo, "Long termbehaviour of laminated veneer lumber (lvl) members prestressed with unbonded tendons," *New Zealand Timber Design Journal*, vol. 16, no. 3, pp. 13–20, 2008.

[158] T. Sullivan, M. Priestley, and G. Calvi, "A model code for the displacement-based seismic design of structures," *IUSS pressEarthquakes and Structures, Pavia, Italy.*, 2012.

[159] S. Pampanin, "Nzcs presss design handbook," *New Zealand Concrete Society, Wellington, New Zealand*, 2010.

[160] T. Sullivan, M. Priestley, and G. Calvi, "Estimating the higher-mode response of ductile structures," *Journal of Earthquake Engineering*, vol. 12, no. 3, pp. 456–472, 2008.

[161] G. Adhikari, L. Petrini, and G. Calvi, "Application of direct displacement based design to long span bridges," *Bulletin of Earthquake Engineering*, vol. 8, no. 4, pp. 897–919, 2010.

[162] N. Reggiani-Manzo and M. Vassiliou, "Displacement-based analysis and design of rocking structures," *Earthquake Engineering & Structural Dynamics*, vol. 48, no. 14, pp. 1613–1629, 2019.

[163] K. Tsai, H. Chen, C. Hong, and Y. Su, "Design of steel triangular plate energy absorbers for seismic-resistant construction," *Earthquake Spectra*, vol. 9, no. 3, pp. 505–528, 1993.

[164] R. B. Srl, *Screws and connectors for wood.* Cortaccia(BZ), Italy, 2019.

[165] N. Luco and P. Bazzurro, "Does amplitude scaling of ground motion records result in biased nonlinear structural drift responses?," *Earthquake Engineering & Structural Dynamics*, vol. 36, no. 13, pp. 1813–1835, 2007.

[166] H. Dávalos and E. Miranda, "Evaluation of bias on the probability of collapse from amplitude scaling using spectral-shape-matched records," *Earthquake Engineering & Structural Dynamics*, vol. 48, no. 8, pp. 970–986, 2019.

[167] Fema 356, *Prestandard and commentary for seismic rehabilitation of buildings*. 2000.

[168] C. Málaga-Chuquitaype, M. Psaltakis, G. Kampas, and J. Wu, "Dimensionless fragility analysis of seismic acceleration demands through low-order building models," *Bulletin of Earthquake Engineering*, vol. 17, pp. 3815–3845, 2019.

[169] J. Carballo and C. Cornell, "Probabilistic seismic demand analysis. Reliability of Marine Structures Program Report No. RMS-41," *Department of Civil and Environmental Engineering, Stanford University, Stanford*, 2000.

[170] P. Bazzurro and N. Luco, "Parameterization of non-stationary acceleration time histories," *Report on PEER-LL Program Task 1G00, Richmond*, 2003.